MICROCOPY RESOLUTION TEST CHART
NATIONAL BUREAU OF STANDARDS-1963-A

AFOSR-TR- 85-0666

AMRC-R-692
Copy 16

AD-A159 394

FINAL REPORT OF THE MILLIMETER WAVE VIRCATOR

Donald J. Sullivan
Donald E. Voss
Richard J. Adler
Kenneth O. Busby
E. Michael Bollen
Robert H. Jackson
Michael K. Williams
John E. Walsh*
Evangelos A. Coutsias**

June 1985

Prepared for: Air Force Office of Scientific Research
                  Physics Directorate
                  Bolling Air Force Base
                  Washington, D.C. 20332

Under Contract: F49620-82-C-0014

Approved for public release;
distribution unlimited.

Prepared by: MISSION RESEARCH CORPORATION
                  1720 Randolph Road, SE
                  Albuquerque, New Mexico 87106

DTIC
ELECTE
SEP 25 1985

A

* Dartmouth College
** University of New Mexico

This manuscript is submitted for publication with the under-
standing that the United States Government is authorized to
reproduce and distribute reprints for governmental purposes.

DTIC FILE COPY   85 9 09 075

REPORT DOCUMENTATION PAGE		READ INSTRUCTIONS BEFORE COMPLETING FORM
1. REPORT NUMBER **AFOSR-TR- 85-0666**	2. GOVT ACCESSION NO. AD. A159394	3. RECIPIENT'S CATALOG NUMBER
4. TITLE *(and Subtitle)* FINAL REPORT OF THE MILLIMETER WAVE VIRCATOR		5. TYPE OF REPORT & PERIOD COVERED FINAL REPORT 1 JAN 82 - 31 MAR 85
		6. PERFORMING ORG. REPORT NUMBER AMRC-R-692
7. AUTHOR(s) D. J. Sullivan K. O. Busby John E. Walsh D. E. Voss E. M. Bollen E. A. Coutsias R. J. Adler R. H. Jackson M. K. Williams		8. CONTRACT OR GRANT NUMBER(s) F49620-82-C-0014
9. PERFORMING ORGANIZATION NAME AND ADDRESS Air Force Office of Scientific Research Bolling Air Force Base Washington, DC 20332		10. PROGRAM ELEMENT, PROJECT, TASK AREA & WORK UNIT NUMBERS 61102F 2301/A8
11. CONTROLLING OFFICE NAME AND ADDRESS MISSION RESEARCH CORPORATION 1720 Randolph Road, SE Albuquerque, NM 87106		12. REPORT DATE May 1985
		13. NUMBER OF PAGES 318
14. MONITORING AGENCY NAME & ADDRESS*(if different from Controlling Office)*		15. SECURITY CLASS *(of this report)* UNCLASSIFIED
		15a. DECLASSIFICATION DOWNGRADING SCHEDULE
16. DISTRIBUTION STATEMENT *(of this Report)* APPROVED FOR PUBLIC RELEASE; DISTRIBUTION UNLIMITED		
17. DISTRIBUTION STATEMENT *(of the abstract entered in Block 20, if different from Report)*		
18. SUPPLEMENTARY NOTES		
19. KEY WORDS *(Continue on reverse side if necessary and identify by block number)* Virtual Cathode, Space-Charge Limiting Current, Virtual Anode Millimeter Microwaves Virtual Cathode Oscillator Spectrometer, VIRCATOR Space-Charge Limit		

20. ABSTRACT *(Continue on reverse side if necessary and identify by block number)*

The millimeter wave vircator has achieved a frequency in excess of 39.9 GHz and a peak power of the order of 21 kilowatts ($f \gtrsim 26.35$ GHz) for a pulse duration of as short as 5 ns full width at half maximum. A new moderate voltage, high current density, field emission gun has been tested to a voltage of 67 kV and an inferred current density of 7 kA/cm^2. A new compact capacitive voltage monitor, similar to those commonly used in radar modulators, has been developed for short pulse, fast risetime, low to moderate impedance pulse lines.

DD $_{1\ JAN\ 73}^{FORM}$ 1473   EDITION OF 1 NOV 65 IS OBSOLETE

Roth smooth bore and resonant cavity microwave structures have heen tested. The resonant cavity appears to operate at much higher powers.

ABSTRACT

The millimeter wave vircator has achieved a frequency in excess of 39.9 GHz and a peak power of the order of 21 kilowatts ($f \geq 26.35$ GHz) for a pulse duration of as short as 5 ns full width at half maximum. A new moderate voltage, high current density, field emission gun has been tested to a voltage of 67 kV and an inferred current density of 7 kA/cm^2. A new compact capacitive voltage monitor, similar to those commonly used in radar modulators, has been developed for short pulse, fast risetime, low to moderate impedance pulse lines.

Both smooth bore and resonant cavity microwave structures have been tested. The resonant cavity appears to operate at much higher powers.

i

TABLE OF CONTENTS

LIST OF ILLUSTRATIONS

I. BASIC THEORY AND IT'S APPLICATION TO AN EXPERIMENTAL DEVICE

The oscillator in the virtual cathode oscillator is a dense electron plasma trapped between the real cathode of an electron gun and a virtual cathode due to an excess of electron space charge. The virtual cathode is usually formed by passing an intense electron beam through a volume where the space charge limit is exceeded. The electrons are stopped and reflected by this virtual cathode, and thus oscillate back and forth between the real and virtual cathodes.

The natural oscillation period is the round trip electron transit time between the anode and the virtual cathode. These oscillations couple to the longitudinal electric field of a microwave mode. See Figure 1 for a typical geometry. The oscillation frequency is given by[1]:

$$f_{osc} = 10.2 \sqrt{\frac{j}{\beta_z \gamma}} \quad \text{GHz} \quad , \tag{1}$$

where j is the current density (kA/cm^2) at the anode, β_z is the longitudinal velocity to the speed of light ratio at the anode, and γ is the relativistic factor.

The geometry of Figure 1 naturally leads to a quasi-optical type device assuming that the virtual cathode is a reasonable distance from the anode. No linear or nonlinear calculations have been done to predict the behavior of a virtual cathode oscillator in this situation, but drawing upon the experience of the NRL quasi-optical gyrotron,[2] we can make some reasonable estimates. Based upon an output power of 1MW, the Q of the cavity would need to be roughly 1000. The quasi-optical waist would be $\geq 2\lambda$, where λ is the free space wavelength of the microwave radiation. The electron gun voltage would need to be chosen such that the virtual cathode would form at least one free space wavelength λ away from the anode. The mirror separation would be approximately several inches so that the cavity fill time is no longer than ten.

3
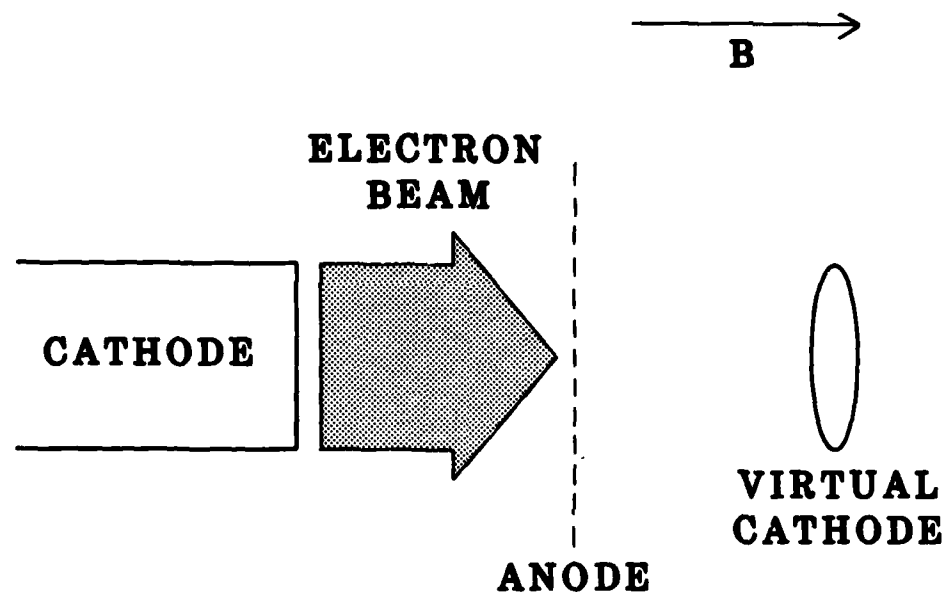
Figure 1. Virtual cathode oscillator.

nanoseconds. The type of magnet required to confine the electron beam would be Helmholtz coils in order to have access to the transverse area of the virtual cathode. The pulse coil technology would require the mirror mounts and supports be constructed of a plastic or some other non-metal. The mirrors would be made by plating gold or painting a silver compound on the plastic forms. The coupling of the cavity to the outside world could be controlled by the thickness of the gold or silver or by apertures machined into the mirrors. A conceptual drawing of this device is shown in Figure 2.

In practice, the above quasi-optical system may be difficult to implement because the virtual cathode forms much too close to the anode. Modeling the vircator as a nonrelativistic klystron[3], we find:

$$f \geq .188 \, V_0/d \, ,$$

where f is the microwave frequency, V_0 is the electron velocity at the anode and d is the anode-virtual cathode gap. For a 51 kV electron beam and f = 30 GHz, the anode-virtual cathode spacing is $\leq$ 1 mm. There is no way we can fit the quasi-optical beam waist (~ 2 cm) into the available space.

Two alternate tunable cavity vircators are presented in Figures 3 and 4. Figure 3 presents a novel approach that overcomes the problem of a short anode-virtual cathode spacing by placing the quasi-optical waist concentric with the vircator's z axis. Thus the anode becomes one mirror of the resonator and not an obstacle to the microwave mode envelope and mirrors, as in Figure 2.

Another approach using conventional microwave hardware is presented in Figure 4. The resonator would be formed from a segment of rectangular waveguide, terminated at one end by a thin metal piece with a small aperture and at the other end by a sliding short. This arrangement may allow us to couple the output through the aperture into the fundamental TE_{10} rectangular waveguide mode. Note that while operating in a fundamental mode is attractive, the waveguide at mm wavelengths is small and has limited power capabilities because of microwave breakdown.
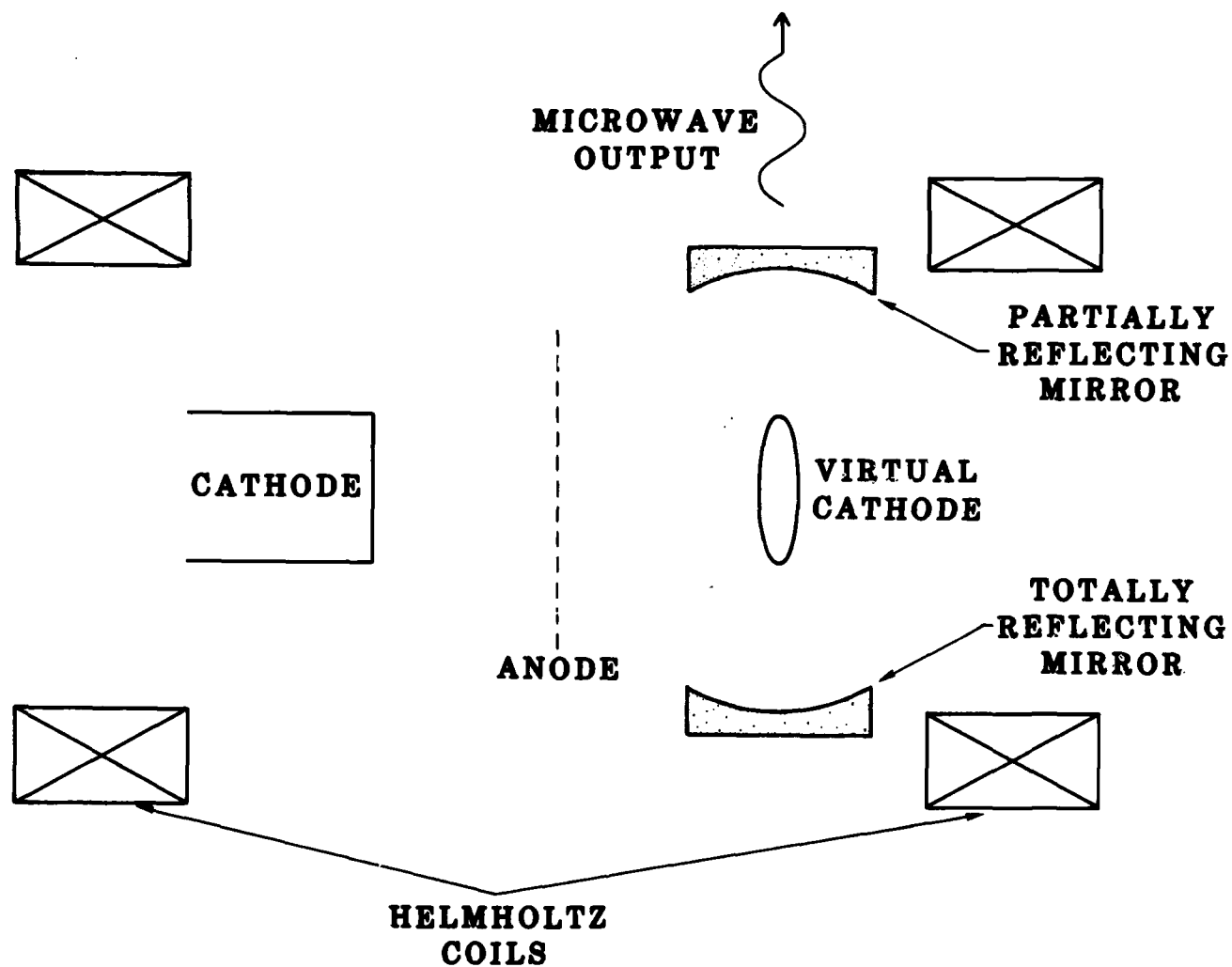
Figure 2. Quasi-optical vircator.

6
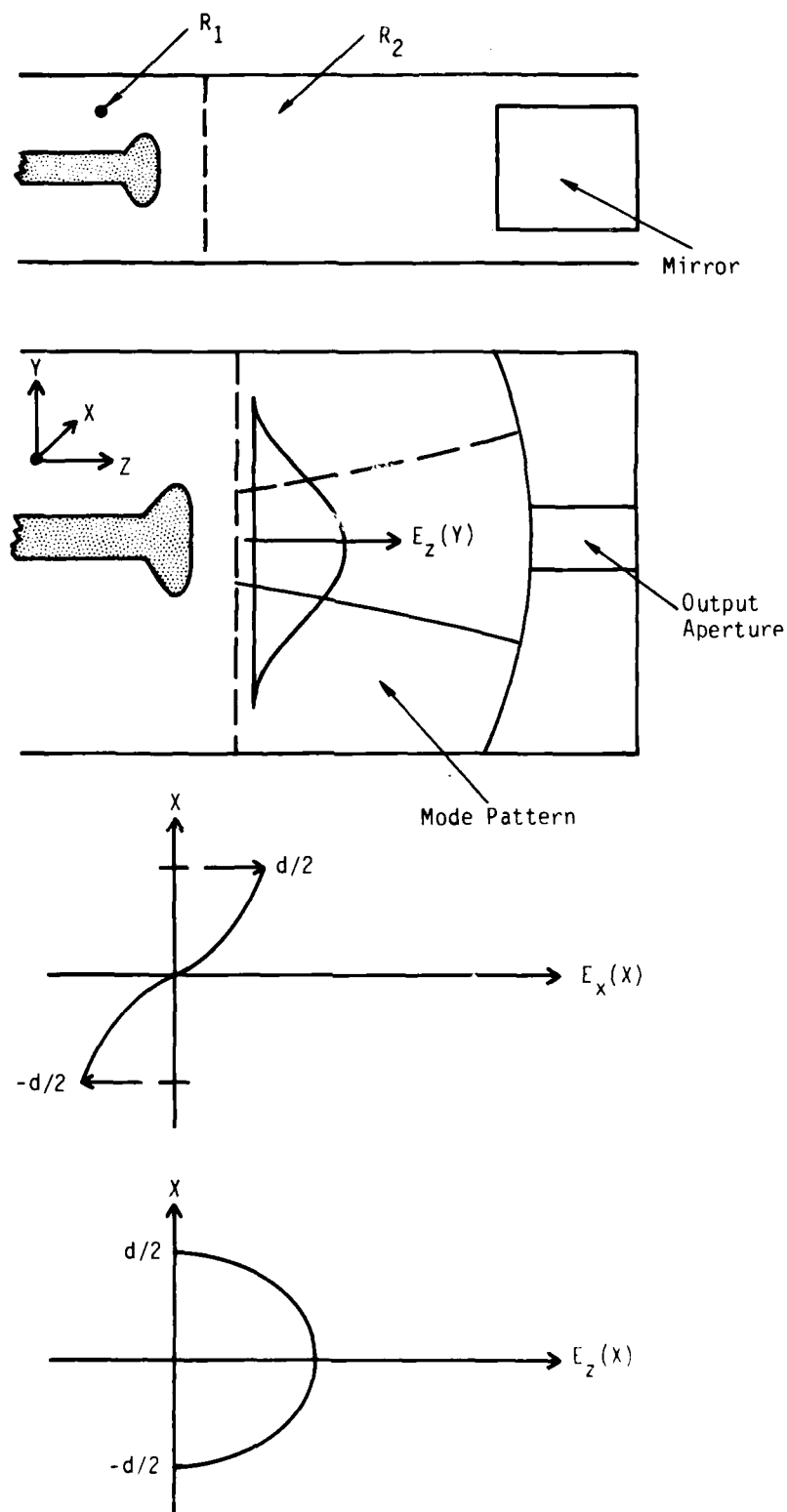
Figure 3. An alternative quasi-optical oscillator.[4]
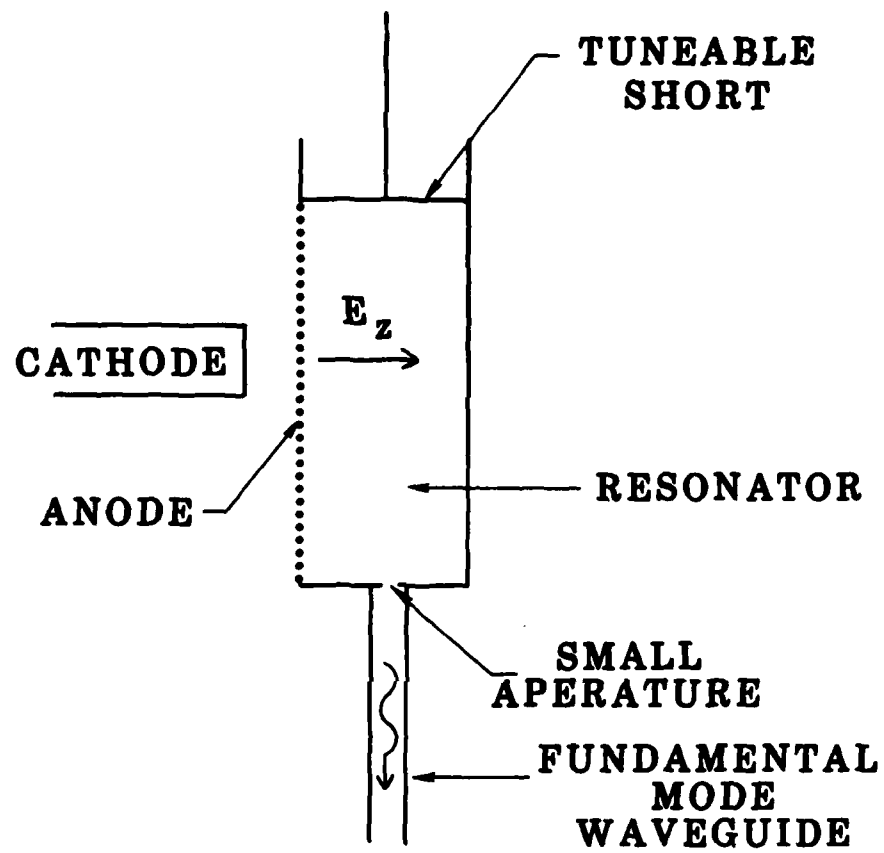
Figure 4. A vircator design using rectangular waveguide.[5]

The conventional approach for a high power microwave cavity is the right circular cylinder, as shown in Figure 5. Its advantage is that it is simpler to construct than a quasi-optical cavity, but the quasi-optical cavity can be made tunable in a straightforward manner.

There are two different approaches to the conventional cavity; one being a long, moderate to high Q cavity and the other a short, low Q cavity. The first type would have many sinusoidal variations in the longitudinal electric field profile. For a 1 MW microwave output, the Q should be roughly 1000, and the cavity would be four to ten free space wavelengths (λ) long[6]. For 50 GHz microwaves, the free space wavelength is 6 mm.

The second type would be a short cavity whose length would be about one free space wavelength (λ) long. Its longitudinal electric field profile would be half sinusoidal or Gaussian. A Q in the 100's should result in a multimegavolt power output. See Figure 6 for a schematic of the conventional cavity types. As before, the virtual cathode will be located ≤ 1 mm from the anode. Our cavity in the experiment was 2.49 cm long, which is 2.2λ for f = 26.35 GHz and 3.3λ for f = 39.9 GHz.

The third and most common approach is not to use a microwave cavity at all. The virtual cathode is formed within a large volume or pipe and is allowed to radiate freely. This approach has produced the most impressive peak power to date, but the efficiencies (except for the Russian experiments[7]) still remain low (1 to 5%). Our smooth bore experiments would fit into this category.

In the short term, the effort should be concentrated towards making the vircator 10 to 50% efficient at a modest (1 to 10 Hz) repetition rate in a microwave mode useful to some application. In the longer term, an efficient virtual cathode amplifier will need to be demonstrated.
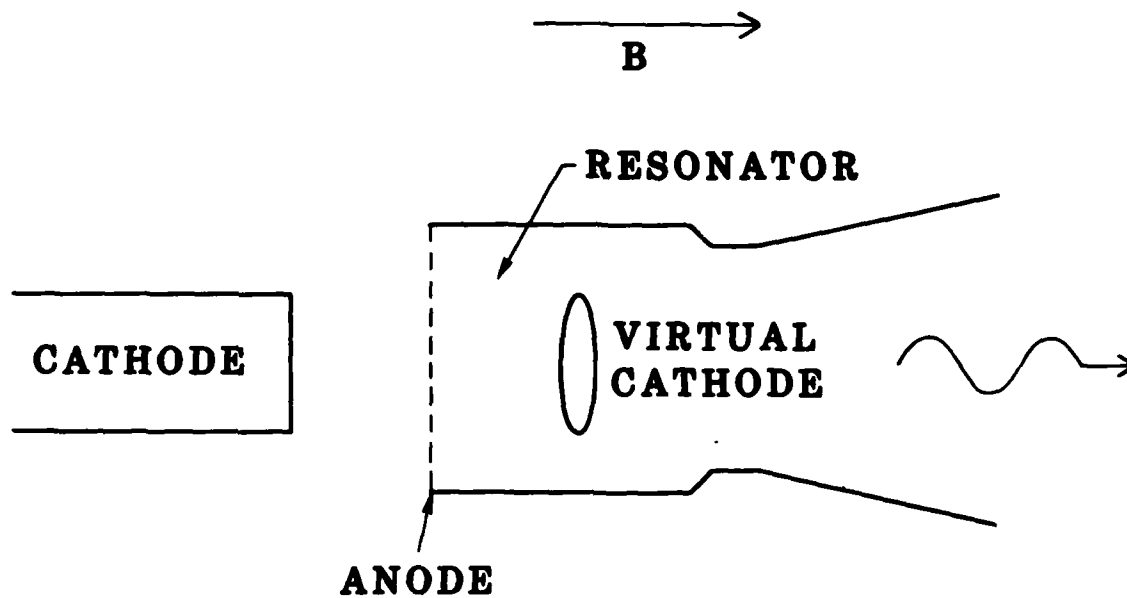
Figure 5.   Conventional cavity vircator.
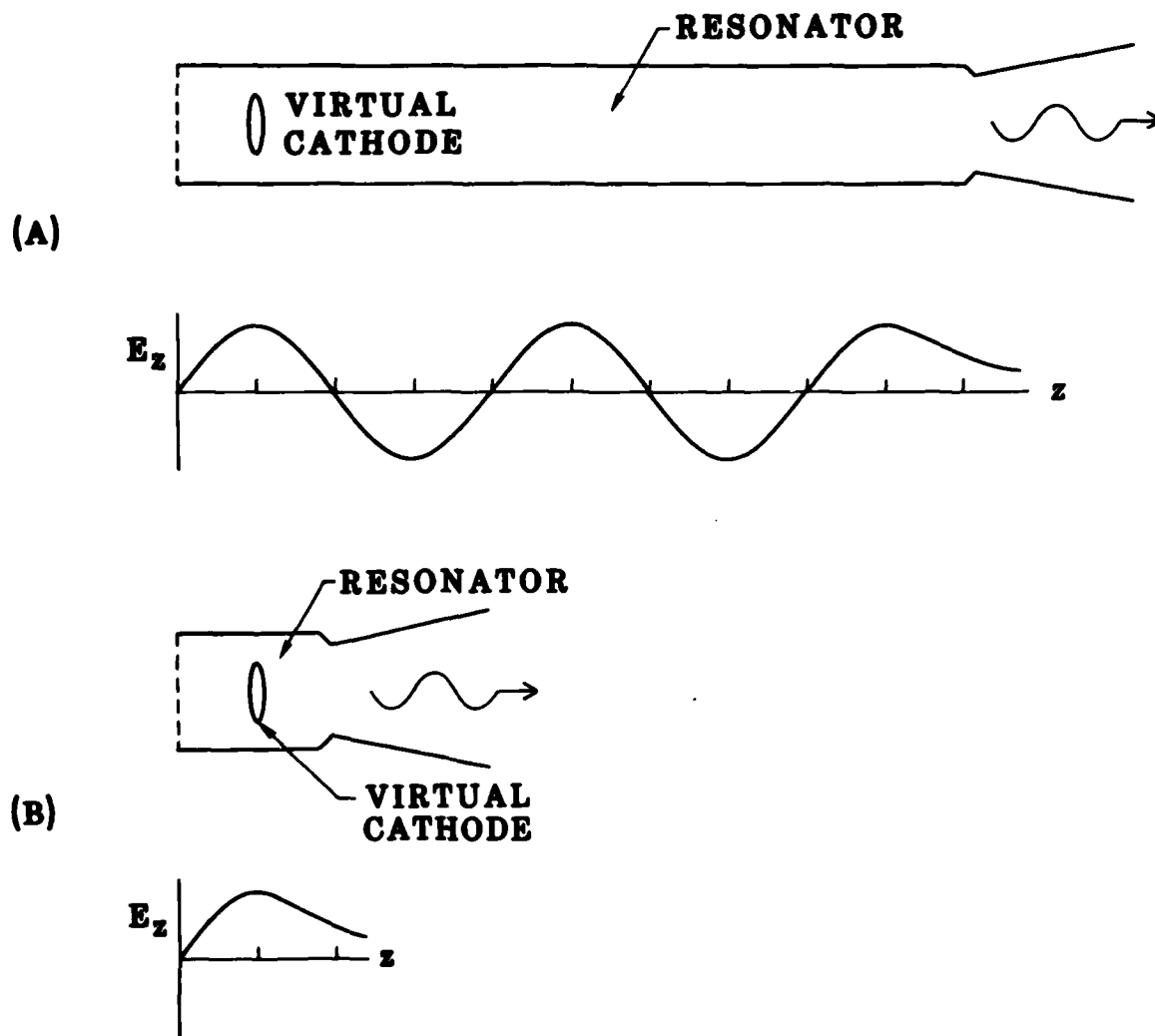
Figure 6. Long (A) and short (B) conventional cavities.

The organization of this report will be as follows. Vircator design considerations and some realities in microwave measurement are discussed in Chapter 2. In Chapter 3, the basic components of the vircator will be described. The descriptions of the cable Blumlein, the pulse forming network, the vacuum system, and the magnet power supply are given in Appendices C and D and will not be repeated here. In Chapter 4, the smooth bore and resonant cavity experimental results are presented. Some recommendations are given in Chapter 5. Appendices A and B contain Abstracts for New Technology for our voltage monitor and electron gun. Previous annual reports are given in Appendices C and D.

II. VIRCATOR DESIGN AND MICROWAVE
MEASUREMENT ISSUES

For a virtual cathode to be formed, the space charge limiting electron current I_L that can be propagated through a drift tube must be exceeded. The limiting current is given by[8]

$$I_L \approx 17.0 \; \frac{(\gamma_0^{2/3} - 1)^{3/2}}{1 - f(\epsilon) + 2 \ln (\frac{R}{b})} \; kA \qquad (1)$$

where

$$f(\epsilon) = \frac{(1 - \epsilon)^2}{1 - \frac{\epsilon}{2}} \; \left| \frac{\ln(1-\epsilon)}{\epsilon} \right| \qquad (2)$$

and

$$\epsilon = \frac{b-a}{b} \; . \qquad (3)$$

γ_0 is the electron relativistic factor; R, a, and b are the inner radius of the grounded drift tube, the inner radius of the electron beam, and the outer radius of the beam, respectively. See Figure 7. Assuming a 51 kV electron beam and R = 8.64 mm, which is the radius of the experiment's drift tube, we find that the limiting currents for the two cathodes used are:

Poco Graphite: $I_L \approx 140$ A   a = 3.07 mm,   b = 3.18 mm
Stainless Steel: $I_L \approx 110$ A   a = 2.24 mm,   b = 2.34 mm

The above calculation implicitly assumes that the electron beam dimensions are the same as the cathode's. Witness targets are difficult to interpret due to A-K gap closure and averaging over many shots, but they indicate the electron beam's average radius is within ±1.5 mm of the cathode diameter.

13
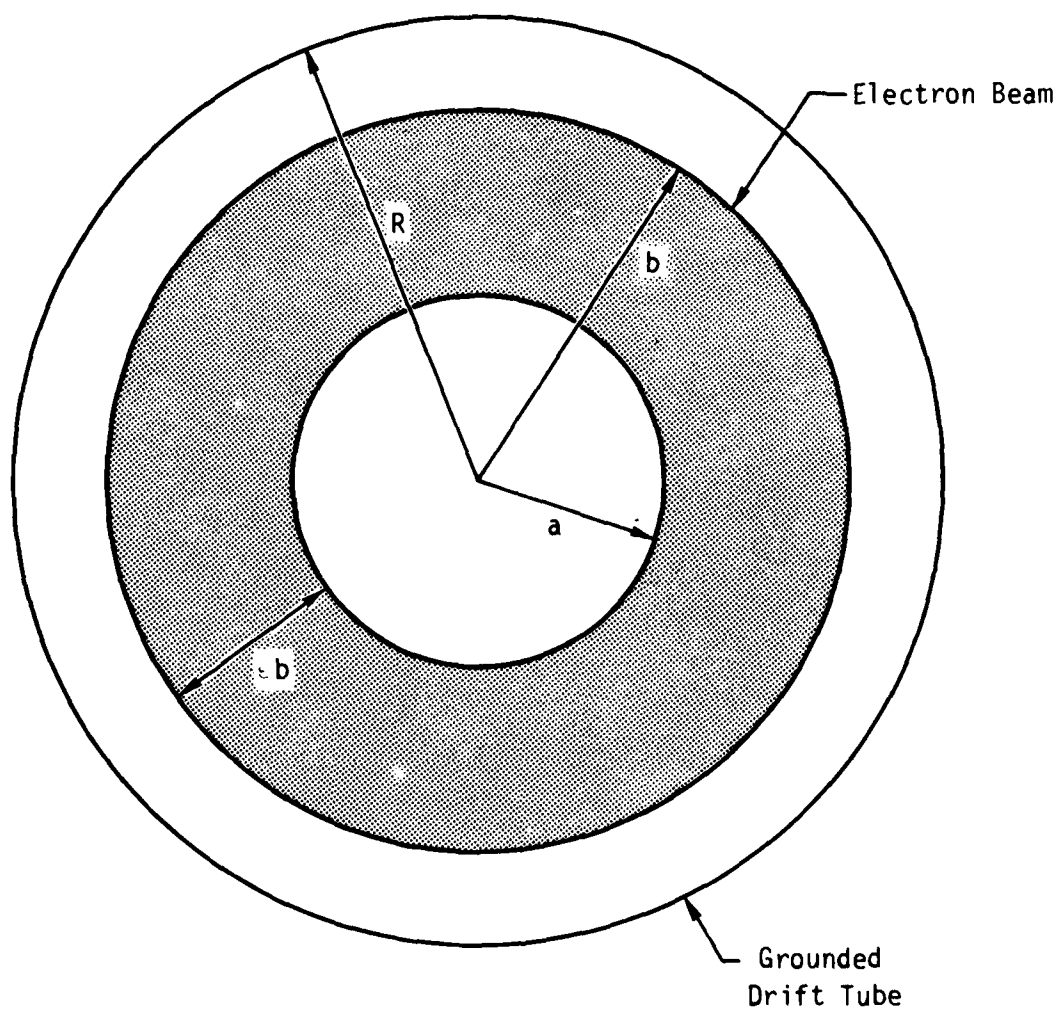
Figure 7. The electron beam geometry.[9]

However, the beam thickness is somewhere between 1.3 and 5 times the cathode thickness ($= \epsilon b$). Even so, the limiting currents listed above are approximately correct.

We can also develop a simple model to determine if the observed microwave production is due to a collective interaction or to single particle scattering. In a single scattering event, an electron may emit a photon. To call the interaction collective, we require that each electron, on the average, emit at least 1000 photons. This model can be expressed by the formula:

$$P_{collective} \geq .0041 \, fI, \qquad (4)$$

where $P_{collective}$ is the minimum power for a collective interaction, f is the microwave frequency in GHz, and I is the electron beam current in amperes. For example, if the beam current is 200 A and the frequency is 10 GHz, then $P_{collective} \geq 8$ W. If the beam current is 1 kA and the frequency is 40 GHz, then $P_{collective} \geq 160$ W.

It is important to know the basic properties of the microwave circuit. The circuit basically consists of a 17.3 mm diameter tube. The four most fundamental cut-offs for this tube are:

TE_{11} : $f_{co} = 10.2$ GHz

TM_{01} : $f_{co} = 13.3$ GHz

TM_{11} or TE_{01} : $f_{co} = 21.2$ GHz.

It's apparent that high order microwave modes can result as we push into the 50 GHz regime. Also note that the conditions for virtual cathode formation (i.e. large drift tube) and for operation in a fundamental mode at mm wavelengths (i.e. small drift tube) compete with each other and require an engineering compromise.

Since the vircator experiment has not yet produced enough power to use our spectrometer for absolute frequency measurements, we have to use the high pass characteristics of our standard microwave components. For example, V band components are routinely used for microwave frequencies from 50 to 75 GHz. V band waveguide will propagate frequencies as low as 39.9 GHz and perhaps as high as ultraviolet radiation. The response of the 1N53 crystals used in our V band detectors usually drop off quickly above 110 GHz. The cutoff frequencies of the waveguide bands we used are as follows:

X band (8-12 GHz)   : $f_{co} = 6.56$ GHz
KU band (12-18 GHz)   : $f_{co} = 9.525$ Ghz
B band (33-50 GHz)   : $f_{co} = 26.35$ GHz
V band (50-75 GHz)   : $f_{co} = 39.90$ GHz
W band (75-100 GHz)   : $f_{co} = 59.05$ GHz .

Originally the B and V band detectors were to be used only for the measurement of frequency and an air breakdown chamber was to measure the total power. Unfortunately no air breakdown has been observed thus far. However, the use of standard microwave detectors on short pulse experiments is common, but this practice has several pitfalls. The first is that the detector crystals need to be terminated into 50Ω in order to achieve a ns video response. We derated the Q and V band detector outputs by a factor of 40 from the detector response when terminated into 1 MΩ. Presently, no mm wave sweeper is available to verify this derated crystal response, but generally a 1 kΩ termination cuts the crystal voltage in half and a 50Ω termination should reduce the crystal voltage by another factor of 20. The second pitfall is that these detectors are easily driven into a nonlinear range where a factor of 2 in voltage may correspond to a factor of 10 in power. We assumed the detector response to be linear with the power in the calculations because extrapolating several orders of magnitude in power on standard detector response charts is unacceptable. Comparing our signals (some as high as 600 mV into 50Ω) with standard diode response charts, we found that the signals may correspond to many watts.

The third and possibly most misleading pitfall is the antenna pattern. With calibrated detectors, an antenna pattern measurement can be made. Since the vircator has a broad frequency spectrum ($\leq$ 10 GHz to $\geq$ 39.9 GHz), there may be several different modes, each with its own antenna pattern. For comparison sake, the formula generally used for the power calculations is:[10]

$$P_t = \frac{P_r (4\pi R)^2}{G_r G_t \lambda^2} \tag{5}$$

where P_t is the transmitted microwave power and P_r is the received microwave power. G is the horn gain, R is the distance between the transmitting and receiving horns, λ is the radiation wavelength, and the subscripts t and r denote the transmitter and receiver, respectively. The effective area (A_{eff}) of a horn is defined as:[11]

$$A_{eff} = \frac{G\lambda^2}{4\pi} \tag{6}$$

The derivation of Equation (5) is based upon the model of an isotropic radiator where G is a measure of a horn's directivity. Calibrated curves for the B and V band horns are given in Figures 8 and 9. For the calculation of power, the B and V band horns were assigned the gains of 23.4 db and 24.0 db, respectively, because we using the microwave hardware as high pass filters at or near the cut-off frequencies. The gains of the open ended B and V band waveguides are calculated from Equation (6) to be $2.0/\lambda^2$ and $0.89/\lambda^2$ based on the actual areas of 0.16 cm^2 and 0.071 cm^2 respectively. R, the distance from the transmitter to receiver horns, ranged from 65.4 cm to 78.5 cm. G, the gain, is for a TE_{11} circular mode or a TE_{10} rectangular mode.

The above theory is standard for forward directed antenna patterns from a rectangular horn in the TE_{10} mode or from a circular horn in a TE_{11} mode. Unfortunately, TM modes are expected to be produced by vircators and the TM_{on} antenna patterns are donuts directed outward in cones at angles

17
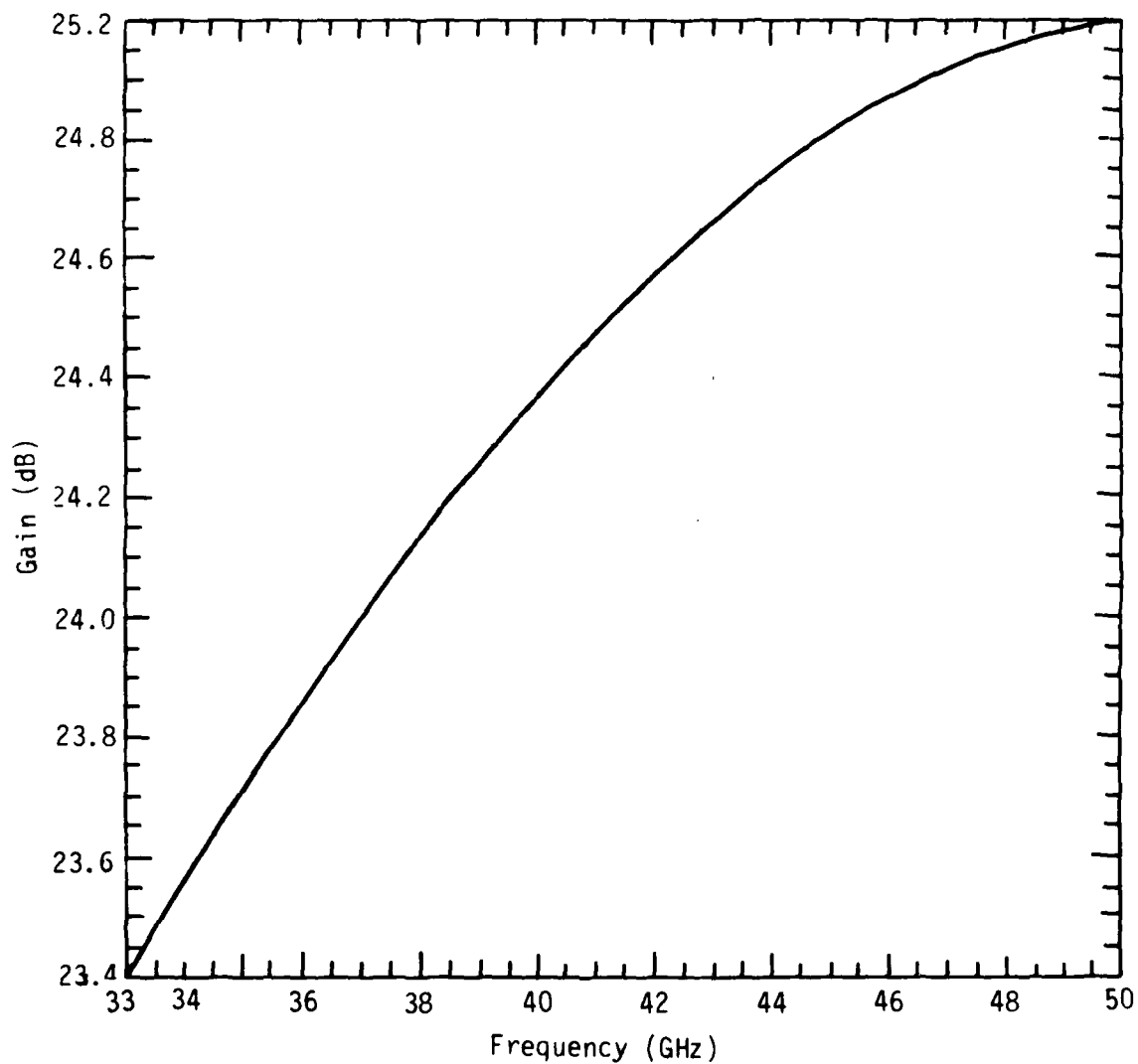
Figure 8. Manufacturer provided calibration curve for the B band (33-50 GHz) 25 db standard gain horn (TRG Model #B861).
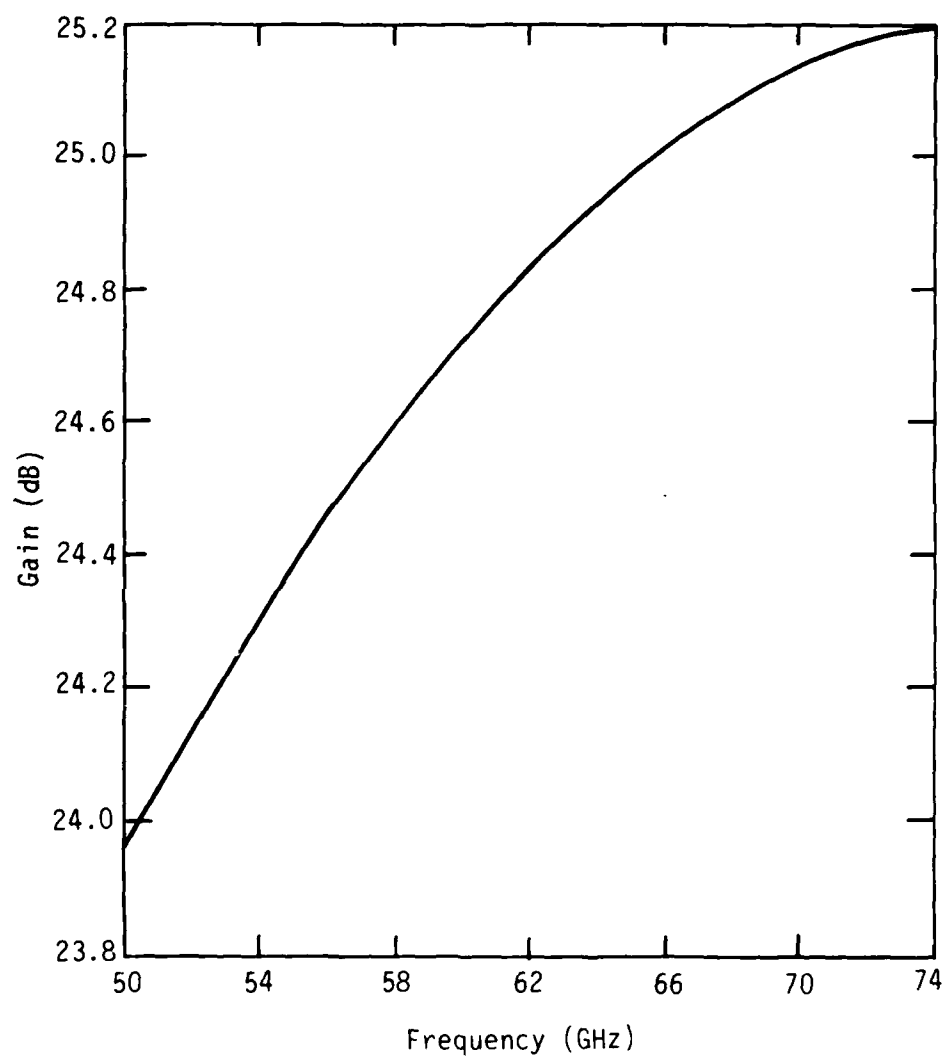
Figure 9. Manufacturer provided calibration curve for the V band (50-75 GHz)
25 db standard gain horn (TRG Model #V861).

ranging from one-half to the full cone angle of the transmitting horn.[12]
An approximate formula for the TM antenna patterns is given by:[13],[14]

$$E_\theta = -j \frac{kaK_{mn}}{2R} \left[\frac{\beta_{mn}}{K} + \cos\theta \right]$$

$$\times \frac{J_0(ka\sin\theta) \, J_0'(K_{mn}a)}{\sin^2\theta - (\frac{K_{mn}}{K})} \sin\theta \, e^{-jkR} \tag{7}$$

where the effects of reflections from the horn's mouth are neglected. The
geometry is presented in Figure 10 and the definitions of the variables in
Equation (7) are:

$$K = \frac{2\pi}{\lambda} \tag{8a}$$

$$\beta_{mn} = \frac{2\pi}{(\lambda_{guide})_{mn}} \tag{8b}$$

$$K_{mn} = 2.4048, \, 5.5201, \, 8.6537 \qquad (m = 0, \, n = 1,2,3) \tag{8c}$$

The approximations in the derivation of Equation (7) are that the wall cur-
rents at the aperture are excluded and the aperture is surrounded by an
infinite plane with no electric or magnetic fields. Essentially, the
higher order fields at the aperture are excluded, but if the aperture diam-
eter is one or more radiation wavelengths, λ, wide, then the approximations
are valid. Also, (7) is for a straight piece of waveguide that is open on
one end and not for a horn. Our detectors were located at $\theta = 0°$, and
according to (7), $E_\theta = 0$. Obviously, this was not the case in reality.
A more complete theoretical analysis is beyond the scope of this report.
For the sake of a reasonable estimate of power, the power derived from
Equation (5) shall be multipled by a factor of 100 (20 db).

$$P = 100 \, \frac{P_r(4\pi R)^2}{G_r G_t \lambda^2} \tag{9}$$
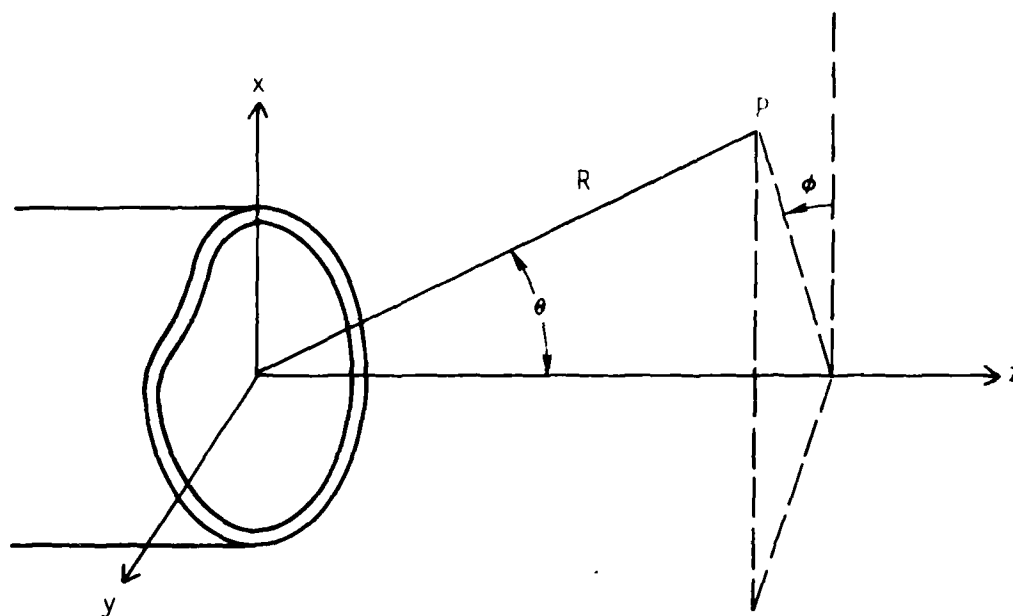
Figure 10.   The geometry for Equation 7.[15]

Considering the two factors that the detectors were probably nonlinear and may have a degraded response due to use and that the power should be theoretically zero at the position of the detectors, a multiplication factor of 20 or 30 db is not beyond reason. A factor of 20 db is chosen as a compromise figure. The powers to be quoted should be considered as a guide. The actual power could be 10 times lower or 10 times higher. Equation (9) will be applied only to the B and V band detectors. G_t, the gain of the conical horn output of the vircator, will be calculated using a standard chart.[16] For B band, G_t is 17 db and for V band, G_t is 20 db. The X and Ku band detectors were at point blank range of the vircator output and it is assumed that they collected the total power in a particular polarization. Until either we obtain the microwave sweepers to calibrate the detectors and map out a meaningful antenna pattern (which is not presently possible) or achieve air breakdown, this is the best that can be done.

III. THE EXPERIMENTAL APPARATUS

A conventional microwave cavity was chosen to be used in the initial
vircator design. While in the long run, the quasi-optical vircator has the
advantage of tunability and better microwave mode control, the conventional
cavity was immediately applicable to the available pulse solenoid.

An assembly drawing of the vircator electron gun, magnet, and micro-
wave circuit is shown in Figure 11. The electron gun is powered by a con-
ventional cable Blumlein. The gun will operate nominally at 50 to 67 kV
and 1 to 2 kA for a pulse length of 50 to 150 ns. This range of the
operating parameters is due to different anode-cathode (A-K) gaps and the
effects of gap closure. A typical A-K gap is 2 to 3 mm, but occasionally
is as large as 12 mm. A cable Blumlein capable of 75 kV at 1.5 kA for a
pulse duration of 200 ns was used.[17] The pulse solenoid which provides the
confining magnetic field for the electron beam provides a nominal 10 to
15 kG longitudinal field and is capable of providing up to 39 kG. Its
quarter cycle risetime is 1.1 ms. The magnet power supply consists of a
1050 µF capacitor and ignitron and the basic circuitry has been described
in a previous report.[18]

Two different electron gun cathodes were used. The graphite cathode
is a 6.35 mm diameter cylinder bored out such that only a 0.1 mm thick
annular electron emitter remains. The stainless steel cathode was an
annulus with an I.D. and O.D. of 4.47 mm and 4.67 mm, respectively. The
anode was either a flat metallic screen (nickel, bronze, or tungsten) or
the stainless steel piece shown in Figure 11.

The microwave circuit consists of a 17.3 mm I.D. stainless steel tube
and an anode. The anode accelerates the electrons and inhibits the micro-
waves from traveling back into the gun region. The anode shown in Figure
11 incorporates a cutoff section of 6.9 mm I.D. and 12.7 mm length. In the
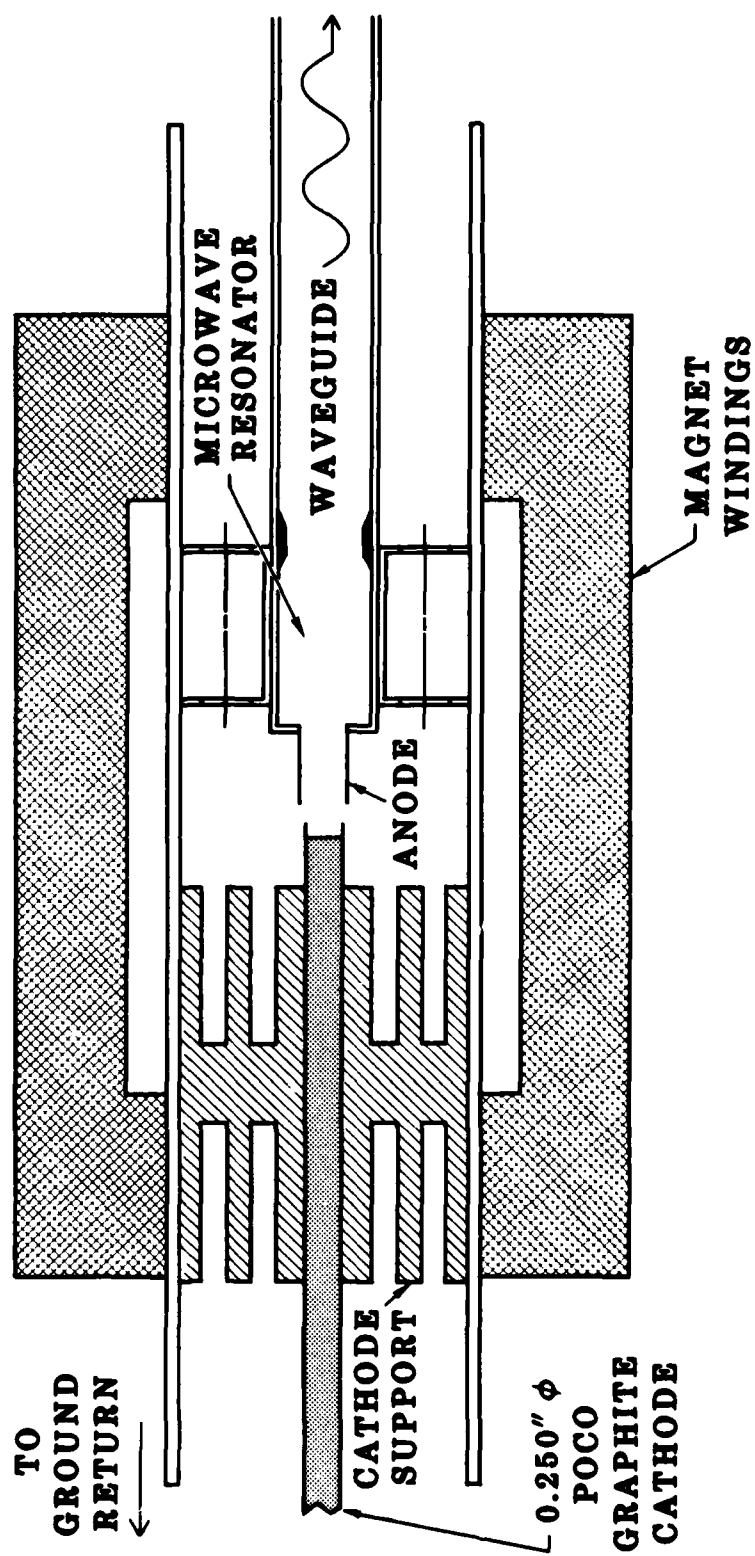
Figure 11. Vircator electron gun and microwave circuit assembly.

MICROWAVE
RESONATOR

WAVEGUIDE

MAGNET
WINDINGS

ANODE

TO
GROUND
RETURN

CATHODE
SUPPORT

0.250" φ
POCO
GRAPHITE
CATHODE

24

smooth bore runs, no cavity termination is used and the microwaves travel
travel down the ~ 53.1 cm long smooth circular waveguide, through a thin
teflon vacuum window, a 4 mm long straight section and a 5° half-angle horn
into the laboratory. In the resonant cavity runs, a stainless steel cavity
termination of 15.9 mm I.D., 3.2 mm length, and 3.2 mm long transitions on
both sides to fit the 17.3 mm I.D. tube is used. It is placed ~ 24.9 mm
from the back wall of the anode. After passing out through the rear exit
of the cavity, the microwaves travel down a ~ 50.6 cm long smooth cir-
cular waveguide, through a thin teflon vacuum window, a 4 mm long straight
section and a 5° half-angle horn into the laboratory.

Seven basic diagnostics were used. The first two were the electron
gun voltage and current monitors. The voltage was measured either by a
$CuSO_4$ resistive divider or the capacitive divider described in Appendix A.
The current was measured by either a Pearson model #1010 current transfor-
mer with a 50 ns risetime or a Stangenes model #2-0.1 current transformer
with a 20 ns risetime.

A Stangenes model #2-0.04, current transformer monitored the magnet
current. Standard Baytron microwave detectors and microwave components in
the B(33-50 GHz), V(50-75 GHz), and W(75-110 GHz) bands monitored the
vircator microwave characteristics.

The spectrometer built by Mike Bollen[19] was tried, but the vircator's
output power proved to be too low for results. A vacuum chamber/open
shutter camera system suitable for air breakdown testing was built and
tried, but no air breakdown was observed.

IV. THE EXPERIMENTAL RESULTS

To start, we used the smooth bore circuit and the stainless steel
cathode in the electron gun. We observed microwaves in the X, Ku, B, and
V bands. In the X and Ku bands, the power was calculated using an 8 GHz
detector response.[20] The coupling factor between the vircator output mode
and the microwave horn is assumed to be 1, but could be as low as 0.1 for
microwaves which are in the detector's frequency bandwidth. Thus the power
to be quoted is very conservative.

In X band, we observed a microwave pulse of ~ .6 W peak power for a
total pulse width of 150 ns duration. The nominal electron gun peak vol-
tage and current were 60 kV and 200 A, respectively for a 5.0 mm anode-
cathode gap, a 150 ns FWHM voltage duration, and a microwave duration of
160 ns. A 30 line per inch nickel mesh was the electron gun anode. Using
Equation (1), we would expect a microwave frequency of 53.4 GHz, assuming
that the electron beam dimensions are the same as the cathode's. The mag-
netic field was 5.25 kG, which corresponds to a relativistic electron
cyclotron frequency (f_{ce}) of 13 GHz. Thus, the electron beam was expand-
ing in the radial direction and the current density used the calculation
above was a factor of 17 too high. It is reasonable to observe microwaves
in X band.

Keeping the same electron gun and magnetic field parameters, a 10 GHz
low pass filter was inserted in series with our microwave detector. ~0.7W
peak power was measured. The voltage pulse was 130 ns FWHM and the micro-
wave duration was 150-160 ns. Knowing that f_{ce} ~ 13 GHz, a 10 GHz microwave
frequency is reasonable. Note that the 0.7 W power measurement (6.56 < f <
10 GHz) is slightly higher than the 0.6 W power measured without the low
pass filter (6.56 < f < ∞), but this is probably due to shot to shot
variations.

The efficiency of the X band microwave production was ~ 5×10^{-6}%.
We quickly discovered that the electron gun was much too intense for the
nickel anode mesh because 10 to 13 mm diameter holes were quickly formed
due to electron impact.

Switching to a Ku band detector while the stainless steel cathode and
the nickel mesh anode were still in place, we observed ~ 2.3 W of micro-
wave power. The nominal electron gun voltage and current were 65 kV and
175-225A, respectively. The anode-cathode gap was 5.0 mm and the external
magnetic field was 21 kG. The voltage pulse was 120 ns FWHM and the micro-
wave duration was 110-120 ns. Assuming that the electron beam's cross sec-
tion is the same as the cathode's, the microwave frequency should be about
49 to 56 GHz according to Equation (1). Due to the 21 kG external magnetic
field, f_{ce} ~ 52 GHz. There should be little or no power in the Ku band
(12-18 GHz). Either the detector was responding to very high frequencies
(which is possible, but requires substantial power) or there is a low fre-
quency, low power tail in the microwave spectrum. The apparent efficiency
is ~ $1.5 - 2 \times 10^{-5}$%.

Keeping the stainless steel cathode, we switched to a 40 line per inch
tungsten mesh anode, epoxing along the boundary edge (and two thin strips
in a cross pattern through the center for strength. Some electron current
would be intercepted by the epoxy.

In B band, the measured peak power was ~ 70 W. The electron gun
peak voltage and current were nominally 65 kV and 850 A, respectively for a
5.0 mm anode-cathode gap. The voltage pulse was 65 ns FWHM and the micro-
wave pulse was 30 ns FWHM. The microwave production efficiency was
1×10^{-4}%. The expected microwave frequency based on the current density
(Eq. 1) is ~ 110 GHz and the relativistic electron cyclotron frequency
due to the 21 kG external magnetic field is 52 GHz. For a B band detector,
the minimum detectable frequency is ~ 26.35 GHz.

Switching to a V band detector, the peak power decreased to approximatly 5 W for nominal electron gun parameters of 65 kV and 500 A. The anode-cathode gap was 3.0 mm and the microwave efficiency was 1.5×10^{-5}%. The voltage pulse was 120 ns FWHM and the microwave pulse was 45 ns FWHM. The expected frequency due to current density is 82 GHz and the electron cyclotron frequency due to 21 kG magnetic field is 52 GHz. For a V band detector, the cut-off frequency is 39.9 GHz.

Changing the anode to a 14 x 18 squares per inch bronze screen with the boundaries epoxied and an epoxy dot on center, the microwave power decreased to ~ 2.4 W in V band. The gun voltage and current were 64 kV and 850 A, respectively, for an anode-cathode spacing of 3.0 mm. The voltage pulse was 45 ns FWHM and the microwave pulse was 25 ns FWHM. The expected microwave frequency due to current density is ~ 110 GHz and the electron cyclotron frequency corresponding to the 21 kG field is 52 GHz. The efficiency is 4×10^{-6}%.

This concludes the smooth bore experiments. The attenuators for the diagnostics were checked before going on to the resonator studies. It was found that the attenuator for the current was bad. The attenuation was a function of position and frequency. But the currents quoted above are accurate to a factor of 2. Considering the low efficiencies, our results indicate that a smooth bore circuit is inadequate.

Next, we added a resonant cavity to the microwave circuit. The anode mesh of the previous runs was replaced by a more durable stainless steel endcap shown in Figure 11. The long neck on the new anode is a microwave cutoff section and is a technique commonly used in gyrotrons.

In the X and Ku bands, no microwave radiation was observed. This was an unexpected result since X and Ku band radiation was observed in the smooth bore setup.

A microwave pulse detected by a B band detector is shown in Figure 12. The frequency is greater than or approximately equal to 26.35 GHz. We estimate the power to be ~21 kW. The peak voltage and current are 63 kV and 1.6 kA, resulting in an efficiency of .02%. The magnetic field was 10.5 kG, which corresponds to a relativistic electron cyclotron frequency of 26 GHz. The B band signals were maximum for 10.5 kG magnetic fields.

A microwave pulse detected by a V band detector is shown in Figure 13. The frequency is greater than or approximately equal to 39.90 GHz. The peak power is estimated to be 80 W at a 14.7 kG magnetic field. The peak voltage and current are 67 kV and 1.3 kA, respectively, and the microwave production efficiency is 9×10^{-5}%. The observed V band radiation is maximum with a 13.7 kG magnetic field, which corresponds to a relativistic electron cyclotron frequency of 34 GHz. The maximum power observed is estimated to be 130 W.

In Figures 12 and 13, the microwave pulse is a short burst (5 ns full width at half maximum) followed by low level power for roughly the flat top portion of the voltage pulse (~ 25 ns). The cause of the short bursts may be due to a disruption to the formation of the virtual cathode, and/or microwave breakdown. It would require at least 1 to 10 MW of microwave power in the resonator to cause breakdown.

The diagnostics on this experiment still should not be completely trusted. The voltage waveforms have slower risetimes than would be expected. The spikes near the beginning of the voltage waveforms of Figures 12 and 13 could be due to an open circuit voltage reflection before the electron gun starts emitting or to a faulty Tektronix attenuator. Tektronix makes excellent response attenuators, but they are easily damaged. When these attenuators are damaged, they do not quit working, but instead their attenuation and/or frequency response changes. The current monitor purchased from Stangenes should be adequate for our purposes, but
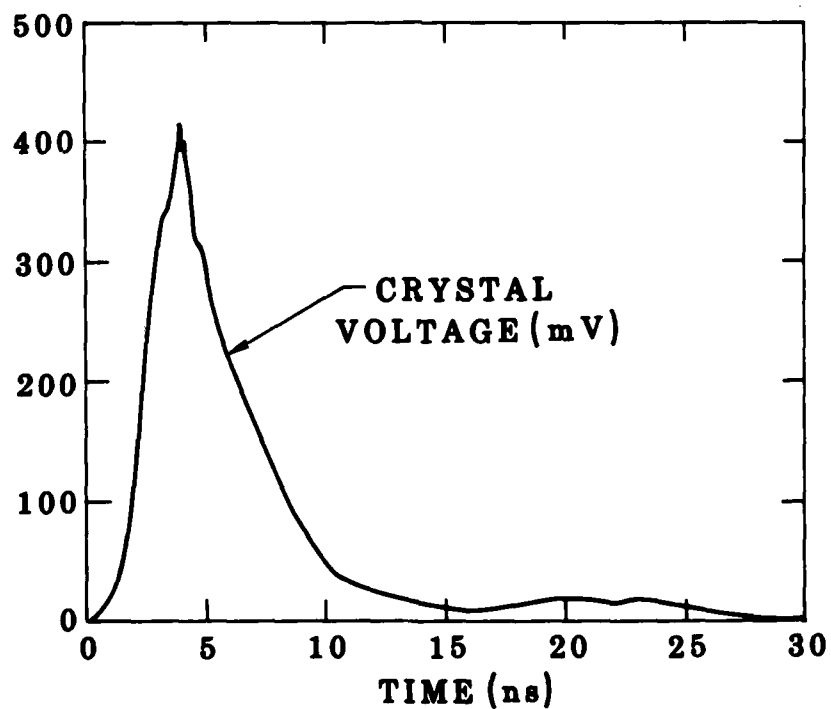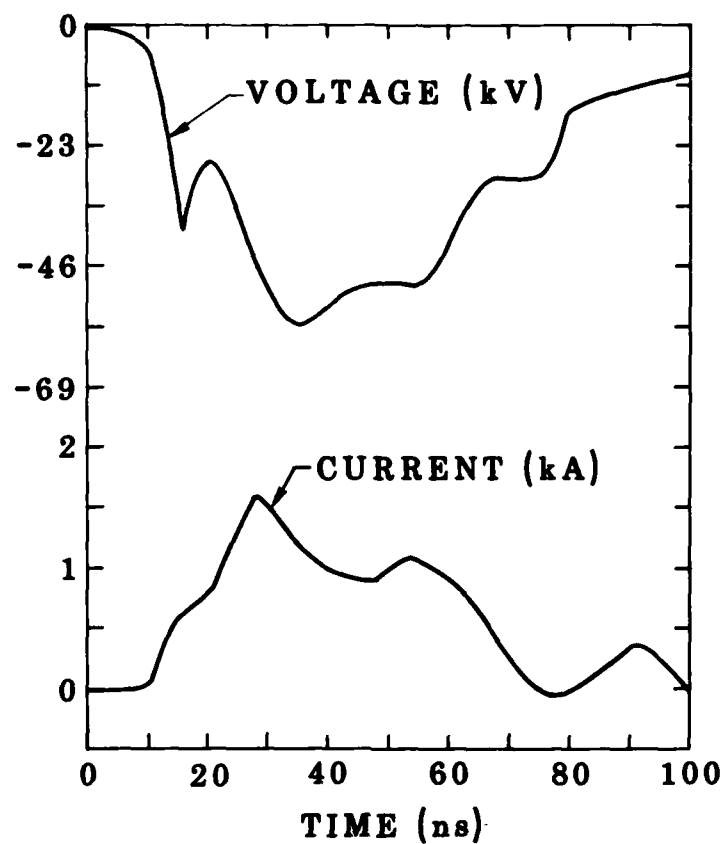
Figure 12. Electron gun voltage and current and microwave B band detector waveforms. The frequency is < 26.35 GHz. An open ended waveguide pickup is 78.5 cm from the vircator output and the microwave detector is terminated into 50Ω.

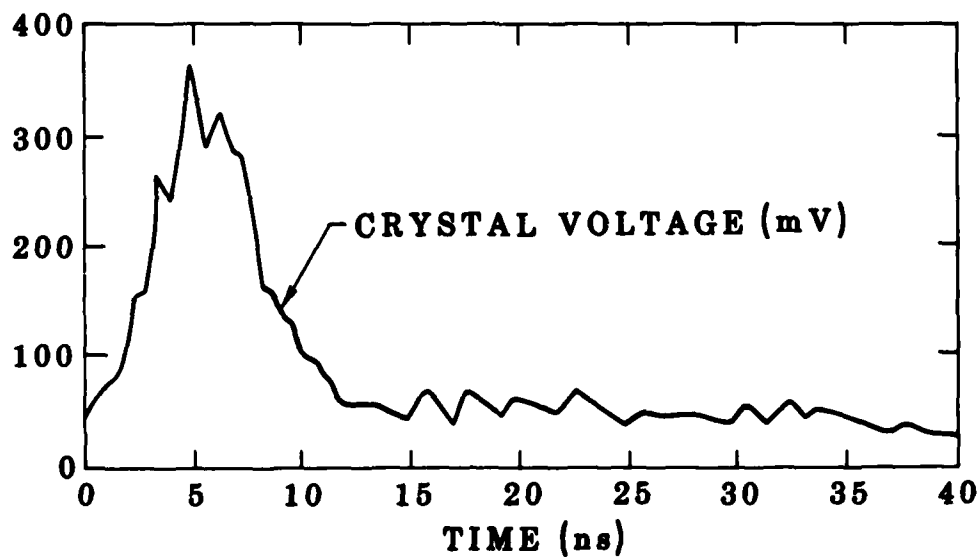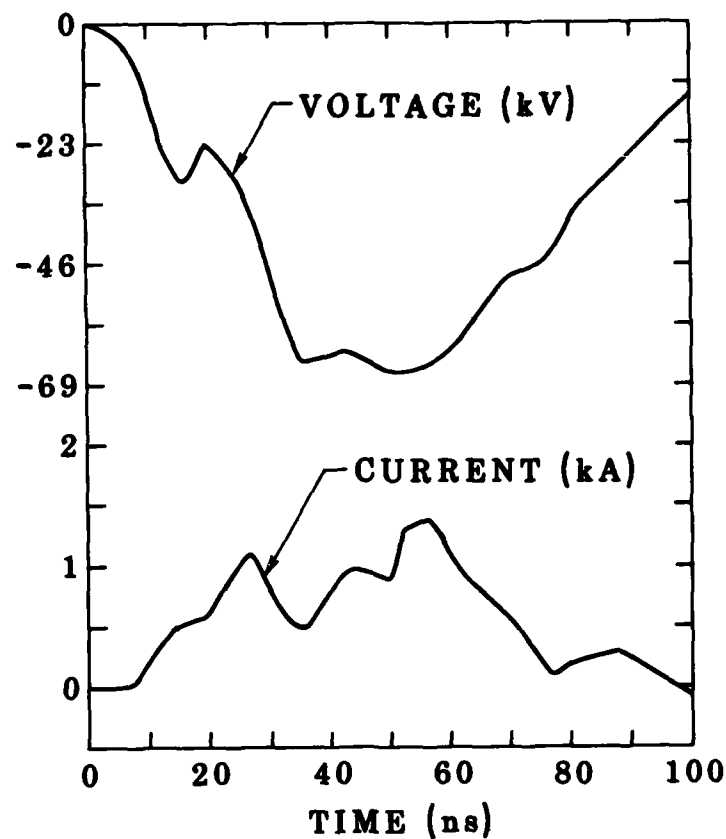Figure 13. Electron gun voltage and current and microwave V band detector waveforms. The frequency is $\geq$ 39.9 GHz. A nominal 25 db gain receiver horn is 66.5 cm from the vircator output and the microwave detector is terminated into 50Ω.

31

the current waveforms in Figures 12 and 13 bounce around in magnitude more than would be expected and the current should increase steadily for 200 ns instead of going to zero after just 70 ns. Obviously, a faster response current monitor is required. Finally, the attenuator of the current monitor for the magnetic field was damaged. A back-up diagnostic was used to calculate the magnetic fields, but it also cannot be relied upon. The magnetic fields have been calculated as carefully as possible under the circumstances, but the values should be considered as a guide.

There is an obvious large discrepancy between the measured power (21 kW) and the estimated power due to microwave breakdown within the resonator (MW's). Since we have not observed air breakdown at the microwave output window, we will have to bracket the total output power between 21 kW and 1 MW and wait for future studies to resolve the issue.

In summary, the powers and efficiencies quoted above are conservative. For an optimistic estimate, multiply the quoted powers and efficiencies by a factor of 10.

The four most important finds of this research effort are:

1) the observation of frequencies $\geq$ 39.9 GHz,
2) a resonator structure provides much more microwave power than a smooth bore structure,
3) reasonably efficient operation (as compared to unmagnetized vircators) of a vircator with an axial magnetic field,

and

4) the rapid decline of efficiency with frequency.

We either excede or tie the highest frequency observed from a vircator. The other two contenders are Mahaffey et. al.[21] at NRL (36.6 GHz) and Bartsch and Davis[22] at LANL (30-40 GHz). To the best of our knowledge, we are the first to find more efficient operation with a resonator than with a smooth bore circuit. This could be due either to our electron beam power

(50-100 MW) not being large enough to exceed some threshold for efficient operation with a smooth hore circuit or to the use of a strong axial magnetic field. Lasers, free electron lasers, and gyrotrons have current thresholds for high power oscillation and vircators may have a similar type of threshold. Everyone, except the Russians,[23] have steered away from the use of axial magnetic fields because these fields destroy efficiency. We have worked to learn how to obtain reasonable vircator operation with high axial fields. Using the optimistic estimates described in the paragraph above, our high field efficiencies in B band are approximately the same as the zero field efficiencies in the NRL and LANL experiments mentioned above.

The efficiency does decrease rapidly with frequency, but we are confident that the situation can be much improved with a shorter length, smaller diameter cavity.

If these experiments are to be continued, the three most important tasks would be:

1) improvement of all diagnostics,
2) push vircator operation toward higher frequencies, and
3) begin side extraction and/or quasi-optical studies.

V. SUGGESTIONS FOR THE FUTURE

For future work, I have two suggestions. First, I recommend a repeat of the Russian experiment by Didenko, et. al.[24] They claim efficiencies of 25 to 50% at 3.3 GHz. This efficiency is about 10 times higher than any reported in the U.S. If vircator research is to remain viable, we must figure out how they achieved this remarkable efficiency.

My second suggestion is to continue with millimeter wave vircator research. Of course, power, frequency, and efficiency will be important goals. If there is a desire to build mm wave devices in the 10's of GW and if high space charge electron beams are unavoidable, vircators will be a powerful contender because they thrive on excess space charge, whereas other mm wave devices such as gyrotrons and FEL's do not.

REFERENCES

1. D. J. Sullivan, G. F. Kiuttu, R. J. Adler, D. E. Voss, and J. Walsh, "Phase I Report: Resonant Vircator Study," Mission Research Corporation, AMRC-R-654, p. 35.

2. T. A. Hargreaves, R. Seeley, J. H. McAdoo, R. C. Lee, K. Yoshinko, and M. E. Read, Bull. Am. Phys. Soc. 29, 1284 (1984).

3. AMRC-R-654, p. 50.

4. D. Sullivan, "Phase II SBIR Proposal: Development of Resonant Virtual Cathode Oscillators (Vircators)," Mission Research Corporation, P527.05, p. 32.

5. P527.05, p. 24.

6. K. O. Busby, J. Condon, G. Bergeron, M. Rhinewine, K. Killian, A. Fliflet, R. Lee and M. Read, "94 GHz Gyrotrons," Bull. Am. Phys. Soc. 28, No. 8, 1193 (1983).

7. A. N. Didenko, A. G. Zherlitsyn, A. S. Sulakshin, G. P. Fomenko, V. I. Tsvetkov, and Yu G. Shteyn, Pisma v. Zhur. Tek. Fiz. 9, 1510 (1983).

8. T. C. Genoni and W. A. Proctor, International Conference on Plasma Science, 1978, p. 94.

9. D. J. Sullivan, D. E. Voss, E. M. Bollen, R. H. Jackson, and E. A. Coutsias, "Annual Report: Virtual Cathode Theory and Design of a Millimeter Wave Vircator," Mission Research Corporation, AMRC-R-451, p. 7.

10. Reference Data for Radio Engineers, 6th ed., Howard W. Sams and Co., Inc., ITT, 1982, p. 27-8.

11. Ibid., p. 27-8.

12. Collins Clark and Bill Ballard, Private Communications, 1985.

13. J. R. Risser in Microwave Antenna Theory and Design, S. Silver (Ed.), McGraw-Hill Book Co., Inc. 1949, p. 338.

14. L. J. Chu, "Calculation of the Radiation Properties of Hollow Pipes and Horns," Jour. App. Phys. 11, 603-610 (1940).

15. Risser, p. 336.

16. A. P. King, "The Radiation Characteristics of Conical Horn Antennas," Proceedings of IRE, 38, March 1950, pp. 249-251.

REFERENCES (Continued)

17. The cable Blumlein was built by G. Kiuttu and R. Adler.

18. D. J. Sullivan, D. E. Voss, R. J. Adler, W. M. Bollen, R. H. Jackson, and E. A. Coutsias, "Annual Report: Virtual Cathode Oscillator Study," Mission Research Corporation, AMRC-R-614, pp. 10-38.

19. AMRC-R-614, pp 39-69.

20. AMRC-R-654, p. 65

21. R. A. Mahaffey, P. Sprangle, J. Golden and C. A. Kapetanakos, Phys. Rev. Lett. $\underline{39}$, 843 (1977).

22. R. R. Bartsch and H. A. Davis, Bull. Am. Phys. Soc. $\underline{29}$, 1179 (1984).

23. Didenko, et. al.

24. Didenko, et. al.

APPENDIX A

A COMPACT VOLTAGE MONITOR FOR FAST RISETIME,
LOW IMPEDANCE PULSE LINES

A COMPACT VOLTAGE MONITOR FOR FAST RISETIME, LOW IMPEDANCE PULSE LINES

K. Busby, and M. Williams
Mission Research Corporation
Albuquerque, New Mexico 87106

Compact voltage monitors for conventional modulators with voltage risetimes and pulse lengths of microseconds to tens of microseconds have widespread commercial use. Their applications range from monitoring the modulators of civilian and military radars to measuring voltage waveforms in basic physics experiments. These monitors are not suitable for the fast risetime pulse power technology.

Figure A.1 provides a circuit description of the device. A typical RC time for the monitor is approximately 2.5 ns, resulting in an overall monitor response time of approximately 10 ns. The theoretical voltage division ratio is about 230 to 1 and the actual ratio is 230 to 1. The DC resistance of the monitor is 2260 ohms. Thus the device is useful for pulse lines of 100 ohms impedance or less.

The voltage monitor responses are shown in Figures A.2 and A.3. In Figure A.2, the 50 ns risetime pulse is measured with a 400 MHz bandwidth oscilloscope. The 10 ns risetime response as is shown in Figure A.3.
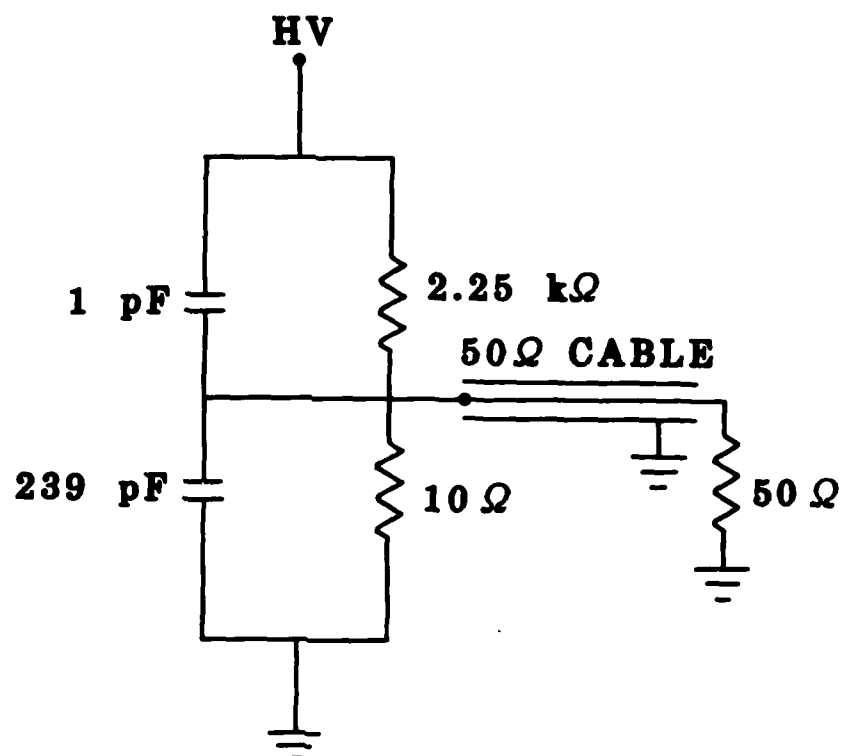
Figure A.1. Voltage divider circuit.

VOLTAGE
(-23 kV/div)

TIME
(50 ns/div)

Figure A.3. Response of the capacitive voltage monitor to the voltage across an 84Ω resistor when driven by a 50Ω cable Blumlein in series with an overvoltage spark gap.
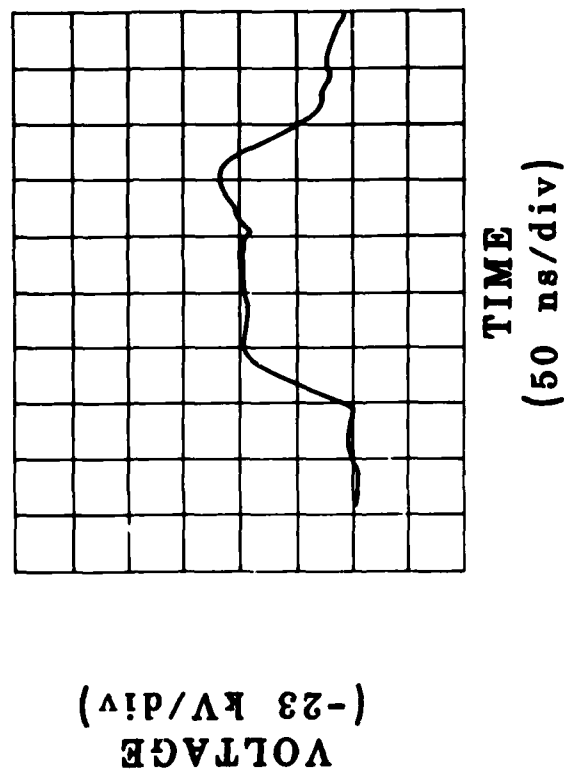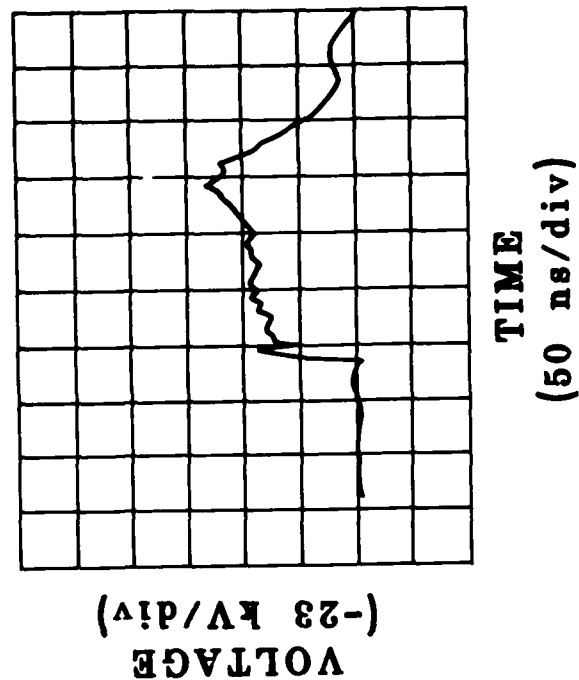
VOLTAGE
(-23 kV/div)

TIME
(50 ns/div)

Figure A.2. Response of the capacitive voltage monitor to the voltage across an 84Ω resistor when driven by a 50Ω cable Blumlein.

APPENDIX B

A MODERATE VOLTAGE, HIGH CURRENT DENSITY ELECTRON GUN

A MODERATE VOLTAGE, HIGH CURRENT DENSITY ELECTRON GUN

K. Busby, D. Sullivan, R. Adler and M. Williams
Mission Research Corporation
Albuquerque, New Mexico 87106

A 50 kV, 1000 A field emission electron gun has been designed to operate at current densities as high as 50 kA per square centimeter. The electron gun assembly is shown in Figure B.1. The cathode material is graphite and the cross sectional area of the annual electron emitter is 0.02 cm^2. Typical anode to cathode spacings range from 2 to 12 mm. An axial external magnetic field is required to confine the electron beam.

The performance characteristics can be indirectly derived from the microwave output of a virtual cathode oscillator on which this gun was used. With an external magnetic field of 14 kG, voltage and current waveforms as shown in Figure B.2, the microwave frequency was nominally 40 GHz, indicating that the electron gun current density was approximately 7 kA/cm^2.
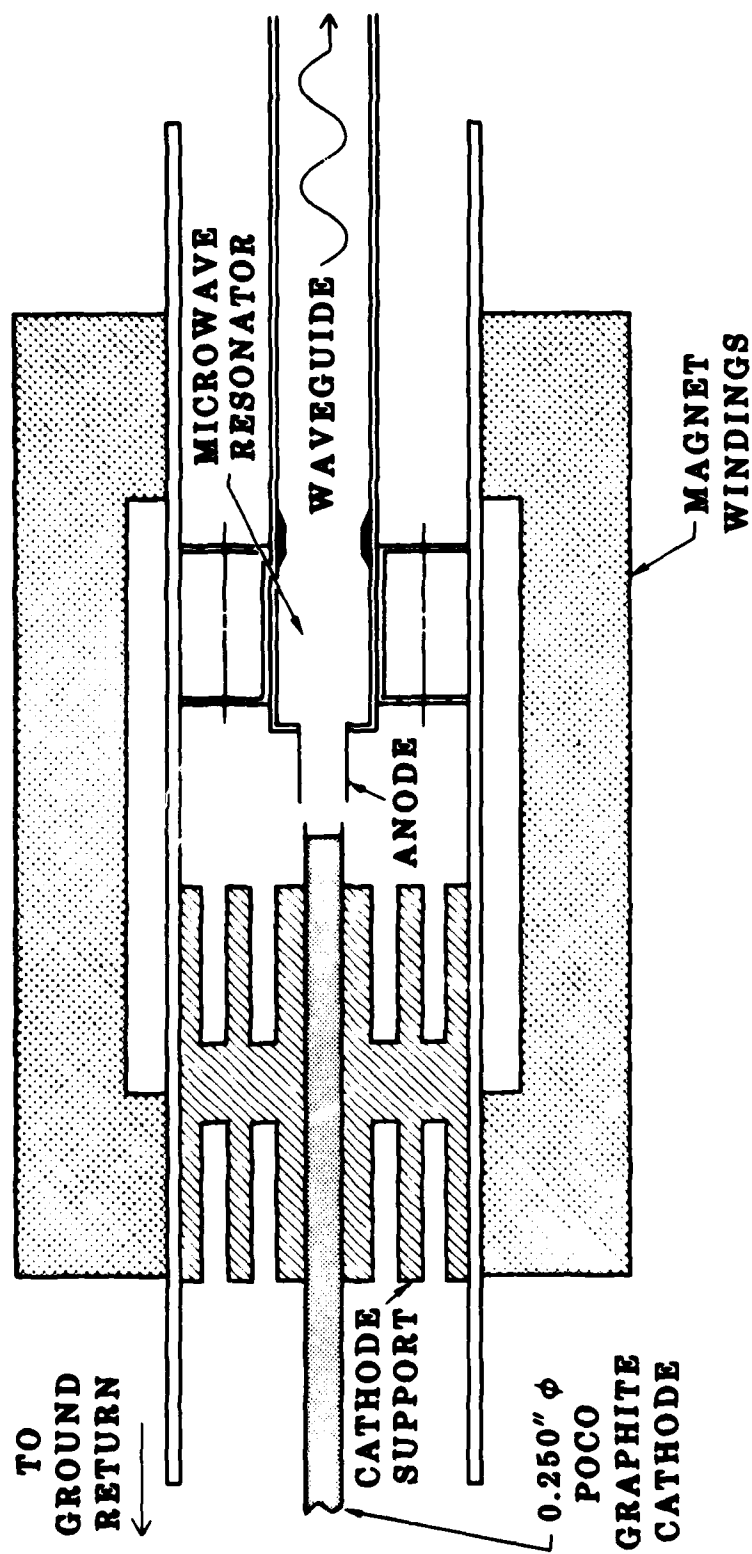
Figure B.1. Vircator electron gun and microwave circuit assembly.

TO
GROUND
RETURN

MICROWAVE
RESONATOR

WAVEGUIDE

MAGNET
WINDINGS

ANODE

CATHODE
SUPPORT
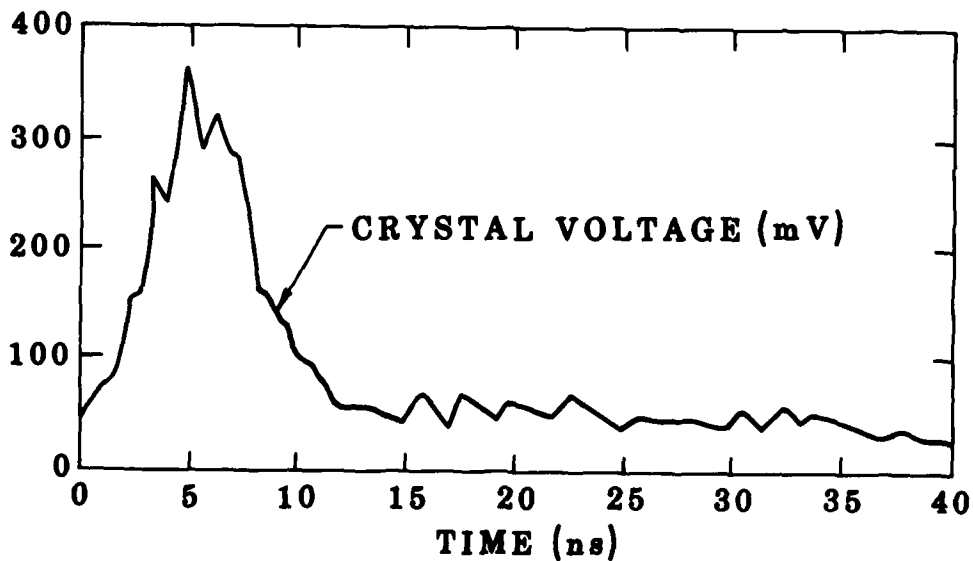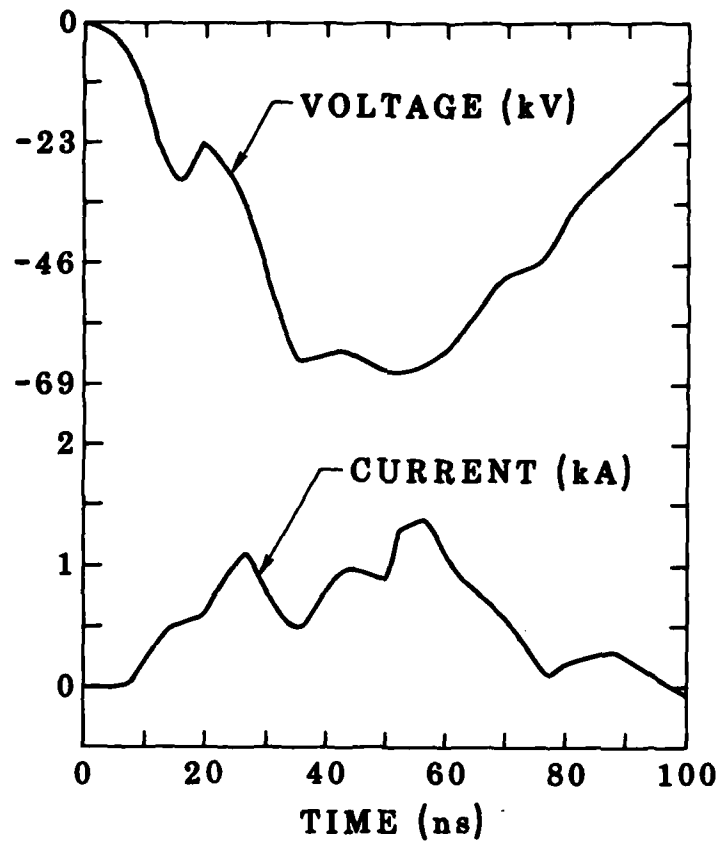
0.250" φ
POCO
GRAPHITE
CATHODE

Figure B.2. Electron gun voltage and current and microwave V band detector
waveforms. The frequency is ≥ 39.9 GHz. A nominal 25 db gain
receiver horn is 66.5 cm from the vircator output and the
microwave detector is terminated into 50Ω.

B-4

AMRC-R-451
Copy ___

ANNUAL REPORT

VIRTUAL CATHODE THEORY AND DESIGN OF A MILLIMETER
WAVE VIRCATOR

Donald J. Sullivan
Donald E. Voss
W. Michael Bollen
Robert H. Jackson
Evangelos A. Coutsias (UNM)

January 1983

Prepared for: Air Force Office of Scientific Research
                       Physics Directorate
                       Bolling Air Force Base, DC 20332

Under Contract: F49620-82-C-0014

Prepared by: MISSION RESEARCH CORPORATION
                       1720 Randolph Road, S.E.
                       Albuquerque, New Mexico 87106

SECURITY CLASSIFICATION OF THIS PAGE (When Data Entered)

REPORT DOCUMENTATION PAGE		READ INSTRUCTIONS BEFORE COMPLETING FORM
1. REPORT NUMBER	2. GOVT ACCESSION NO.	3. RECIPIENT'S CATALOG NUMBER
4. TITLE (and Subtitle) VIRTUAL CATHODE THEORY AND DESIGN OF A MILLIMETER WAVE VIRCATOR		5. TYPE OF REPORT & PERIOD COVERED ANNUAL REPORT 1/82 - 12/82
		6. PERFORMING ORG. REPORT NUMBER AMRC-R-451
7. AUTHOR(s) D. J. Sullivan, D. E. Voss, W. M. Bollen R. H. Jackson, E. A. Coutsias (UNM)		8. CONTRACT OR GRANT NUMBER(s) F49620-82-C-0014
9. PERFORMING ORGANIZATION NAME AND ADDRESS Air Force Office of Scientific Research Bolling Air Force Base Washington, DC 20332		10. PROGRAM ELEMENT, PROJECT, TASK AREA & WORK UNIT NUMBERS
11. CONTROLLING OFFICE NAME AND ADDRESS Mission Research Corporation 1720 Randolph Road, S.E. Albuquerque, New Mexico 87106		12. REPORT DATE January 1983
		13. NUMBER OF PAGES
14. MONITORING AGENCY NAME & ADDRESS(if different from Controlling Office)		15. SECURITY CLASS. (of this report) UNCLASSIFIED
		15a. DECLASSIFICATION DOWNGRADING SCHEDULE

16. DISTRIBUTION STATEMENT (of this Report)

APPROVED FOR PUBLIC RELEASE; DISTRIBUTION UNLIMITED

17. DISTRIBUTION STATEMENT (of the abstract entered in Block 20, if different from Report)

18. SUPPLEMENTARY NOTES

19. KEY WORDS (Continue on reverse side if necessary and identify by block number)

Virtual Cathode	Space-Charge Limit
Virtual Anode	Space-Charge Limiting Current
Virtual Cathode Oscillator	Bifurcation
VIRCATOR	Millimeter Microwaves

20. ABSTRACT (Continue on reverse side if necessary and identify by block number)

The theory of a virtual cathode oscillator and a detailed experimental design of a millimeter wave virtual cathode oscillator (VIRCATOR) are presented. It is found that second order analytical approximations give an accurate value for the space-charge limiting current of an electron beam in cylindrical geometry. The same Green's function approach could be used on other geometries as well. Exceeding the space-charge limiting current is the necessary condition for virtual electrode formation. However, it does not explain the nature of the space-charge limit instability. The oscillatory stable state of the

DD $_{1 \text{ JAN } 73}^{\text{FORM}}$ 1473   EDITION OF 1 NOV 65 IS OBSOLETE

virtual cathode is found to originate at the bifurcation point of several stable and unstable electron beam states. An analysis of the nonlinear growth rate of the instability is derived.

The virtual cathode is in effect a relaxation oscillator. The advantage of the vircator over a reflex klystron is that the virtual cathode moves opposite to the electron beam propagation direction during the bunching phase resulting in enhanced electron densities unobtainable otherwise. The periodic time-dependent nature of the bunching results in efficient microwave generation. Experimental efficiencies of 12% and theoretical efficiencies of 20% have been obtained. The microwave frequency scales as the relativistic beam plasma frequency. This can be adjusted via an externally applied axial magnetic field. The result is an oscillator which is frequency agile over an order of magnitude without externally changing the physical configuration. Output powers of from kilowatts to gigawatts are obtainable based on the power source. Experimental results are reviewed and explained. The rationale for using a foilless diode as the electron beam source is given.

A detailed mechanical and electrical design is described. It entails placing the vircator in a high vacuum vessel with flexibility for further development. The electrical power is pulse formed using a lumped artificial Blumlein line. The axial magnetic field is critically damped for component safety and circuit design simplicity. The beam source is a foilless diode with an annular limiter for collimation and prevention of electrons reflexing into the diode. A W-band (75-110 GHz) microwave grating spectrometer has been designed and constructed for diagnosis of the electromagnetic wave signal. The vircator goal is 1 Megawatt at 100 GHz.

TABLE OF CONTENTS

LIST OF ILLUSTRATIONS

ABSTRACT

The theory of virtual cathode oscillation and a detailed experimental design of a millimeter wave virtual cathode oscillator (VIRCATOR) are presented. It is found that second order analytical approximations give an accurate value for the space-charge limiting current of an electron beam in cylindrical geometry. The same Green's function approach could be used on other geometries as well. Exceeding the space-charge limiting current is the necessary condition for virtual electrode formation. However, it does not explain the nature of the space-charge limit instability. The oscillatory stable state of the virtual cathode is found to originate at the bifurcation point of several stable and unstable electron beam states. An analysis of the nonlinear growth rate of the instability is derived.

The virtual cathode is in effect a relaxation oscillator. The advantage of the vircator over a reflex klystron is that the virtual cathode moves opposite to the electron beam propagation direction during the bunching phase resulting in enhanced electron densities unobtainable otherwise. The periodic time-dependent nature of the bunching results in efficient microwave generation. Experimental efficiencies of 12% and theoretical efficiencies of 20% have been obtained. The microwave frequency scales as the relativistic beam plasma frequency. This can be adjusted via an externally applied axial magnetic field. The result is an oscillator which is frequency agile over an order of magnitude without externally changing the physical configuration. Output powers of from kilowatts to gigawatts are obtainable based on the power source. Experimental results are reviewed and explained. The rationale for using a foilless diode as the electron beam source is given.

A detailed mechanical and electrical design is described. It entails placing the vircator in a high vacuum vessel with flexibility for further

development. The electrical power is pulse formed using a lumped artific-
ial Blumlein line. The axial magnetic field is critically damped for com-
ponent safety and circuit design simplicity. The beam source is a foilless
diode with an annular limiter for collimation and prevention of electrons
reflexing into the diode. A W-band (75-110 GHz) microwave grating spec-
trometer has been designed and constructed for diagnosis of the electromag-
netic wave signal. The vircator design goal is 1 Megawatt at 100 GHz.

I. INTRODUCTION

Since the discovery of the Child-Langmuir relation[1,2] it has been
known that exceeding the limiting current of a diode leads to the develop-
ment of a virtual cathode. Subsequently, numerous papers were written on
experiments and theory relating to space-charge limited flows. Reference 3
provides an excellent background and bibliography. More recently, the
exact steady state solutions for electron beams in one-dimensional relativ-
istic diodes[4] and bounded drift spaces[5] were derived. It is easily seen
that for sufficiently large currents there exist two steady states for an
electron beam, only one of which is stable.[6] At the space-charge limit
(SCL) these two states coalesce and above the SCL they disappear.[7] As cur-
rent is increased past the SCL, the beam develops a jump instability and
relaxes into an oscillating state.

In the early 1960's, computer models were developed which quantita-
tively depicted the nonlinear oscillatory nature of the virtual
cathode.[8-10] These were one-dimensional, non-relativistic, electrostatic,
multiple sheet models. References 8 and 9 qualitatively pointed out many
interesting dependencies of the oscillation frequency and potential minimum
position on injected curent, thermal spread and circuit resistance. Refer-
ence 10 presents computer experiments with one and two species.

The phenomenon of virtual cathode formation in intense relativistic
electron beams figures prominently in a number of high interest research
areas. Devices used to produce high current ion beams for inertial con-
finement fusion--pinch reflex diode[11,12] and reflex triodes[13,14]--
depend on the virtual cathode to inhibit electron transport and use its
potential well to accelerate ions. The recent concept of the spherical
electron-to-ion converter[15] requires a virtual cathode.

The virtual cathode plays a dominant role in areas other than production of light ion beams for fusion. It is attributed with the main role in collective ion acceleration in neutral gas.[16,17] Control of virtual cathode motion is the mechanism for acceleration in the Ionization Front Accelerator.[18,19] It is also the acceleration method in two concepts for collective effect accelerators.[20,21] A final application is the use of virtual cathode oscillations to produce high power, short wavelength microwaves.[22-25] Experiments using reflex triodes have already been produced 1.4 GW of power with 12% beam-to-RF efficiency.[26] It is this latter application which will be considered in this report.

The report is organized as follows. Section II provides an in-depth review of the analytical approach to determining the space-charge limiting current. It is shown by comparison with particle-in-cell simulations that this value can be predicted quite accurately. Section III analyzes the nature and nonlinear growth rate of the space-charge limit instability which leads to the formation of a virtual cathode. In Section IV the basic considerations in the application of the virtual cathode for generating coherent microwaves is presented. Finally, Section V gives a detailed design, both mechanical and electrical, of the millimeter wave vircator being built for this project.

II. THE SPACE-CHARGE LIMITING CURRENT

A. Theory

The concept of limiting current can be visualized in the following over-simplified physical picture. As particles from the electron beam (see Figure 1) enter the drift tube, the charge which they carry creates a potential barrier against further transmission of current. If the injected current is greater than the limiting current, the potential energy, $e\phi$, will exceed the kinetic energy of the beam $(\gamma_0 - 1)mc^2$, where

- e = electronic charge
- ϕ = electrostatic potential ≤ 0
- γ = relativistic factor $(1 - \beta^2)^{-1/2}$
- γ_0 = value of γ at injection

- β = v/c
- v = electron velocity
- m = electron rest mass

At that position the barrier is large enough to stop the current and cause reflection of beam electrons. Thus, the deep potential well is called a virtual cathode. Note, however, that since the amplitude of the well fluctuates in time and space, the beam is never completely cut off by the virtual cathode.

The general space-charge limiting current problem does not lend itself to analytical solution. Instead theoretical work on the subject has attempted to solve for limiting currents, which develop in REBs, in the strictly electrostatic case. The solutions derived are only valid for beams in steady state equilibrium, i.e., I_0, < I_L. Also, the derivations depend on the following assumptions:

3
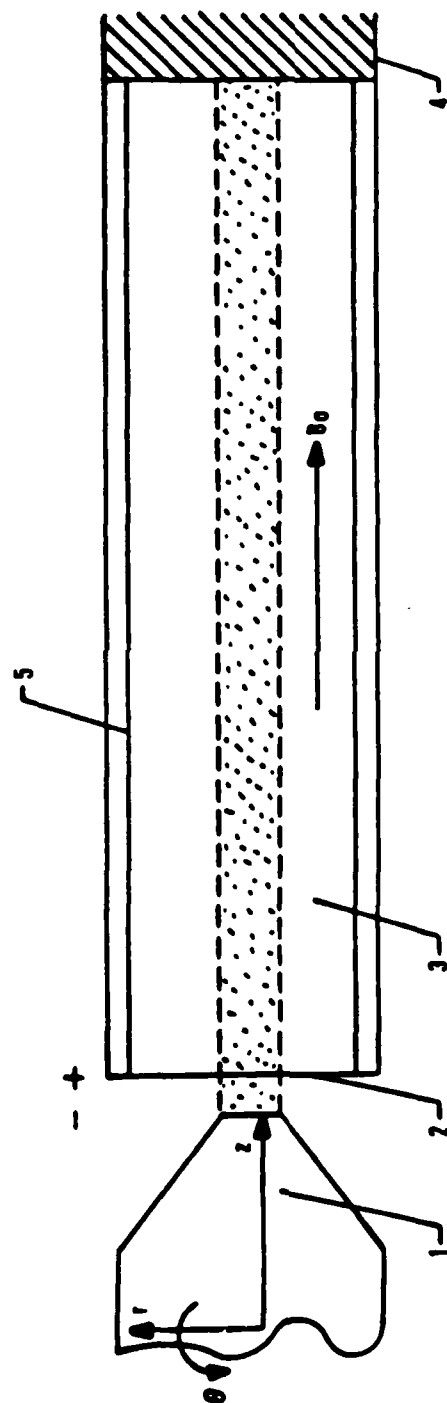
Figure 1. Schematic of a relativistic electron beam (REB): (1) cathode; (2) anode; (3) drift space; (4) collector; (5) return current conductor. The principal coordinate axes z, r, and θ are shown.

4

1. The electon beam is a cold plasma, $T_e = 0$. It implies the electrons are collisionless, and it allows one to neglect the $\vec{\nabla}P_e$ and viscosity terms in the momentum transfer equation. Here, T_e is the electron temperature and P_e the electron pressure.

2. The electron beam is axially homogeneous and infinite. In real terms the infinite beam assumption implies $L \gg R$, where L is the drift tube length, and R is the drift tube radius. This allows the beam to reach a steady state far enough downstream from the injection plane to make the equilibrium beam density, n_b^0, velocity, $\vec{v}^0$, and electric field, $\vec{E}^0$, independent of z.

3. The equilibrium radial density and velocity profiles are azimuthally symmetric about the magnetic axis. In conjunction with paragraph 2 this means that n_b^0, $\vec{v}^0$ and $\vec{E}^0$ are functions only of the radial distance, r.

4. The electron particle density and kinetic energy are independent of r at the anode plane. Therefore, the beam is uniform in space and monoenergetic at injection into the drift tube--anode foil scattering is neglected.

5. The externally imposed longitudinal magnetic field, $\vec{B}_0$, is effectively infinite. If this assumption is not made, the current-induced equilibrium self-magnetic fields would play a major role in determining the equilibrium radial profile of the beam. Since $\vec{B}_0$ is taken as infinite, the electrons are guided and contained by it, and the self-fields can be treated as perturbations. Another way of expressing this assumption is to state that the Larmor radius of an electron in the $\vec{B}_0$ field must be much less than the beam radius, $r_L \ll r_b$.

5

Since assumptions 1 through 5 reduce the problem to the electrostatic case, solving Poisson's equation will give the desired result. Using this approach several researchers have derived expressions for the space-charge limited current of electron beams in vacuum and in charge neutral plasmas. Excellent reviews have been written.[27],[28] The most widely cited results are those of Bogdankevich and Rukhadze.[27] Using the conservation of energy and momentum they are able to write Poisson's equation for a cylindrically symmetric electron beam as

$$\frac{1}{r}\frac{\partial}{\partial r}\left(r\frac{\partial \phi}{\partial r}\right) = \begin{cases} -\frac{4\pi j}{c}\left[1-\left(1-\frac{e\phi}{mc^2}\right)^{-2}\right]^{-1/2} & 0 < r \leq r_0 \\ \\ 0 & r_0 < r \leq R \end{cases}$$

with appropriate boundary conditions. Here, j is the current density. The radial cross section of the beam is given in Figure 2a, where R is the drift tube radius, and r_0 is the radius of the axially centered beam.

Equation (1) is a nonlinear differential equation. The approach taken in Reference 27 is to obtain solutions by making certain analytical approximations. These approximations are related to beam energy at injection (the nonrelativistic, $\gamma \approx 1$, or ultrarelativistic, $\gamma \gg 1$, limits) and beam geometry (the pencil beam, $\ln (R/r_0) \gg 1$, or fat beam, $\ln (R/r_0) \ll 1$ limits. The result is a series of first order analytical approximations which are restricted in validity to narrow regimes. Indeed, the most often used relation is an interpolation formula which utilizes the uniform density approximation. It neglects the radial variations in ϕ, γ, and number density, n. This equation consistently underestimates the true value of limiting current.
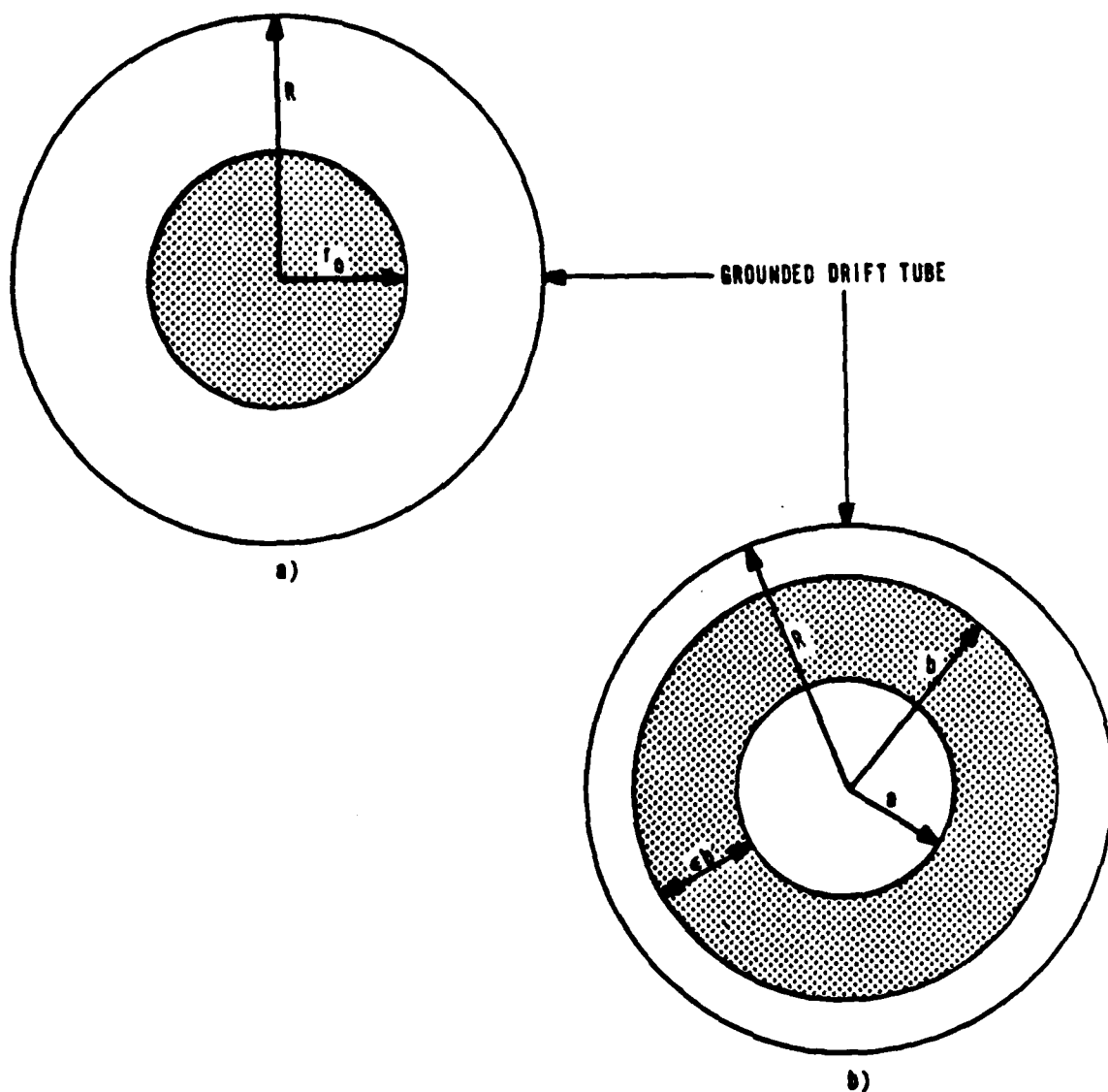
Figure 2. Radial cross section of two electron beams.
(a) Solid beam where r_0 is the beam radius
and R is the drift tube radius. (b) Annular
beam where a is the inner radius, b the outer
radius, R the drift tube radius and
$\varepsilon = \frac{b-a}{b}$.

The work of Genoni and Proctor[29] produces a more accurate, less restricted relation for space-charge limiting current. In particular, it is a second order analytical expression which takes into account the radial dependence of γ, ϕ, and n. Also, the beam is neither confined to the ultrarelativistic limit, nor is the beam geometry valid in only certain regimes. The general electron beam radial configuration is given in Figure 2b. As seen from the figure, R is the drift tube radius, a and b are the inner and outer beam radii, respectively, and $\epsilon = \frac{b-a}{b}$.

Their derivation also begins with conservation of energy and momentum, so that Poisson's equation for a cylindrically symmetric beam takes the form

$$\frac{1}{r} \frac{d}{dr} \left[r \frac{d\gamma(r)}{dr} \right] = \begin{cases} \dfrac{4\nu[(b/R)^2 - (a/R)^2]}{\beta(r)} & a \leq r \leq b \\ \\ 0 & \text{elsewhere} \end{cases} \tag{2}$$

subject to the boundary conditions

$$\gamma(R) = \gamma_0 \qquad\qquad\qquad \gamma(0) \geq 1 \text{ and finite} \tag{3}$$

where $\nu = Ie/mc^3$ is dimensionless current independent of r and z. This is a nonlinear differential equation, as expected, showing the radial dependence of γ. By choosing an appropriate Green's function one can express equations (2) and (3) as an integral equation and obtain a numerical solution. More importantly, by assuming a uniform density radial profile of γ inside the beam as a zeroth order guess, one can iterate on the integral equation to obtain a second order analytical approximation to the current. Thus, not only can the limiting current be found by determining the value of γ which maximizes the current, but also the current in the drift tube for any value of γ and r can be evaluated. Using this approach an equivalent integral equation, valid for $a \leq r \leq b$, is

8

$$\gamma(r) = \gamma_0 - \frac{4\nu}{b^2-a^2} \left\{ \ln\frac{R}{r} \int_a^r \frac{x}{\beta(x)}\,dx + \int_r^b \frac{x}{\beta(x)} \ln\frac{R}{r}\,dx \right\} \quad (4)$$

A first approximation $\gamma(r) \approx \gamma^I(r)$ is obtained by putting $\beta = K$ (a constant) in the integrals of equation (4). If K is fixed by requiring $\gamma^I(a) = (1-K^2)^{-1/2}$, one obtains the following approximation to the limiting current:

$$\nu_L \approx \nu_L^{BR} \equiv \frac{(\gamma_0^{2/3} - 1)^{3/2}}{1 - f(\epsilon) + 2 \ln R/b} \quad (5)$$

where

$$f(\epsilon) = \frac{(1 - \epsilon)^2}{1 - \epsilon/2} \left| \frac{\ln(1 - \epsilon)}{\epsilon} \right| \quad (6)$$

Equation (5), which appears in a paper by Miller and Straw[30], is the logical generalization to annular beams of the widely used Bogdankevich-Rukhadze[27] interpolation formula for solid beams, to which it reduces in the limit $\epsilon \to 1$. A second approximation, $\gamma^{II}(r)$, is obtained by repeating this procedure using $\beta = [1 - (\gamma^I)^{-2}]^{1/2}$ in the integrals of equation (4). In the special case of a solid beam (a = 0), the integrals can be evaluated in closed form, but for the general case of an annular beam they must be done numerically. Genoni and Proctor[29] have obtained useful analytical approximations to $\gamma^{II}(r)$ for annular beams by doing the second iteration with $\beta = (1 - \Gamma^{-2})^{1/2}$ where $\Gamma(r)$ is a quadratic fit to $\gamma^I(r)$ which yields the exact $\gamma^{II}(r)$ in the solid beam limit. A particular choice of K then yields a definite relation between ν and $\gamma_a \equiv \gamma(a)$. The simplest of these that gives good agreement with numerical results is evidently

$$\nu = \frac{(\gamma_0 - \gamma_a)^2}{(\Gamma_b^2 - K)^{1/2} - (\gamma_a^2 - 1)^{1/2}} \frac{1 - g}{(1 - f + 2 \ln R/b)^2} \quad (7)$$

in which

$$\Gamma_b = \gamma_a + (\gamma_0 - \gamma_a) \frac{1 - g}{1 - f + 2 \ln R/b} \tag{8}$$

and

$$g(\epsilon) = \frac{8(1 - \epsilon)^2}{\epsilon(4 - 3\epsilon)} \ln \frac{1 - \epsilon/2}{1 - \epsilon} \tag{9}$$

In the limit $\epsilon \to 1$, both g and f tend to zero, and equation (7) reduces to a formula (equation 14) obtained by Thompson and Sloan (Ref. 8) in their analysis of solid beams. It should be noted that different quadratic fits, while producing more complicated analytical expressions, produce more accurate results.[29]

B. Simulation

The space-charge flow simulations were carried out using a two-dimensional particle-in-cell plasma simulation code, CCUBE, which is fully relativistic and electromagnetic.[32],[33] CCUBE (Version One) solves self-consistently for the time-dependent trajectories of tens of thousands of plasma particles over thousands of plasma periods. The critical portion of the code consists of a leap frog procedure. At each time step, the charge and current associated with the particles are interpolated bilinearly onto a spatial mesh. The quantities then serve as source terms in Maxwell's equations for determining the electromagnetic scaler and vector potentials on the mesh. Finally, the potentials are interpolated back to the particle positions. The basic coordinate system is cylindrical with azimuthal symmetry assumed. A uniform axially directed magnetic field can be imposed to insure beam equilibrium.

All variables are expressed in dimensionless terms. In particular, the depth of the potential well formed by the electronic space-charge is given by ϕ, where

10

$$\phi(r) = \frac{e\phi(r)}{mc^2} = \gamma(r) - \gamma_0 \leq 0 \tag{10}$$

The five components in configuration-momentum space are $X1 = z\,\omega_p^0/c$, $X2 = r\,\omega_p^0/c$, $V1 = \gamma\beta_z$, $V2 = \gamma\beta_r$, $V3 = \gamma\beta_\theta$ where β_z, β_r, and β_θ are the components of β in the z, r, and θ directions, respectively. $\omega_p^0 = (4\pi n_b^{inj} e^2/m)^{1/}$ is the electron plasma frequency arising from the beam density at injection, n_b^{inj}.

In these simulations the code is made to model the injection of cold, monoenergetic, relativistic electrons with uniform density into a long, evacuated, equipotential, cylindrical drift tube along an effectively infinite magnetic guide field in order to comply with the assumptions of the previous section. This is accomplished in the following manner.

1. A cold bean is obtained by setting the electron thermal velocity components equal to zero.

2. Miller and Straw[34] provide a criterion for neglecting the presence of end plates and effectively having $L \gg R$.

$$L/R \geq 2.58 \ (b/R)^{0.133} \tag{11}$$

For the annular beam simulations this yields $L/R \geq 2.50$, whereas the worst case simulation is $L/R = 9.84$. In addition, two runs were made with the downstream axial boundary grounded. The presence of end plates did not affect the results.

3. Azimuthal symmetry is assured by the nature of the code.

4. The code injection can be made to neglect anode foil scattering, so that the particles are monoenergetic and spatially uniform at injection.

5. Thode, et al.[35], give a numerical relation to insure that the imposed magnetic field is effectively infinite. It is $\omega_c/\omega_p^0 \geq 5$ where ω_c is the beam cyclotron frequency defined as eB_0/mc. This is met by running the code's dimensionless, external, magnetic field as

$$B_0 = \omega_c/\omega_p^0 = 8.0 \tag{12}$$

The number of cells in the X1 and X2 direction were 190 and 37, respectively. The X1 length was held constant at 50.0 units giving $\Delta X1 = 0.263$ per cell. The X2 radius varied from 2.89 to 5.0 depending on the value of injected current. The boundary conditions for the electrons are reflection at the axis and absorption on both the radial and axial surfaces. Potentials are set to zero at the upstream axial and outer radial boundaries in order to represent metal surfaces. At the downstream axial boundary, however, the normal derivatives of the potentials are set to zero in order to mock up an infinitely long cylinder.

In the next section, the value of γ_a from the simulation calculation is compared, for a given value of ν, with that given by equation (7), as well as with a numerical solution obtained by iterating on equation (4) with $r = a$.[29]

C. Results

Several CCUBE runs were made using $\gamma_0 = 5$ and varying values of ν in order to determine the maximum value of $|\phi|$. This occurred consistently at the radial value $r = a$. Therefore, $|\phi|$ maximizes for $\phi(a) \equiv \phi_a$. The characteristics of the simulation runs are given in Table 1. The last column in Table 1 refers to whether the downstream axial boundary was grounded or open. Such a condition enabled us to check whether or not end plate effects were entering the problem. As seen in Table 1 no effects were noted. The percent error was derived on the basis of the code's management of conservation of energy, which is denoted by a net energy diagnostic. Since net energy continuously increases due to roundoff and truncation errors, the percent error will increase as a function of computer run time. The percent errors given in Table 1 were taken after the run reached a steady state, as denoted by total energy and $|\phi|$ reaching a constant, or a virtual cathode was formed. The latter case was true in runs 3 and 8.

This can be observed in the table, since $|\phi_a| > (\gamma_0 - 1)$. Thus, the space-charge limiting current lies between $\nu = 1.175$ and 1.293 for the solid beam case and $\nu = 2.846$ and 3.034 for the annular beam case.

TABLE 1

CHARACTERISTICS OF SIMULATION RUNS

Run	ν	$|\phi_a|$	Error (%)	a/R	b/R	$L(c/\omega_p^0)$	$R(c/\omega_p^0)$	Downstream Axial Boundary
1	1.175	3.07	1.5	0	0.5	50.0	4.38	0
2	1.175	3.06	1.2	0	0.5	50.0	4.38	G
3	1.293	4.20	2.5	0	0.5	50.0	4.60	0
4	0.982	1.01	0.74	0.4	0.8	50.0	2.89	0
5	1.957	2.05	1.1	0.4	0.8	50.0	4.08	0
6	2.846	3.18	1.2	0.4	0.8	50.0	4.92	0
7	2.846	3.18	1.1	0.4	0.8	50.0	4.92	G
8	3.034	4.25	3.1	0.4	0.8	50.0	5.08	0

A comparison is made between the numerical, analytical and simualtion models in Table 2. All three methods produce consistent values of γ_a for given values of sublimiting injected current. Table 2 lists the values given by the three methods, where

$$\gamma_a = \gamma_0 - |\phi_a| \tag{13}$$

is used to define γ_a for the simualtions. Note that if a virtual cathode is formed, $|\phi_a| > (\gamma_0 - 1)$, γ_a as defined by equation (13) does not have a physical meaning. Rather, it is simply a mathematical relation between γ_0 and $|\phi_a|$.

13

TABLE 2
COMPARISON OF MODELS

ν	γ_a Numerical	γ_a Analytical	γ_a Simulation	Beam Type
1.175	1.893	1.93	1.93	Solid
1.293	Virtual Cathode	Virtual Cathode	Virtual Cathode	Solid
0.982	4.004	4.00	3.99	Annular
1.957	2.976	2.98	2.95	Annular
2.846	1.867	1.92	1.82	Annular
3.034	Virtual Cathode	Virtual Cathode	Virtual Cathode	Annular

A more important comparison can be made between the values for space-charge limiting current, ν_L, derived from the numerical, analytical, and simulation models and that produced by the widely used Bogdankevich-Rukhadze interpolation formula, equation (5). This is done in Table 3. Equation (5) predicts values for ν_L which are significantly lower than those of equation (4) and (7). However, the analytical results differ from the figures given by the integral equation by roughly 3 percent. ν_L is obtained from equation (4) by determining numerically the largest value of ν for which a solution exists. The limiting current for equation (7) is derived from the value of γ_a which maximizes ν.

TABLE 3
. LIMITING CURRENT COMPARISON

Beam Type	ν_L Numerical	ν_L Analytical	ν_L Simulation	ν_L B-R
Solid	1.27	1.31	1.175 - 1.293	1.118
Annular	3.03	3.12	2.846 - 3.034	2.712

The discrepancy in the limiting value of ν between the Bogdankevich-Rukhadze and Genoni-Proctor formulations is due to the error involved in assuming the uniform density approximation. Figure 3 is a plot of the relation between ν and γ_a in the uniform density approximation and in a second order analytical expression using a better quadratic fit than equation (7). The simulation points are added. It is clear that the uniform density approximation underestimates the value of ν for all values of γ_a. Finally, Figure 4 plots $\gamma(r) - 1$ versus r. It shows the dependence of beam kinetic energy on r for the annular beam modeled. The successively more energetic lines of dots correspond to the more recent injections of charge through anode. As expected, the minimum kinetic energy occurs at the inner beam edge, and the maximum occurs on the outer edge. The unifrom density approximation neglects this dependence.
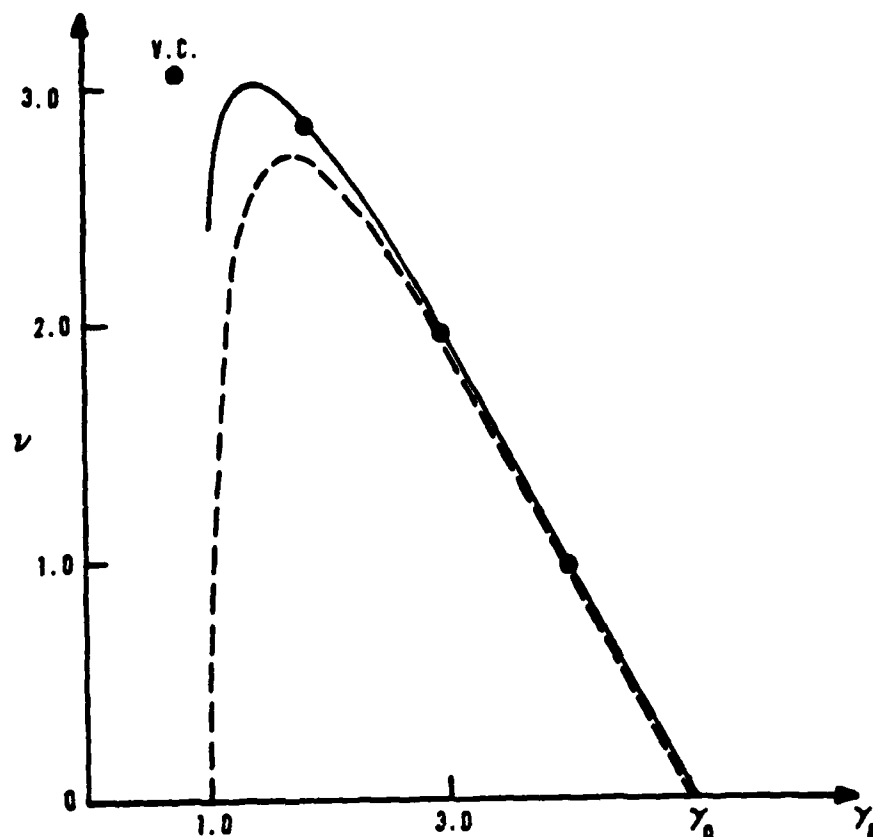
Figure 3. Plot of ν versus γ_a for $\gamma_0 = 5$, $^a/R = 0.4$, $^b/R = 0.8$. The dashed line represents the uniform density approximation. The solid line results from an approximate second order analytical relation. The points correspond to simulation results. (N.B. γ_a for the point labeled v.c. (virtual cathode) has no physical meaning. It is defined in terms of equation (13)).
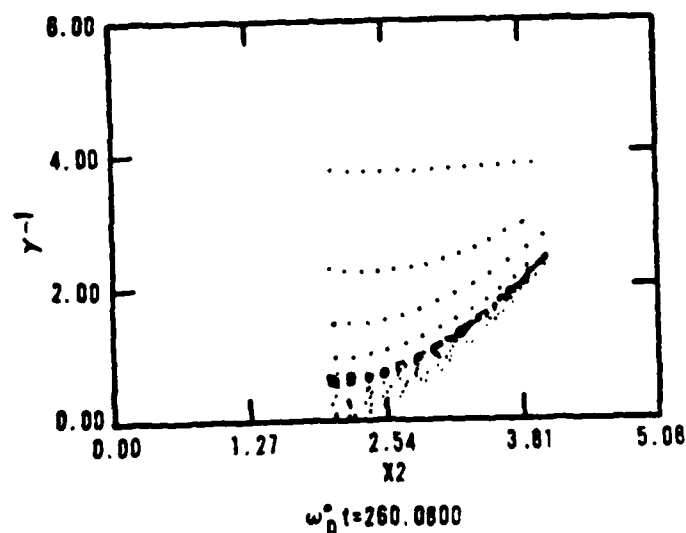

$\omega_p^o t = 260.0800$

Figure 4. A CCUBE diagnostic of particle kinetic energy versus r for the annular beam showing the radial dependence of γ.

16

III. THE SPACE-CHARGE LIMIT INSTABILITY

We have visualized the space-charge limiting current as a point at which the electrostatic potential exceeds the kinetic energy of the beam. However, it is easily noted from Figure 3 that at the SCL the beam kinetic energy is approximately $\gamma_0^{1/3}mc^2$. Thus, although the onset of virtual cathode formation can be exactly predicted as the point at which the beam exceeds a critical current, the dynamics of its formation and subsequent oscillations are not well understood.

A small signal perturbations analysis can be performed just below the SCL which seems to predict instability above the limiting current value,[6,9] however, it is not rigorous and in fact produces misleading results. Instead one can use multiple scaling perturbation techniques to study the time dependent behavior of a beam when the SCL is exceeded. We derive estimates for the nonlinear growth rate of the ensuing instability and show that even below the SCL the beam is unstable to sufficiently large perturbations. The method can be applied to a wide class of problems, but here we treat the short-circuited one-dimensional electrostatic diode depicted in Fig. 5 as the simplest model containing the appropriate physics. We show that, at least in one dimension, an arbitrarily heavy ion background does not alter the qualitative behavior of the beam, and present numerical results that exhibit virtual cathode oscillations for a neutral beam. Before starting this analysis, it is worthwhile to describe the results of numerical simulations to present a picture of time-dependent virtual cathode dynamics.
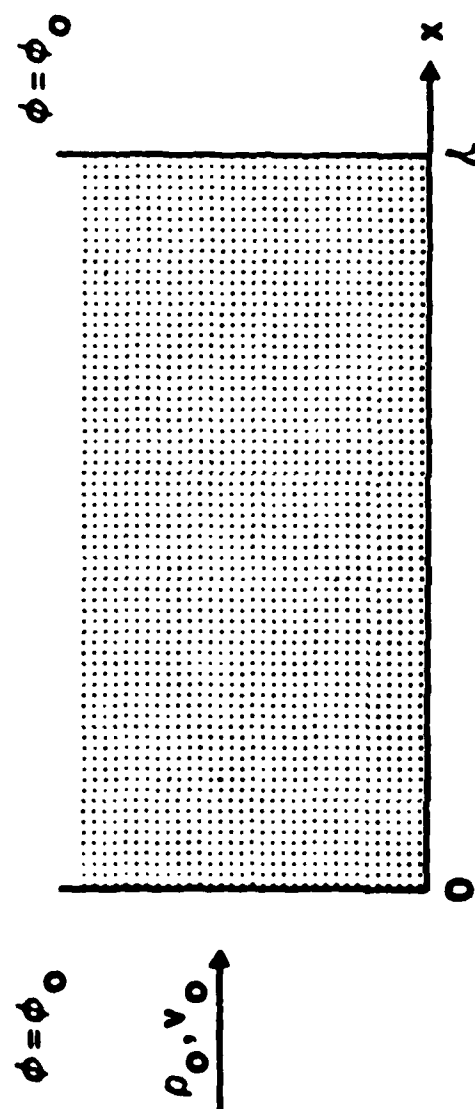
17

Figure 5. Schematic of the short-circuited one-dimensional electrostatic diode modelled in this study.

18

A. Physical Description of the Virtual Cathode

Simulations were carried out in conjunction with the theory presented in the next section using a two-dimensional, relativistic, electrostatic, particle-in-cell code. The code can solve self-consistently for the time dependent trajectories of tens of thousands of plasma particles over thousands of plasma periods. All variables are expressed in dimensionless terms. Therefore, length is in units of c/ω_p; time is measured in units of ω_p^{-1}, and particle velocity is given by $v_i = \beta_i \gamma$ ($i = 1,2,3$), where ω_p is the initial electron plasma frequency.

In these simulations a monoenergetic 51 keV electron beam is injected into a Cartesian geometry. The left and right boundaries are grounded representing a planar short-circuited diode. Periodic boundary conditions in the transverse direction make configuration space effectively one-dimensional. In general, the simulation had 62 cells in the longitudinal direction modelling a length of 1.0 c/ω_p. The time step was 0.0125 ω_p^{-1}. Twenty particles were injected per cell.

A detailed discussion of the physical dynamics of the virtual cathode based on these numerical results is appropriate here. The usual graph of potential minimum, ϕ_m, in the diode versus electron beam current, α, is shown in Fig. 6. The parameter α will be discussed later. When α is increased above the space-charge limit, ϕ_m jumps from the stable normal-C branch to the oscillatory stable branch. The amplitude and position of ϕ_m while on the oscillatory branch describe a limit cycle, as expected for a relaxation oscillation which this represents. Typical limit cycles are depicted in Fig. 7. As α is increased further, ϕ_m, the oscillation frequency, and virtual cathode position within the diode asymptotically approach limiting values. If α is decreased, the oscillation amplitude, $\Delta\phi_m$, decreases and the position of ϕ_m moves toward the diode center.
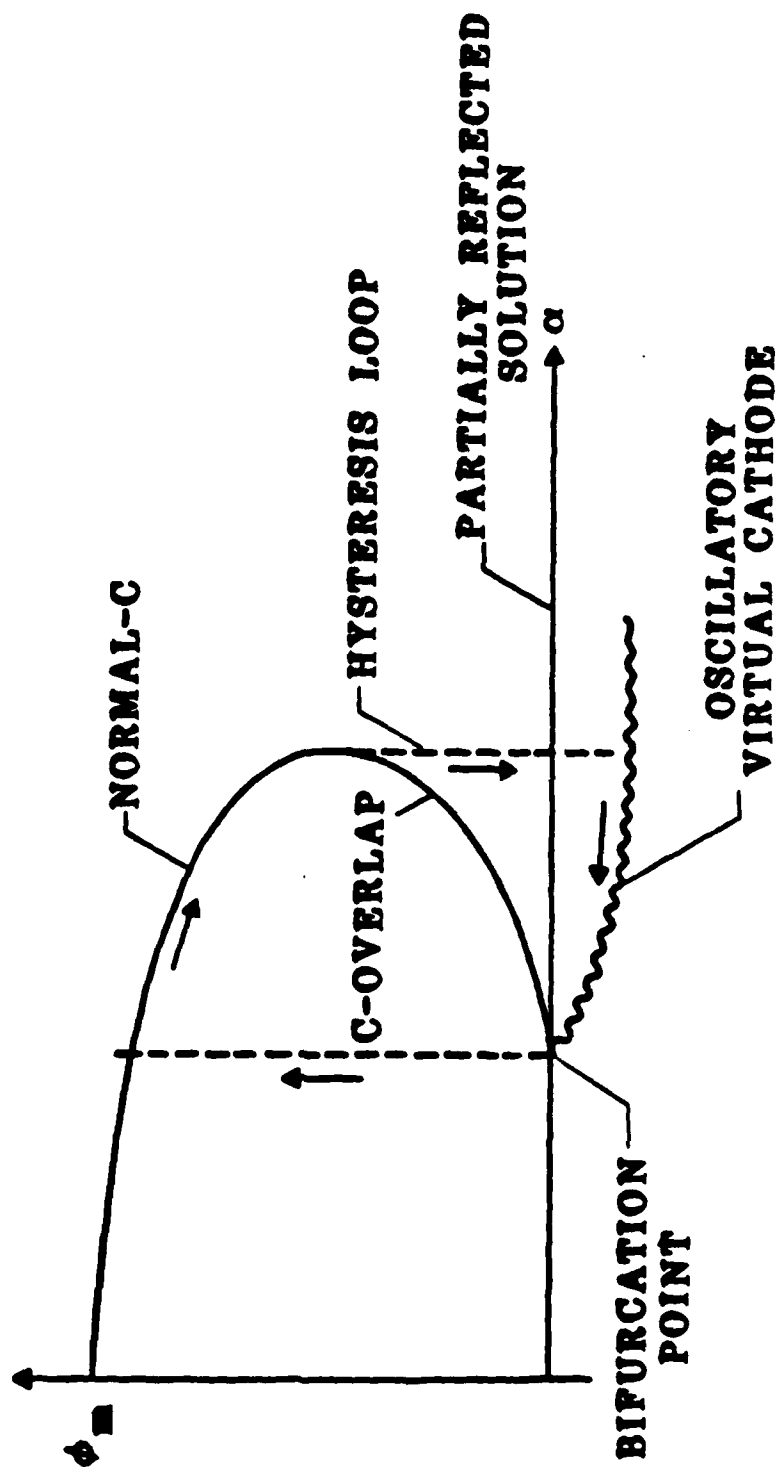
19

Figure 6. Electrostatic potential minimum as a function of current, α. The plot depicts the various possible solutions such as normal-C flow (stable), C-overlap (unstable), the partially reflected solution (unstable) and the oscillatory virtual cathode (stable). The motion around the hysteresis loop is denoted by arrows.
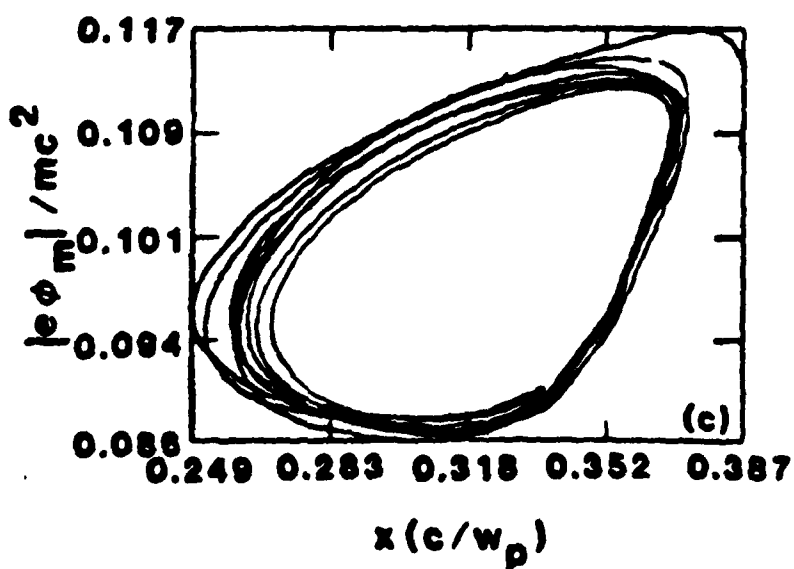
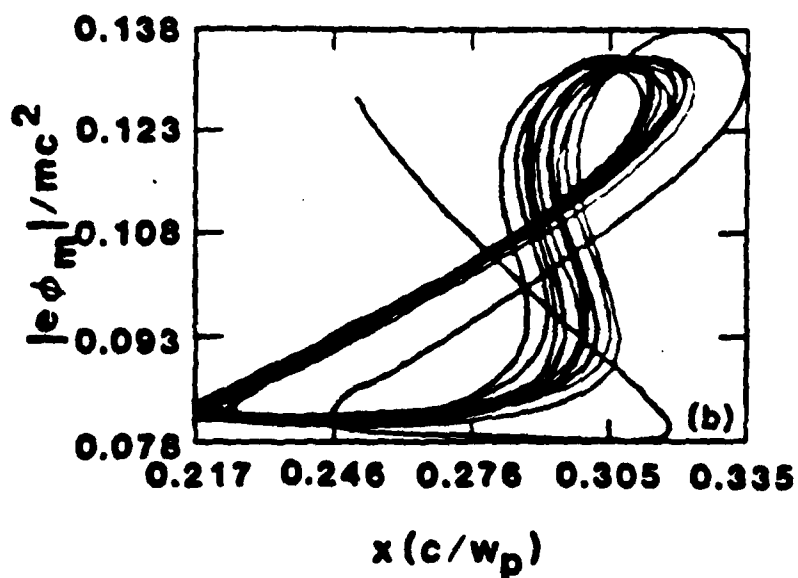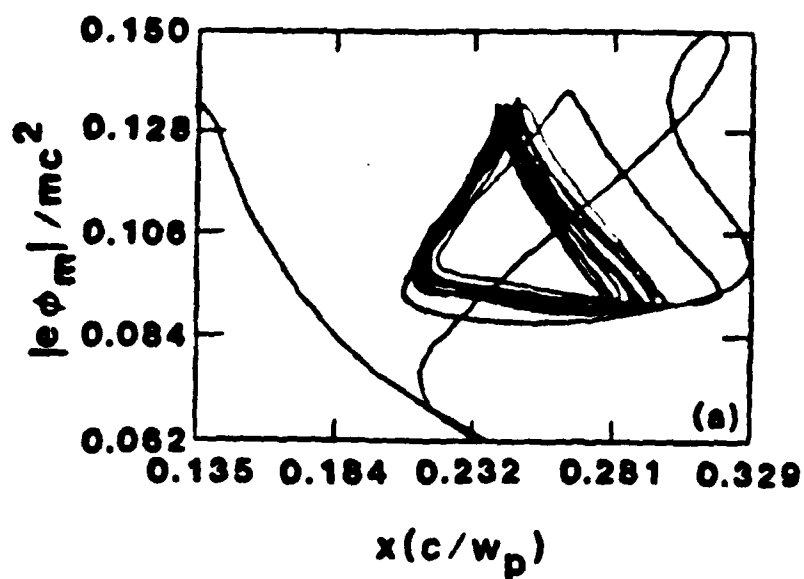Figure 7. Typical virtual cathode limit cycles in the classical short-circuited one-dimensional diode with an injection energy of 51 keV. a) α = 2.5, b) α = 2.0, c) α = 1.4. The motion in a) is clockwise and in c) is counterclockwise. ℓ = 1.0 c/ωp.

The electron flow reverts to the equilibrium steady state when the perturbation due to the rate of change of diode current below the space-charge limit is sufficiently large. This normally occurs before the bifurcation point is reached. The entire process forms a hysteresis loop, which is depicted in Fig. 6.

The virtual cathode originates at the bifurcation point. This is the intersection of the oscillatory state with the C-overlap[7] and partially reflected solution branches.[5] The bifurcation point cannot be reached in the short-circuited diode. Of the three branches emanating from it two (the steady ones) are physically unstable while the oscillatory branch is numerically unstable at this point. This results because the limit cycle at the bifurcation point is infinitesimally small, so that simulation codes lose resolution before it can be reached. Loss of resolution creates a small amplitude, high frequency oscillation observed in this study and previously.[9] This result is numerical, not physical.

This problem can be overcome, if we eliminate the hysteresis loop. Then the C-overlap branch disappears and we can get to the bifurcation point along the stable normal-C branch. This can be accomplished in several ways. The most appropriate in this study is to have a retarding potential difference across the diode equal to the injected electron kinetic-energy. Then the C-overlap solution vanishes and the bifurcation takes place at the space-charge limit, α_{SCL}. The oscillation can be described as a small perturbation on the beam rather than the radical change that results in the short-circuited diode when α_{SCL} is exceeded. This analysis indicates that the onset of virtual cathode formation occurs when the electron velocity in the steady state vanishes at some point inside the diode. For the short circuited diode this occurs at the diode center; for the biased diode it occurs at $x \lesssim \ell$. Because the oscillation is a small perturbation on the steady state fields in the biased diode, it is readily seen that the virtual cathode oscillation period at

onset is the electron transit time from the injection plane to the position where velocity vanishes.

Finally, consider the particle dynamics during the oscillation period for counterclockwise limit cycles ($\alpha \leq \alpha_{SCL}$) as in Fig. 7c. At the point where the virtual cathode position is a minimum and the potential well is starting to move to the right, its amplitude is too small to stop the electrons. When its motion is to the left it opposes the electron beam and causes particle bunching. Since the well is deeper, the stream velocity will vanish at some location and then become negative. Here, the second derivative of the velocity (d^2u/dx^2) is also negative. In this process the stream is continuously deformed to create a double valued negative velocity protrusion. The entire system is three valued (Fig. 8), as in a collisionless shock wave.[36] Here, the region of triple flow is not limited, as in usual collisionless shocks, by the presence of a transverse magnetic field,[37] but rather by the presence of the walls. Indeed, the reflected part detaches from the main beam and exits through the anode periodically, thus being responsible for the onset of oscillatory behavior in beam characteristics. As the potential minimum reaches the end of its left motion the two "lips" of the back reflected stream close. At this point no more electrons are reflected and the well moves to the right repeating the cycle.

For larger values of α the limit cycle is distorted into a figure 8 with one lobe having clockwise and the other counterclockwise motion (Fig. 7b). This transition continues until the motion is completely clockwise (Fig. 7a). It indicates a change in the particle bunching process and is related to the fraction of current which is reflected versus transmitted from the injected electron beam. In Figure 7a most of the beam is reflected whereas in Fig. 7c most electrons are transmitted.
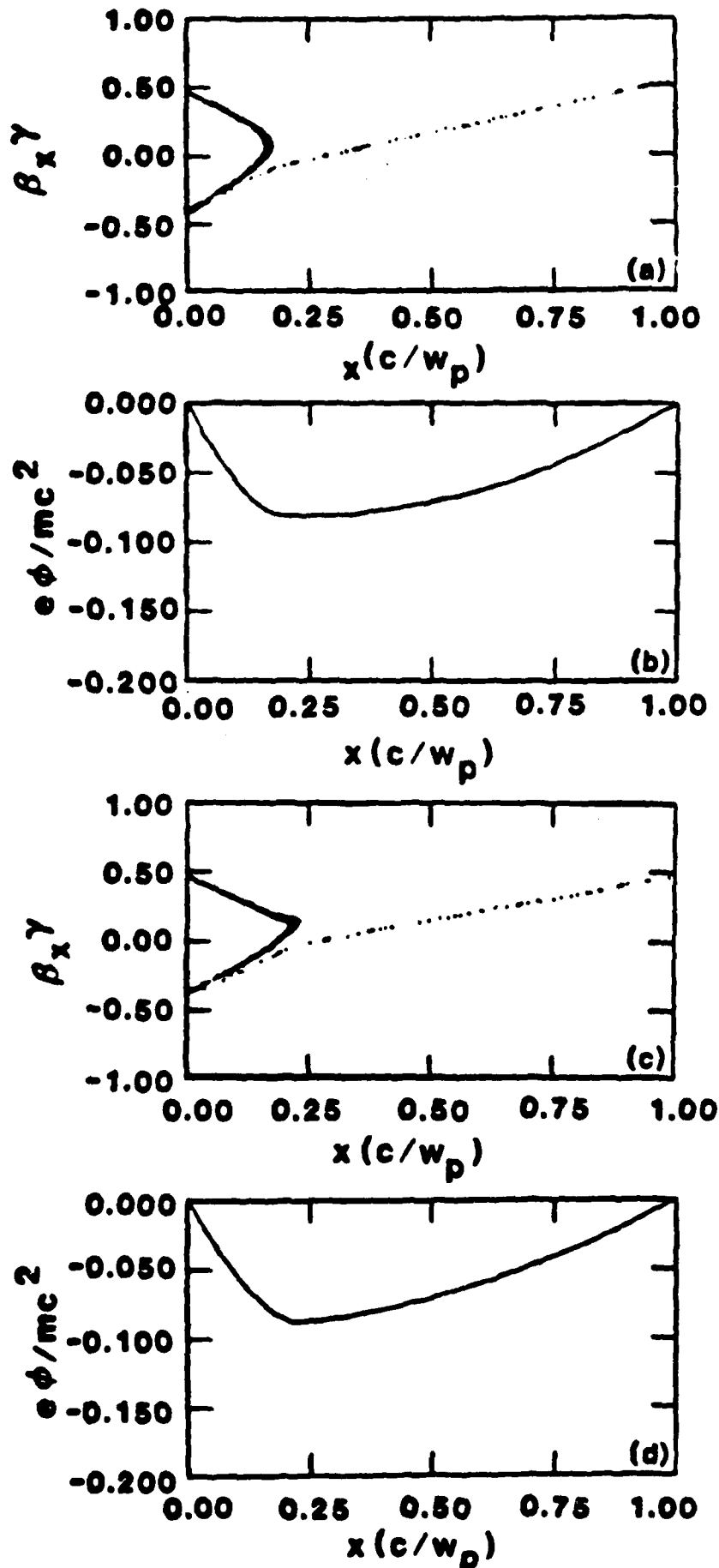
23

Figure 8. Successive snapshots of electron beam momentum space and corresponding potential shape in the diode for $\alpha = 2.0$, $\ell = 1.0$ c/ω_p. The time between frames is .5 ω_p^{-1}. The initial beam kinetic energy is 51 keV.
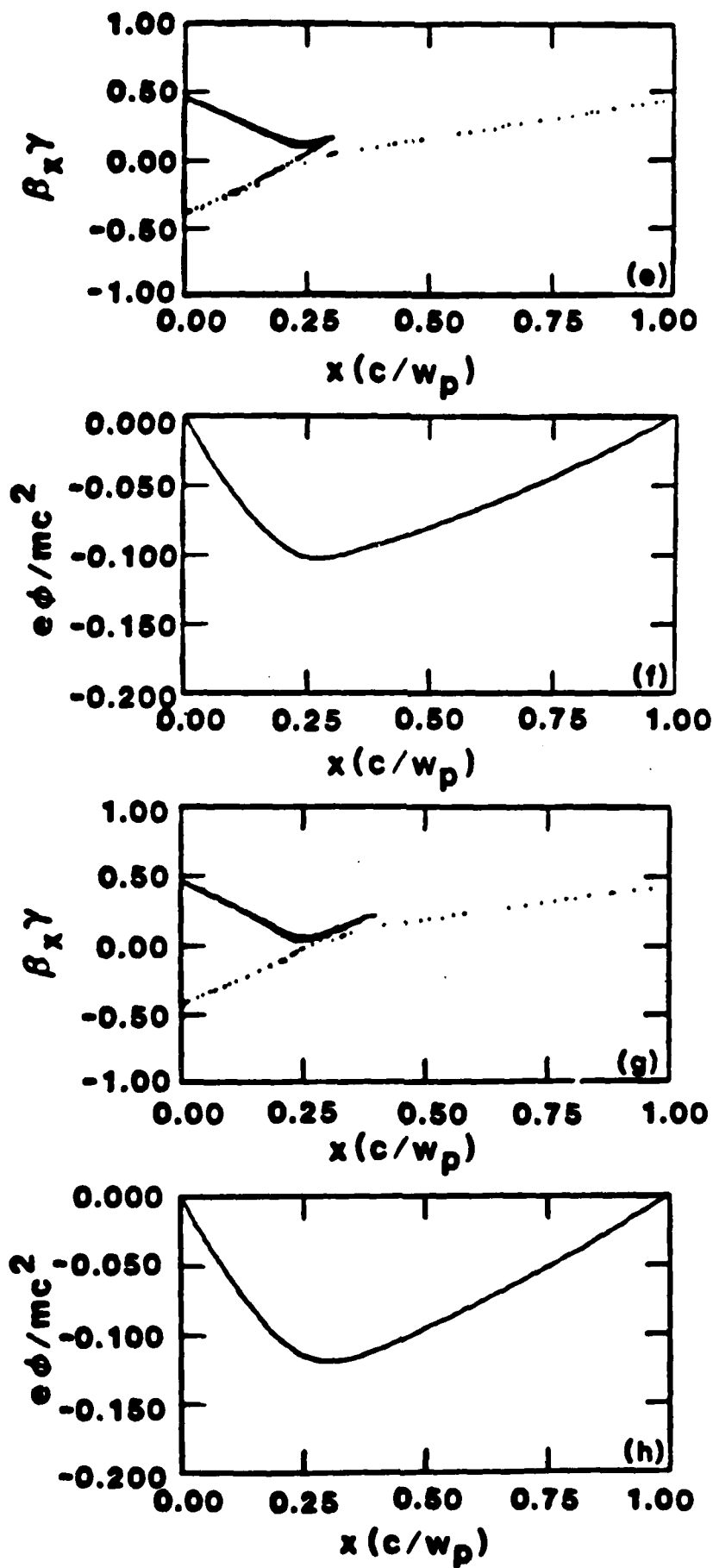
Figure B. Concluded.

B. Theory

The one-dimensional motion of electrons in the diode is given by the
equations of continuity, and momentum conservation for the electrons plus
Poisson's equation. They are expressed here as

$$\rho_t^- + (\rho v)_x^- = 0 \tag{14a}$$

$$v_t^- + v v_x^- = -\frac{e}{m} \xi \tag{14b}$$

$$\epsilon_0 \xi_x^- = \rho + \rho_h \tag{14c}$$

where $0 \leq x^- \leq \ell$. The subscripts denote differentiation with respect to
that variable. Electron and heavy ion charge density, electron velocity,
electric field, time and position are indicated by ρ, ρ_h, v, ξ, t^-, and x^-,
respectively. The appropriate boundary conditions are $v(o,t^-) = v_0$,
$\rho(o,t^-) = \rho_0$ and $\int \xi \, dx^- = 0$. An ion component is placed in Poisson's
equation in order to discuss two-specie space-charge flow. Conservation
equations of mass and momentum for the heavy ions are not included, because
it is assumed that their velocity does not change appreciably during their
passage through the diode.

In order to simplify the mathematics, we introduce dimensionless equa-
tions for our model. They are

$$n_t + (nu)_x = 0 \tag{15a}$$

$$u_t + uu_x = -\alpha E \tag{15b}$$

$$E_x = \alpha(n + I) \tag{15c}$$

where $n = \rho/|\rho_0|$, $u = v/v_0$, $E = (e\varepsilon_0/m|\rho_0|)^{1/2} \xi/v_0$, $t = v_0\bar{t}/\ell$, $\bar{x} = x/\ell$, $\alpha = (e|\rho_0|/\varepsilon_0 m)^{1/2} \ell/v_0$ a dimensionless parameter related to current, and I the ratio of heavy ion to electron charge densities, $I = \rho_h/|\rho_0|$. Alternatively, α may be written as $\ell\omega_p/v_0$ where ω_p is the beam plasma frequency. The boundary conditions for electrons become $u(o, t) = 1$, $n(o, t) = -1$, and $\int_0^1 E \, dx = 0$. For an ion beam $n(o, t) = 1$, otherwise the following derivation is the same.

1. Unneutralized Beams

For an unneutralized beam, setting $I = 0$ and solving by the method of characteristics[38,39] we find

$$n^{-1} = -\frac{\alpha^2}{2}(t-s)^2 + \alpha E_0(s)(t-s) - 1 \tag{16}$$

where s is the entry time for the particle occupying position x at time t and $E_0(s)$ is the electric field at $x = 0$. The particle trajectories are found by utilizing equation 15a, from which it follows that

$$\left(\frac{\partial x}{\partial s}\right)_t = n^{-1}. \tag{17}$$

This yields

$$x = \frac{\alpha^2}{6}(t-s)^3 + \alpha \int_t^s E_0(s)(t-s) \, ds + (t-s) \tag{18}$$

27

Integration of the trajectory equation is hard for general time-dependent situations, because imposing the proper boundary conditions leads to a nonlinear integral equation for $E_0(t)$. However, several special cases can be solved exactly. The problem of injection into an empty diode can be integrated until the formation of a singularity in n, indicating the crossing of trajectories.[39] In this case the stream velocity becomes 3-valued and one must use a Vlasov equation description,[40] rather than system (15) that is derived assuming a single stream of monoenergetic particles. As described in the previous section this multistreaming is characteristic of the oscillatory state created when α exceeds its SCL value.

Using these equations we can derive a similar representation for Fig. 6 in terms of E_0 and α. For steady states, $E_0(t) = E_0$, a constant, we find

$$u \;=\; -n^{-1} \;=\; \frac{\alpha^2}{2}\,(t-s)^2 - \alpha E_0(t-s) + 1 \qquad (19a)$$

$$x \;=\; \frac{\alpha^2}{6}\,(t-s)^3 - \frac{\alpha}{2}\,E_0(t-s)^2 + (t-s) \qquad (19b)$$

Imposing the conditions $x = 1$, $u = 1$ at $t-s = t_0$, the particle transit time, we note that t_0 must satisfy

$$\frac{\alpha^2}{12}\,t_0^3 - t_0 + 1 = 0 \qquad (20)$$

This equation has two positive solutions for $0 \le \alpha \le 4/3$, coalescing at $\alpha = 4/3$. The largest one, for $0 \le \alpha < 2\sqrt{2}/3$ does not correspond to a real flow. In Fig. 9 we show E_0 ($= \alpha t_0/2$) vs. α. This representation will be used in the discussion of nonlinear stability.
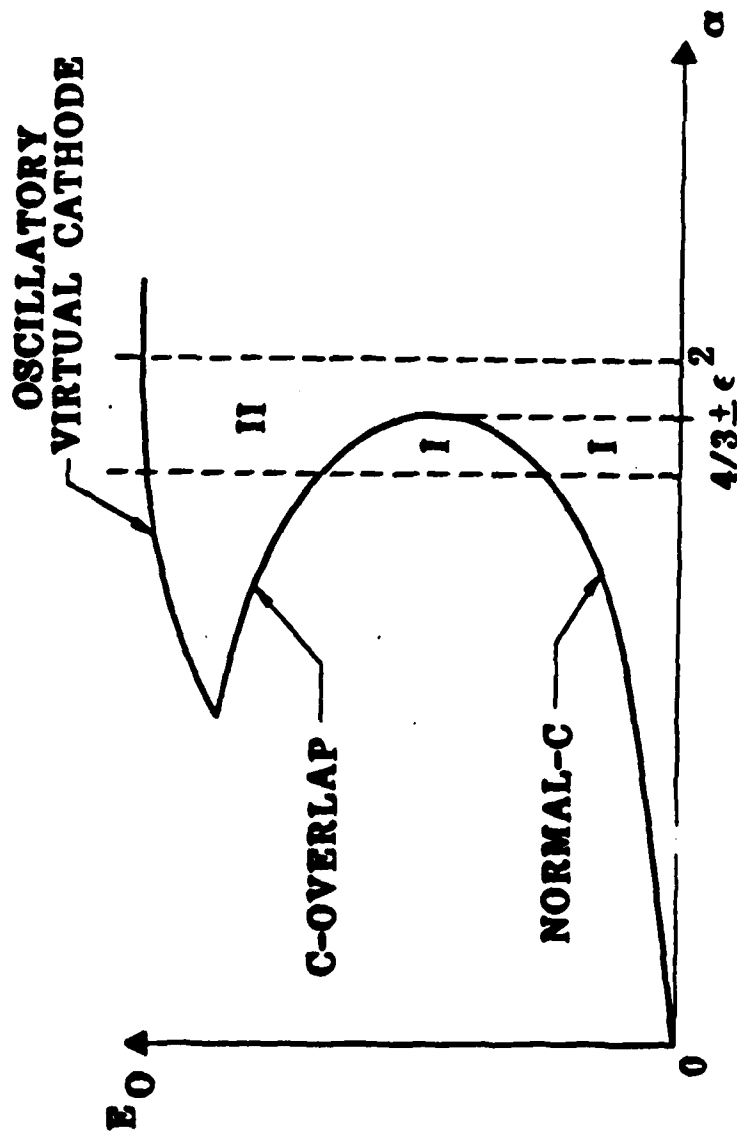
Figure 9. Electric field at the injection plane versus current, α, for $I=0$. The plot depicts the normal C-flow (stable) and C-overlap (unstable) solutions. The oscillating virtual cathode (stable) solution is also shown. Regions I and II define the domains of attraction of the normal-C and virtual cathode solutions near the SCL, $\alpha = 4/3$.

2. Neutralized Beams

The Pierce instability occurs when electron and ion space-charge flow
is considered in finite geometries where there is no potential difference
across the boundaries.[41] The ions can be stationary or moving with respect
to electrons. Charge neutrality is maintained at the injection plane.
This instability may have ramifications for charged particle inertial con-
finement fusion because of its effect on neutralized beam propagation in
the reactor.[42] In this section we show that the Pierce instability is a
special case of electron and ion space-charge flow. In general, two
species flow has steady and oscillatory states analogous to one species
space-charge flow.

The steady state behavior for the case of arbitrary I can be found in
a manner similar to I = 0. Rewriting system (15) in characteristic coor-
dinates we arrive at

$$\frac{d^2}{dt^2} \left(1 + \frac{I}{n}\right) + \alpha^2 I \left(1 + \frac{I}{n}\right) = 0 \tag{21}$$

For positive ions (I > 0) the solution of (21) after satisfying the bound-
ary conditions is

$$1 + \frac{I}{n} = (1 + I)\cos\alpha\sqrt{I}(t-s) + E_0\sqrt{I}\sin\alpha\sqrt{I}(t-s) \tag{22}$$

Imposing conditions $x = 1$, $u = 1$ at $t-s = t_0$, we find the system

$$1 = \frac{1}{I} t_0 - \left(\frac{1-I}{\alpha I^{3/2}}\right) \sin\alpha\sqrt{I} \, t_0 + \frac{E_0}{\alpha I} (\cos\alpha\sqrt{I} \, t_0 - 1) \tag{23a}$$

$$1 = \frac{1}{I} - \frac{1-I}{I} \ \cos\alpha\sqrt{I} \ t_0 - \frac{E_0}{I} \ \sin\alpha\sqrt{I} \ t_0 \qquad (23b)$$

For $I = 1$, which implies charge neutralization, these equations reduce to the relations given in Reference 43 for the Pierce instability. However, by varying I the curves shown in Figure 10 are obtained. These are cuts at constant I through a three-dimensional contiguous surface. The space is defined by the axes $\bar{E} = E_0 I^{1/2}$, $A = \alpha I^{3/2}$ and I. The surface is 2π periodic in A with the vertical plane at $A = 2\pi$ being common for all values of I. For given A a linearized analysis establishes that the equilibria denoted by the curves are stable (unstable) for the lowest (highest) value of $\bar{E}$. At $I = 1$ exchange of stability takes place at odd multiples of π. For $I < 1$ exchange of stability occurs at the points where $dE_0/d\alpha \to \infty$.

It is evident from Fig. 10 that, for $I < 1$, there are no stable equilibrium solutions in the neighborhood of $A = \pi$. Therefore, one expects a virtual cathode to form when $I < 1$ and A adiabatically increases to π. We have found, by using numerical simulation, that in this case the beam settles to an oscillatory state, similar to the virtual cathode for unneutralized beams.[40] By slowly increasing I past the neutral beam value of 1 in our simulation, we have established that this oscillation persists. Indeed, finding this oscillatory state for $I > 1$ by other means would have been difficult, because the simulation would tend to follow the stable steady branch that is present for all values of current.

3. Nonlinear Stability Analysis

For $I < 1$, it is of interest to establish the properties of the beam instability at the SCL - generalized for $I \neq 0$ to mean the point where
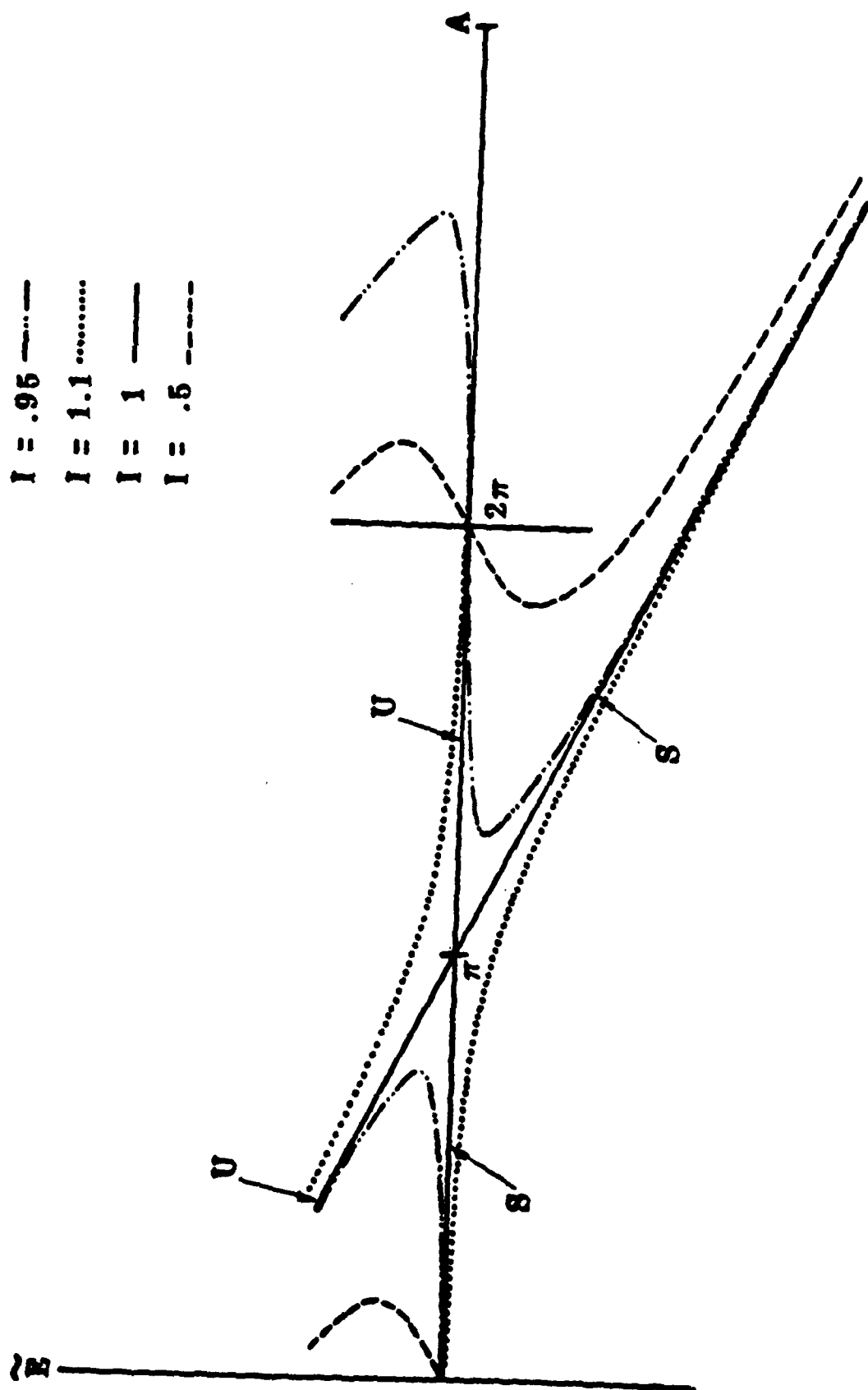
Figure 10. Curves of scaled electric field at the injection plane, $\tilde{E}$, versus scaled current, A, for various values of charge neutralization, I. The curves represent slices through a 3-dimensional surface. The S and U indicate stable and unstable branches for the I=1 slice.

$d\alpha/dE_0 = 0$. We shall carry out the analysis for $I = 0$, but our method can be applied to any similar jump phenomenon.

A linear stability analysis[6] about the steady state described by (20) results in the dispersion relation

$$(2 + \beta) e^{-\beta} = 2 - \beta + \frac{\beta^3}{\alpha^2 t_0^3} \tag{24}$$

where $\beta = i\omega t_0$. We have written the expression derived in Reference 6 in terms of our dimensionless variables. For α near the SCL value we let

$$\alpha = \frac{4}{3} - \epsilon^2, \qquad \epsilon \ll 1. \tag{25}$$

and find from (20) that near this value, t_0 is approximately

$$t_0 \approx \frac{3}{2} \mp \epsilon \frac{3}{2\sqrt{2}} + C(\epsilon^2) \tag{26}$$

where the $-(+)$ sign corresponds to the lower (upper) branch in Fig. 9.

By substituting in (24), and assuming β small, we find that

$$i\omega \approx \beta \approx \mp 2\sqrt{2} \epsilon + 0(\epsilon^2) \tag{27}$$

Since the linearized analysis led to time factors of the form $e^{i\omega t}$ in the perturbations, it follows that the lower branch in Fig. 9 is stable and the upper unstable, while at the SCL ($\epsilon = 0$) we have neutral stability.

Above the value $\alpha = 4/3$, linearized theory is not applicable. Utilizing multiple scaling perturbation theory[44] we can carry out a nonlinear

stability analysis near $\alpha = 4/3$. In system (15) we set $\alpha = 4/3 \pm \epsilon^2$. In this neighborhood perturbations evolve on a "slow" time scale, depicted by $\tau = \epsilon t$.

Eliminating the electric field by combining (15b) and (15c) and utilizing τ, system (15) becomes

$$\epsilon n_\tau + (nu)_x = 0 \tag{28a}$$

$$(\epsilon u_\tau + uu_x)_x = - (\tfrac{4}{3} \pm \epsilon^2)^2 n \tag{28b}$$

with conditions $u(o,\tau) = 1$, $n(o,\tau) = -1$ and $\int_0^1 E dx = 0$ rewritten as

$$\epsilon \int_0^1 u_\tau dx + \tfrac{1}{2} [u^2(1,\tau) - u^2(0,\tau)] = 0 \tag{29}$$

Substituting the asymptotic expansions

$$u \sim \sum_{i=0}^{j} \epsilon^i u_i(x,\tau) + 0(\epsilon^{j+1}), \quad n \sim \sum_{i=0}^{j} \epsilon^i n_i(x,\tau) + 0(\epsilon^{j+1}) \tag{30}$$

for u and n into (28) and equating coefficients of various powers of ϵ, there results a hierachy of equations for the u_i and n_i.

Solving the $0(1)$ system gives

$$(u_0 - \tfrac{1}{2})(u_0 + 1)^2 = 2(2x - 1)^2 \tag{31a}$$

$$n_0 = - 1/u_0 \tag{31b}$$

34

To solve the $O(\epsilon)$ system we introduce a new variable q by

$$x = \frac{16}{9}\left(\frac{q^3}{6} - \frac{3}{8}q^2\right) + q \tag{32}$$

so that

$$u_0 = \frac{16}{9}\left(\frac{q^2}{2} - \frac{3}{4}q\right) + 1 \tag{33}$$

We then find

$$n_1 = \frac{1}{u_0^2}\, u_1 \tag{34a}$$

$$u_1 = C\, \frac{q(q - 3/2)}{u_0} \tag{34b}$$

with C a constant of integration which is, in general, a function of the slow time τ. To find $C = C(\tau)$ which determines the slow evolution of the perturbation $u_1(x,\tau)$ we need to go to the next order, $O(\epsilon^2)$. By substituting in the expressions for u_0, u_1, n_0, n_1 and eliminating n_2, we find that $u_2(x,\tau)$ satisfies

$$(u_0 u_2)_{xx} + \frac{16}{9}\, \frac{1}{u_0^2}\, u_2 = \frac{16}{9}\frac{C_\tau}{u_0} \int_0^q \frac{q(q-3/2)}{u_0^2}\, dq + C^2\, \frac{q^2(q-3/2)^2}{u_0^3}$$

$$- C_\tau\left(\frac{q(q-3/2)}{u_0}\right)_x \pm \frac{8}{3}\, \frac{1}{u_0} \tag{35a}$$

$$u_2(0,\tau) = 0, \quad u_2(1,\tau) = +\frac{9}{16}\, C_\tau \tag{35b}$$

The solution to this inhomogeneous two-point boundary value problem exists provided a certain orthogonality condition between the right hand side and the solution of the adjoint problem that takes account of the boundary conditions is satisfied (Fredholm alternative theorem).[45] This leads to the desired equation determining $C(\tau)$:

$$aC_\tau + bC^2 \pm c = 0 \tag{36}$$

where a, b, and c are found to be

$$a = -\int_0^{3/2} \frac{q(q-3/2)}{u_0^2} \left[\frac{16}{27} q^2(q-9/4) + \frac{3}{2} \right] dq = 1.6850 \tag{37a}$$

$$b = \frac{8}{3} \int_0^{3/2} \frac{q^3(q-3/2)^3}{u_0^4} dq = -3.7968 \tag{37b}$$

$$c = \frac{8}{3} \int_0^{3/2} q(q-3/2) dq = -1.5 \tag{37c}$$

In (36) the (+) or (-) signs indicate that we are above or below the SCL, respectively.

Above the SCL, we find

$$C(\tau) = -\frac{c}{b} \tan\left[\sqrt{cb}\, (\frac{\tau+\tau_0}{a}) \right] \tag{38}$$

and below

$$C(\tau) = \frac{c}{b} \tanh\left[\sqrt{cb}\, (\frac{\tau+\tau_0}{a}) \right] \quad \text{if} \quad |C(o)| < \sqrt{c/b} \tag{39}$$

$$C(\tau) = \frac{c}{b} \coth \left[\sqrt{cb} \left(\frac{\tau + \tau_0}{a} \right) \right] \quad \text{if} \quad |C(0)| > \sqrt{c/b} \tag{40}$$

where τ_0 is a constant of integration. In general, small initial perturbations will lead to the solution

$$u(x,t) \sim u_0 + \sum_{i=1}^{j} C_i(\tau) e^{\omega_i t} u_i(x) + O(\epsilon^2) \tag{41}$$

where ω_i are the various distinct solutions of the dispersion relation (24) at $\alpha = 4/3$.[44],[46] It is straightforward to show that all modes are such that $Re(\omega_i) < 0$ except one for which $\omega = 0$. Thus, all other modes will decay in the fast time scale and only the neutral mode ($\omega = 0$) will persist. Our solution after a short time will look like

$$u \sim u_0 + \epsilon \, C(\tau) \, \frac{q(q - 3/2)}{u_0} + O(\epsilon^2) \tag{42}$$

From the given initial conditions it is easy to determine the initial condition for the neutral mode. Below the SCL, if the initial conditions are such that $C(0) > -\sqrt{c/b}$, the solution will evolve to the stable lower branch in Fig. (9) (Region I), while if $C(0) < -\sqrt{c/b}$, $C \to \infty$ in finite time. (Fig. 9, Region II). Blow up in finite time also occurs above the SCL for any $C(0)$. This does not mean that the actual solution blows up, just that it evolves to a final state far away from the two steady branches shown in Fig. (9), and thus, is not accessible by perturbation theory.

As can be seen in (38), the blow up above the SCL is described by a tangent function, therefore, the growth rate we find for this case must be appropriately interpreted. Note that the linearized dispersion relation

37

seems to suggest an imaginary exponential growth rate above the space charge limit.[3,6] In view of our results, we see that this is actually misleading. Moreover, we find that even below the SCL the stable steady branch can be destabilized by sufficiently large perturbations.

Our results agree with the linear theory, provided we consider the limit where the latter becomes applicable. Thus, we must compare the linear theory with (39) as $\tau \to +\infty$ (near the stable branch) and (40) as $\tau \to -\infty$ (near the unstable branch). To demonstrate this we set $\tau = \epsilon t$ in (39) and consider the limit $t \to +\infty$. Then

$$C(t) = \frac{c}{b} \tanh\left[\frac{\sqrt{cb}}{a} (\epsilon t + \tau_0)\right]$$

$$= \frac{c}{b} \left\{ \frac{1 - \exp - \left[\frac{2\sqrt{cb}}{a} (\epsilon t + \tau_0)\right]}{1 + \exp - \left[\frac{2\sqrt{cb}}{a} (\epsilon t + \tau_0)\right]} \right\}$$

$$= \frac{c}{b} \left\{ 1 - 2 \exp - \left[\frac{2\sqrt{cb}}{a} (\epsilon t + \tau_0)\right] + \ldots \right\} \tag{43}$$

We see that the decay rate of the perturbations as $t \to +\infty$ is equal to

$$\frac{2\sqrt{cb}}{a} \epsilon \approx 2.83\epsilon \tag{44}$$

which is the same as that found by the linearized analysis.[6] This quantity is important as it also determines an initial "growth rate" for the jump instability above the SCL described by (38). If we substitute the original dimensional time variable into our expressions and write the deviation of α from its value at the SCL as

38

$$\epsilon = (\alpha - \alpha_{SCL})^{1/2} = (\alpha - \frac{4}{3})^{1/2} \tag{45}$$

we find that the "growth rate" is given by

$$D = (\alpha - \frac{4}{3})^{1/2} \frac{\sqrt{cb}}{a} \frac{v_0}{\ell} \tag{46}$$

or

$$D = \left(\frac{\ell \, \omega_p}{v_0} - \frac{4}{3}\right)^{1/2} \sqrt{2} \frac{v_0}{\ell} \tag{47}$$

Of course, for the expansions in (41) to be valid, we must have $C(\tau) \ll 1/\epsilon$. However, while C is not too large (38) gives a reliable estimate for the growth rate of the instability.

IV. MICROWAVE GENERATION

Of the several millimeter sources that are in various stages of development (see Figure 11), the virtual cathode oscillator (Vircator) has a combination of characteristics which recommend it for high frequency use. First, the frequency of the vircator is tunable by changing the magnitude of an imposed axial magnetic field, eliminating any requirement to change the physical structure of the device. A single vircator will be tunable over an order of magnitude in frequency (e.g., 10 GHz - 100 GHz). Second, the bandwidth of the generator can be narrow or broad based on magnetic field shaping. Third, because the vircator functions above the space-charge limiting current for the electron beam, given efficient operation, it should be capable of much higher power than other microwave sources. Finally, the lack of passive resonating structures to produce the transmitted wave reduces the problem of field emission. This also increases the maximum possible generator power.

Experimentally, the virtual cathode has already proven itself to be a copious microwave source.[22-24],[26],[47] Table 4 lists experiments which have been carried out to date. With the exception of the Didenko experiment at Tomsk,[26] the frequency spectra have all had a broad bandwidth and relatively low efficiency. Nevertheless, even at low efficiency the experiment at Harry Diamond Laboratories[47] using a foilless diode (1 MV, 30 kA) produced 3 GW of power in the Ku band. It is one of the most powerful centimeter wavelength microwave sources available. The experiments at the Naval Research Laboratory[22] (Mahaffey et al.) and Tomsk will be reviewed in detail, because these experiments had the most useful diagnostics. Based on analytical work and computer simulations these experimental results can now be explained. It will be shown later that the foilless diode in a shaped axial magnetic field represents the best configuration for a high frequency device.
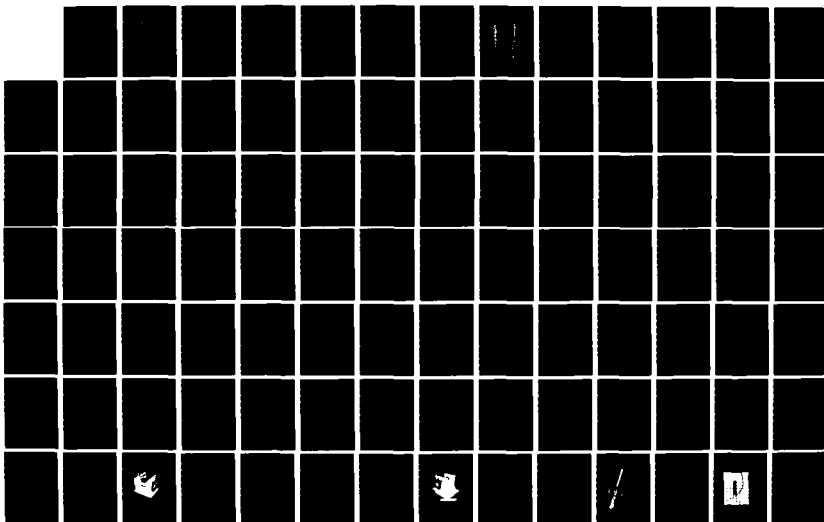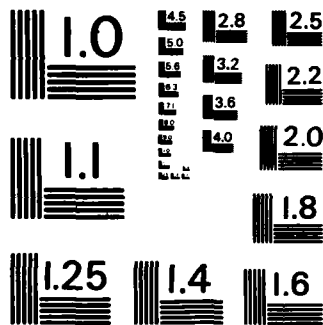
MICROCOPY RESOLUTION TEST CHART
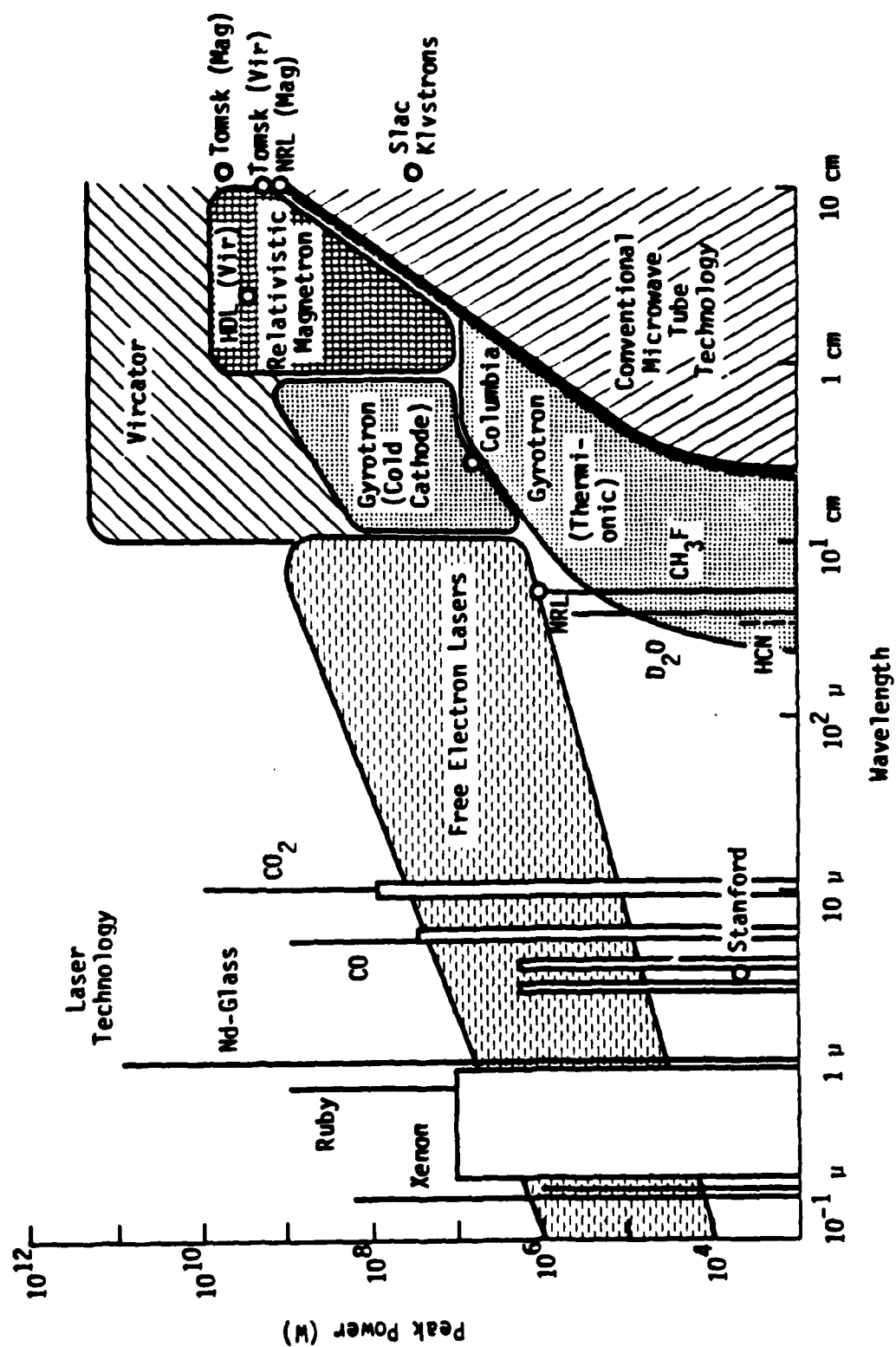
NATIONAL BUREAU OF STANDARDS-1963-A

Figure 11. Anticipated optimal operating ranges for various sources of high power electromagnetic radiation. Several experimental points are included.

TABLE 4

HIGH POWER MICROWAVE GENERATION HAS BEEN WITNESSED IN VARIOUS ELECTRON BEAM CONFIGURATIONS WHEN VIRTUAL CATHODES ARE FORMED.

REFERENCE	SYSTEM	PEAK POWER	FREQUENCY	EFFICIENCY
1. MAHAFFEY, et al.	REFLEX TRIODE	100 MW	11 GHz (10.0 – 12.4 GHz)*	1.5%
2. BRANDT, et al.	REFLEX TRIODE	- - -	9.8 GHz (7.0 – 13.0 GHz)*	- - -
3. BUZZI, et al.	FOIL DIODE	1 GW	10 GHz (9.0 – 14.0 GHz)*	1.25%
4. DIDENKO, et al.	REFLEX TRIODE	1.4 GW	3.3 GHz (2.1 – 5.0 GHz)*	12%
5. BROMBORSKY, et al.	FOILLESS DIODE	3 GW	15 GHz (8.2 – 18.0 GHz)*	5%
6. CLARK, et al.	FOILLESS DIODE	- - -	WIDEBAND (1.7 – 40.0 GHz)*	- - -
7. EKDAHL, et al.	FOILLESS DIODE	>100 MW	>70 GHz	- - -

* DETECTOR BANDWIDTH IN PARANTHESES

42

Although only scaling relations are presently available, qualitative dependencies of virtual cathode parameters on beam kinetic energy and injected current are known.

1. Potential amplitude, position, and oscillation frequency all have the same functional dependence on injected beam current. The positional dependence of the virtual cathode is given in Figure 12 for a 50 kV diode.

2. These parameters asymptotically approach a limiting value for current above the space-charge limit.

3. The fundamental oscillation frequency is approximately the relativistic beam plasma frequency given by

$$\omega_p^o = \left(\frac{4\pi n_b^o e^2}{\gamma_o m}\right)^{1/2} \tag{48}$$

where n_b^o is the electron beam number density at injection. In particular the oscillation frequency from numerical simulations varies such that

$$\omega_p^o \leq \omega_{osc} \leq \sqrt{2\pi}\, \omega_p^o \tag{49}$$

The end result is creation of an electrostatic potential minimum which oscillates in time and space. This fluctuating potential barrier acts as a gate to reflect some electrons and transmit others. The motion
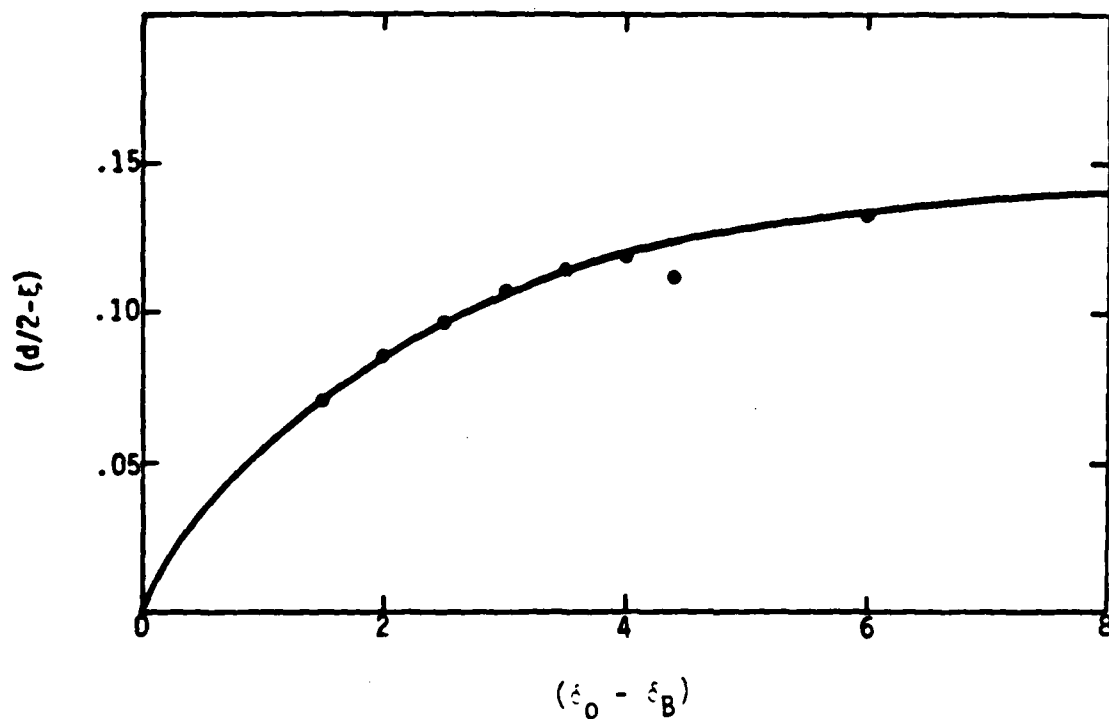
Figure 12. Variation of virtual cathode distance, ξ, from the one-dimensional diode center versus the difference between the injected current, δ_0, and the current needed for bifurcation, δ_B, in units of the Child-Langmuir value. δ_B is assumed to have a value of 4 from the classical analysis.

of the gate bunches charge. However, the charge bunch and virtual cath-
ode are separated spatially as shown in Figure 13.

By analogy this configuration represents an LC oscillator. The
virtual cathode acts as a capacitor to store the beam kinetic energy.
During that portion of the limit cycle in which the potential is greater
than the injected beam energy, charge is constrained to remain near the
anode. This starves the virtual cathode so that its amplitude decreases
below $(\gamma_0 - 1)$ mc^2/e. Once this occurs the charge bunch is trans-
mitted. The electron motion represents a large time varying current
through an inductor. The presence of charge away from the anode reestab-
lishes the virtual cathode, and the cycle repeats. The effect on beam
current can be examined using simulations. A net current diagnostic is
given in Figure 14 where the probe is positioned between the anode and
virtual cathode. The injected current in units of mc^3/e, ν_0, is three
times the limiting current, ν_ℓ, and γ_0 is 5. Note that the virtual
cathode can actually reverse the direction of current. The average cur-
rent value is ν_ℓ.

The oscillating current generates microwaves.[25] The wave frequency
is the oscillation frequency of the virtual cathode. The wave propagates
down the drift tube in a TM waveguide mode, which determines the wave-
length and phase velocity of the wave in the guide. The field configura-
tion is evident in simulations where there is no axial magnetic field.
If a cold beam is injected and azimuthal symmetry is assumed by the code,
the only nonzero fields are E_z, E_r, and B_θ in cylindrical geom-
etry. These three fields define a TM wave traveling in the z direction.
A time history and frequency spectrum of the B_θ field downstream of the
virtual cathode is given in Figure 15. The oscillation frequency of the
virtual cathode and its first three harmonics are clearly visible. Also
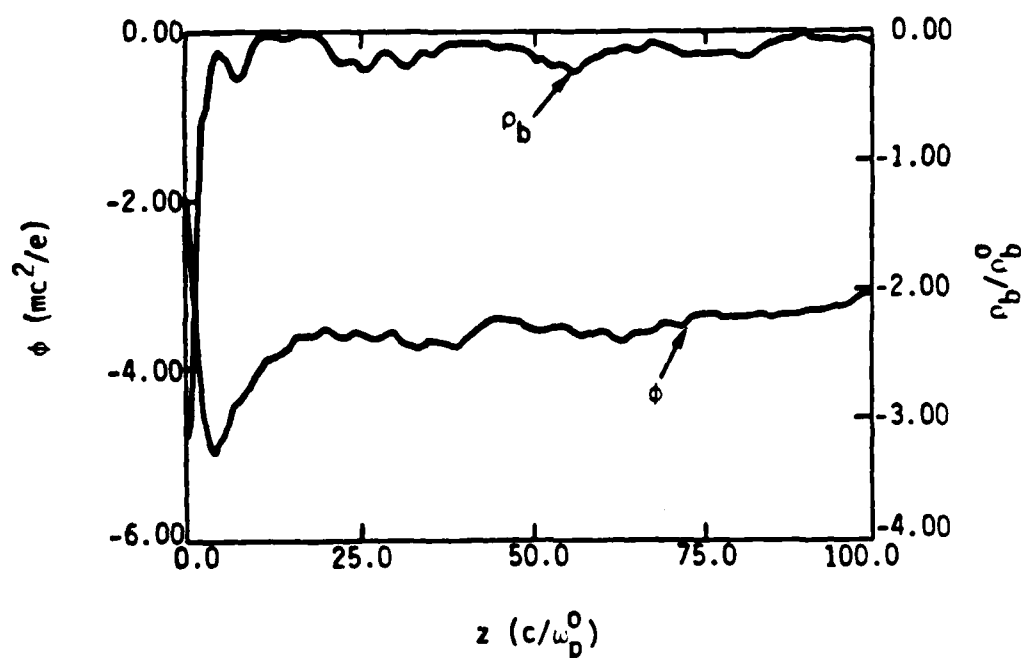included is a history of the E_z field on axis later in time. The

45

Figure 13. CCUBE diagnostic of charge density, ρ_b, and potential, ϕ, as a function of a longitudinal distance, z, for an electron beam in a two-dimensional drift space with an imposed large axial magnetic field. ρ_b is normalized to its value at injection. The value of (γ_0-1) is 4. Note that the minimum charge density and potential are separated in z.
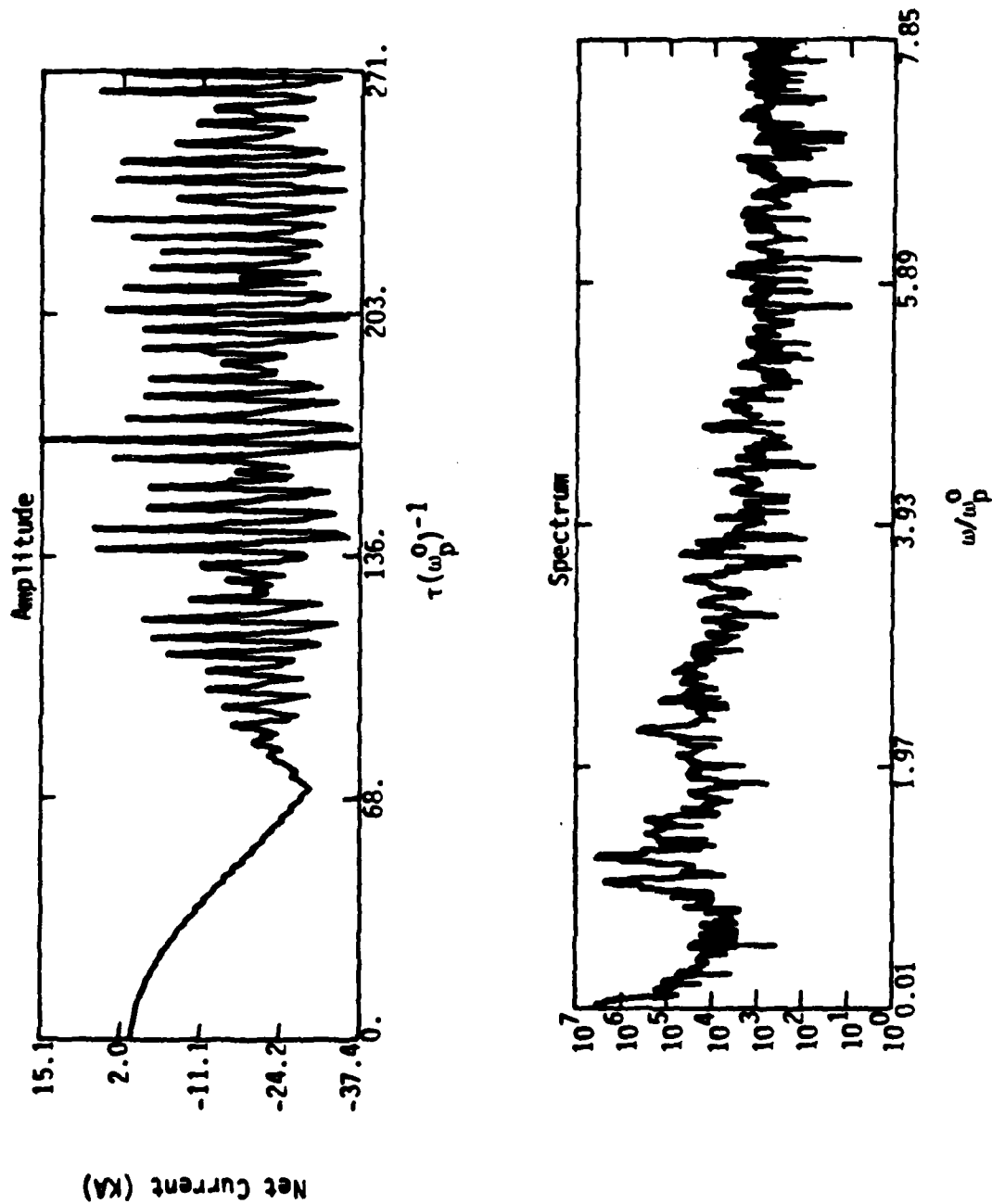
Figure 14. Net current amplitude and spectrum for a probe placed between the anode and virtual cathode. $\gamma_0 = 5$ and $\nu_0 = 3\nu_\ell$.

47
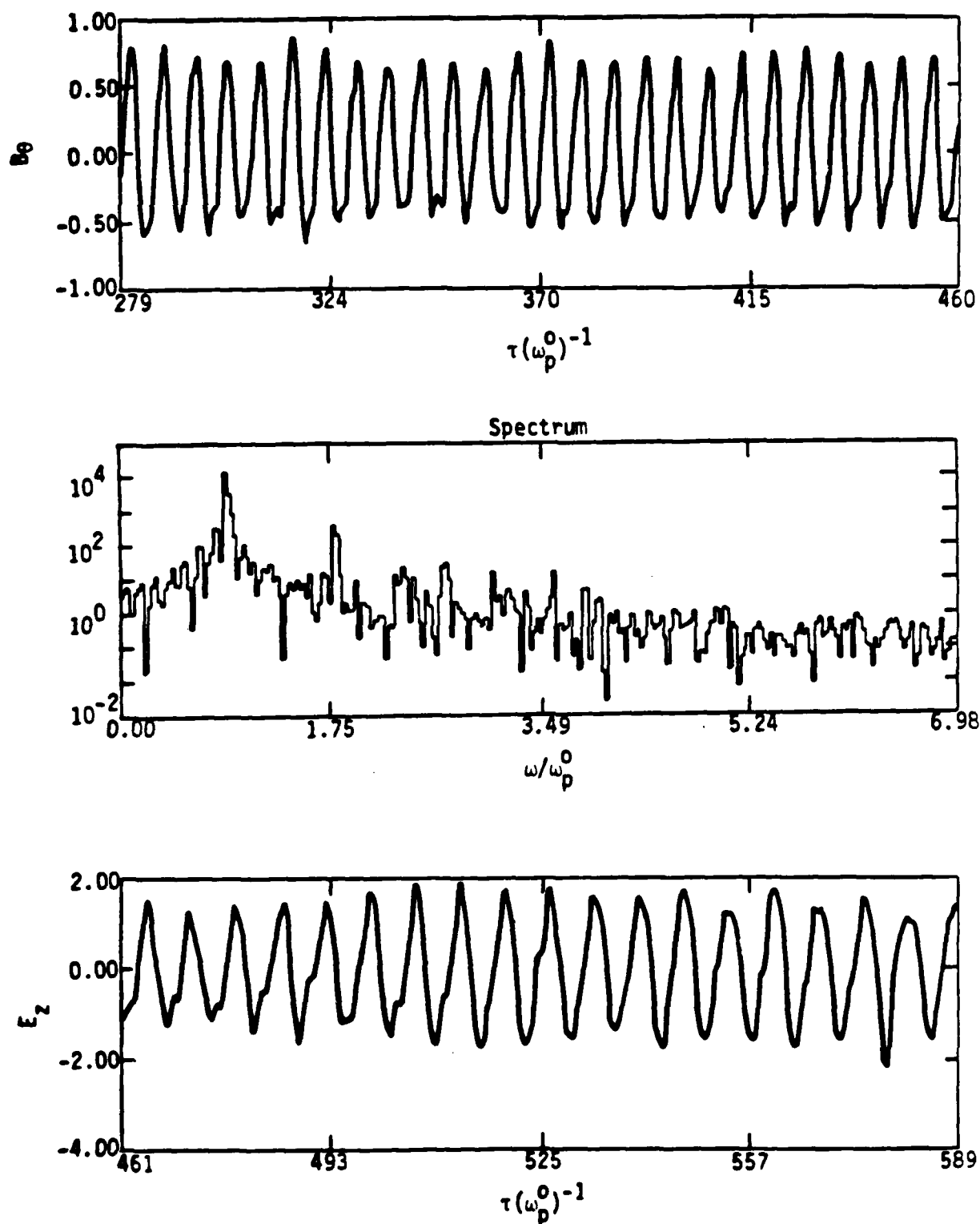
Figure 15. B_θ and E_z field probe histories and frequency spectrum for a simulation with $\gamma_0 = 5$, $\nu_0 = 3.7$ and $B_z = 0$. Field units are MeV/cm for a beam density of 10^{12}.

48

frequency spectrum, which is not included, is almost identical to that of B_θ. No attenuation of the field strengths is noted over the length of the drift tube which is equivalent to one meter for a beam density of 10^{12} cm^{-3}. The waveguide mode is TM_{02} with an RF conversion efficiency of greater than 20%. Because there is no axial magnetic field in this case few electrons are transmitted to the end of the drift tube. The loss of transmitted electrons does not reduce the RF efficiency.

As noted earlier, several experiments have already generated high power microwaves from virtual cathodes. The most informative experiments took place at the Naval Research Laboratory and at the Institute of Nuclear Physics at Tomsk. Both experiments used a reflex triode configuration. The electron beam machines were almost identical (350 kV, 50 kA versus 450 kV, 65 kA). Some salient features were

1. The average microwave frequency increased as the square root of triode voltage, V (see Figure 16).

2. Enlarging the anode cathode gap spacing, d, decreased wave frequency.

3. The microwave bandwidth is related to the change in voltage over the beam pulse, $\Delta V/V$. In the Russian experiment where $\Delta V/V$ - 5% - 10% the power FWHM occurred at ± 10% of the peak frequency.

4. For a constant voltage the frequency decreased as cathode shape was changed from solid to thick annular and finally thin annular plates of comparable area.
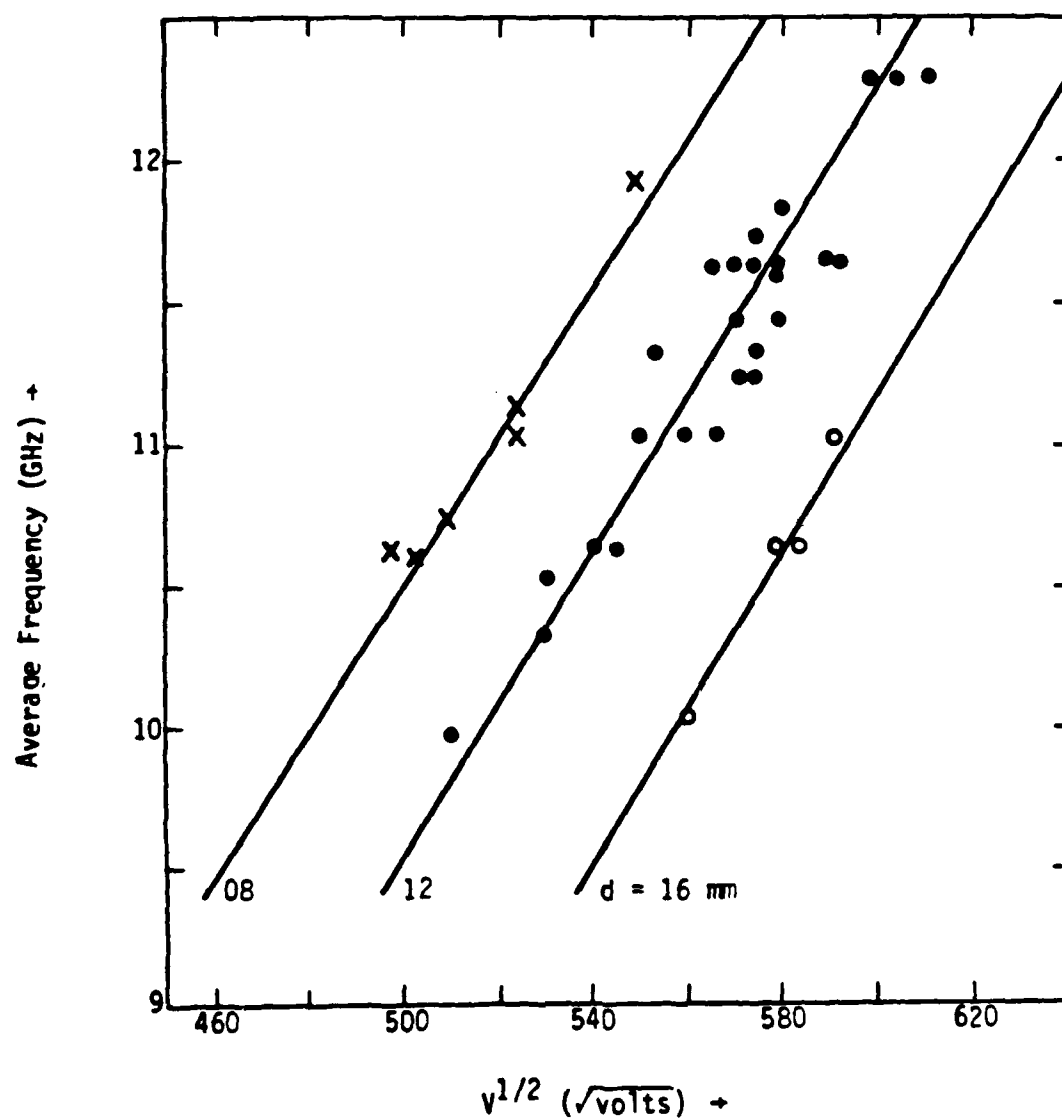
Figure 16. Average microwave frequency dependence on the square root of triode voltage (after Mahaffey et al.).

50

5. The imposition of an axial magnetic field greatly decreased
   the RF signal detected.

Each result can be explained in terms of virtual cathode characteristics. For a nonrelativistic beam in a semi-infinite one-dimensional drift space the vircator frequency, ω_{osc}, is directly proportional to the beam plasma frequency given by Equation 48. This is a good approximation for both experiments being considered here, because the beams are of low energy and the drift tube 'ength is much greater than its radius. Therefore, $\omega_{osc} \propto n_b^{1/2}$. The current density extracted from the cathode is defined by the nonrelativistic Child-Langmuir relation, which is

$$j_{CL} = \frac{4}{9} \left(\frac{2e}{m}\right)^{1/2} \frac{V^{3/2}}{4\pi d^2} = n_b ev \tag{50}$$

An expression for velocity is obtained from conservation of energy. It is

$$v = \left(\frac{2e}{m}\right)^{1/2} V^{1/2} \tag{51}$$

Combining Equations 3 and 4 and solving for n_b, one obtains

$$n_b = \frac{1}{9\pi e} \frac{V}{d^2} \tag{52}$$

or

$$\omega_{osc} \propto \omega_b = \frac{2}{3} \left(\frac{e}{m} \frac{V}{d^2}\right)^{1/2} \tag{53}$$

Thus, $\omega_{osc} \propto (V/d^2)^{1/2}$, which is precisely the experimental result. In addition, this *dependence of vircator frequency on voltage explains* the importance of a flat top voltage pulse in producing a narrow band-width. The closure of the A-K gap, which is due to plasma motion inherent in any foil system, also makes the spectrum broader. The Tomsk experiment used a mesh anode which would minimize the latter effect. An expression for these observations, which is obtained by differentiating Equation 53, is

$$\frac{\Delta \omega_{osc}}{\omega_{osc}} = \frac{\Delta V}{2V} + \frac{\Delta d}{d} \tag{54}$$

Cathode shape plays a role in defining the space-charge limiting current via a two-dimensional geometrical factor. The value of v_ℓ for a solid beam is less than for a thin annular beam of the same energy, current, and area. In the solid beam case the position of the virtual cathode is closer to the anode. This leads to a higher oscillation frequency, because the electron transit time between the anode and virtual cathode is less.

The final characteristic of the experiments is the apparent reduction of microwave generation in the presence of an axial magnetic field. However, two dimensional simulations, which include the diode physics, show that microwaves are still being produced.[48] The magnetic field forces the reflected electrons to reenter the A-K gap region along field lines. In the case of a foil diode or reflex triode the electrons suffer energy losses and are scattered by the foil. After several foil transits the beam electron distribution is nearly Maxwellian. This is equivalent to having electrons of widely varying voltage interacting with the virtual cathode. Thus, an extremely broad RF spectrum is produced which greatly reduces the detectable signal in any particular frequency band. The same result also occurs in foilless diodes. The broad electron

52

velocity distribution results from a two stream instability between part-
icles with positive and negative axial velocities in the region between
the real and virtual cathodes. The instability heats the two beams until
there is a homogeneous electron distribution in velocity space.

Based on our current theoretical knowledge of the virtual cathode,
numerical simulations, and experimental results, the following points
must be considered in the design of a coherent, high frequency vircator.

1. Both the oscillation frequency and net current asymptotically
    approach a value as injected current is increased above the
    space-charge limit. Thus, using a large value of v_0/v_ℓ
    does not substantially increase frequency or RF efficiency
    where efficiency is given by

$$n \leq \frac{e\Delta\phi}{(\gamma_0-1)\ mc^2} \tag{55}$$

A foilless diode in a strong axial magnetic field produces a
very thin annular beam. Since v_ℓ for an annular beam is
larger than for a solid beam of the same area, the value of
v_0/v_ℓ will be smaller for the same beam current.

2. Generation of high microwave frequencies requires large beam
    densities. Extremely high beam densities ($n > 10^{14}$ cm^{-3})
    have been obtained from a foilless diode.[48] The beam plasma
    frequency scales linearly with the electron cyclotron fre-
    quency due to the magnetic field.[49]

3. The following characteristics must be met to assure narrow
   bandwidth microwave generation from the vircator.

   a) No reflexing of electrons in the region between the real
      and virtual cathodes must occur. Any axial magnetic
      field must be shaped to divert the electrons, or flux
      excluders must be employed to confine the magnetic field
      to the diode region. The latter arrangement will allow
      the radial space-charge electric field to perform the
      role of expelling electrons to the waveguide wall.

   b) The electron beam must be cold. Experimental[50] and theo-
      retical[49] results indicate that foilless diodes create
      low emittance beams. Laminar flow, where the electron
      Larmor orbit is smaller than the beam thickness, is
      obtained when[50]

$$\omega_c > (\gamma_0 - 1)^{1/2} \frac{c}{\sqrt{a\delta/2}} \tag{56}$$

   where a is the orbit radius, δ is the radial spacing
   between the cathode and drift tube wall (which acts as
   the anode) and ω_c is the electron cyclotron frequency
   given by eB_z/mc. Low beam scatter is also assured,
   because of the lack of a foil.

   c) The diode voltage and injected current must be constant.
      Flat-top voltage pulses can be attained in a variety of
      ways in several diode configurations. However, absence
      of diode closure in some foilless diode experiments makes
      a long pulse device possible. Also, at high voltages the
      foilless diode operates as a purely resistive load,

therefore $\omega_{osc} \propto \sqrt{\frac{I}{V}} = \sqrt{Z}$ is constant.

54

It is evident from this discussion that the foilless diode in a strong axial magnetic field represents the optimal configuration for a high frequency vircator. It optimizes microwave power and efficiency while generating high frequency, coherent radiation.

V. Experimental Apparatus

1. Introduction

This section decribes the VIRCATOR experimental apparatus in detail. The general design philosophy has been to include as much flexibility as possible in the mechanical and electrical systems. This approach allows for the inevitable changes in experimental geometry and diagnostics to be made easily, and will also permit a straight-forward maximization of the output microwave power over the various degrees of freedom available.

Mechanical aspects of the experiment are described in Section 2. Included are the vacuum vessel design and descriptions of the anode positioning assembly and the cathode. Electrical systems are summarized in Section 3. Electronic schematics for the pulsed 50 kilogauss magnet power supply and for the lumped element Blumlein electron beam driver are presented. Diagnostics of the pulsed power systems and of the electron beam are also described. Measurements of the microwave emission power spectrum will be made with the microwave spectrometer described in Appendix A.

2. Mechanical Design

The successful operation of the VIRCATOR device requires that the electrostatic potential surfaces have a particular structure, and that these equipotential surfaces be appropriately oriented with respect to the applied magnetic field. These criteria will be satisfied if the cathode, anode, annular limiter, and solenoidal magnetic field are aligned concentrically, and if all are cylindrically symmetric. However, the required accuracy of this concentric relationship has yet to be thoroughly investigated, since it requires making several runs of a fully three-dimensional simulation code. Rather than attempt to fabricate the entire experiment to

56

exacting tolerances, it was therefore decided to build a mechanical system capable of changing the geometrical relationships between the various components in small incremental steps. This approach allows performance of the experiment to be optimized in a systematic fashion, and will also provide a measurement of the system sensitivity to geometrical relationships between the components.

Vacuum System

The components associated with electron beam production are enclosed in a standard 18 inch diameter bell jar vacuum system, and pumped by a NRC 4 inch diffusion pump to a base pressure less than 10^{-6} torr. In order to allow for high voltage and mechanical vacuum feedthroughs, a custom stainless steel collar, designed by MRC and fabricated by Huntington Mechanical Laboratories, is positioned between the baseplate and glass bell jar. Design drawings for this unit are shown in Figure 17. Conflat type vacuum flanges are used on all ports because of the wide variety of electrical and mechanical feedthroughs manufactured for this style flange. Use of off-the-shelf type hardware yields cost savings and increased system flexibility relative to custom machined vacuum feedthroughs.

The experiment is arranged on the feedthrough collar of Figure 17 as follows. A 135 kV high voltage feedthrough (Ceramaseal Inc. #908C1854-1) is mounted on vacuum port 1, positioning the carbon cathode at approximately 5 cm from the center of the chamber. The pulsed magnet is mounted to the stainless steel brackets shown so that it is concentric with the cylindrical cathode. The brackets are slotted to allow for magnet positioning along its axis; vertical adjustments are made by screws in the magnet base. The beam target assembly, consisting of the stainless steel anode, annular limiter, and waveguide entrance port, is located concentrically with the cathode and magnet by means of a positioning assembly

57

FEEDTHROUGH COLLAR
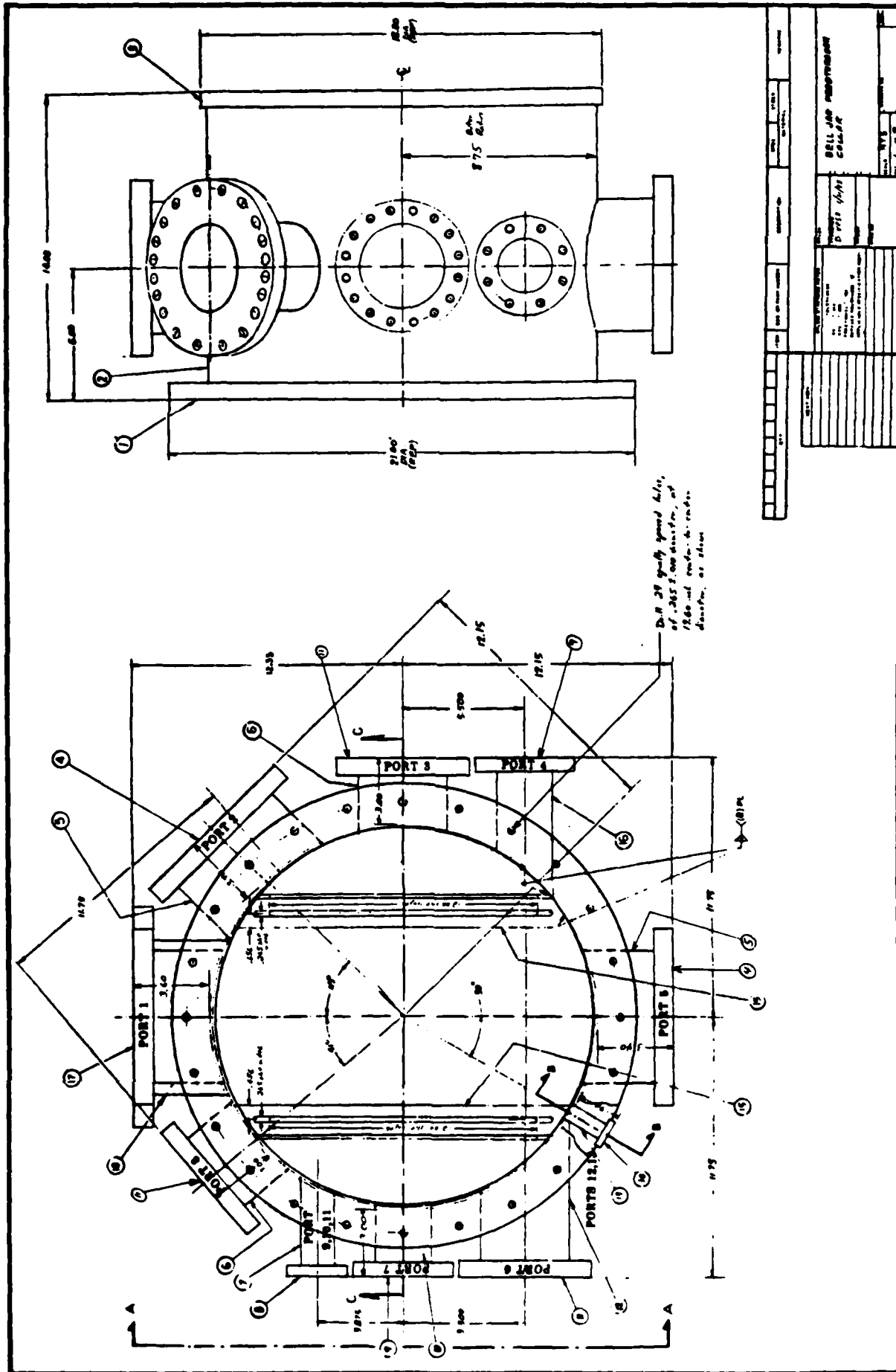
Figure 17. Fabrication drawing of the VIRCATOR vacuum vessel. All flanges are Conflat type to accept standard feedthrough hardware.

FEEDTHROUGH COLLAR

Figure 17. Concluded.

59

mounted in vacuum port 3. Microwave emission into the microwave spectrometer is through vacuum port 5. The remaining vacuum ports accomodate the electrical and mechanical feedthroughs related to beam and microwave diagnostics.

Beam Target Assembly

The ideal experimental configuration would allow manipulation of the various electrical components from outside the vacuum vessel, eliminating the need to break vacuum when an adjustment is required. Because mechanical motion vacuum feedthroughs are costly, the design allows only the beam target assembly, consisting of the anode, annular limiter, and the waveguide entrance port, to be manipulated from outside the vacuum vessel. A commercial micrometer positioning assembly capable of 100 micron spatial resolution (Huntington Mechanical Laboratories #PM-600-XYZTR) has been chosen for this application. This unit allows full 5 degree-of-freedom motion of the target assembly relative to the cathode.

The relative geometry of the cathode, beam target assembly, and magnet is shown in Figure 18. The cathode consists of a hollow carbon rod of outside diameter 0.70 cm with a 0.08 cm diameter wall. Two chacteristics make carbon a strong choice for the cathode. First, its high resistivity allows magnetic field penetration on a sub-microsecond time scale, ensuring that the magnetic field lines will be nearly normal to the cathode surface at the time that the beam fires. Second, it has a low macroscopic electric field threshold for field emission, of order 10 kV/cm[51]. However, for the design operating voltage of 50 kV, the electric field at the cathode surface is 625 kV/cm, ensuring that cathode field emission can be obtained at substantially lower voltages and promoting uniform field emission. The purpose of the thin cathode wall is to promote formation of an annular electron beam by eliminating emission from the cathode center.
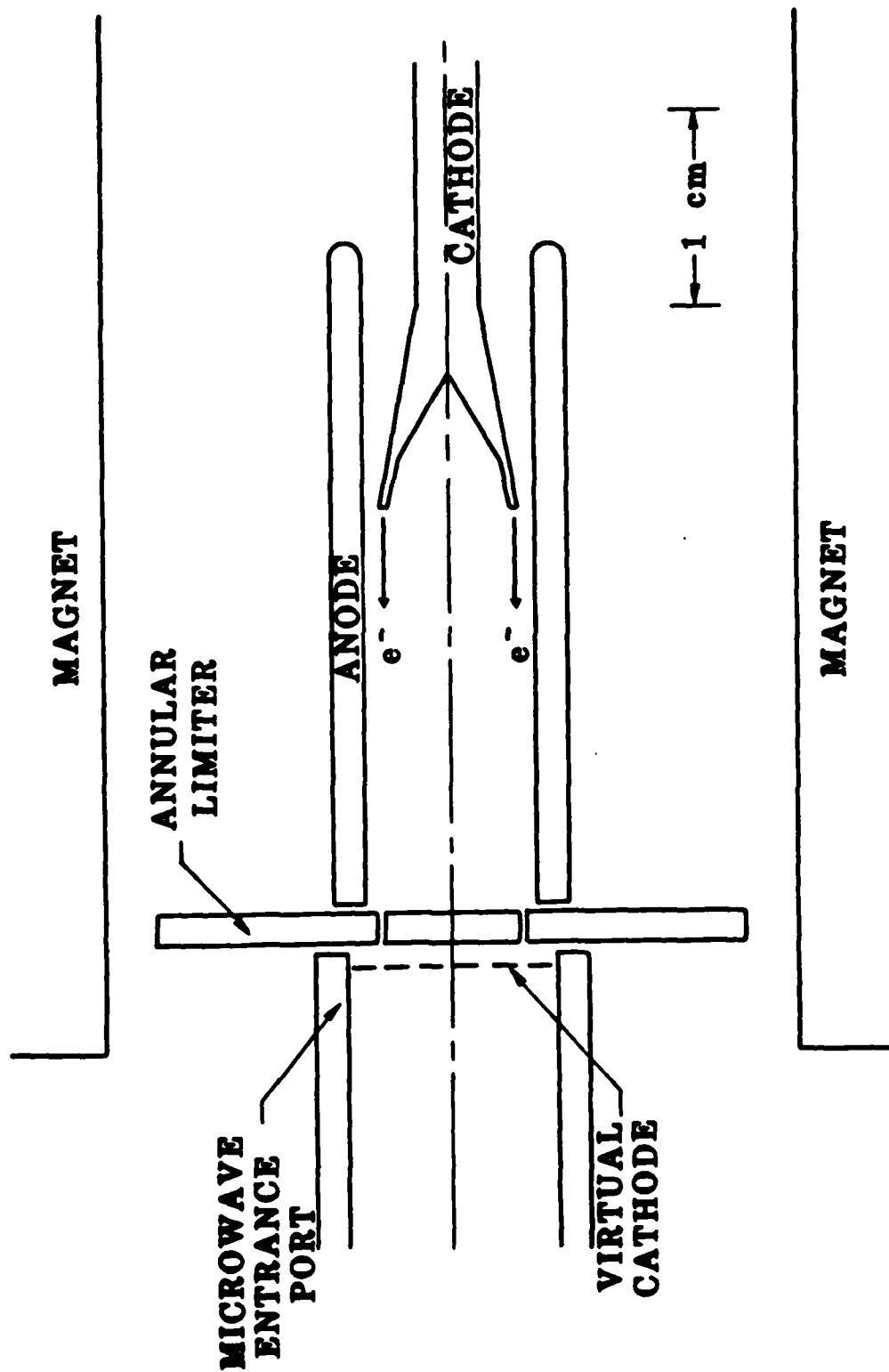
60

Figure 18. Sketch of the beam target assembly. The anode, annular limiter, and microwave entrance port are operated at ground potential, and the cathode is operated at negative high voltage.

In order to maximize the space-charge limited current emission from the cathode, the cylindrical anode of inside diameter 0.43 cm surrounds the cathode with a narrow 0.08 cm gap. This geometry yields a diode impedance for a 50 kV beam of 66 ohms, with a space-charge limited current of 760 amps. The annular limiter serves a dual role. It acts as ground plane for electron beam production in the source region and also prevents electrons reflected from the virtual cathode from re-entering the source region. Beam equilibrium considerations dictate an axial spacing between the annular limiter and cathode of several anode radii, yielding a design gap of 2.0 cm. The radial gap of the annular limiter is chosen to match the expected electron beam thickness, 0.035 cm, and is centered just outside the cathode radius at 0.37 cm. The diameter of the cylindrical waveguide entrance port in the virtual cathode region is chosen as 1.06 cm, causing the space-charge limited current in this region to drop to 45% of its value in the source region. The ensuing virtual cathode formation drives the production of 50 GHz, 6 mm wavelength microwaves for a 30 kilogauss applied field.

The components of the beam target assembly of Figure 18 are all nominally grounded, with the cathode driven at negative high voltage. In order to diagnose the electron beam operation, however, the anode, annular limiter, and waveguide entrance port are mounted in such a way that, although rigidly attached as a unit, the components are electrically floating. In this way the current to each of the electrodes can be monitored, either by use of a shunt or with a Rogowski coil. Comparing the cathode current to the anode current will then yield an estimate of shank emission and gap closure time; the current to the annular limiter and waveguide entrance port will give an estimate of how well the assembly is centered as well as the beam thickness. These simple beam diagnostics will be supplemented by a Faraday cup current collector mounted on a mechanical probe drive mechanism for making detailed measurements of the electron beam profile.

Magnet Design

The main design criteria for the VIRCATOR magnet are related to field
intensity and field homogeneity. The maximum design field is 60 kilogauss,
required to drive 100 GHz microwaves in the above experimental configura-
tion. Since diverging magnetic field lines increase beam divergence, mag-
netic field homogeneity is required in order that the beam particle density
at injection into the virtual cathode region be the same as the beam elec-
tron density at the source. An additional constraint imposed on the design
is that the working magnetic field volume be several times larger in radius
and length than the nominal anode size described in the previous section.
The magnet has been designed oversize to allow for the contingency that
anode-cathode gap closure problems with the nominal 0.08 cm wide gap may
require using a much larger anode-cathode radial spacing, of order milli-
meters. Maintaining diode impedance in the 50 ohm range would then require
increasing the anode diameter to centimeters. The present magnet design
admits this option.

The magnet overall length is 15.2 cm with a usable inside diameter of
3.5 cm. To produce a 60 kilogauss field on axis at the center of the mag-
net requires a linear current density of 49,500 amp-turns/cm. The magnet
is wound with 284 turns of 1 mm diameter solid copper wire so that the coil
current is 2.6 kA and magnet inductance is 1 millihenry. In order to
enhance field homogeneity, the coil is wound with additional turns at the
ends. The self forces on the magnet tend to squeeze it axially and expand
it radially. Self-compression forces in the axial direction are taken up
by the copper windings and the epoxy binder, and the radial expansion
forces are born by an encapsulating cylindrical stainless steel tube.
Neglecting the restoring forces provided by the copper windings and epoxy
binder yields a stress of 15,300 psi in the 3.2 mm thick, 6.4 cm outside
diameter tube for a 60 kG field. Since the yield strength of type 304
stainless steel exceeds 40,000 psi, the design provides an acceptable
safety factor.

The magnetic field risetime is determined by the magnetic inductance, source capacitance, and series resistance. As described in the next section, these were chosen to give a 300 microsecond risetime. Since the field penetration time for the anode, cathode, and the stainless steel magnet casing are all less than 15 microseconds, the magnetic field in the electron beam source region can be accurately calculated using computer codes which neglect eddy-current effects.

3. Electrical Design

The VIRCATOR electrical system consists of the magnet capacitive discharge circuit, the lumped element Blumlein pulse forming line for driving the electron beam, and associated timing and data recording channels. In order to minimize the emission of electromagnetic radiation from the high speed switching circuits, all high voltage components are enclosed in a grounded Faraday cage formed from bronze screen. Additional shielding for the data channels, consisting of five single trace oscilloscopes and recording cameras, is provided by a fully screened instrumentation rack. Because of the limited number of data channels, the generation of a complete data set will require multiple shots. Due to the expected high shot frequency, one every 5 minutes, data acquisiton will still be relatively rapid, provided shot reproducibility is acceptable.

Magnet Pulsed Power Supply

A schematic for the circuit which drives the magnetic field coil is shown in Figure 19. A 90 microfarad energy storage capacitor is discharged into the magnetic field coil through a series resistance which is chosen so that the circuit is critically damped. Since the current does not ring, the lifetime of both the capacitors and the magnetic field coil are increased. The price paid is an increase by a factor of approximately 2.5 in the required bank capacitance relative to a lightly damped circuit.
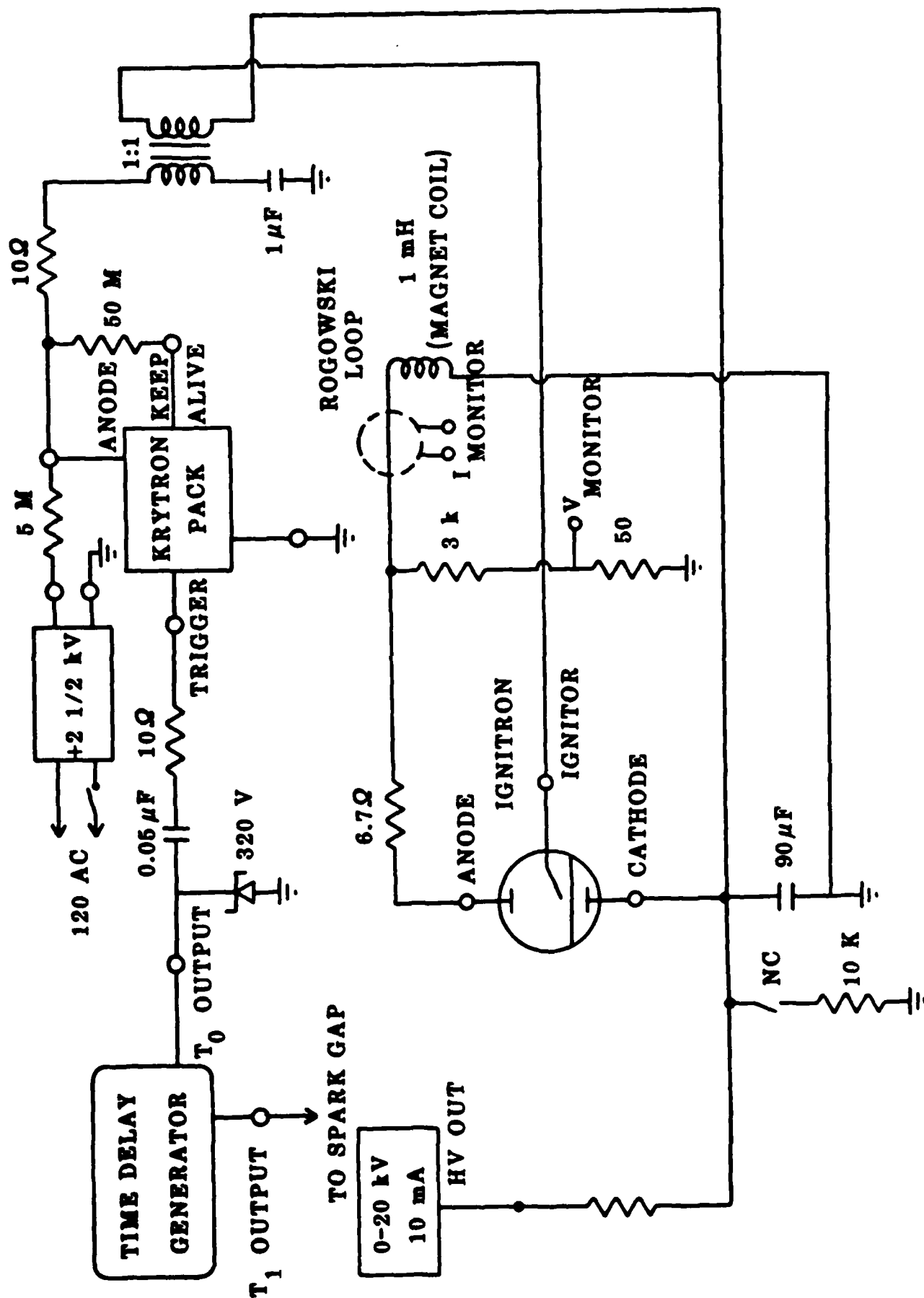
Figure 19. Schematic of the pulse power circuit which drives the magnetic field coil.

The same result could be achieved by crowbaring the current at peak field with an ignitron, and eliminating the series resistance. Since the cost of the increased capacitance is small compared to the cost of the ignitron and its driving circuit, the former option was chosen.

The magnet energizing circuit of Figure 19 operates as follows. A 20 kv, 10 mA power supply (Del Electronics #RIU-20-10) charges the 90 micro-farad capacitor bank to its charge voltage, about 10 kv for a 40 kilogauss field. A krytron gas tube switch is command triggered to discharge a 1 microfarad capacitor charged to 2.5 kv into the ignitor terminals of a mercury ignitron (General Electric #GL-7703). The triggered ignitron then discharges the main capacitor bank into the inductive load through a 6.7 ohm series resistor. The peak magnetic field occurs at 300 microseconds, and decays with a time constant of 300 microseconds. A time delay gener-ator (California Avionics #113CR) command fires a spark gap, initiating the electron beam at peak magnetic field time.

Electron Beam Pulsed Power Supply

The ideal voltage pulse shape for driving the electron beam would have a fast leading edge for initiating field emission at the cathode, followed by a somewhat lower voltage flat top for driving constant current in an assumed constant impedance load provided by the diode. A good apporoxima-tion to this ideal source is provided by a lumped element artificial Blumlein pulse-forming line shown in Figure 20, which uses high energy density barium titanate capacitors as the energy storage medium. This cir-cuit provides twice the charge voltage into an open load, thereby initiat-ing breakdown at the cathode, followed by an approximately flat top signal equal to the charge voltage when driving a matched load. For a N-stage pulse-line the risetime τ, pulse length T, and impedance Z are given by

66

ELECTRON BEAM PULSED POWER SUPPLY
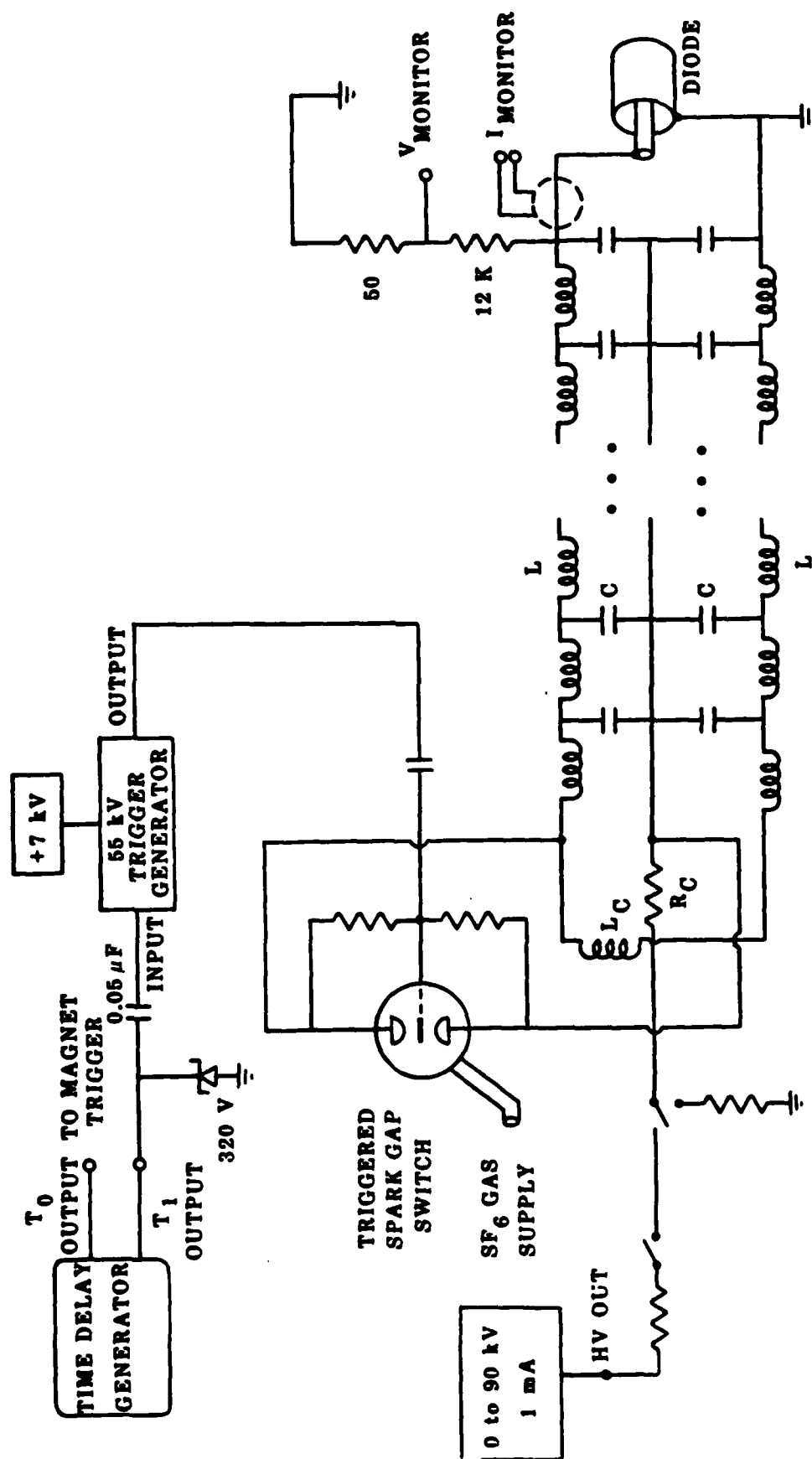
Figure 20. Schematic of the lumped element Blumlein pulse-forming line. Initally 10 stages will be used to give a pulse length of 600 nanoseconds.

$$\tau = \sqrt{LC}/2 \tag{57}$$

$$T = 2N\sqrt{LC} \tag{58}$$

$$Z = 2\sqrt{L/C} \tag{59}$$

where L and C are the component inductances and capacitances, respectively. In order to build in future capability for 100 kV operation, three 40 kV disc capacitors will be connected in series to give 900 pF rated at 120 kV. Matching the pulse-line impedance to the desired diode impedance of 66 ohms requires an inductance of .98 microhenries. For a ten stage pulse forming line the risetime and pulse length follow from above as 15 and 594 nanoseconds, respectively. Increasing the number of stages to provide full 1 microsecond pulse length capability is straight-forward and will be done after any gap closure problems occuring at the shorter pulse lengths have been solved. Increasing the number of stages has an additional benefit of smoothing the flat top portion of the voltage pulse.

The trigger and charging circuit for the electron beam driver are shown in Figure 21. The Blumlein array is charged by a 90 kV power supply (Del Electronics #RIU-90-1-1) and command fired at the time of peak magnetic field by a signal from the time delay generator. The time delay generator triggers a 55 kV pulse generator (Pacific Atlantic Electronics #PT-55-M) which in turn drives the spark gap (Pulsar #670). The spark gap discharges the pulse-forming line into the load provided by the electron beam. A Rogowski coil and voltage divider monitor the diode current and voltage, respectively.
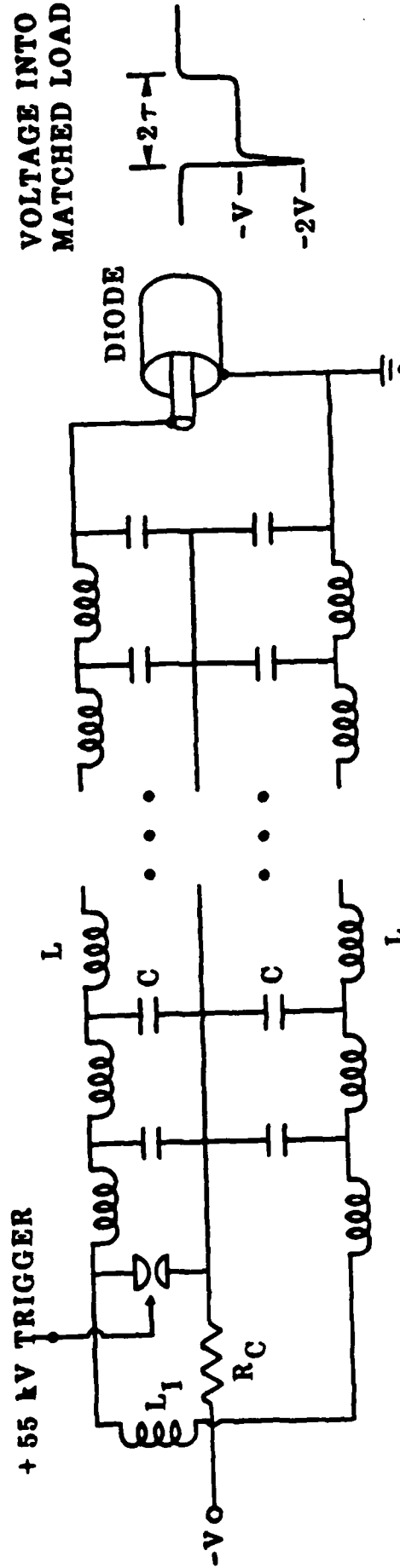
Figure 21.   Schematic of the Blumlein charging and trigger circuit which drive the electron beam.

VI. TECHNICAL REQUIREMENTS AND TASKS

HOW THE STATEMENT OF WORK HAS BEEN SATISFIED

In this section we review the tasks encompassed by the statement of work and detail how these technical requirements have been satisfied. We also include a list of publications and talks given on this subject, professional personnel associated with the research effort, and consultative and advisory functions.

Statement of Work (0001AA)

1. Theoretically determine an optimal configuration for a proof-of-principal vircator which operates in the millimeter wavelength regime.

We have reviewed in detail how one can accurately calculate the space-charge limiting current, which is a necessary requirement for determining if a virtual cathode will form, in Section II. For the first time both the nonlinear treatment of the space-charge limit instability and the scaling of key parameters (oscillation frequency, potential depth, location of the virtual cathode) has been accomplished. This is presented in Section III. Work is now in progress on the effect of electron temperature and multiple virtual cathode formation. (See list of proposed publications.)

It is now clear, based on simulations performed at Los Alamos National Laboratory (LANL) and from our analytical efforts that beam temperature not only effects virtual cathode frequency bandwidth, but more importantly microwave generation efficiency. The conclusion of this report that a foilless diode and some means of preventing electron reflexing are optimal for producing a narrowband, efficient oscillator is certainly justified. This work is presented in Section IV.

70

2.   Accomplish the technical design of the proof-of-principle vircator.

The technical design of the vircator is given in Section V. Of greatest importance is the flexibility which is provided by this plan. For instance, the field coil is devised to allow a 60 kG field with an acceptable margin of mechanical safety. Also the artificial Blumlein willallow us to obtain 100 kV pulses, if we used three rather than two barium titanate capacitors per stage.

3.   Fabricate portions of the vircator incorporating long lead items.

We have designed the custom bell jar vacuum feedthrough system. It is currently being manufactured. All of the electrical components (capacitors, vacuum feedthroughs, delay generators, switches, and power supplies) have been specified, ordered and delivered. Mechanical components for accurate positioning of the beam-target assembly and raw materials for the assembly have been ordered and delivered. The construction of the Blumlein and assembly will be completed shortly.

4.   Design, construct and calibrate a quasi-optical microwave spectrometer.

The design of the spectrometer is presented in Appendix A. It has been constructed. Calibration using high frequency sources available at the Naval Research Laboratory (NRL) will be completed in the month of February. In order to maximize the utility of the spectrometer its current frequency range (75-110 GHz) will be extended down to 35 GHz. This addition will be accomplished by April 1, 1983.

5. Characterize the microwave emission (power, frequency and band-width) of a relativistic electron beam in a vircator configuration using the microwave spectrometer.

This last task has not been accomplished. The lack of availability of time on such a beam machine at the Air Force Weapons Laboratory (AFWL) and the longer than anticipated time required to complete task 4, both contrib-uted to this situation. We have postponed this requirement to CY 1983.

Bibliography of Talks and Publications

Archival Scientific Publications

"Design of a Millimeter Wave Source Using a Virtual Cathode Oscillator (VIRCATOR)", in Conference Record - 1982 IEEE International Conference on Plasma Science, p. 64.

"Effects of Temperature on the Space-Charge Limit of Electron Beams", to be submitted to Applied Physics Letters (E. A. Coutsias and D. J. Sullivan).

"Formation of Singularities in One-Dimensional Electron Flows", to be submitted to Physics of Fluids (E. A. Coutsias and D. J. Sullivan).

"High Power Microwave Generation from a Virtual Cathode Oscillator", to be published in IEEE Trans. Nuc. Sci., June 1983 (D. J. Sullivan).

Classified Scientific Reports

"Theory and Design of a High Power Virtual Cathode Oscillator (VIRCATOR)", to be published in Proceedings of the 2nd National Conference on High Power Microwave Technology (D. J. Sullivan).

Internal MRC Reports

"Theory and Application of the Virtual Cathode in Charged Particle Beams," AMRC-R-433 (1982).

Talks and Meetings
1982 IEEE International Conference on Plasma Science, Ottawa, Canada

"Design of a Millimeter Wave Source Using a Virtual Cathode Oscillator (VIRCATOR)"

MGX Review Meeting - Lawrence Livermore National Laboratory (22 Sep 82)

"MGX Simulations Using CCUBE"

Virtual Cathode Microwave Design Review - Los Alamos National Laboratory (31 Jan 83)

"VIRCATOR Theory and Design at Mission Research Corporation"

"The Mission Research Corporation VIRCATOR"

Second National Conference on High Power Microwave Technology - Harry Diamond Laboratories (Mar 83)

"Theory and Design of a High Power Virtual Cathode Oscillator (VIRCATOR)"

1983 Particle Accelerator Conference - Santa Fe, New Mexico

"High Power Microwave Generation from a Virtual Cathode Oscillator (VIRCATOR)"

Professional Personnel (Alphabetical order)

W. Michael Bollen
Evangelos A. Coutsias (UNM Department of Mathematics and Statistics)
Carl A. Ekdahl
Robert H. Jackson
Bret E. Simpkins
Donald J. Sullivan
Donald E. Voss
John Walsh (Dartmouth College, Department of Physics and Astronomy)

Consultative and Advisory Functions

Consulting Agreement with Lawrence Livermore National Laboratory (LLNL) to aid in design of the Microwave Generator Experiment (MGX) which uses a VIRCATOR as the microwave source. Points of contact at LLNL Drs. Hriar Cabayan, Wayne Hohfer, Raymond Scarpetti and George Vogtlin. Dates present at LLNL 25-27 May 1982 and 20-23 September 1982.

Numerous informal discussions with Los Alamos National Laboratories (LANL) personnel in Groups R-1 and A-8 on using the VIRCATOR as a microwave source. In particular discussions with Drs. Carl Ekdahl and Thomas Kwan.

REFERENCES

1. G. D. Child, Phys. Rev. Ser. I 32, 492 (1911).

2. I. Langmuir, Phys. Rev. 21, 419 (1923).

3. C. K. Birdsall and W. B. Bridges, Electron Dynamics of Diode Regions, Electrical Science Series (Academic Press, 1966), Chapter 3.

4. H. R. Jory and A. W. Trivelpiece, J. Appl. Phys. 40, 3924 (1969).

5. V. S. Voronin, Yu, T. Zozulya and A. N. Lebedev, Zh. Tekh. Fiz. 42, 546 (1972), [Sov. Phys.-Tek. Phys. 17, 432 (1972)].

6. R. J. Lomax, Proc. IEE Pt. C 108, 119 (1961).

7. C. E. Fay, A. L. Samuel, and W. Shockley, Bell System Techn. J. 17, 49 (1938).

8. C. K. Birdsall and W. B. Bridges, J. Appl. Phys. 32, 2611 (1961).

9. W. B. Bridges and C. K. Birdsall, J. Appl. Phys. 34, 2946 (1963).

10. D. A. Dunn and I. T. Ho, A.I.A.A.J. 1, 2770 (1963).

11. S. A. Goldstein and R. Lee, Bull. Am. Phys. Soc. 23, 763 (1978).

12. R. A. Meyer, S. A. Goldstein, D. D. Hinshelwood and G. Cooperstein, Bull. Am. Phys. Soc. 24, 977 (1979).

13. D. S. Prono, J. M. Creedon, I. Smith and N. Bergstrom, J. Appl. Phys. 46, 3310 (1975).

REFERENCES (Continued)

14. D. S. Prono, J. W. Shearer and R. J. Briggs, Phys. Rev. Lett. 37, 2 (1976).

15. P. A. Miller, J. A. Halbleib, J. W. Poukey and J. T. Verdeyen, J. Appl. Phys. 52, 593 (1981).

16. J. W. Poukey and N. Rostoker, Plasma Phys. 13, 897 (1971).

17. C. L. Olson, "Collective Ion Acceleration with Linear Electron Beams," in Collective Ion Acceleration-Springer Tracts in Modern Physics, Vol. 84, (Springer-Verlag, 1979).

18. C. L. Olson, IEEE Trans Nuc. Sci. NS-26, 4231 (1979).

19. C. L. Olson, J. R. Woodworth, C. A. Frost and R. A. Gerber, IEEE Trans. Nuc. Sci. NS-28, 3349 (1981).

20. R. B. Miller, in Proc. of the 2nd Intl. Top. Conf. on High Power Electron and Ion Beam Research and Technology, (Cornell University, 1977), p. 613.

21. R. B. Miller, in Collective Methods of Acceleration, edited by N. Rostoker and M. Reiser (Harwood Academic Publishers, 1979), p. 675.

22. R. A. Mahaffey, P. Sprangle, J. Golden and C. A. Kapetanakos, Phys. Rev. Lett. 39, 843 (1977).

23. H. E. Brandt, A. Bromborsky, H. B. Bruns, and R. A. Kehs, in Proc. of the 2nd Intl. Top. Conf. on High Power Electron and Ion Beam Research and Technology, (Cornell University, 1977), p. 649.

REFERENCES (Continued)

24. J. M. Buzzi, H. J. Doucet, B. Etlicher, P. Haldenwang, A. Huetz, H. Lamain, C. Rouille, J. Cable, J. Delvaux, J. C. Jouys and C. Peugnet, *idem*, p. 663.

25. D. J. Sullivan, in Proc. of the 3rd Intl. Top. Conf. on High Power Electron and Ion Beam Research and Technology, (Institute of Nuclear Physics, 1979), p. 769.

26. A. N. Didenko, G. P. Fomenko, I. Z. Gleizer, Ya. E. Krasik, G. V. Melnikov, S. F. Perelygin, Yu. G. Shtein, A. S. Sulakshin, V. I. Tsvetkov, and A. G. Zerlitsin, idem, p. 683 (1979).

27. L. A. Bogdankevich and A. A. Rukhadze, Soviet Phys. Upsekhi, 14, 163, (1971).

28. B. N. Brejzman and D. C. Ryutov, D. C., Nucl. Fusion, 14 875, (1974).

29. T. C. Genoni and W. A. Proctor, 1978 IEEE Conf. on Plasma Sciences, Poster Session 2P1.

30. R. B. Miller and D. C. Straw, J. Appl. Phys., 47, 1897, (1976).

31. J. R. Thompson and M. L. Sloan, Proceedings of the 2nd International Conference on High Power Electron and Ion Beam Research and Technology, Vol. II, p. 734, Eq (14), Laboratory for Plasma Studies, Cornell University, Ithaca, New York, October 3-5, 1977.

32. B. B. Godfrey, J. Comp. Phys., 15, 504 (1974).

33. B. B. Godfrey, J. Comp. Phys., 19, 58 (1975).

REFERENCES (Continued)

34. R. B. Miller and D. C. Straw, J. Appl. Phys., 48, 1061 (1977).

35. L. E. Thode, B. B. Godfray and W. R. Shanahan, Phys. Fluids, 22, 747 (1979).

36. R. Z. Sagdeev, Reviews of Plasma Physics, Vol. 4, edited by M. A. Leontovich, (Consultants Bureau, 1966), p. 23.

37. S. S. Moiseev and R. Z. Sagdeev, Plasma Phys. 5, 43 (1963).

38. G. B. Whitham, Linear and Nonlinear Waves, (Wiley, 1974).

39. E. A. Coutsias and D. J. Sullivan, to be submitted to Physics of Fluids.

40. D. J. Sullivan and E. A. Coutsias, in High Power Beams '81, edited by H. J. Doucet and J. M. Buzzi, (Ecole Polytechnique, 1981), p. 371.

41. J. R. Pierce, J. Appl. Phys. 15, 721 (1944).

42. J. W. Poukey, J. P. Quintenz and C. L. Olson, Appl. Phys. Lett. 38, 20 (1981).

43. B. B. Godfrey, Mission Research Corpration, AMRC-R-282 (1981), unpublished.

44. J. Kevorkian and J. D. Cole, Perturbation Methods in Applied Mathematics, (Springer, 1981).

45. G. Birkhoff and G. Rota, Ordinary Differential Equations, (Ginn and Company, 1962).

REFERENCES (Continued)

46. A. V. Paschenko and B. N. Rutkevich, Fiz. Plazmy $\underline{3}$, 774 (1977), [Sov. J. Plasma Phys. $\underline{3}$, 437 (1977)].

47. A. Bromborsky, H. Brandt, and R. A. Kehs, Bull. Am. Phys. Soc., $\underline{26}$, 165 (1981); and private communication.

48. D. J. Sullivan, Bull. Am. Phys. Soc., $\underline{25}$, 948 (1980).

49. M. E. Jones and L. E. Thode, J. Appl. Phys., $\underline{51}$, 5212 (1980).

50. R. B. Miller, K. R. Prestwich, J. W. Poukey, and S. L. Shope, J. Appl. Phys., $\underline{51}$, 3506 (1980).

51. R. Prohaska and A. Fisher, Rev. Sci. Instr. $\underline{53}$, 1092 (1982).

APPENDIX A

MRC/WDC-R-046

TECHNICAL REPORT

A W-BAND DIFFRACTION GRATING SPECTROMETER

W. Michael Bollen
R. H. Jackson

December 1982

SECTION 1
INTRODUCTION

1.1   Background

In characterizing electromagnetic radiation, the intensity and
wavelength of the radiation are used. A device for measuring these two
quantities is the spectrometer. Spectrometers are a commonly used device
in the UV, visible and IR region of the spectrum. A variety of techniques
for performing the spectrometry may be used: Fabry-Perot interferometry,
Fourier transform spectroscopy, and diffraction grating spectroscopy. For
the microwave spectrum, the Fourier transform technique, commonly called a
spectrum analyzer, has been used. The other methods have not had
widespread use with microwaves.

Spectrometry for non-repetitive, short pulse length microwave
radiation can only be easily performed using the grating spectrometry
method mentioned above, and it has been used with some success[2,3,4].
The main difficulty encountered has been in calibration of the
spectrometer. Calibration is required because the response typically is
not flat; the signal output varies with wavelength for a constant
intensity input. Further, calibration sources are not easily available
except at very low power levels (milliwatts). In our design we have
attempted to make the response flat; however, we are limited by the
nonuniform response of the microwave detectors.

1.2   The Diffraction Grating Spectrometer

A basic description of diffraction grating spectrometers can be
found in many optics texts (see, for example, reference 5). The physics
of the diffraction process is described by

$$m\lambda = d(\sin\alpha \pm \sin\beta) \tag{1}$$

1

where m is the order of the diffraction (0, ± 1, ± 2, ...), λ is the wavelength, d is the spacing between the grating grooves, α and β are the angles of incidence and diffraction respectively (see Figure 1). The plus sign is used in equation 1 if α and β are the same sides of the surface normal; otherwise, the minus sign is used. Figure 1 depicts the commonly used echelette grating (ninety degree apex angles). The echelette is popular because it is easy to fabricate, and it has been shown experimentally to give the best efficiency for a ruled grating.

The dispersion of the grating (for fixed incident angle, α) is expressed as

$$d\beta/d\lambda = m/(d \cos \beta) \tag{2}$$

where terms are defined as before. The resolving power, R, is

$$R = \lambda/\Delta\lambda = mN \tag{3}$$

where N is the number of grooves; however, there is a fundamental limitation on R,

$$R \leq 2W/\lambda \tag{4}$$

where W is the width of the grating (W = Nd). The details of our design using these equations may be found in the next section.
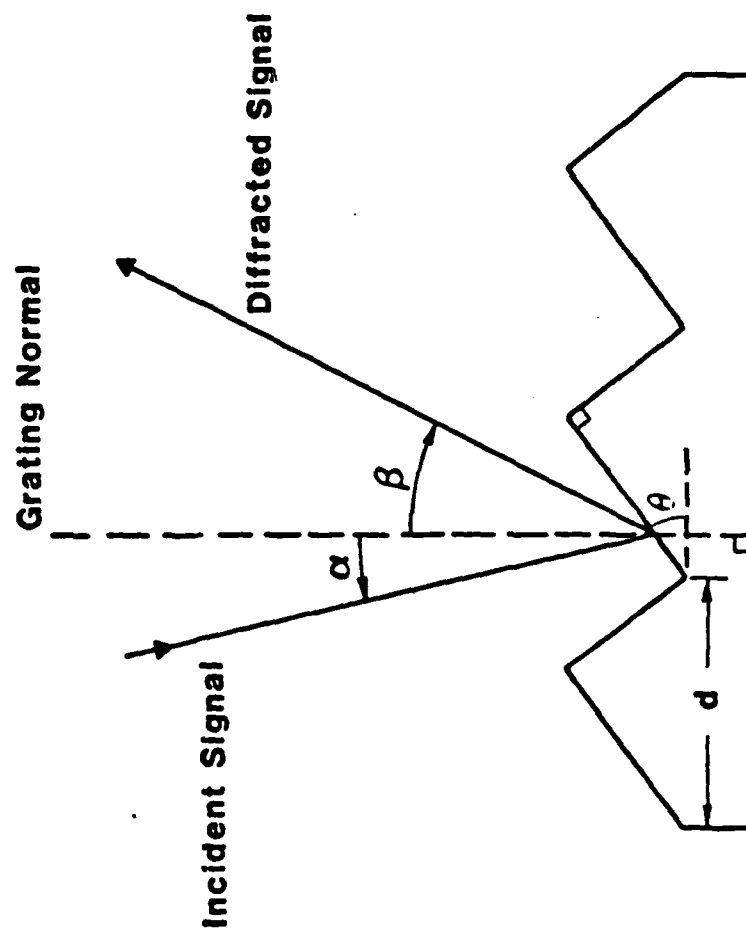
Figure 1. Definition of geometry for an Echellette grating.

3

SECTION 2
DESIGN OF A W-BAND SPECTROMETER

2.1   Design Philosophy

A microwave spectrometer has been designed to measure frequency
and bandwidth for radiation from the Mission Research Corporation (MRC)
vircator experiment. An effort has been made to improve upon the basic
design currently in use[2,3,4] by incorporating new knowledge on
diffraction gratings[6] and by the use of innovative design concepts.
Computational modeling suggests 3-4 mm radiation from the vircator with
fine structure of 2 GHz. These were used as the basic design
constraints. Additionally, we imposed the following constraints to make
the device easier to use: 1) limit the wavelength range to remove high
order ($m > 1$) diffraction, 2) demand uniform (flat) device response, 3)
require wide device bandwidth, 4) require wide bandwidth for any single
input pulse, 5) allow for modification to different wavelength bands, 6)
minimize unwanted signal noise, and 7) keep the device small and
portable. Clearly, all these constraints can not be simultaneously met,
and trade-offs were required.

The final design is shown in Figure 2. This spectrometer is
designed to operate at W band (2.7-4 mm) with a minimum of 2 GHz
resolution over the entire band. The bandwidth of the device is limited
on the long wavelength end by the W-band input waveguide, and on the short
wavelength end by the low-pass diffraction grating. This effectively
eliminates higher-order ($m > 1$) diffraction. Care was taken in the design
of the diffraction gratings to choose a design with a flat frequency
response. The main limitation encountered in obtaining uniform response
was in the microwave detectors. These do not have uniform response, and
their response varies with each detector. Wide device bandwidth is
obtained by the use of a rotatable diffraction grating. Wide, single-shot
bandwidth is obtained by using a large reflection mirror (allowing for
more than one diffraction angle) and use of a multichannel detection
array. We have chosen a six-channel detection array designed for 10 GHz

Figure 2. The MRC W-band spectrometer.

5
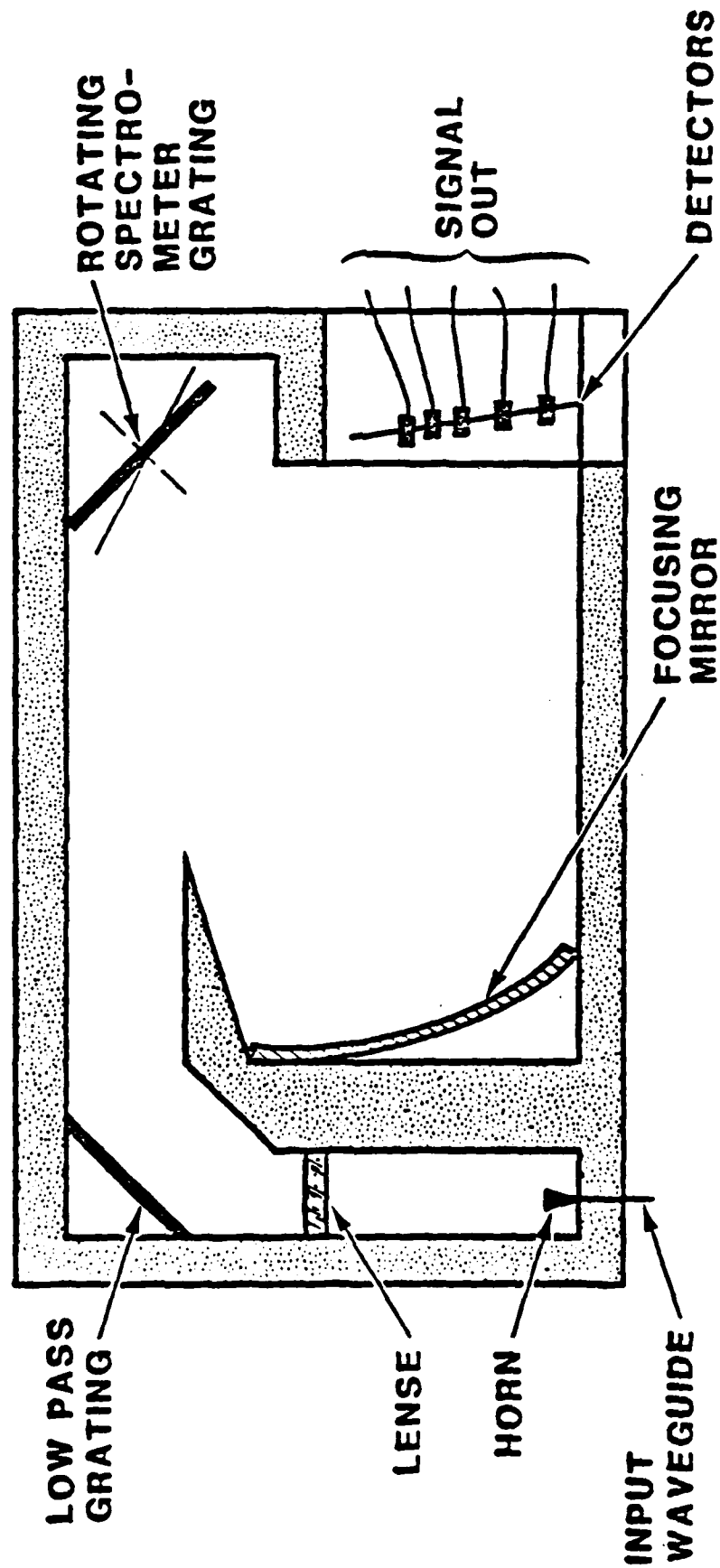
full-width band response centered at 4 mm (75 GHz). Modification to different bands is possible by replacing the two diffraction gratings. Where possible, device size was reduced. For example, folding of path length was done. Path length folding and use of microwave absorber also removed any direct line of sight between the initial input signal and the diffracted signal detectors. Additionally, a collimating horn/lense system was used allowing a slight savings in size over that achieved using a mirror system. The details concerning the design of individual components is found in the next section.

2.2   Design of the MRC W-Band Spectrometer

2.2.1   Microwave Input

The microwaves enter the spectrometer through a length of W-band waveguide (see Figure 2). The waveguide performs the first filtering by rejecting microwave wavelengths greater than 4 mm. The input signal must be attenuated to a level of a few hundred milliwatts to prevent damage to the microwave detectors. Some attenuation (10-20 dB) will occur in the spectrometer itself (due to losses); however, the main attenuation must be performed externally. This is performed geometrically by moving the input of the waveguide away from the output of the microwave source; then geometrical, $1/R^2$, attenuation will occur. A 10 MW signal will be attenuated to 100 mW in the waveguide input for a separation, R, of 10 meters.

Geometrical attenuation assumes a uniform distribution of the microwaves over a spherical surface (actually half of the surface for our case). The accuracy of this assumption depends on two factors. First, the spectrometer must be located in the far field;

$$R \geq D^2/\lambda \tag{5}$$

6

where D is the diameter of the source aperture, λ is the wavelength of the radiation, and R is the separation distance. For most cases of interest to us, this is usually easily satisfied. For example, for a 1 cm wide output aperture at 4 mm, the separation must be 2.5 cm. Second, a TE_{11} mode (dominant mode) in circular waveguide has been assumed. Other modes can cause the distribution of power to be peaked at certain angles. For this reason, a mapping of the angular power distribution should be performed. If it is not uniform, then the spectrometer measurements should be made at several angles. It is conceivable that the frequency of the microwaves from the source is linked to the mode. Thus, a measurement of the entire spectrum requires a sampling of all modes.

Inside the spectrometer the input signal is expanded using a standard gain, rectangular horn. This horn has a beam width (FWHM) of 20°. A collimating lense is placed in the far field of the horn and at a distance such that half of the input signal is intercepted. The lense is a standard hyperbolic design.[7] The front surface is hyperbolic in shape and is described mathematically by

$$R = \frac{(n - 1) \, L}{n \cos \theta - 1} \tag{6}$$

where n is the index of refraction and R, L, and θ are shown in Figure 3. The lense is made from Rexolite (n = 1.6). Rexolite has a large index of refraction and low attenuation for millimeter microwaves.[8] The horn/lense collimation technique is compact and aids in reducing the overall size of the spectrometer.
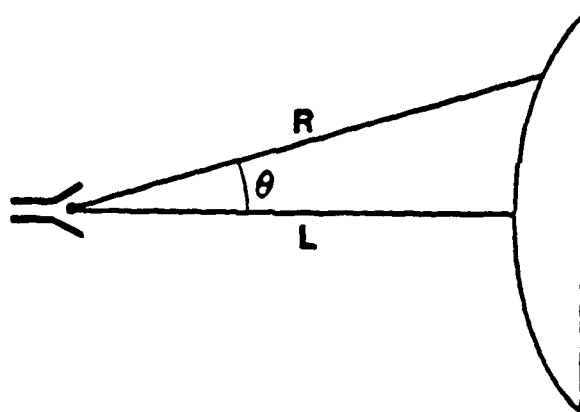
Figure 3. The geometry used for determining the surface of a hyperbolic lense.

2.2.2   Diffraction Grating

Although the basic theory of diffraction gratings has already been discussed in Section 1.2, a few more definitions are required. When discussing gratings, the typical mount used is the Littrow mount. For this case, the incident and diffracted rays occur on the same line ($\beta = -\alpha$). Under these conditions equation (1) simplifies

$$m\lambda = 2d \sin \alpha . \tag{7}$$

Further, if the angle of the grooves, θ (see Figure 1), is the same as α, maximum diffraction will occur since the diffracted and reflected angles are the same. This condition is referred to as being "in blaze" and θ is the blaze angle. The Littrow mount is obviously not realizable in actual practice; however, for TM radiation (H parallel to the grooves), a departure from Littrow still yields a high and nearly uniform efficiency, provided that $0.85 \leq \lambda/d \leq 1.5$. This is true up to 45° off Littrow. Therefore, the gratings were designed using TM radiation and assuming a Littrow mount. An Echelette grating design was chosen and a blaze angle of 30° was picked. For this blaze angle, nearly uniform transmission occurs for $.7 \leq \lambda/d \leq 1.7$ (see Figure 4)[6]. From Figure 4 it is clear that the grating operates best for $1 \leq \lambda/d \leq 1.5$. This fixes d for the grating. The grating characteristics are shown in Table 1. In order to use a rotating diffraction grating, the angle $\alpha - \beta$ was fixed. The detectors and collecting mirror can then be fixed with respect to the incoming microwaves, and the frequency is scanned by rotating the grating. In our design $\alpha - \beta$ is set equal to 25°. This angle is kept as small as possible to stay near Littrow, but must be made large enough so the reflecting mirror does not occlude the diffraction grating.

In addition to the diffraction grating which disperses the microwaves for wavelength measurements, another grating is used in the zeroth order ($m = 0$) to limit the wavelength of the radiation to the dispersing grating. It can be shown[6] that a grating acts like a mirror in $m = 0$ for sufficiently large wavelength radiation. The criteria is

$$d < \lambda_{min}/(1 + \sin \alpha) \tag{8}$$

9
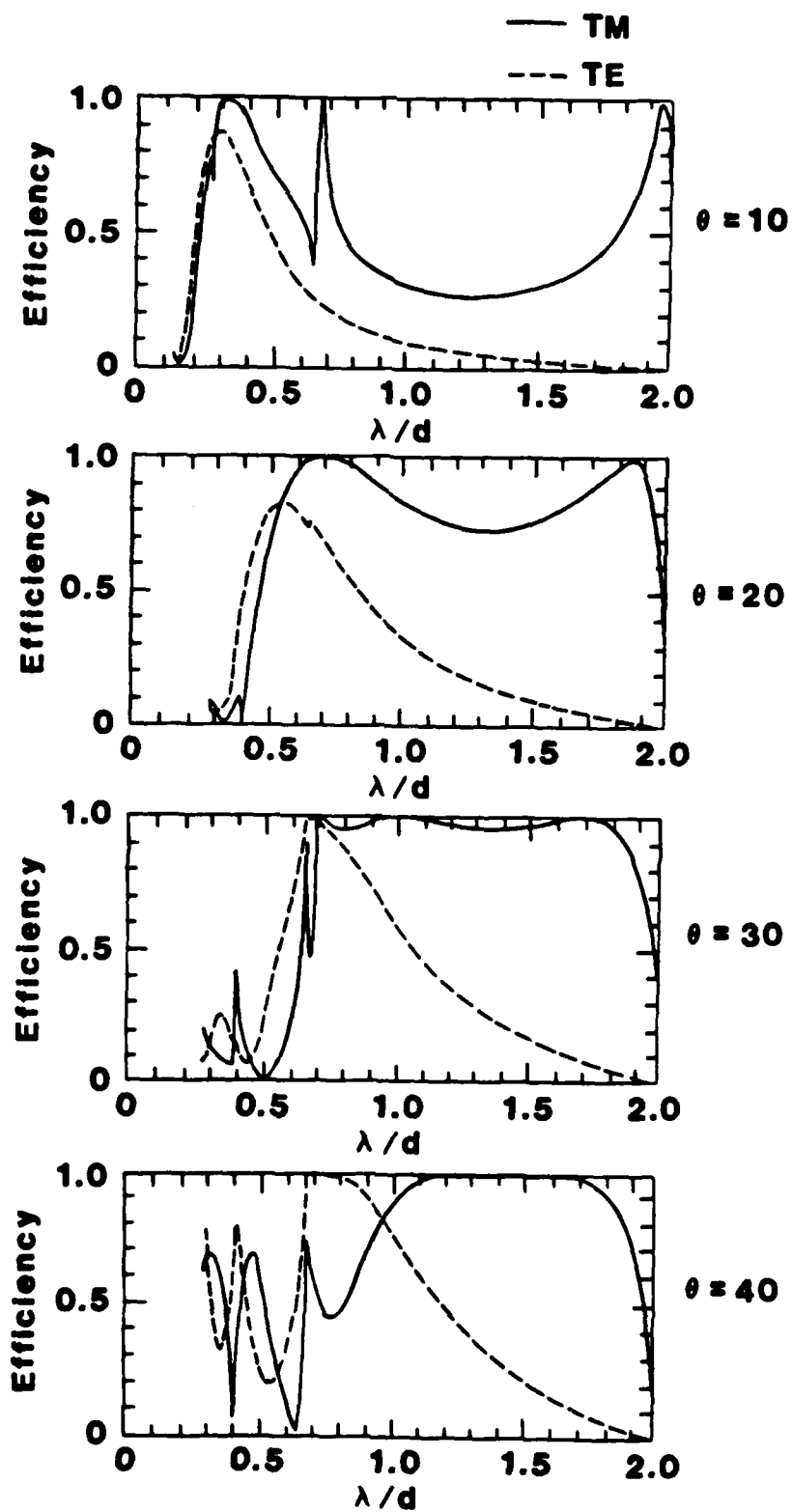
Figure 4. Efficiency of Littrow mount Echellete gratings with
blaze angle θ. The solid line is TM polarization
(H parallel to grating grooves) and the dashed line
is TE polarization (E parallel to grating grooves.

10

TABLE 1

F	λ/d	α	β
110	1.01	43.65	18.50
100	1.11	47.2	22.2
90	1.24	52.0	27.0
80	1.39	58.0	33.0
75	1.48	61.85	36.85

F is frequency   α is angle of incidence
λ is wavelength   β is angle of diffraction
d is groove spacing
refer to Figure 1 for definition of geometry

For the grating   d = 0.27 cm
                    θ = 30° (Note: The grating is also in blaze for
                                    90 - θ = 60°)

α and β are computed based on α - β = $2\theta_D$ ≈ 25°.

where λ_{min} is the shortest wavelength for which the grating will act as a mirror. We chose α equal to 45° and λ_{min} equal to 2.2 mm (140 GHz). Using this grating as a reflecting mirror effectively removes the possibility of higher order radiation appearing on our detectors. (For example, 2 mm radiation for m = 2 will appear the same as 4 mm radiation for m = 1.) The mirror/grating then reflects all radiation with a wavelength greater than 2.2 mm and diffracts all shorter wavelength radiation. We have placed microwave absorbers in the proper position to remove the diffracted short wavelength radiation.

2.2.3   Diffracted Signal Detection

As mentioned before, a multichannel detection system was decided upon to give broadband response on a single-shot basis. It was decided to design for a 10 GHz bandwidth centered at 75 GHz (4 mm). The detection system consists of six microwave detectors. A spherical mirror is used to concentrate the diffracted radiation. The mirror and detector locations were designed graphically using ray tracing. The mirror is 55 cm wide and has a 200 cm radius of curvature. The detectors are located on a focal line which is approximately 100 cm from the mirror. The mirror itself is made using thermoform plastic. A wooden master is machined. The plastic is then formed to the master and coated with a silver, high-conductivity paint.

The actual signal detection is performed using 1N53 diode crystals mounted in W-band waveguide. Although these detectors are not as flat in response as others, their response is not sufficiently poor to justify the increased expense of more uniform response detectors. Expense becomes an important factor due to the potentially short lifetime of the detector. A large microwave signal permanently destroys the crystal. It has been our experience in high-power microwave diagnostics that diode crystals are continually being burned out. This is due to the large power fluctuations that occur in the experimental microwave sources. Due to

12

this non-uniform response each detector will have to be individually calibrated for frequency response. The output of the detectors will be available on 50 *ohm* BNC connectors located on the outside of the spectrometer. If long cables will be used, it is recommended that line driver amplifiers also be used.

REFERENCES

1. Gebbie, H. A., "Fourier Transform vs. Grating Spectroscopy," Applied Optics 8, 501 (Mar 1969).

2. Pasour, J. A., "Reflection of Electromagnetic Radiation for the Front of a Magnetically-Confined, Relativistic Electron Beam," Thesis - North Carolina State University at Raleigh, Dept. of Physics 1977.

3. Felch, K. and L. Vallier, "Calibration of a Millimeter Microwave Grating Spectrometer: 55-350 GHz," Report PMI 1052, Laboratoire de Physique des Milieux Ionises, Ecole Polytechnique (Aug 1980).

4. Gold, S. H., W. M. Black, R. H. Jackson, V. L. Granatstein, H. P. Freud, P. C. Efthimion, and A. K. Kinkead, "Study of Emission Spectrum in a Millimeter-Wave Free-Electron Laser Operating in the Collective Regime," Bull. Am. Phys. Soc. 27, 1092 (Oct 1982).

5. Madden, R. P. and John Strong, "Diffraction Gratings," in Concepts of Classical Optics, Appendix P, W. H. Freeman and Co., San Francisco, CA, 1958.

6. Petit, R. ed., Electromagnetic Theory of Gratings, Springer-Verlog, New York, NY, 1980.

7. Kraus, J. D. and K. R. Carver, Electromagnetics, 2nd Ed., McGraw-Hill, Inc. New York, New York, p. 685, (1973).

8. Breeden, K. H. and A. P. Sheppard, "Millimeter and Submillimeter Wave Dielectric Measurements," The Microwave Journal, p. 59, (Nov. 1967).

ANNUAL REPORT: VIRTUAL CATHODE OSCILLATOR STUDY

November 1984

D. J. Sullivan
D. E. Voss
R. J. Adler
W. M. Bollen
R. H. Jackson
E. A. Coutsias*

Prepared for: Air Force Office of Scientific Research
                           Physics Directorate
                           Bolling Air Force Base, D.C. 20332

Under Contract   F49620-82-C-0014

Prepared by: MISSION RESEARCH CORPORATION
                           1720 Randolph Rd., SE
                           Albuquerque, NM 87106

*University of New Mexico

REPORT DOCUMENTATION PAGE		READ INSTRUCTIONS BEFORE COMPLETING FORM
1 REPORT NUMBER	2 GOVT ACCESSION NO.	3 RECIPIENT'S CATALOG NUMBER
4 TITLE (and Subtitle) ANNUAL REPORT: VIRTUAL CATHODE OSCILLATOR STUDY		5 TYPE OF REPORT & PERIOD COVERED
		6 PERFORMING ORG REPORT NUMBER AMRC-R-614
7 AUTHOR(s) D. J. Sullivan (MRC) W. M. Bollen (MRC) D. E. Voss (MRC) R. H. Jackson (MRC) R. J. Adler (MRC) E. A. Coutsias (UNM)		8 CONTRACT OR GRANT NUMBER(s) F49620-82-C-0014
9 PERFORMING ORGANIZATION NAME AND ADDRESS Air Force Office of Scientific Research Bolling Air Force Base Washington, DC 20332		10 PROGRAM ELEMENT PROJECT TASK AREA & WORK UNIT NUMBERS
11 CONTROLLING OFFICE NAME AND ADDRESS MISSION RESEARCH CORPORATION 1720 Randolph Road, S.E. Albuquerque, New Mexico 87106		12 REPORT DATE November 1984
		13 NUMBER OF PAGES
14 MONITORING AGENCY NAME & ADDRESS(if different from Controlling Office)		15 SECURITY CLASS (of this report) UNCLASSIFIED
		15a DECLASSIFICATION DOWNGRADING SCHEDULE

16 DISTRIBUTION STATEMENT (of this Report)

APPROVED FOR PUBLIC RELEASE; DISTRIBUTION UNLIMITED

17 DISTRIBUTION STATEMENT (of the abstract entered in Block 20, if different from Report)

18 SUPPLEMENTARY NOTES

19 KEY WORDS (Continue on reverse side if necessary and identify by block number)

Virtual Cathode	Space-Charge Limit
Virtual Anode	Space-Charge Limiting Current
Virtual Cathode Oscillator	Bifurcation
VIRCATOR	Millimeter Microwaves
	Spectrometer

20 ABSTRACT (Continue on reverse side if necessary and identify by block number)

The theory of a virtual cathode oscillator (VIRCATOR) has been previously described (AMRC-R-451, 1983). It is found that second order analytical approximations give an accurate value for the space-charge limiting current of an electron beam in cylindrical geometry. The same Green's function approach could be used on other geometries as well. Exceeding the space-charge limiting current is the necessary condition for virtual electrode formation. However, it does not explain the nature of the (cont.)

DD FORM 1473 EDITION OF 1 NOV 65 IS OBSOLETE

space-charge limit instability. The oscillatory stable state of the virtual cathode is found to originate at the bifurcation point of several stable and unstable electron beam states. An analysis of the nonlinear growth rate of the instability is derived.

The virtual cathode is in effect a relaxation oscillator. The advantage of the vircator over a reflex klystron is that the virtual cathode moves opposite to the electron beam propagation direction during the bunching phase resulting in enhanced electron densitites unobtainable otherwise. The periodic time-dependent nature of the bunching results in efficient microwave generation. Experimental efficiencies of 12% have been obtained in previous work and theoretical efficiencies of 20% have been obtained in the work described here. The microwave frequency scales as the relativistic beam plasma frequency. This can be adjusted via an externally applied axial magnetic field. The result is an oscillator which is frequency agile over an order of magnitude without externally changing the physical configuration. Output powers of from kilowatts to gigawatts are obtainable based on the power source. Experimental results are reviewed and explained. The rationale for using a foilless diode as the electron beam source is given.

A detailed mechanical and electrical design has been presented in previous reports (AMRC-R-451, 1983). It entails placing the vircator in a high vacuum vessel with flexibility for further development. The electrical power is pulse formed using a lumped artificial Blumlein line. The axial magnetic field is critically damped for component safety and circuit design simplicity. The beam source is a foilless diode with an annular limiter for collimation and prevention of electrons reflexing into the diode.

Several important technical developments have come to a successful conclusion during the period of work covered by this report. The multi-Tesla magnetic field coil, critically important for achieving the high electron densities necessary for driving millimeter wavelenghts, has been designed, and successfully tested. Secondly, a millimeter wavelength spectrometer, necessary for diagnosing the time history and spectral content of the vircator emission, has been designed and calibrated over a wide band from 35 to 110 GHz. Measured frequency selectivity was typically of order 5% or better, i.e., $\Delta f/f_0 \leq .05$. A unique cathode material has been investigated, yielding fast field-emission turn on and low gap closure rates. Details of these results are presented in the main section of this report.

ACKNOWLEDGEMENT

i

TABLE OF CONTENTS

Space-Charge Limit Instabilities in Electron Beams

High Power Microwave Generation from a Virtual Cathode Oscillator (Vircator)

A High Frequency Vircator Microwave Generator

Effects of Thermal Spread on the Space Charge Limit of an Electron Beam

1

LIST OF ILLUSTRATIONS

2

LIST OF ILLUSTRATIONS (continued)

LIST OF ILLUSTRATIONS (continued)

LIST OF ILLUSTRATIONS (concluded)

LIST OF PHOTOGRAPHS

LIST OF TABLES

SECTION I
INTRODUCTION

The main thrust of research in the second year of this program has been experimental. This report summarizes the progress made in developing the hardware for a millimeter wavelength virtual cathode microwave oscillator (Vircator). Fabrication, testing, and calibration of two critical components, the solenoidal magnet and the millimeter microwave spectrometer, is complete. Data summary and complete documentation of the testing of the magnetic field coil at the 30 kG level, is presented in Section II. Calibration data for the spectrometer, covering the entire 35 to 100 GHz frequency range, is presented in Section III. Section IV describes the successful operation of the electron beam pulse power system, based on an artificial Blumlein design. A unique cathode material is described which allows fast turn on of electron field emission, at field strengths of approximately 50 kV/cm and very slow anode-cathode gap closure rates, less than 1 cm/μsec. Our work in this area is further supplemented by reprints of articles compiled in Appendix B.

SECTION II
MAGNET DESIGN

The main criteria for the vircator magnet design are:

(1) Peak magnetic field of 60 kG;

(2) Field homogeneity in the anode-cathode gap region of $\Delta B/B < 1\%$.

(3) Accessibility to the high magnetic field region for grids, elec-
     trodes, diagnostics, and their connecting cables and mechanical
     support structure.

In support of the vircator magnet design, a useful computational tool
has been developed for calculating the field line configuration for
arbitrary solenoidal geometries. The computer code uses a two step
process. Radial and axial components of the magnetic field are calculated
on a two dimensional rectangular grid by summing the weighted contribution
from each circular current loop making up the solenoid. Bilinear
interpolation is then used to follow field line trajectories which are
launched from the center of the solenoid.

The magnetic field for an arbitrary solenoidal configuration follows
from the weighted superposition of the fields from the elemental circular
current loops, with the neglect of helicity and finite-current cross-
section effects. Eddy current effects are also neglected; this is a good
assumption since the skin penetration time through the high resistance
stainless steel casing, approximately 10 microseconds, is small relative to
the 570 microsecond field rise-time. With these approximations, the radial
and axial components of the magnetic field, B_r and B_z, at an arbitrary
point r,z, due to a circular current loop of radius a centered at the
origin of a cylindrical coordinate system (see Figure 1) can be calculated
(in mks units) as[1]:

10
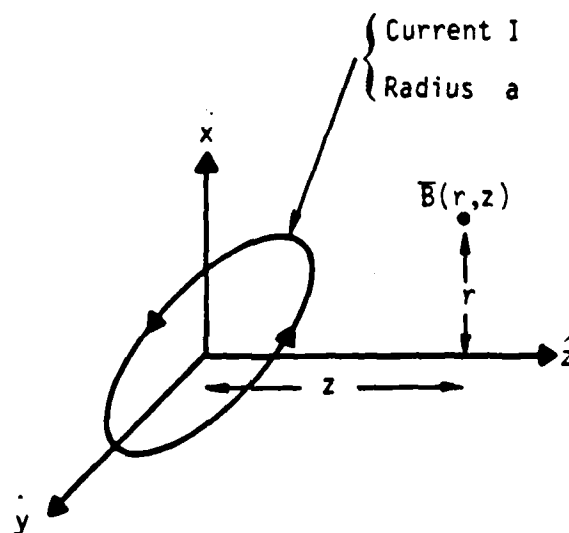
Figure 1. Relation of the cylindrical co-ordinate system to the circular current loop. The center of the loop and the origin of co-ordinates are coincident, and the z axis and the normal to the loop are coincident.

11

$$B_r = \frac{\mu_o I}{2\pi} \frac{z}{r\left[(a+r)^2 + z^2\right]^{1/2}} \left[-K(k) + \frac{a^2 + r^2 + z^2}{(a-r)^2 + z^2} E(k) \right] \quad , \quad (1)$$

$$B_z = \frac{\mu_o I}{2\pi} \frac{1}{\left[(a+r)^2 + z^2\right]^{1/2}} \left[K(k) + \frac{a^2 - r^2 - z^2}{(a-r)^2 + z^2} E(k) \right] , \quad (2)$$

where

$$k^2 \equiv 4\ ar \Big/ \left[(a+r)^2 + z^2\right] \tag{3}$$

and $K(k)$ and $E(k)$ are the complete elliptic integrals of the first and second kind, respectively. It is straightforward to evaluate the elliptic integrals numerically, and sum over the windings of the solenoid to produce a B_r and B_z matrix representing the calculated magnetic field. The first part of the field line plotting carries out these calculations, and is based on a code provided by John Freeman of Sandia National Laboratories.[2] Run time is approximately 30 seconds on a VAX 11/780 for an 84 point (12x7) grid and a 156 turn solenoid.

Field line plots are produced from the $\overline{B}$ field matrix using a shooting technique. Field lines are launched from the center of the solenoid in the $\hat{x}$-$\hat{y}$ plane, nominally a uniform field region, and the trajectory incremented by step sizes which are small relative to the $\overline{B}$ field grid points. Bilinear interpolation allows calculation of B_r and B_z between grid points with second order accuracy.[3]

In order to verify accurate operation of the code, a cross check has been carried out with an analytical calculation of a field line trajectory near the magnet center. The magnetic field in the central zone of a uniform current density, cylindrically symmetric solenoid can be written as a power series with terms of the form

$$\left(r^2 + z^2\right)^n P_{2n} (\cos \theta) \quad , \tag{4}$$

with P_{2n} the even Legendre ploynominals.[4-7] To second order, the $\overline{B}$ field is:

$$B_z = B_0 \left[1 + E_2 \left(\frac{\rho}{a}\right)^2 \quad \frac{1}{2} \left(3u^2 - 1\right)\right] \tag{5}$$

$$B_r = B_0 \left[\frac{-E_2}{3} \left(\frac{\rho}{a}\right)^2 \quad 3 \, u \, u'\right] \tag{6}$$

where

$$u \equiv \frac{z}{\sqrt{r^2 + z^2}} \tag{7}$$

$$u' \equiv \frac{r}{\sqrt{r^2 + z^2}} \tag{8}$$

$$\rho^2 \equiv r^2 + z^2 \tag{9}$$

$$E_2 = \frac{1}{2\beta^2} \quad \frac{C_1^{\frac{3}{2}} - C_3^{\frac{3}{2}}}{\ln \left[\dfrac{\alpha + \sqrt{\alpha^2 + \beta^2}}{1 + \sqrt{1 + \beta^2}}\right]} \tag{10a}$$

$$\approx -\frac{3}{2} \frac{1}{\beta^4} \qquad \text{for} \quad \alpha - 1 \ll 1 \tag{10b}$$

13

$$C_1 \equiv \frac{1}{1 + \beta^2} \qquad (11)$$

$$C_3 \equiv \frac{\alpha^2}{\alpha^2 + \beta^2} \qquad (12)$$

$$\alpha \equiv \frac{\text{solenoid outer radius}}{\text{solenoid inner radius}} \qquad (13)$$

$$\beta \equiv \frac{1}{2} \frac{\text{solenoid length}}{\text{solenoid inner radius}} \qquad (14)$$

$$B_0 = J_0 a \ \frac{4\pi\beta}{10} \ \ln\left\{ \frac{\alpha + \sqrt{\alpha^2 + \beta^2}}{1 + \sqrt{1 + \beta^2}} \right\} \qquad (15)$$

where J_0, the average solenoid current density, has units of amps/cm^2, magnet radius a is in cm, and B_0 is in gauss. The equation defining the field line trajectory in two-dimensional space can be written:

$$\frac{dr}{B_r} = \frac{dz}{B_z} \ . \qquad (16)$$

Keeping only the first term in the $\overline{B}$ field expansion and integrating the resulting differential equation gives the equation for the field line trajectories near the center of solenoid:

$$r = r_0 \ e^{-E_2 z^2 / 2a^2} \qquad (17)$$

For the case of a 10 cm radius, 100 cm long solenoid wound with a single 251 turn layer ($\alpha = 1$, $\beta = 5$, $E_2 = -0.0024$), the code calculation shows that a field line launched from $(r,z) = (0.90000, 0)$ cm intersects a point

(0.90095, 9.375) cm. Taking $r_0 = 0.9$ in Equation (17) yields (r,z) = (0.9009497, 9.375 cm), which agrees with the numerical calculation to within a fraction of one percent. In addition, the $\overline{B}$ field intensity at the center of the magnet for 1 amp current is calculated numerically as 3.081 Gauss, in excellent agreement with an analytical calculation[8] yielding 3.0806 G for this geometry. These cross-checks indicate that both the $\overline{B}$ field and the field line trajectory calculations are working correctly for the case of interest, i.e., near the center of a long solenoid.

The magnetic field code has been the primary tool used in design of the vircator magnet. End windings were used to yield a homogeneous central field. Optimization was carried out by iterating on a base design using the interactive capabilities of the VAX 11/780. A listing of the FORTRAN source code is given in Appendix A. Table I summarizes the final magnet design parameters, and Table II gives the radial and axial magnetic field components over a central region 3 cm in diameter and 8 cm long. Homogeneity in this region is $\Delta B/B_0 \leq 0.008$, $B_r/B_0 \leq 0.007$, with B_0 the field at the center of the magnet.

The magnet overall length is 21.4 cm with a usable inside diameter of 4.6 cm. The magnet is wound with 156 turns of 1 mm diameter wire in 5 layers, yielding an inductance of 0.7 mH and a current of 5.7 kA for the full 60 kG field. Self-forces tending to squeeze the magnet axially are taken up by the copper windings and an epoxy binder. Radial expansion forces are taken up by an encapsulating cylindrical stainless steel tube and the epoxy binder. With the assumption that half the radial expansion forces are borne by the epoxy and half by the encapsulating stainless steel, the stress in the 1.9 mm thick, 11.4 cm O.D. stainless shell is 23,100 psi for a 60 kG field. Since the yield strength of type 304 stainless steel exceeds 40,000 psi, the design provides an acceptable safety factor.

15

TABLE I. VIRCATOR MAGNET CONFIGURATION

Shell Number	Conductor Radius (cm)	Conductor Axial Coordinate Range (cm)	Number of Windings Distributed in Shell	Description
1	2.80	-7.41 to -4.94	7	Inner end-correction winding, left side.
2	2.80	+4.94 to +7.41	7	Inner end-correction winding, right side.
3	3.27	-7.41 to -0.41	17	Outer end-correction, left side.
4	3.27	+0.41 to +7.41	17	Outer end-correction, right side.
5	3.73	-7.41 to +7.41	36	Main winding.
6	4.20	-7.41 to +7.41	36	Main winding.
7	4.66	-7.41 to +7.41	36	Main winding.

Design Magnetic Field .... 60 kG

Total Number of Turns 156

Drive Current for 60 kG Field at Center .... 5.7 kA

Magnet Inductance .... 0.7 mH

Field Energy at Full Current .... 11.4 kJ

TABLE II. MAGNET COMPUTATION REGION DATA

RADIUS= 1.500E+00   LENGTH= 4.000E+00   DR= 5.000E-01
DZ= 1.000E+00   NR= 4   NZ= 5

COIL DATA

R= 2.80E+00	ZL=-7.41E+00	ZR=-4.94E+00	TURNS= 7.00E+00	CURRENT= 5.71E+03
R= 2.80E+00	ZL= 4.94E+00	ZR= 7.41E+00	TURNS= 7.00E+00	CURRENT= 5.71E+03
R= 3.27E+00	ZL=-7.41E+00	ZR=-4.12E-01	TURNS= 1.70E+01	CURRENT= 5.71E+03
R= 3.27E+00	ZL= 4.12E-01	ZR= 7.41E+00	TURNS= 1.70E+01	CURRENT= 5.71E+03
R= 3.73E+00	ZL=-7.41E+00	ZR= 7.41E+00	TURNS= 3.60E+01	CURRENT= 5.71E+03
R= 4.20E+00	ZL=-7.41E+00	ZR= 7.41E+00	TURNS= 3.60E+01	CURRENT= 5.71E+03
R= 4.66E+00	ZL=-7.41E+00	ZR= 7.41E+00	TURNS= 3.60E+01	CURRENT= 5.71E+03

RADIAL MESH LINE LOCATIONS
0.00000E+00   5.00000E-01   1.00000E+00   1.50000E+00

AXIAL MESH LINE LOCATIONS
0.00000E+00   1.00000E+00   2.00000E+00   3.00000E+00   4.00000E+00

THETA = ARCTAN (BR/BZ) (degrees)

LISTING OF BR AND BZ OVER THE COMPUTATIONAL GRID

K	L	R	Z	BR(K,L)	BZ(K,L)	B(K,L)	BR/BZ	THETA
1	1	0.00000	0.0000	0.000	60000.031	60000.031	0.000E+00	0.0000
1	2	0.00000	1.0000	0.000	60017.418	60017.418	0.000E+00	0.0000
1	3	0.00000	2.0000	0.000	59966.418	59966.418	0.000E+00	0.0000
1	4	0.00000	3.0000	0.000	59726.496	59726.496	0.000E+00	0.0000
1	5	0.00000	4.0000	0.000	59156.402	59156.402	0.000E+00	0.0000

K	L	R	Z	BR(K,L)	BZ(K,L)	B(K,L)	BR/BZ	THETA
2	1	0.50000	0.0000	0.000	59995.840	59995.840	6.835E-10	0.0000
2	2	0.50000	1.0000	-4.416	60021.887	60021.887	-7.357E-05	-0.0042
2	3	0.50000	2.0000	33.265	59978.754	59978.762	5.546E-04	0.0318
2	4	0.50000	3.0000	87.598	59743.328	59743.391	1.466E-03	0.0840
2	5	0.50000	4.0000	214.361	59216.949	59217.336	3.620E-03	0.2074

K	L	R	Z	BR(K,L)	BZ(K,L)	B(K,L)	BR/BZ	THETA
3	1	1.00000	0.0000	0.001	59978.680	59978.680	1.345E-08	0.0000
3	2	1.00000	1.0000	-18.919	60036.184	60036.184	-3.151E-04	-0.0181
3	3	1.00000	2.0000	65.006	60017.195	60017.230	1.083E-03	0.0621
3	4	1.00000	3.0000	166.902	59787.082	59787.316	2.792E-03	0.1599
3	5	1.00000	4.0000	365.696	59381.059	59382.184	6.158E-03	0.3528

K	L	R	Z	BR(K,L)	BZ(K,L)	B(K,L)	BR/BZ	THETA
4	1	1.50000	0.0000	0.000	59929.898	59929.898	4.424E-09	0.0000
4	2	1.50000	1.0000	-58.797	60064.949	60064.977	-9.789E-04	-0.0561
4	3	1.50000	2.0000	96.956	60087.793	60087.871	1.614E-03	0.0925
4	4	1.50000	3.0000	241.009	59839.746	59840.230	4.028E-03	0.2308
4	5	1.50000	4.0000	391.128	59583.676	59584.961	6.564E-03	0.3761

17

Encapsulation of the magnet is completed by a 1.6 mm thick inner wall and two 1.6 mm thick end plates. The stainless shell and its relation to the coil windings is shown in Figure 2. The inner stainless cylinder acts to shield the magnet winding from electron and x-ray bombardment which would otherwise reduce the magnet turn-to-turn voltage standoff. Since the highest operating voltage for the vircator is 100 kV, the inner stainless shield provides complete shielding from electron bombardment (50 electron ranges at 100 kV) and better than a factor of 10 attenuation (2.4 mean free paths for 50 kV x-rays) for the most energetic x-rays of interest. Flux penetration constraints do not allow the wall thickness to be substantially increased beyond 2 mm, corresponding to a magnetic field penetration time of approximately 10 microseconds.

Fabrication prints for the stainless steel magnet housing are shown in Figures 3-5. Fabrication prints for the PVC insulators are shown in Figures 6-9, and the assembled magnet is shown in Photo 1. The purpose of the insulator assembly is to provide high voltage standoff between the multi-kV magnet windings and the grounded stainless steel magnet housing. PVC wall thickness is 5.7 mm on the outer wall and 24.9 mm on the side walls, providing voltage standoff to well above the 10 kV required. No PVC is required at the inner radius since the inner-most magnetic winding is relatively close to ground potential.

The cylindrical magnet is held in place by encapsulation between the upper and lower PVC brackets shown in Figure 10. Brackets attach to the upper plate of Figure 11 which is positioned with respect to the lower plate of Figures 12 and 13 by 3 bolts. These bolts provide 3 degrees of freedom for aligning the magnet with the cathode. An additional two degrees of freedom is allowed by positioning the lower plate of Figure 12 relative to the stainless steel mounting brackets which are welded inside the vacuum vessel; both of these pieces have racetrack-type slots for adjustment. Thus, full 5 degree-of-freedom flexibility is allowed by the magnet alignment system. Photo 2 shows the vircator magnet and the assembled alignment system.
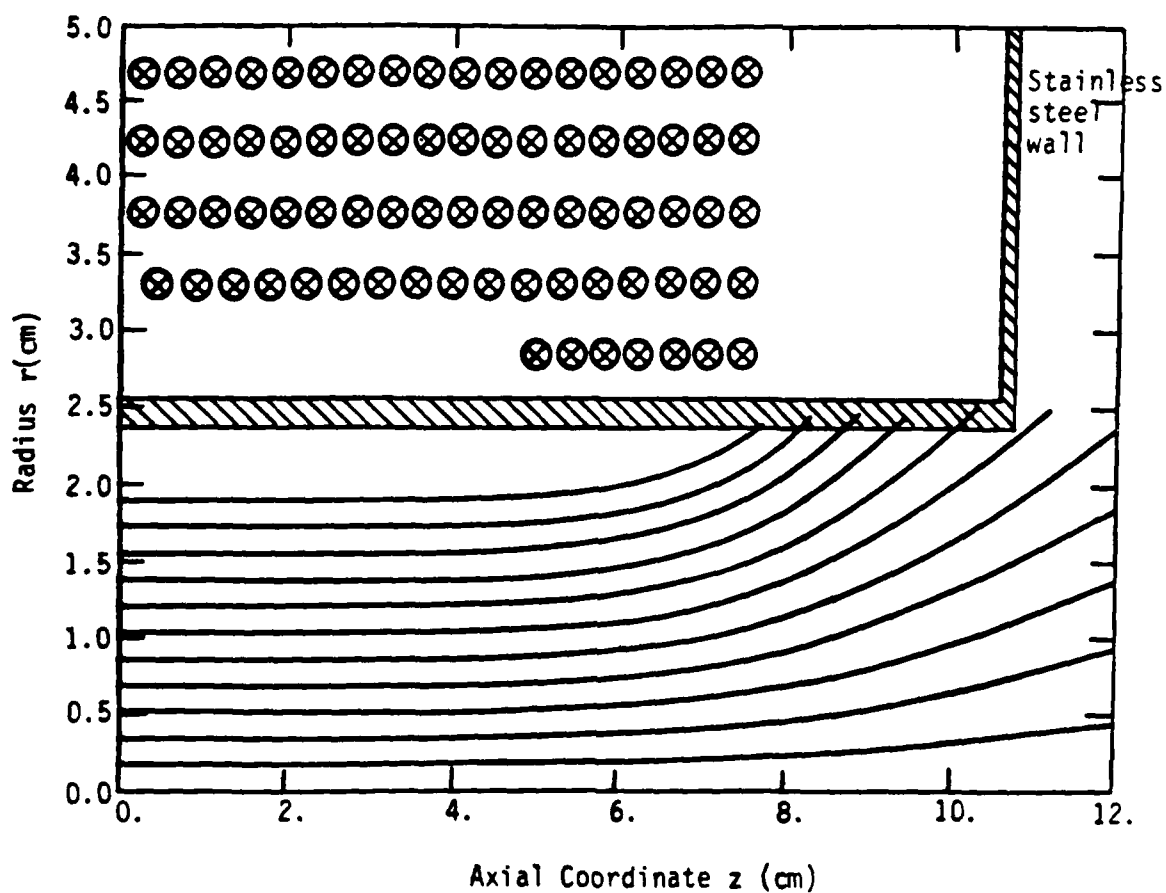
Figure 2. Relationship between the stainless steel encapsulating
shell and the coil windings. Usable inside diameter
of the magnet is 4.6 cm. The calculated magnetic field
lines are shown as solid lines and each winding for the
right side is shown as an x.

STAINLESS STEEL PIPE

Drill and tap eight (8)
#2-56 thru holes,
equally spaced

Drill and tap eight (8) #2-56
thru holes, equally spaced

Drill and tap eight (8) #2-56
thru holes, equally spaced

.251 Radius

.722

.503

.200

8.020

8.420
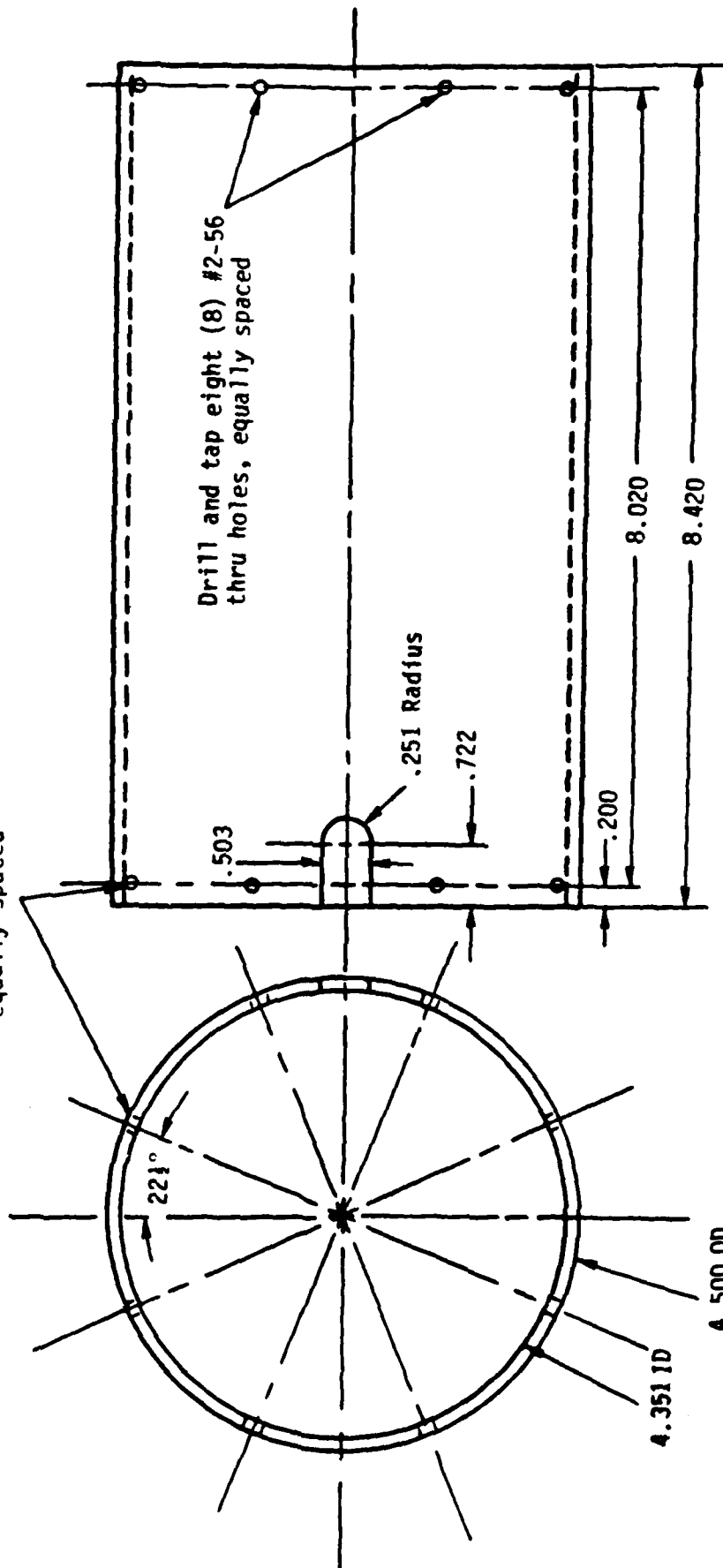
Material: 300 series stainless
steel tube (not provided)

Quantity: One (1)

22½°

4.500 OD

4.351 ID

(Turn ID so that PVC tube
is a snug fit in ID)

Figure 3.   Fabrication print of the magnet outer shell used to take
up the radial stresses induced by the 60 kG magnetic field.

INNER PIPE

Drill and tap eight (8) #2-56 thru holes at each
end, equally spaced.

8.020

8.620

.400

2.000 OD
Tube (provided)

45°

1.870 ID
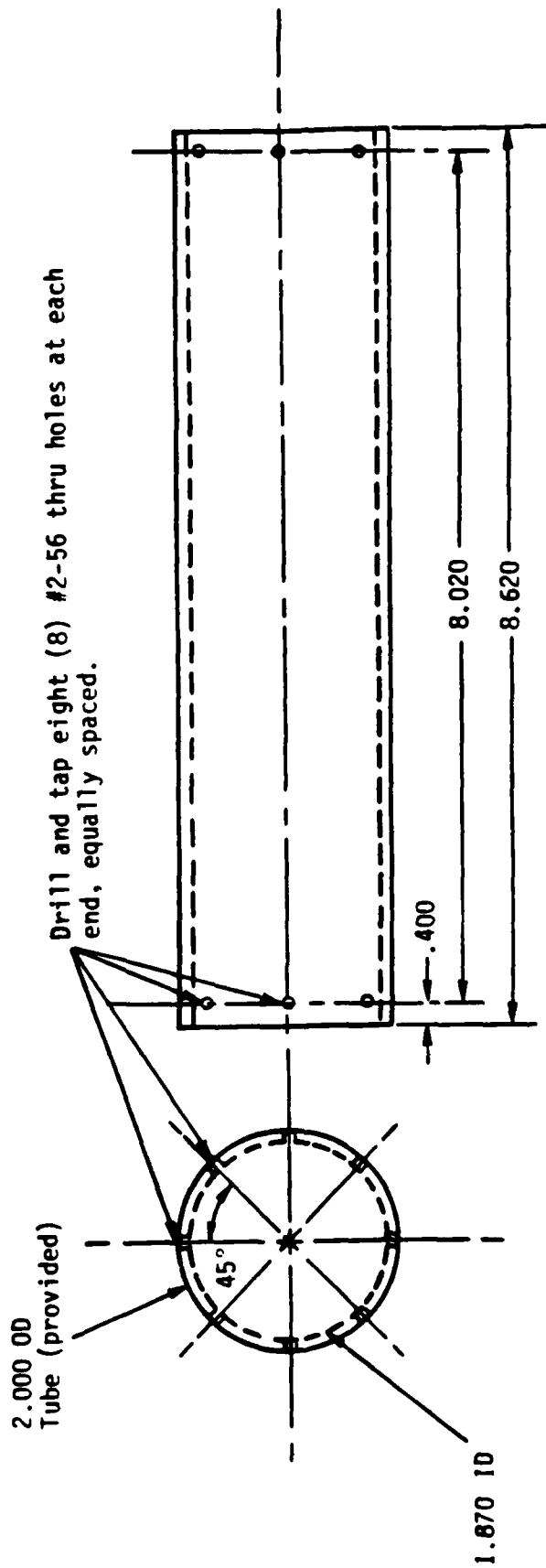
Material: 300 series stainless (provided)
Quantity: One (1)

Figure 4.   Fabrication print of the magnet inner shell used to reduce
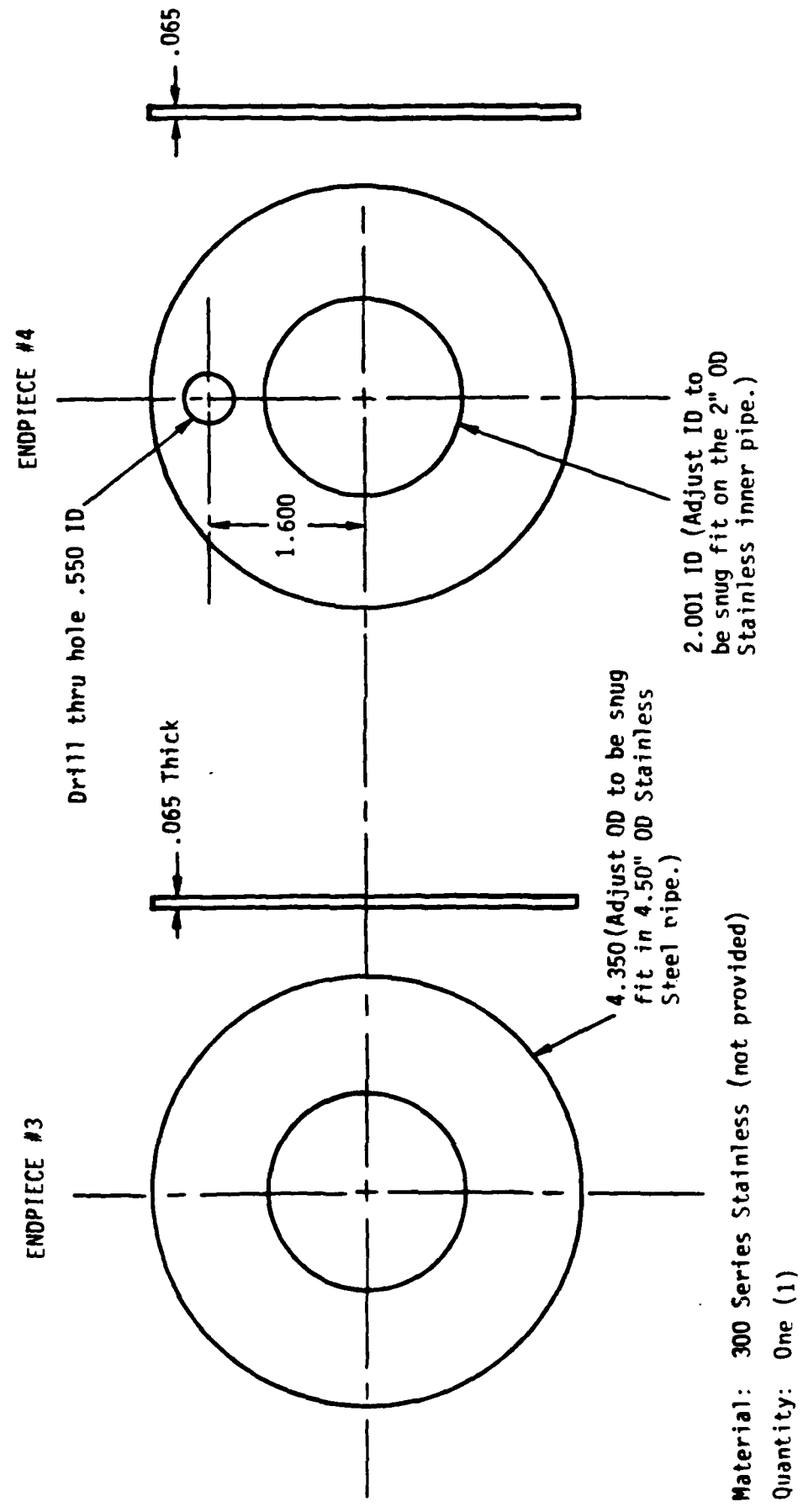electron and photon bombardment of the inner windings.

.065

ENDPIECE #4

1.600

Drill thru hole .550 ID

.065 Thick

2.001 ID (Adjust ID to
be snug fit on the 2" OD
Stainless inner pipe.)

4.350 (Adjust OD to be snug
fit in 4.50" OD Stainless
Steel pipe.)

ENDPIECE #3

Material: 300 Series Stainless (not provided)

Quantity: One (1)

Figure 5. Fabrication print of the magnet end caps.

PVC PIPE

7.957

.251 Radius

.492

.503

3.900 ID
Adjust to be snug fit with
endpieces #1 and #2

4.350 OD
Adjust to be snug fit with
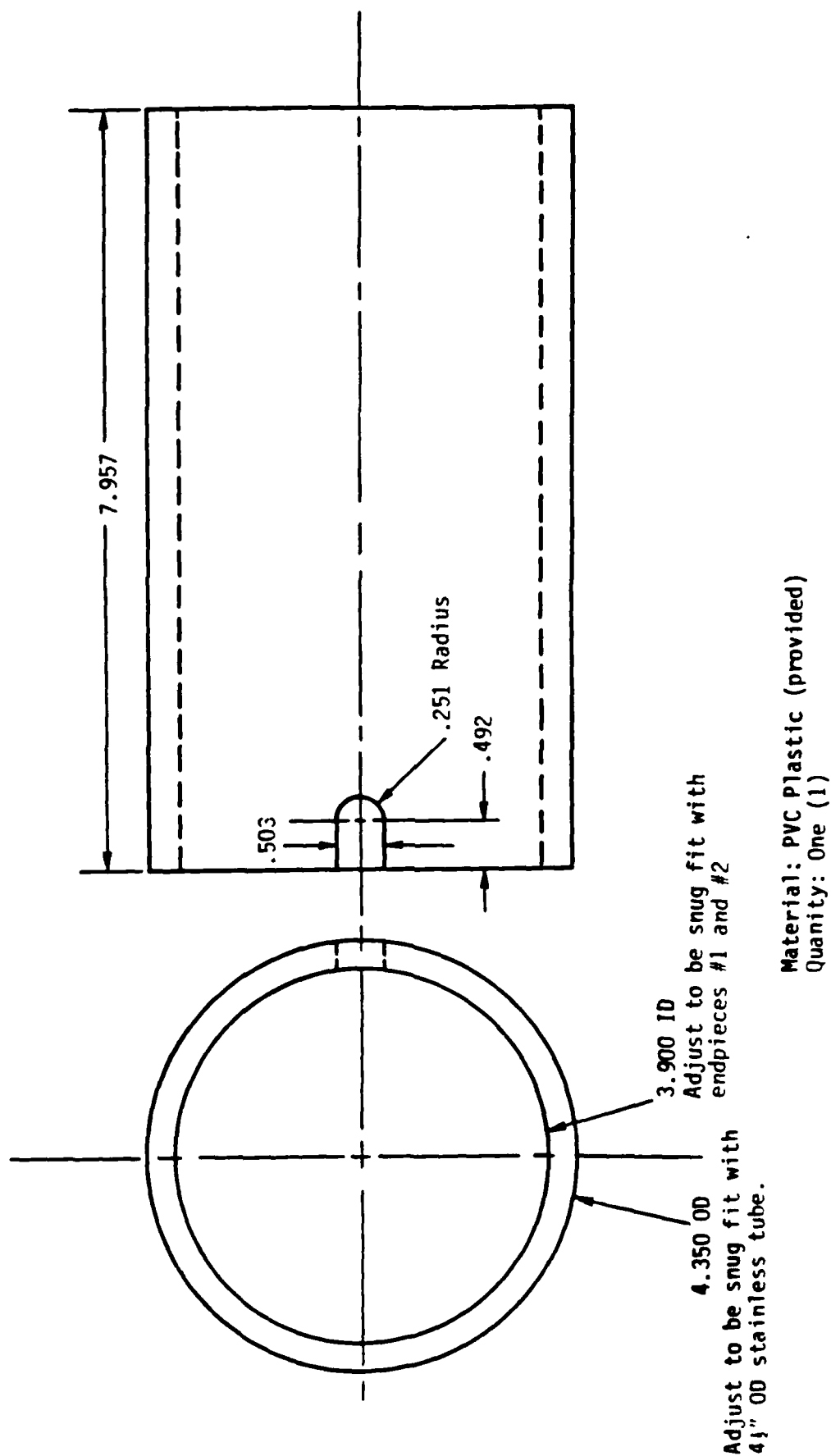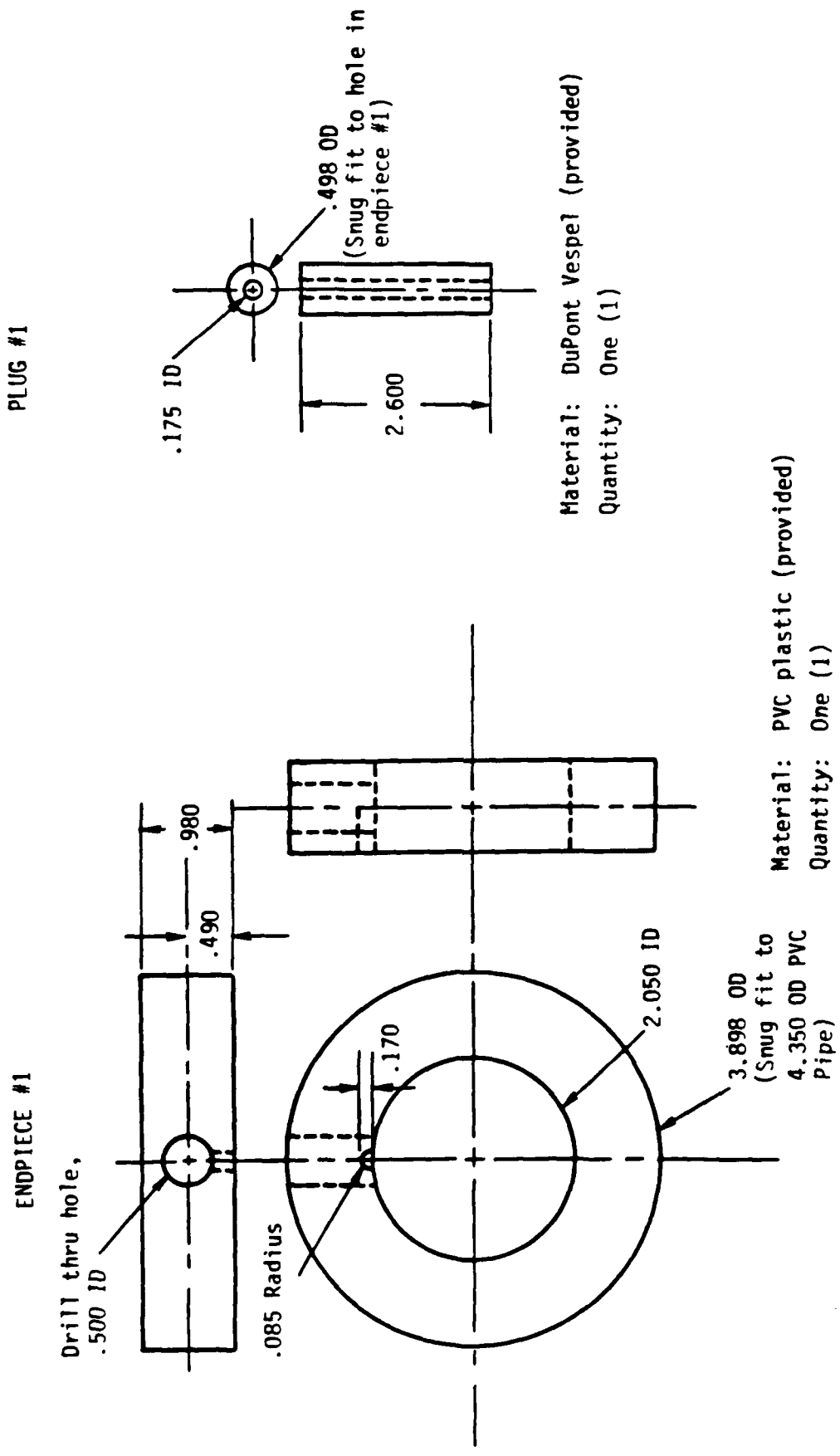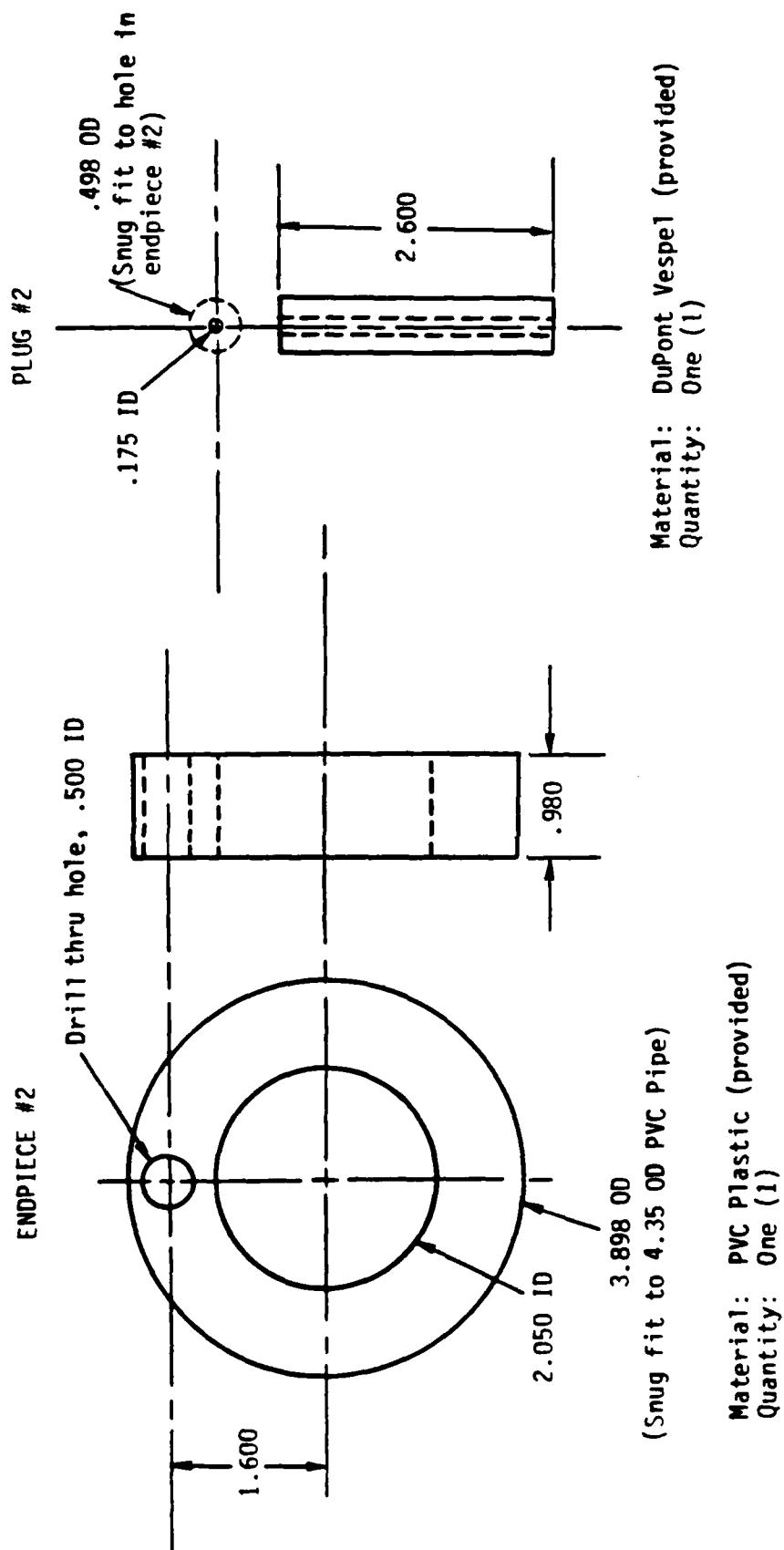4½" OD stainless tube.

Material: PVC Plastic (provided)
Quanity: One (1)

Figure 6.   Fabrication print of the outer PVC shell used to insulate the high
voltage outer magnet windings from the grounded case.

23

PLUG #1

.498 OD
(Snug fit to hole in endpiece #1)

.175 ID

2.600

Material: DuPont Vespel (provided)
Quantity: One (1)

ENDPIECE #1

.980

.490

Drill thru hole,
.500 ID

.085 Radius

.170

3.898 OD
(Snug fit to
4.350 OD PVC
Pipe)

2.050 ID

Material: PVC plastic (provided)
Quantity: One (1)

Note: Critical dimension is OD - adjust so that it is a snug fit in ID of 4.350 OD PVC pipe

Figure 7. Fabrication print of the left PVC endcap and the polyimide insulated feedthrough used to feed the inner windings of the magnet.

PLUG #2

.498 OD

(Snug fit to hole in endpiece #2)

.175 ID

2.600

Material: DuPont Vespel (provided)
Quantity: One (1)

ENDPIECE #2

Drill thru hole, .500 ID

.980

3.898 OD

2.050 ID

1.600

(Snug fit to 4.35 OD PVC Pipe)

Material: PVC Plastic (provided)
Quantity: One (1)

Note: Critical dimension is OD-adjust so that it is a snug fit in ID of the 4.350 OD PVC pipe.

Figure 8. Fabrication print of the right PVC endcap and the polyimide insulated feedthrough used to feed the outer windings of the magnet.
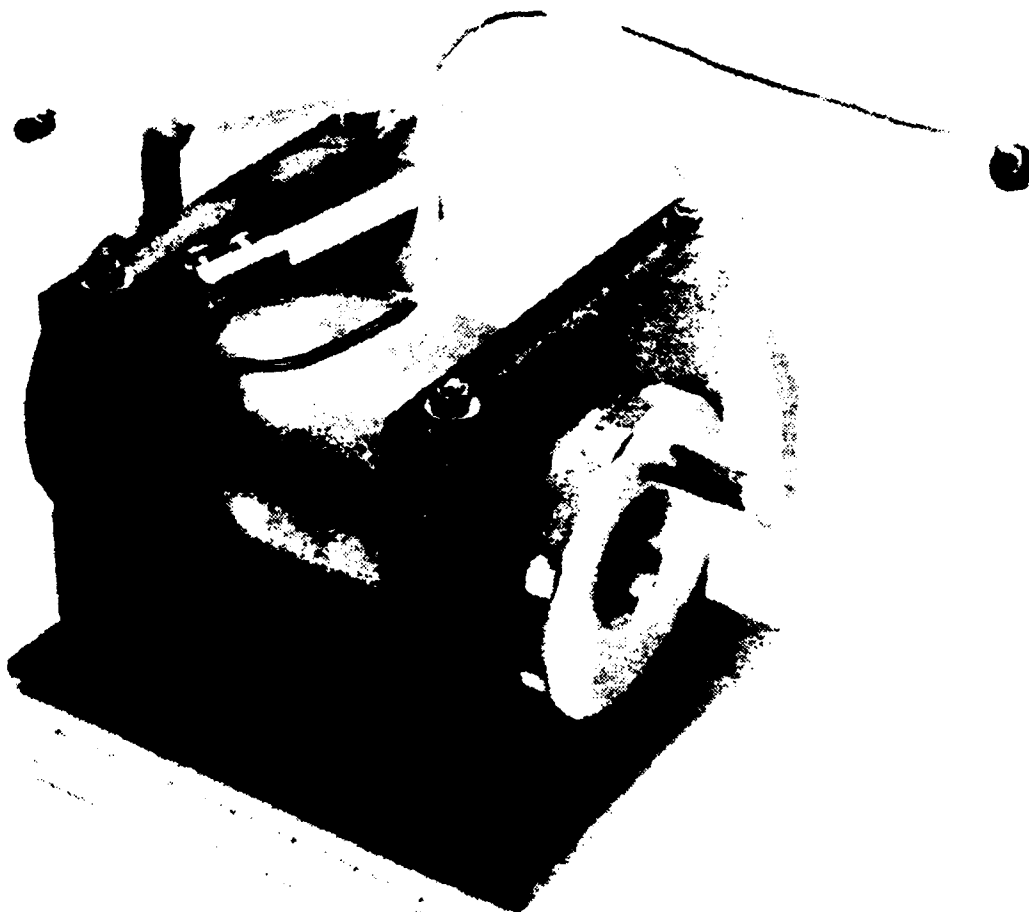
SPACER

.164 Slot Width

3.730

2.050

2.360
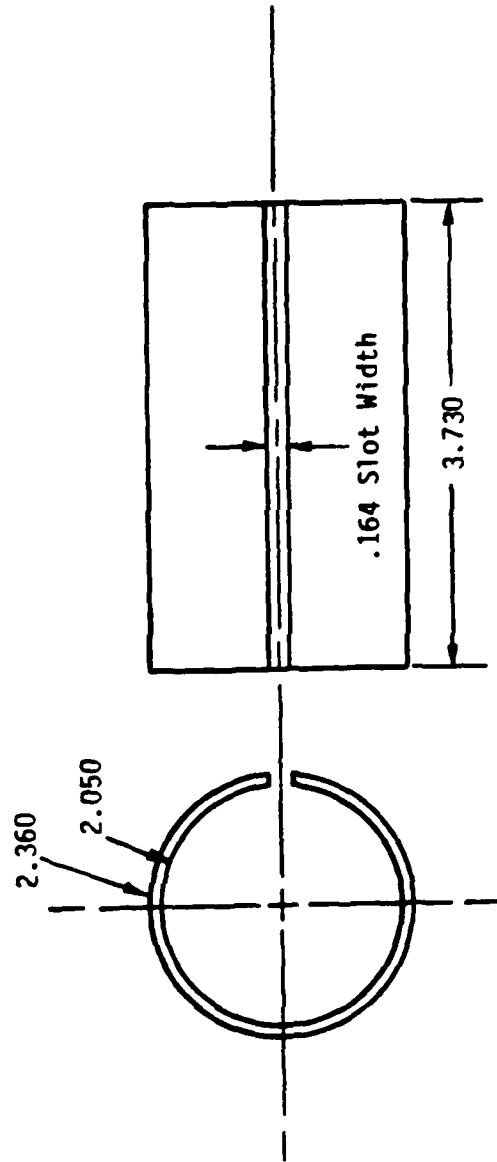
Material: PVC plastic (provided)

Quantity: One (1)

Figure 9. Fabrication print of the PVC spacer separating the left and right inner correction windings.

Photograph 1. Vircator magnet assembly. The cylindrical magnet housing is attached to the PVC baseplate with four stainless steel rods.

27

Figure 10. Fabrication prints for the magnet brackets. The cylindrical magnet is encapsulated between the two brackets and attached to the upper plate of Figure 11.
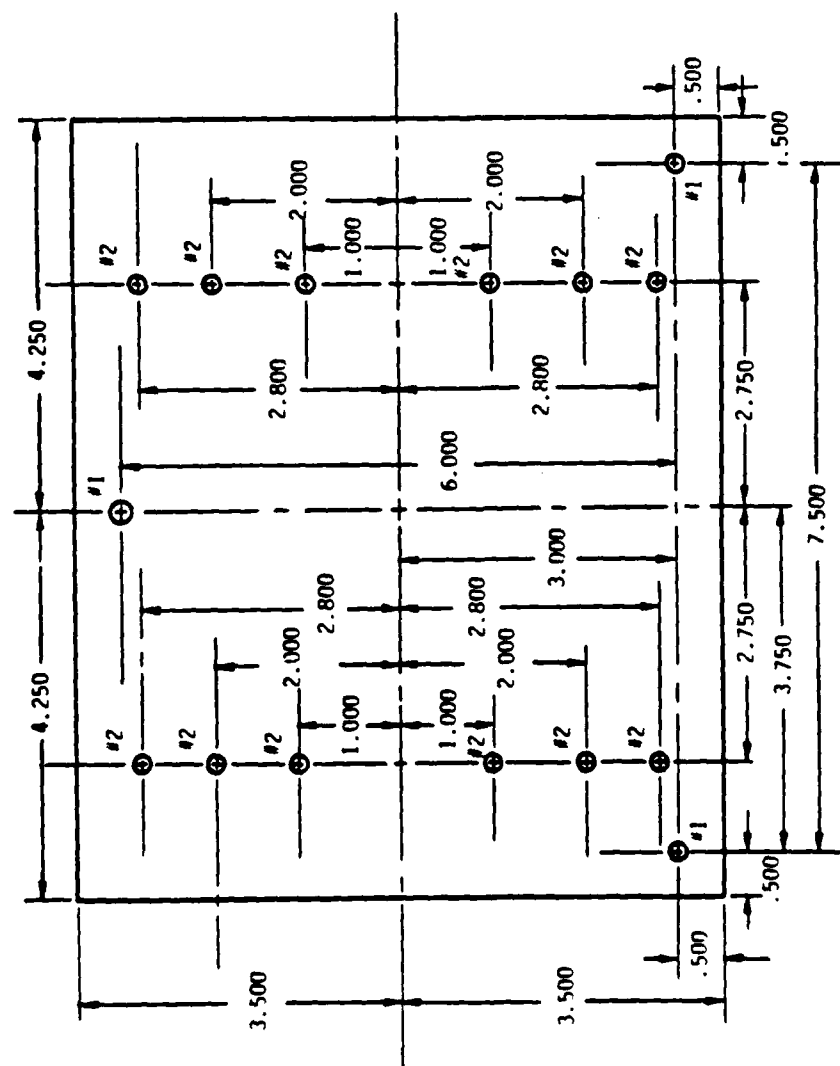
Material: 1/4" thick PVC (provided)
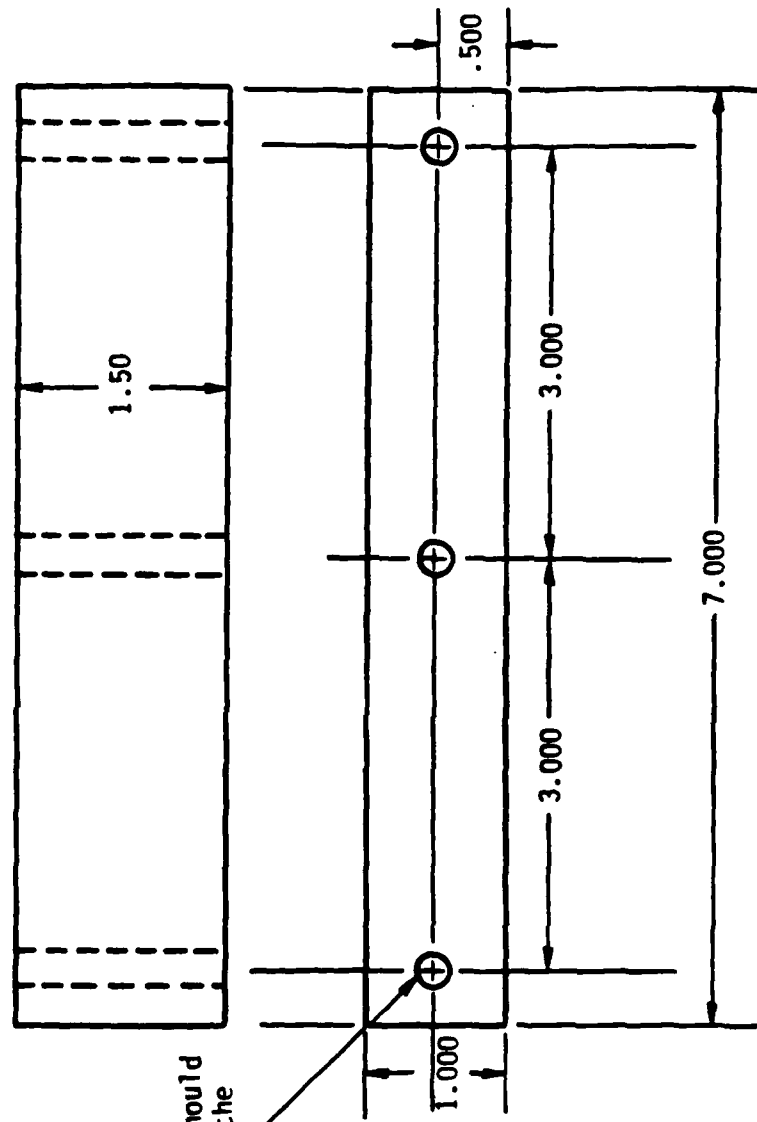Quantity: One (1)

Drill a total of 15 through holes, according to the number of each as follows:

#1: Diameter of these three holes is .285. These three holes should be accurately located relative to each other, as the dimensions indicate.

#2: Diameter of these 12 holes is .250. These holes should accurately line up with the holes drilled and tapped in the lower bracket pieces. They should accept a 1/4" hex head bolt (provided).

UPPER PLATE

Figure 11. Fabrication print of the PVC upper plate which provides a rigid mount for the magnet.

29

Figure 12. Fabrication print of the lower plate. Bolts are inserted through the three 0.248 inch diameter holes to provide 3 point alignment of the magnet with the cathode.
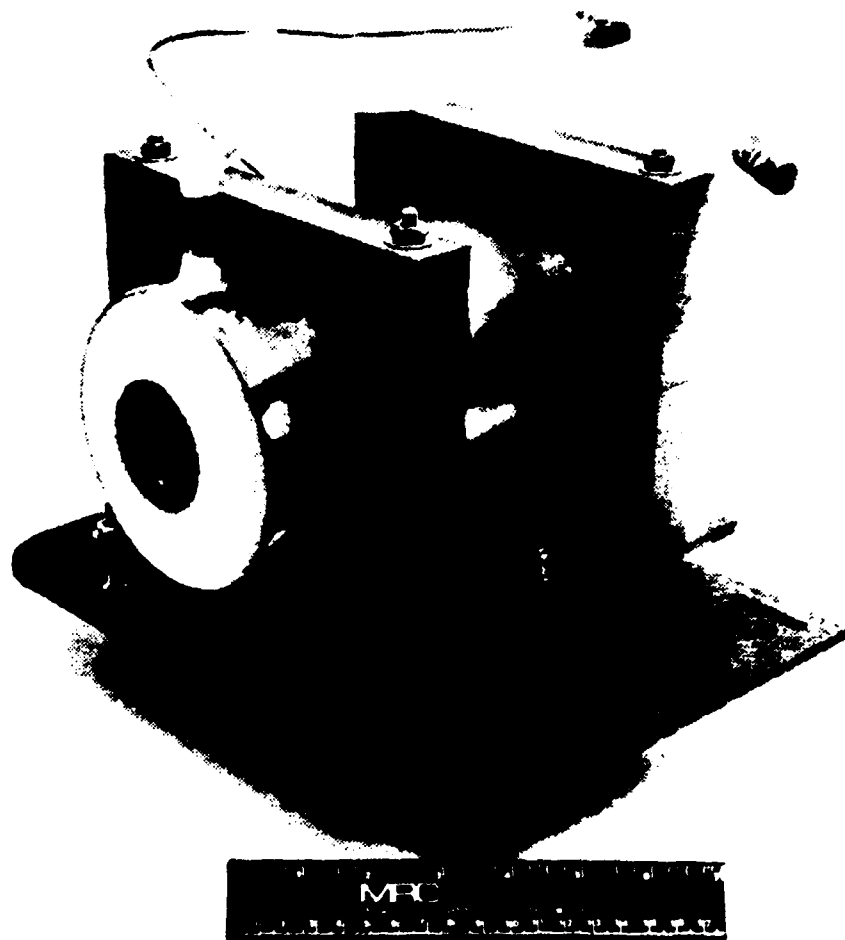
STIFFENER for LOWER PLATE

Drill three (3) holes,
.250 diameter. These should
mate with the holes in the
lower plate piece.

Material: PVC plastic
Quantity: Two (2) required

Figure 13. Fabrication print of the PVC pieces used to
stiffen the lower plate structure.

Photograph 2. Photograph of the vircator magnet and the five degree-of-
freedom positioning assembly for aligning the magnet with
the high voltage cathode.

A schematic for the circuit which drives the magnetic field coil is shown in Figure 14. A 366 microfarad energy storage capacitor bank is discharged into the magnetic field coil through a series resistance which is chosen so that the circuit is strongly, but not critically, damped. Since the current reversal is slight, the lifetime of both the capacitors and the magnetic field coil are increased. The price paid is an increase by a factor of approximately 2 in the required bank capacitance relative to an undamped circuit. The same result could be achieved by crowbaring the current at peak field with an ignitron, and eliminating the series resistance. Since the cost of the increased capacitance is small compared to the cost of the ignitron and its driving and control circuits, the former option was chosen.

The magnet energizing circuit of Figure 14 operates as follows. A 20 kV, 10 mA power supply (Del Electronics #RIU-20-10) charges the 366 microfarad capacitor bank to its charge voltage, about 8 kV for a 30 kilogauss field. A krytron gas tube switch is command triggered to discharge a 1 microfarad capacitor charged to 2.5 kV into the ignitor terminals of a mercury ignitron (General Electric #GL-7703). The triggered ignitron then discharges the main capacitor bank into the inductive load through a 1.8 ohm series resistor. The peak magnetic field occurs at 570 microseconds. A time delay generator (California Avionics #113CR) command fires the spark gap to initiate the electron beam at peak magnetic field time.

Testing of the vircator magnet has been carried out to the 30 kG level using two 183 µF, 8 kV rated capacitors configured in parallel as the energy source. No attempt has been made to exceed this field level, although design calculations indicate reliable operation to 60 kG. Time dependence of the magnetic field has been measured with the probe assembly shown in Photo 3. A 100 turn coil, inside diameter 9.538 mm, outside diameter 11.15 mm, and overall length 3.17 mm, is wound on a PVC rod to
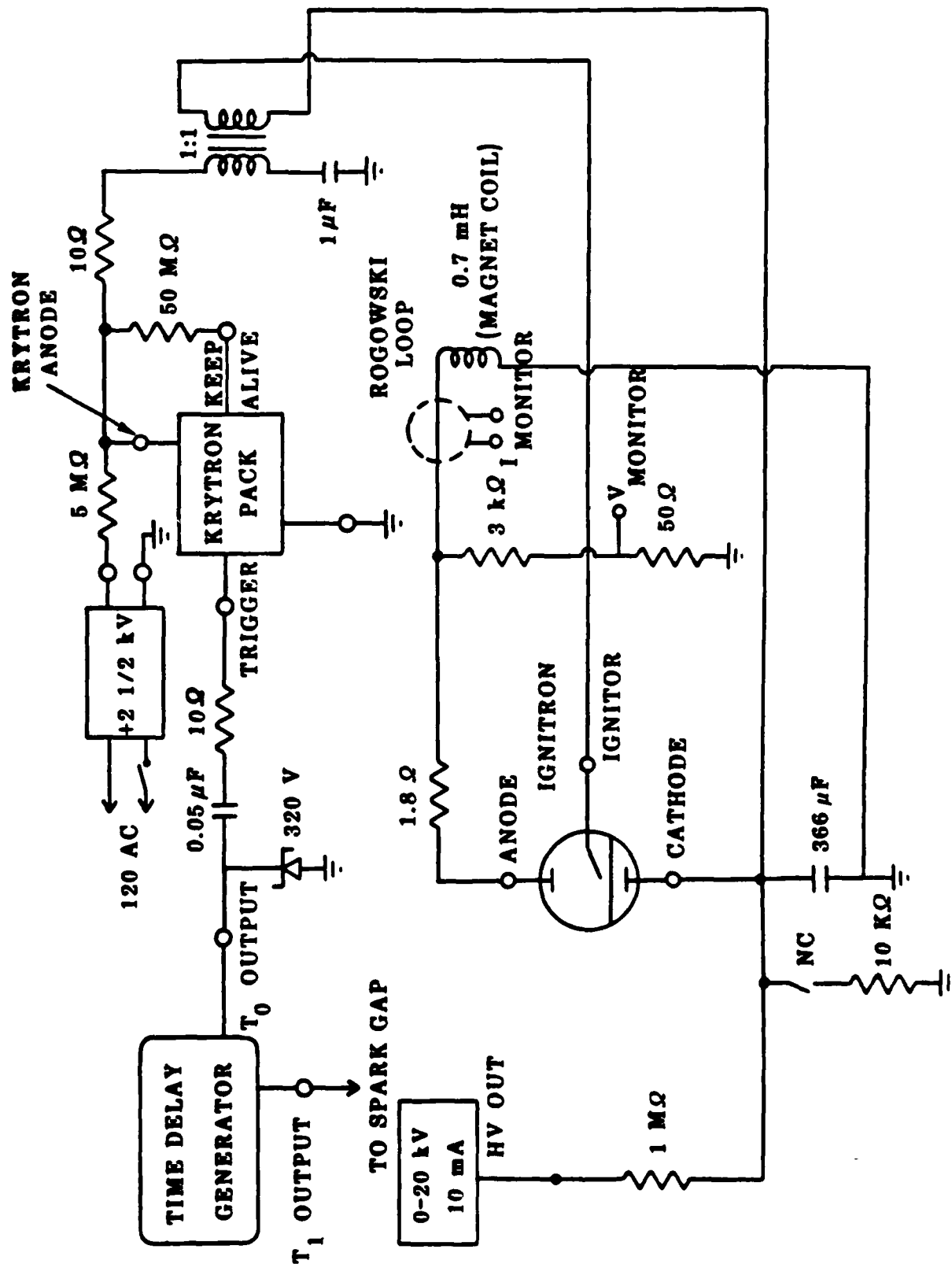
Figure 14. Schematic of the pulse power circuit which drives the vircator magnet coil. The series 1.8 Ω resistor strongly damps the magnet RLC circuit to minimize current reversal.

Photograph 3. Ḃ probe used to measure magnetic field amplitude and risetime. The 100 turn coil is at the far right. Measured values are consistent with the elementary RLC circuit theory described in the text. The probe axial stroke is 6 inches.

sample the B_z field. Because of the slow field rise time and low probe
inductance, the probe is not self integrating and produces a B_z signal.
The peak B_z field follows from the stored voltage output versus time $V(t)$
according to:

$$B_z(t) = 1.19 \times 10^6 \int_0^t dt' V(t') \ . \tag{18}$$

The probe can be positioned anywhere along the axis of the magnet using the
vacuum manipulator of Photo 3 (Huntington Mechanical Laboratories linear
motion feedthrough #VF-158). A typical probe output oscilloscope trace is
shown in Figure 15 for a 4.0 kV capacitor charge voltage with the probe
located on axis. The magnetic field peaks at 570 μsec, and carrying out
the areal integral in the above equation yields a peak field of 14.62 kG.
The measured field level and risetime can be compared with analytical cal-
culations[9] based on a simple series RLC circuit. These calculations show
that for a capacitor C initially charged to a voltage V_0 and discharged
at time t=0 into an underdamped series load of inductance L and resistance
R (mks units), the current peaks at time t_0 at a value I_{max} given by:

$$t_0 = \frac{1}{\omega} \tan^{-1} \left(\frac{2\omega L}{R} \right) . \tag{19}$$

$$I_{max} = \frac{V_0}{\sqrt{L/C}} \ \epsilon \ . \tag{20}$$

where

$$\omega^2 \equiv \frac{1-d}{LC} \ . \tag{21}$$

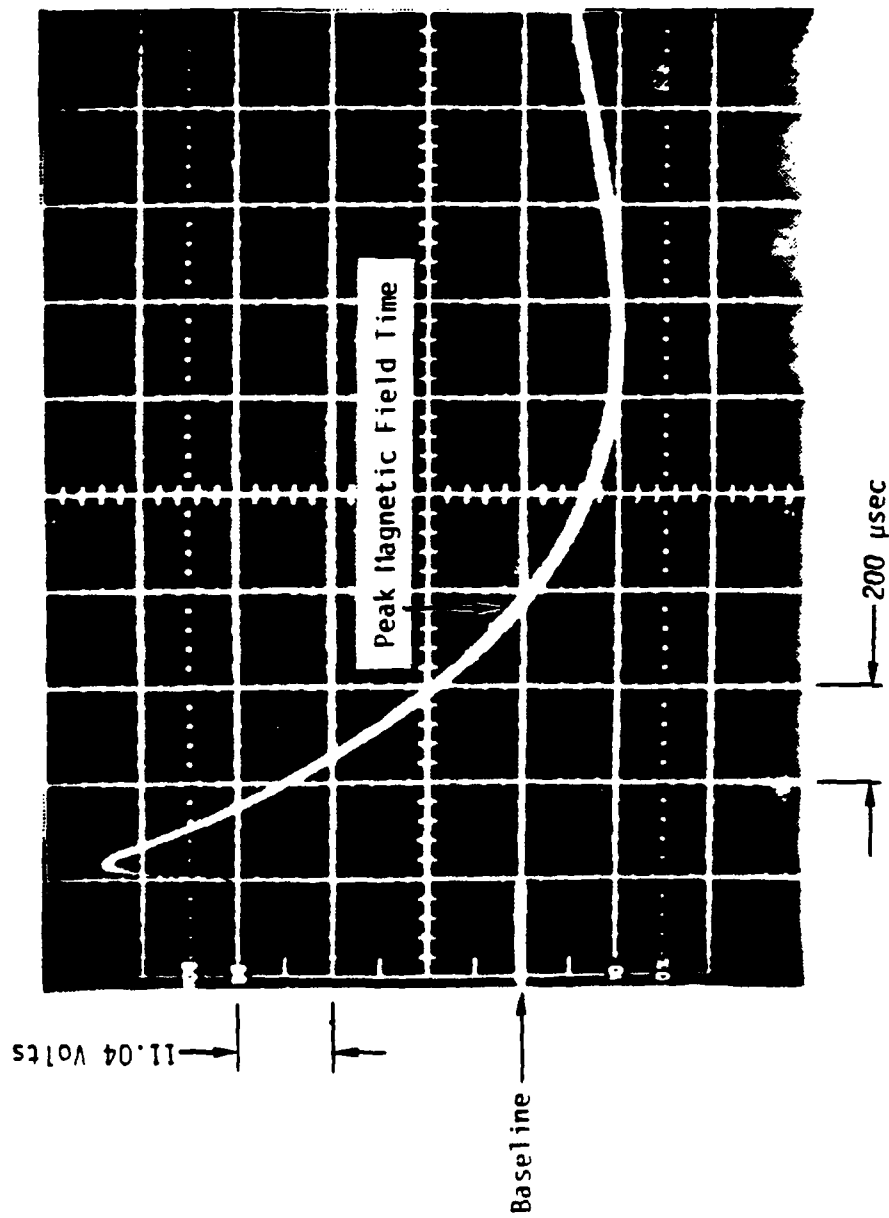$$d \equiv \frac{R^2 C}{4L} \ . \tag{22}$$

and

Figure 15. Output voltage versus time from the 100 turn 10.35 mm diameter $\dot{B}$ coil. Area under the curve is 5.565 div² yielding a peak magnetic field of 14.62 kG at 570 μsec.

37

$$\varepsilon \equiv \exp\left[-\sqrt{\frac{d}{1-d}}\, \tan^{-1}\sqrt{\frac{1-d}{d}}\,\right] \ . \tag{23}$$

Substituting the system impedances for the vircator magnet ($R = 1.8\ \Omega$, $L = 0.7$ mH, $C = 366\ \mu F$, charge voltage $V_0 = 4$ kV) yields $t_0 = 575\ \mu sec$ and $I_{max} = 1.381$ kA. The series resistor in this circuit is a copper sulfate based liquid type with the capacity to dissipate 20 kJ with less than a 20°C temperature increase. The resistance value is determined by a piston type plunger and was not accurately measured; the 1.8 Ω value used here was chosen to give good agreement with experiment. The magnetic field at the center of the magnet B_0 is linearly proportional to the series current I_0 according to (table II shows $B_0 = 60$ kG for $I_0 = 5.71$ kA):

$$B_0 = 10.51\ I_0(kA) \qquad kG. \tag{24}$$

Thus, for 4 kV charge voltage, the calculated field is 14.51 kG, and the risetime 575 μsec. These values are in good agreement with the measured values of 14.62 kG and 570 μsec, indicating the magnet operation is well characterized by a strongly damped series RLC circuit.

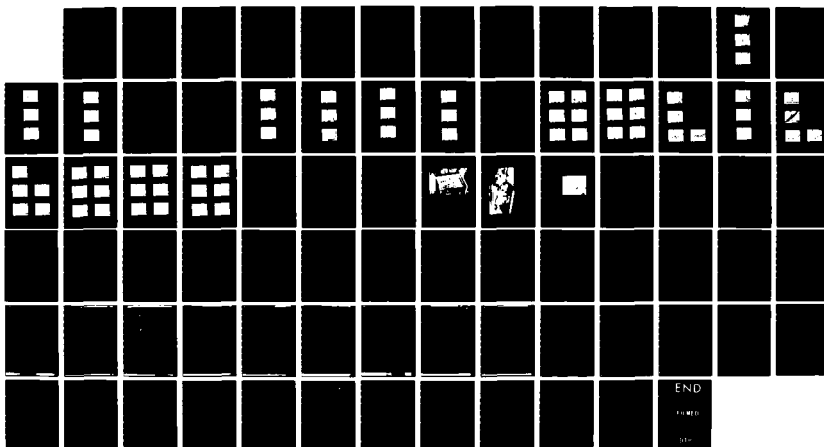AD-A159 394   MILLIMETER WAVE VIRCATOR(U) MISSION RESEARCH CORP
                ALBUQUERQUE NM   D J SULLIVAN ET AL. JUN 85 AMRC-R-692
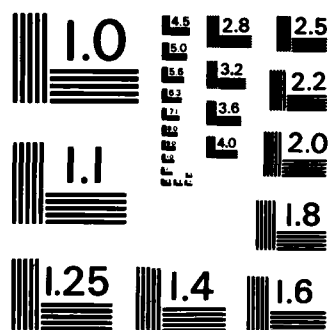   AFOSR-TR-85-0666 F49620-82-C-0014   3/3

UNCLASSIFIED   F/G 9/1   NL

END
FILMED

MICROCOPY RESOLUTION TEST CHART

NATIONAL BUREAU OF STANDARDS-1963-A

SECTION III
CALIBRATION OF THE 35-110 GHz VIRCATOR SPECTROMETER

A useful device for characterizing the intensity and wavelength of electromagnetic radiation is the spectrometer. Although Fabry-Perot interferometry and Fourier transform spectroscopy are commonly used in the UV, visible, and IR regions of the spectrum, diffraction grating spectroscopy carries over conveniently to microwave frequencies. The fast response of crystal detectors which can easily be coupled to a microwave grating spectrometer makes this a good choice for monitoring radiation from pulsed sources. A grating spectrometer specifically designed to monitor millimeter waves has been fabricated. The design philosophy has been previously described.[10,11] Spectrometer calibration is described here.

The main tool used in calibrating the vircator spectrometer is a Micro-Now Model #705B millimeter wave sweeper system with appropriate heads for B-band (35-50 GHz), V-band (50-75 GHz), and W-band (75-110 GHz) frequencies. The manufacturer provided calibration curves in frequency and power for each head are given in Figures 16-18. The sweeper system was lent to MRC by Dan Hunt of White Sands Missile Range Office OMEW/P2. His assistance has been invaluable. Each of the three millimeter bands covered by the spectrometer has its own set of detectors, 3 each for B and V-bands, and 6 for W-band. Type 1N53 crystal detectors have been chosen for all 3 bands, due to their low cost and good availability. The crystal housings are Baytron #4-22-200 for B band, Baytron #4-15-2000 for V band, and Baytron #4-10-200 for W band. Each channel also has its own pair of gratings which have been optimized for use at that particular wavelength window. The spectrometer operates in only one band at a time with only one set of detectors being used at a time. In each band a nominal 25 dB standard gain horn is used as the input to the spectrometer in order to increase the signal. Calibration curves for the horns in each band are presented in Figures 19-21. Calibration of each band for frequency response and sensitivity is carried out separately.
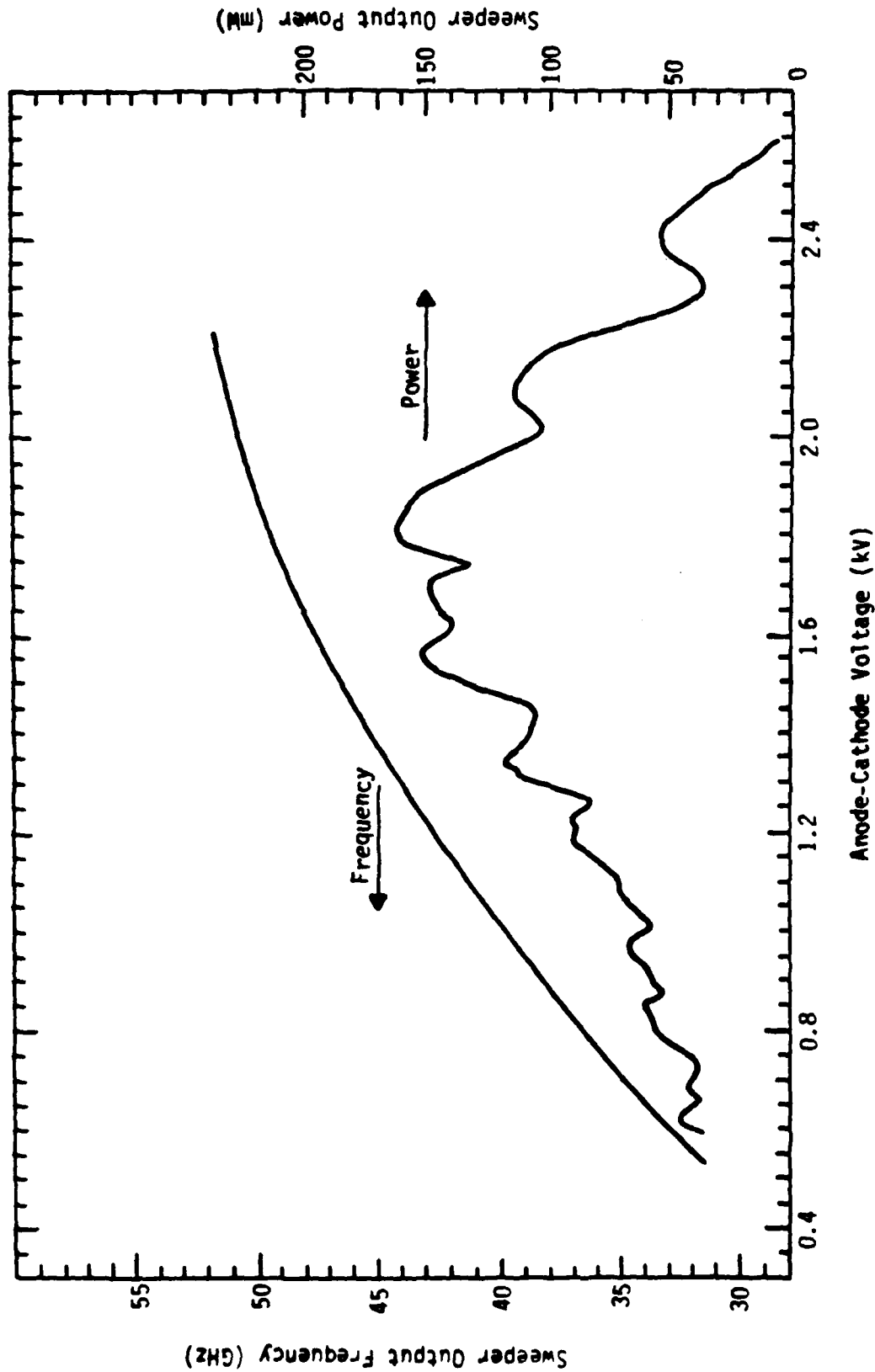
39

Figure 16. Manufacturer provided calibration curve of B-band sweeper power and frequency output as a function of oscillator head anode-cathode voltage (Micro-Now Model #705B mainframe and Model #729 BWO head). The sweeper drives the spectrometer and oscilloscope in the configuration of Figures 22 and 23 to produce the calibration data shown in Figures 24 through 35.
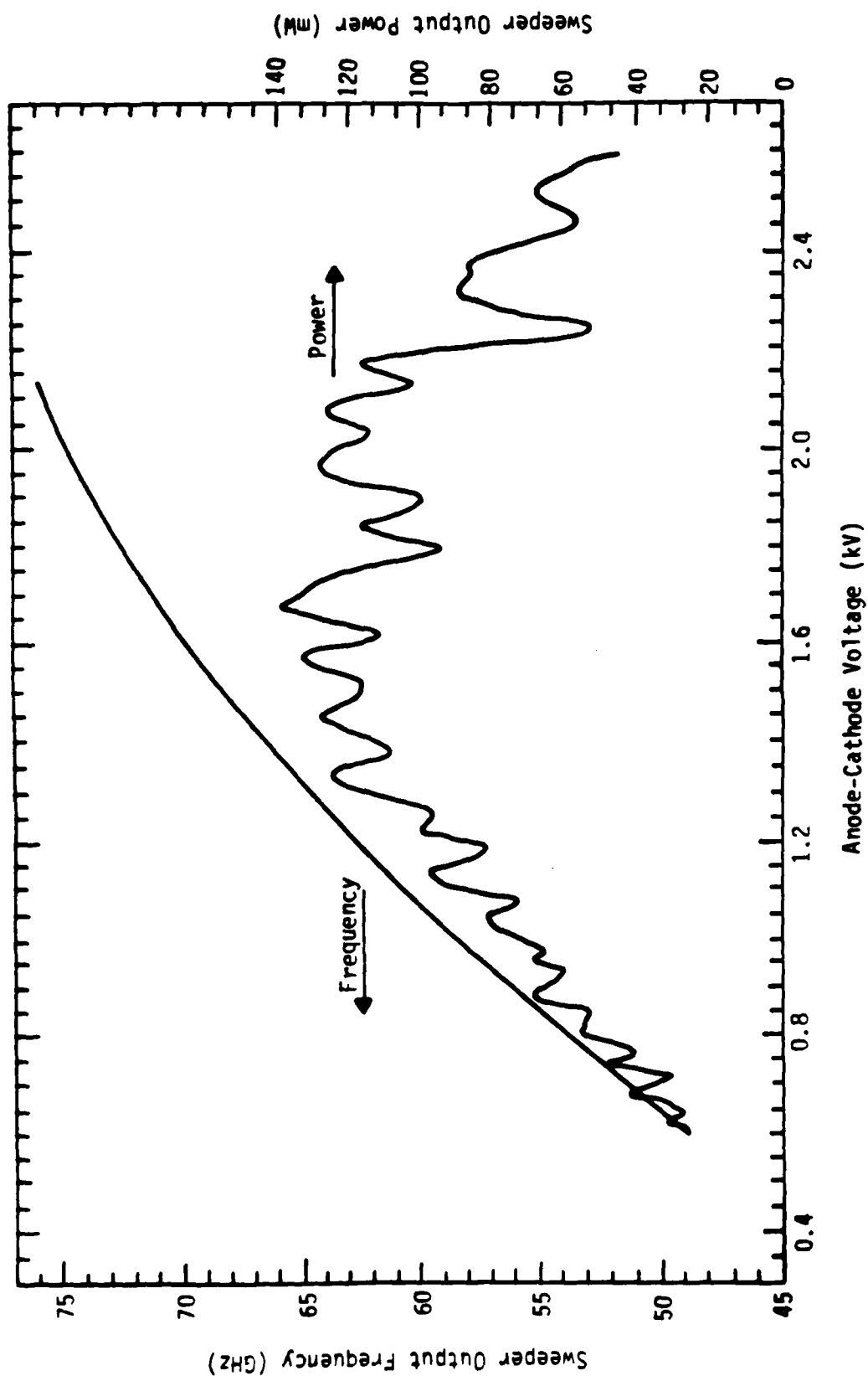
Figure 17. Manufacturer provided calibration curve of V-band sweeper power and frequency output as a function of oscillator head anode-cathode voltage (Micro-Now Model #705B mainframe and Model #725 BWO head).
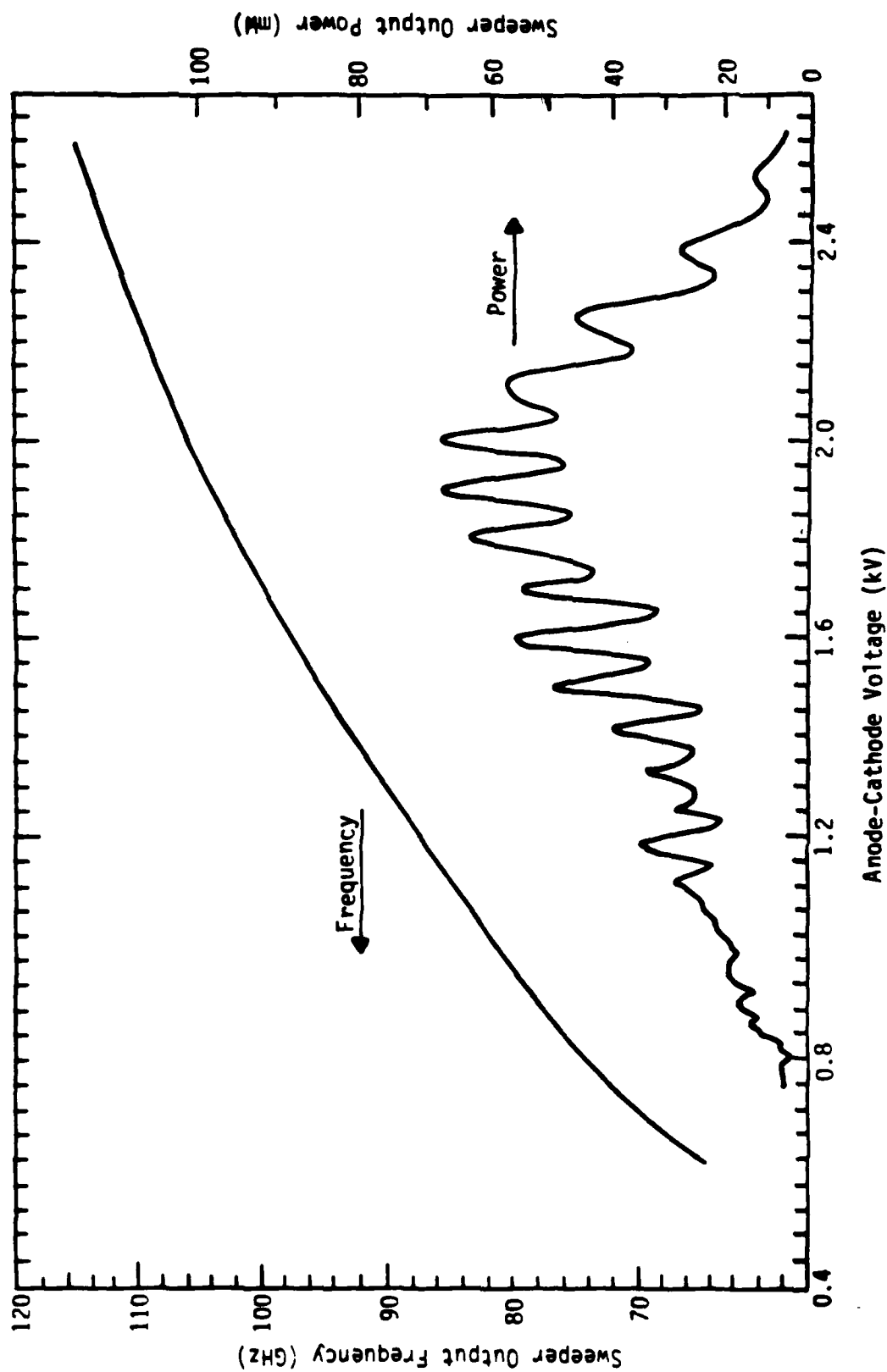
Figure 18. Manufacturer provided calibration curve of W-band sweeper power and frequency output as a function of oscillator head anode-cathode voltage (Micro-Now Model #705B mainframe and Model #728 BWO head).
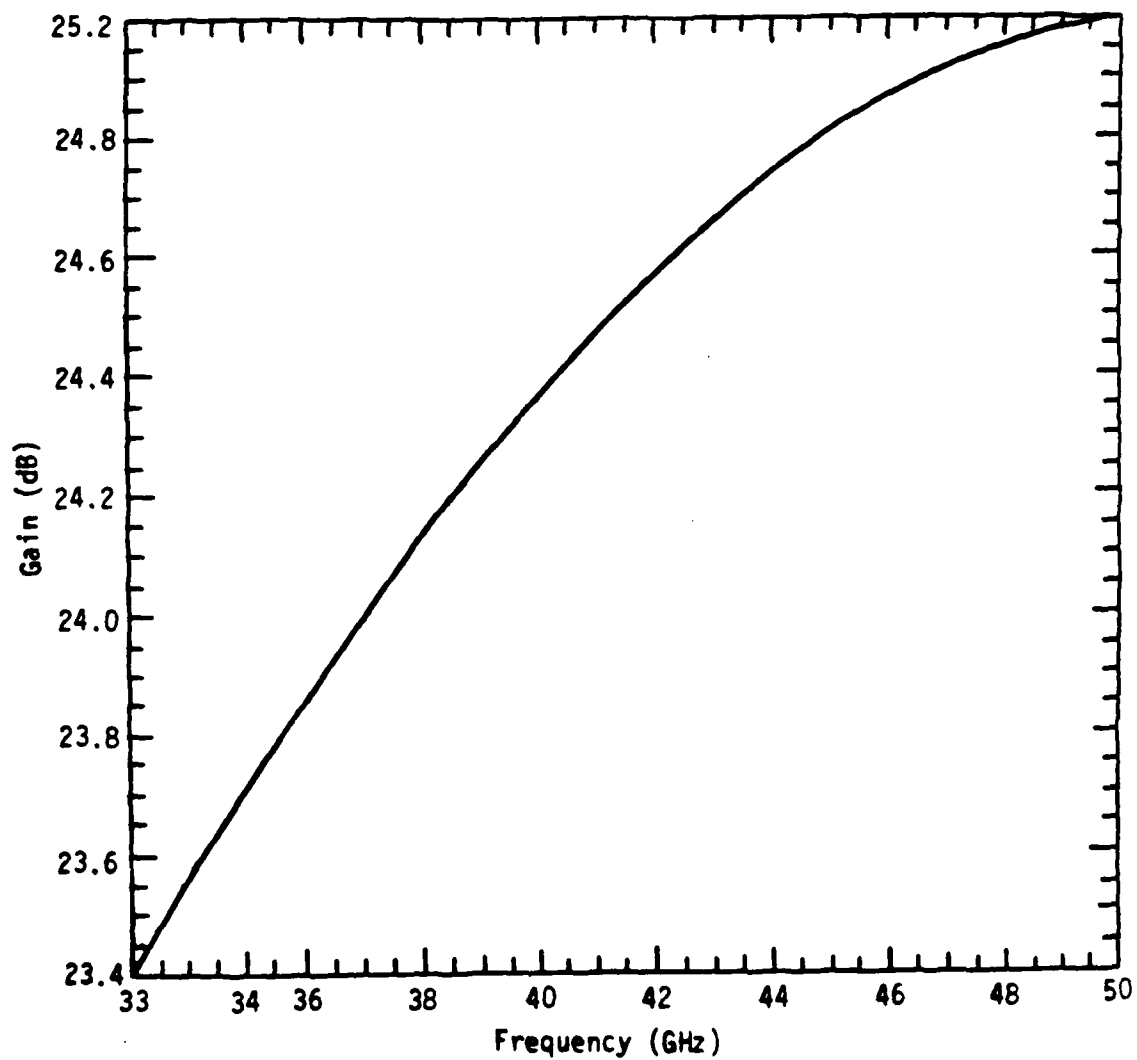
42

Figure 19.   Manufacturer provided calibration curve for the B-band
             (35-50 GHz) 25 dB standard gain horn used in spectrometer
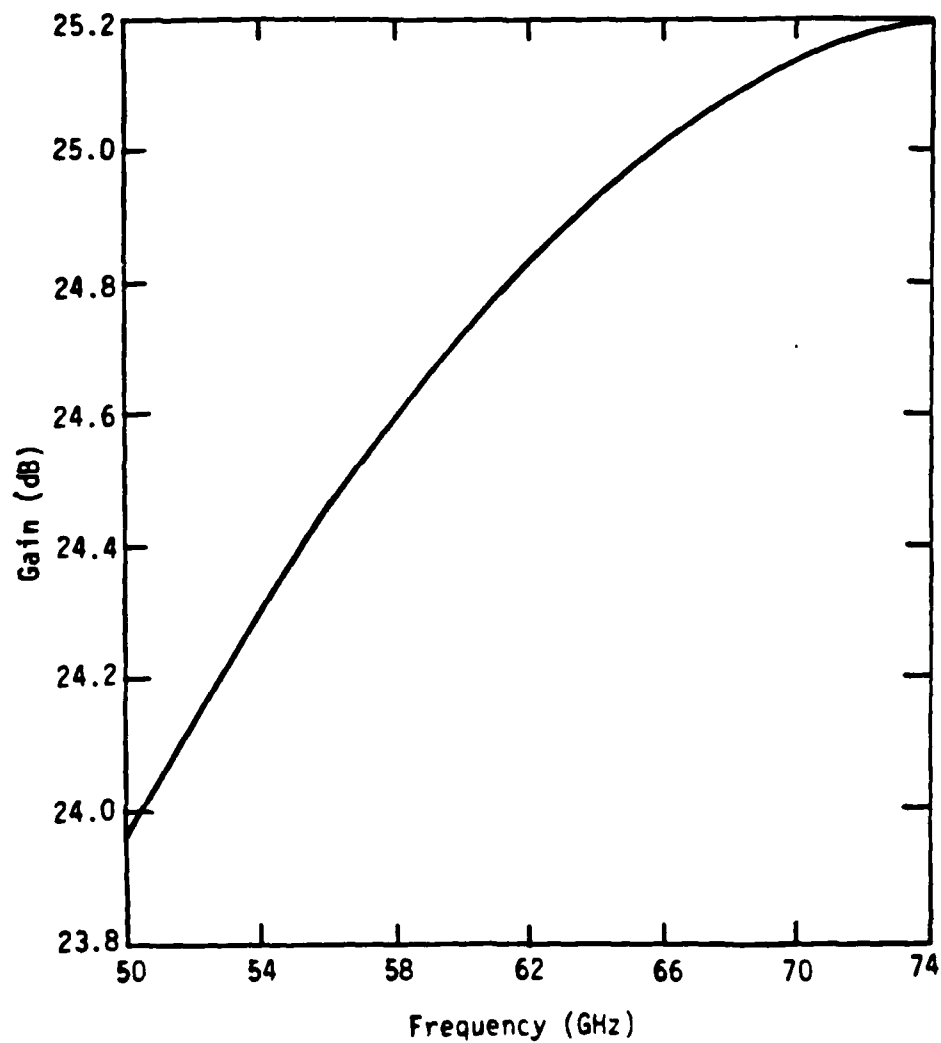   calibration (TRG Model #B861).

Figure 20.   Manufacturer provided calibration curve for the V-band
(50-75 GHz) 25 dB standard gain horn used in spectrometer
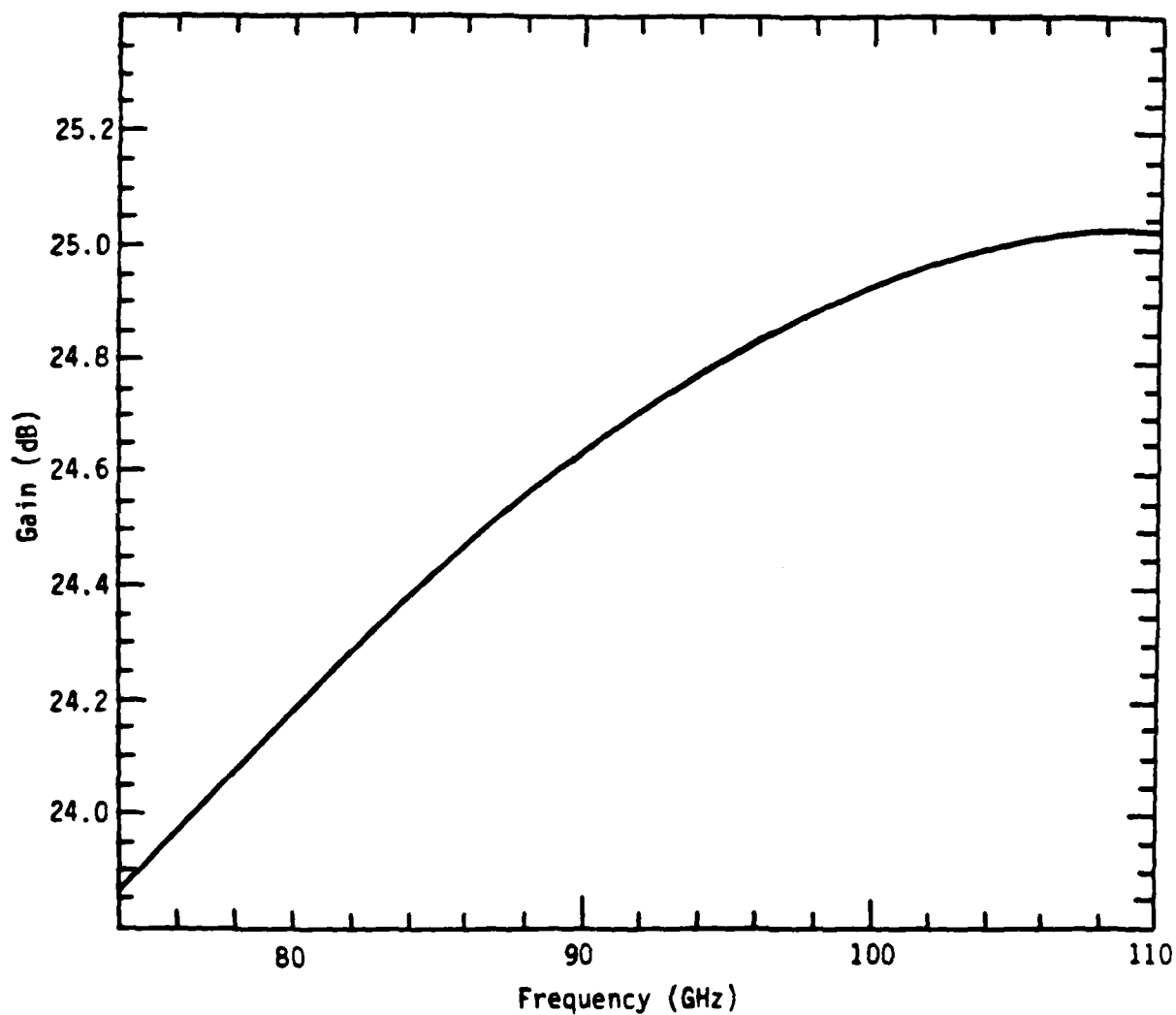calibration (TRG Model #V861).

Figure 21. Manufacturer provided calibration curve for the W-band (75-110 GHz) 25 dB standard gain horn used in spectrometer calibration (TRG Model #W861).

Two calibrations were performed for each band. The flatness of the frequency response of each of the three (or six) detectors is measured using the apparatus shown in Figure 22. Two series 10 or 15 dB couplers are used to attenuate the nominal 100 mW sweeper output to levels which will not overdrive the crystal. As shown in the figure, the sweeper provides a ramp signal to the oscilloscope which varies linearly in time corresponding to the linear time variation of the output frequency. The scope photo then records the frequency response of the crystal, uncorrected for variations in the sweeper output power.

Next the array of detectors is positioned inside the spectrometer so that each samples a different frequency bin. In this configuration shown in Figure 23, the sweeper drives the spectrometer directly, since the spectrometer itself is very lossy, of order 35 dB. In order to increase the signal to a measurable level, a 25 dB standard gain horn is attached to the waveguide entrance flange which feeds each of the crystals. The calibration curves for these horns are shown in Figures 19, 20, and 21 for B, V, and W-band, respectively. Power variation in the sweeper output as a function of frequency is shown in Figures 16, 17, and 18 for B, V, and W-band, respectively. To the extent that the detector crystal response is linear with input power, these curves and the following data allow an absolute power calibration of the spectrometer frequency response.

Raw data for the three B-band detectors' frequency response is shown in Figure 24. In order to determine the actual crystal sensitivity as a function of frequency, this raw data should be divided point-by-point by the sweeper power output as a function of frequency. The latter quantity is available from the plots of Figure 16. Note that this process also involves an assumption that the crystal voltage output is linear in the power input, i.e., the crystal is operating in the square law regime. Since the extensive tests required to verify square law operation over the entire frequency band have not been done, the tedious point-by-point division has not been carried out. Noting that the input power does not vary by more than a factor of 2, some broad conclusions can still be drawn from
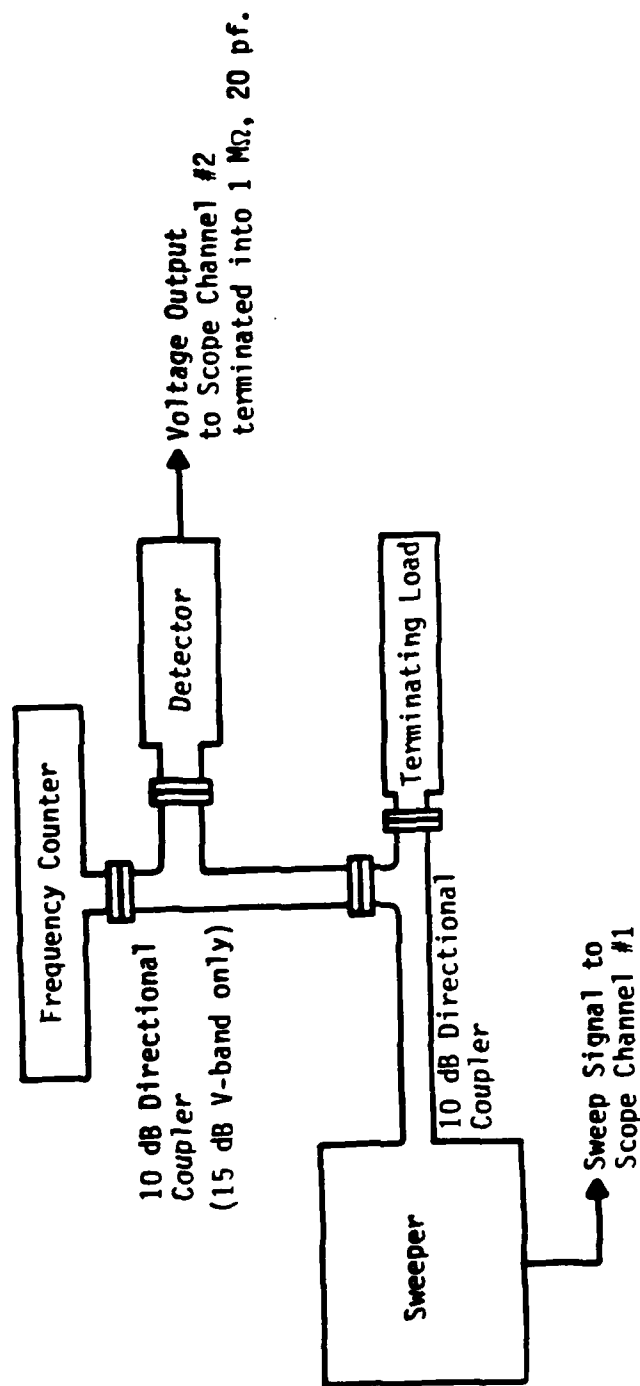
Figure 22. Schematic of the apparatus used in detector calibration. Two directional couplers are configured in series to reduce the sweeper output signal to the mW level which can be tolerated by the detectors.
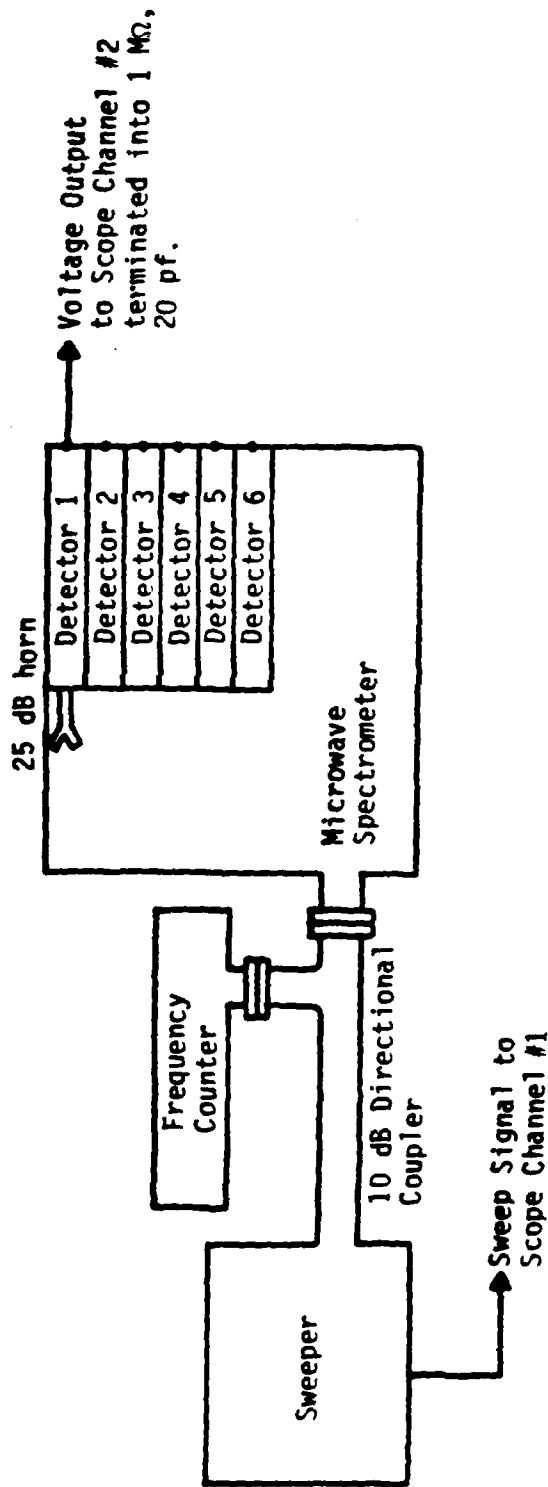
47

Figure 23. Schematic of the apparatus used to calibrate the frequency response of the six (three each in B and V-band and six in W-band) spectrometer channels. The 25 dB horn is inserted during the calibration to increase the signal to a measurable level.
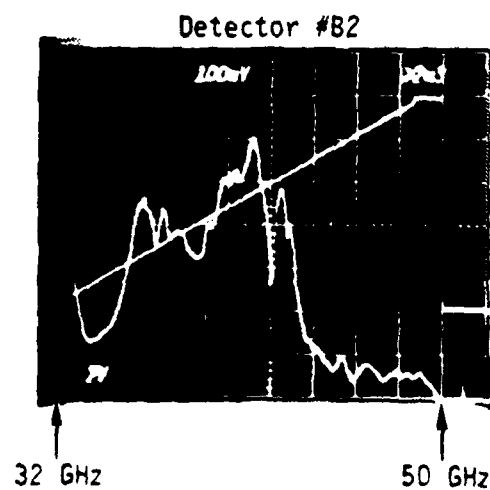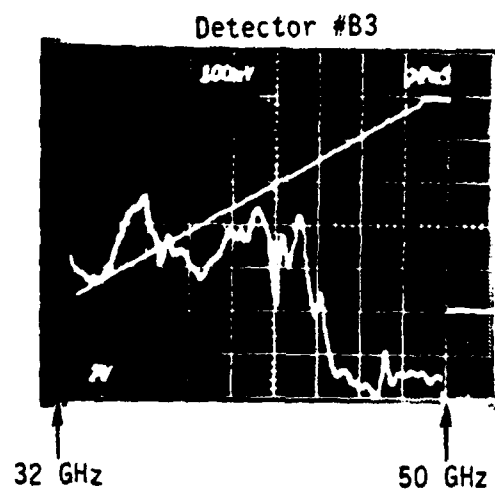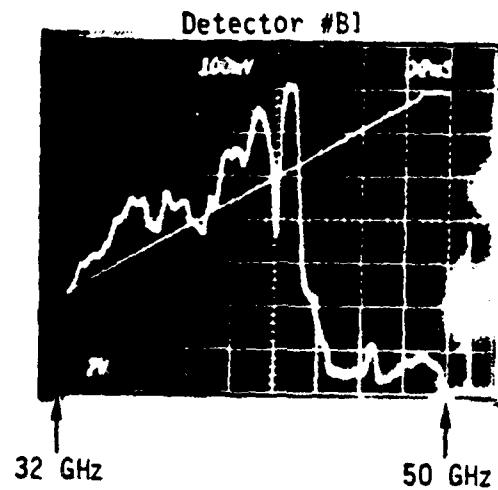
Figure 24. Detector calibration data for the three B-band detectors, taken using the apparatus of Figure 22.

the raw data. First, detector response is down considerably at high frequencies, dropping by the order of one decade above 44 GHz. Second, response is fairly flat, within a factor of 2, in the 32 to 44 GHz frequency bin. The fine structure in the raw data is due to resonances in the detector housing and some inherent non-linearity in the crystal response. Superior quality detectors can be purchased at a premium price for future work, if it becomes necessary to provide flatter response over the entire band.

Next, detectors B1, B3 and B2 were installed in the spectrometer at stations 15.5, 8.0, and 3.0 inches, respectively, and the spectrometer driven with the sweeper in the configuration of Figure 23. Data was taken with the grating angle at 42 degrees and 48 degrees, as shown in Figures 25 and 26. The grating angle determines the acceptance frequency of each detector through the optics criteria described in References 10 and 11.

A summary of the B-band calibration data is presented in Table III for the 42 degree and 48 degree grating angles tested. The center frequency for peak sensitivity and the peak output voltage are listed for each detector. Note that the FWHM response is approximately 2 GHz, yielding a $\Delta f/f_0$ parameter of order 0.06. A figure of merit parameter has been calculated by dividing the output voltage by the sweeper output power, taking into account the frequency dependence of the horn gain and the loss due to the 10 dB coupler preceding the spectrometer. To the extent that the crystal output is linear with input power, the figure of merit is an absolute calibration of the spectrometer sensitivity for that particular detector, frequency, and grating angle. Table III shows that the figure of merit varies by nearly two decades from one frequency bin to another. This is just a reflection of the poor flatness in the frequency response of the individual crystals and can be rectified by purchasing better housings and better crystals.
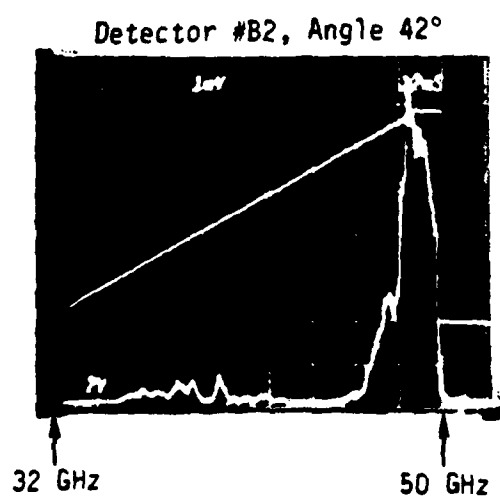
Detector #B1, Angle 42°

32 GHz   50 GHz

Detector #B3, Angle 42°

32 GHz   50 GHz

Detector #B2, Angle 42°

32 GHz   50 GHz

Figure 25.   Spectrometer calibration data for the three B-band detectors
(detector B1 at 15.5 inch, B3 at 8.0 inch, and B2 at 3.0 inch)
taken at a 42 degree grating angle, using the configuration
of Figure 23.

Detector #B1, Angle 48°

32 GHz   50 GHz

Detector #B3, Angle 48°

32 GHz   50 GHz
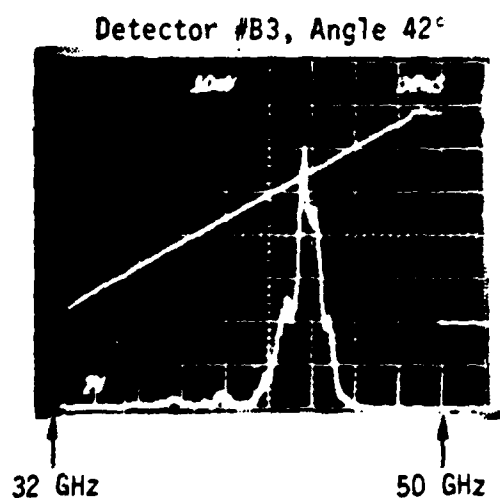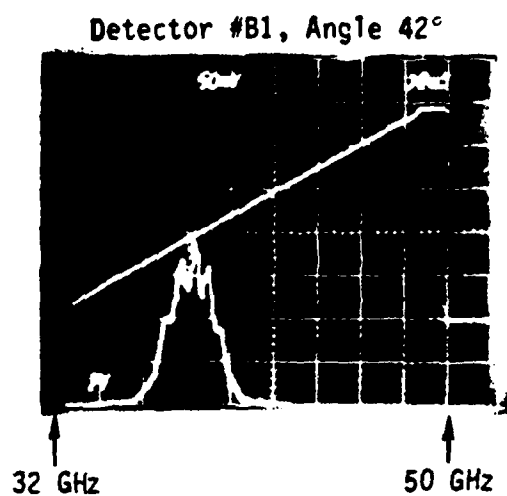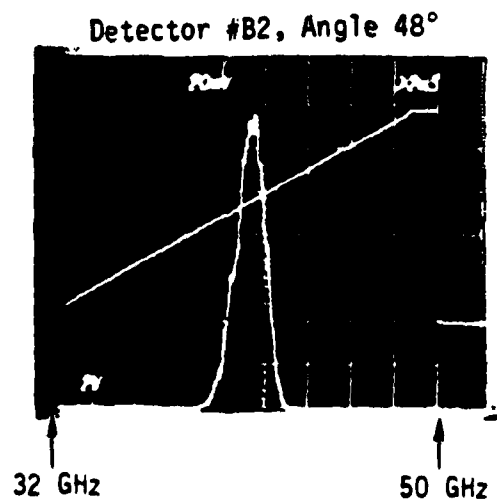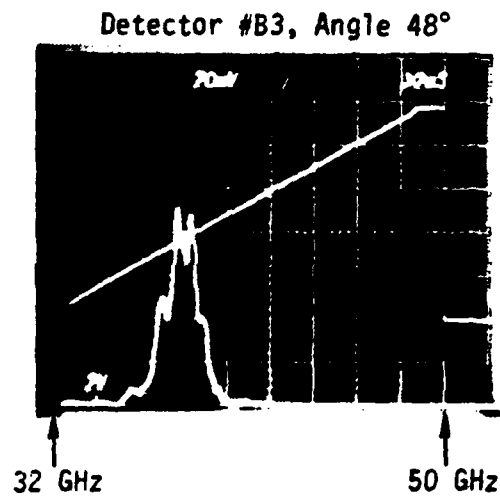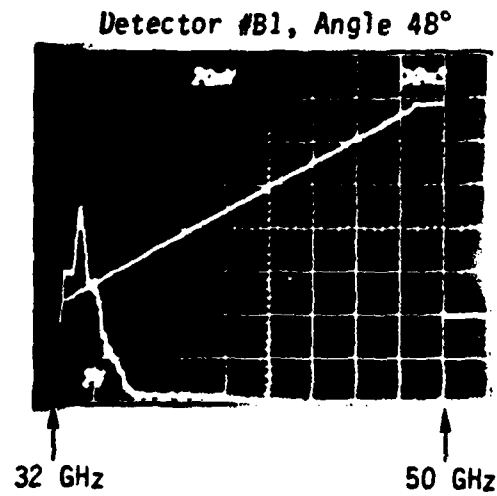
Detector #B2, Angle 48°

32 GHz   50 GHz

Figure 26.   Spectrometer calibration data for the three B-band detectors (detector B1 at 15.5 inch, B3 at 8.0 inch, and B2 at 3.0 inch taken at a 48 degree grating angle.

TABLE III. SUMMARY OF SPECTROMETER B-BAND (32-50 GHz) CALIBRATION DATA

PARAMETER	Detector #B1	Detector #B3	Detector #B2
Detector Position (inches)	15.5	8.0	3.0
For 42° Grating Angle:			
Center Frequency for Peak Sensitivity (GHz)	38.4	43.8	48.8
Output Voltage (mV)	180	59	6.2
Horn Gain (db)	24.2	24.7	25.0
Input Power (mW)	60	96	145
Calculated Figure of Merit (Volts/Watt)	1.27×10^{-2}	2.31×10^{-3}	1.50×10^{-4}
For 48° Grating Angle:			
Center Frequency for Peak Sensitivity (GHz)	33.2	38.0	41.4
Output Voltage (mV)	89	89	134
Horn Gain (db)	23.4	24.1	24.5
Input Power (mW)	43	57	70
Calculated Figure of Merit (Volts/Watt)	1.05×10^{-2}	6.75×10^{-3}	7.55×10^{-3}

Calibration of the V-band response of the detectors and spectrometer
was carried out analagously to the B-band calibration data. Figure 27
shows the response of the three individual crystals and Figures 28, 29, and
30 show the spectrometer response for 44, 46, and 49 degree grating angles,
respectively. Peak frequency response and figure of merit numbers are sum-
marized in Table IV. Note that the separate detector responses are far
from flat, typically varying by the order of one decade between peaks and
valleys. This is the main culprit in the factor of 40 variation in the
sensitivity of the various frequency bins. The data shows typical FWHM of
the frequency response is about 2 GHz, yielding a $\Delta f/f_o$ parameter of
approximately 0.04.

Calibration of the W-band detectors was carried out in a similar man-
ner to the B and V-bands, but was complicated by the extremely hashy and
non-uniform frequency response of these crystals and their housings. The
data of Figures 31A and 31B shows a variation of more than two decades in
the raw frequency response data over the 75-110 GHz frequency band for
several of the 6 detectors. Calibration data for the W-band spectrometer
configuration is shown in Figures 32 through 35, with a data summary in
Table V. Frequency response FWHM is typically 2 GHz, yielding a $\Delta f/f_o$
parameter of order 0.027. The figure of merit parameter continues to show
large variation, roughly two decades, over the frequency band. Thus, the
frequency selectivity of this spectrometer is good although it displays
wide variation in power sensitivity. The latter undesirable characteristic
can be corrected in future work by installing crystals with flatter fre-
quency response in housings with weaker resonance characteristics. How-
ever, in its present form and with the calibration data presented here, the
spectrometer is a unique diagnostic for characterizing the time dependence,
power and spectral content of pulsed, millimeter wavelength microwave
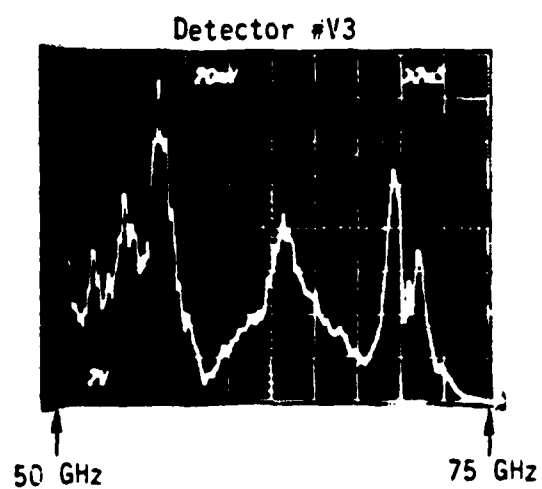sources.

Detector #V1

50 GHz   75 GHz

Detector #V2

50 GHz   75 GHz

Detector #V3

50 GHz   75 GHz

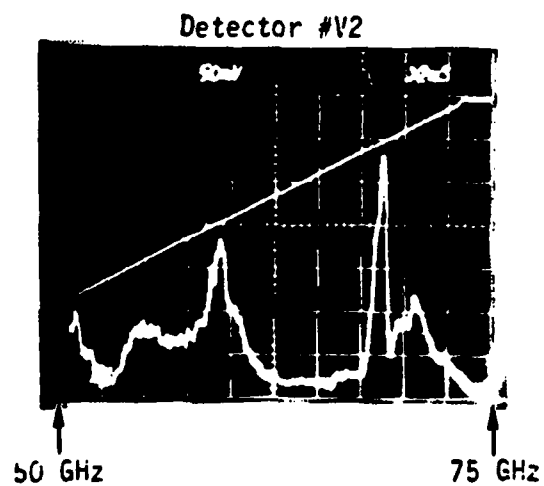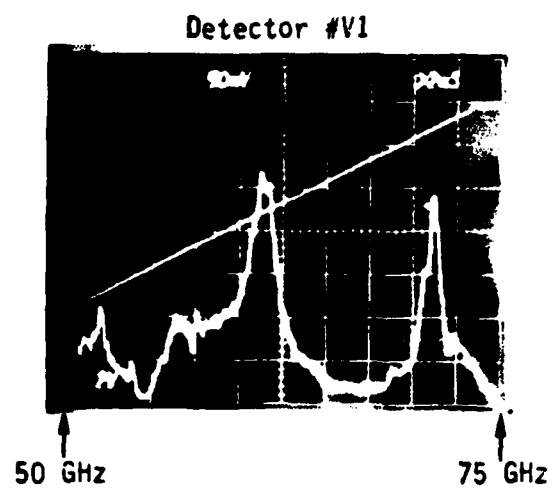Figure 27.   Detector calibration data for the three V-band detectors,
             taken using the apparatus of Figure 22.

55

Detector #V1, Angle 44°

50 GHz   75 GHz

Detector #V2, Angle 44°

50 GHz   75 GHz

Detector #V3, Angle 44°

50 GHz   75 GHz

Figure 28.   Spectrometer calibration data for the three V-band detectors
(detector V1 at 15.5 inch, V2 at 8.0 inch, and V3 at 3.0 inch
taken at a 44 degree grating angle, using the configuration
of Figure 23.

56

Detector #V1, Angle 46°

50 GHz   75 GHz

Detector #V2, Angle 46°

50 GHz   75 GHz
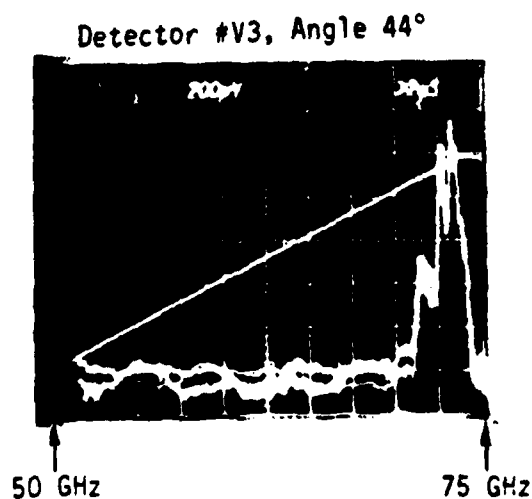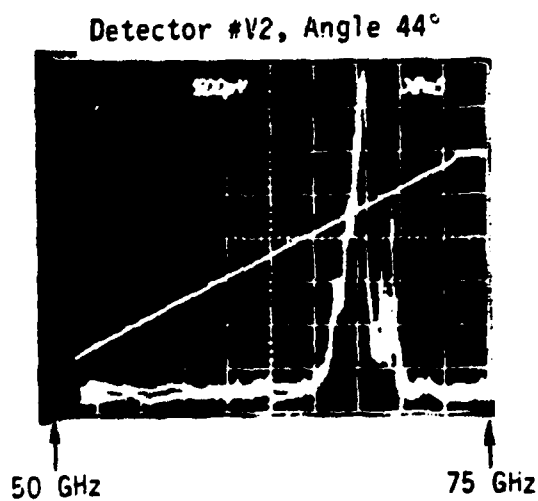
Detector #V3, Angle 46°

50 GHz   75 GHz

Figure 29.   Spectrometer calibration data for the three V-band detectors (detector V1 at 15.5 inch, V2 at 8.0 inch, and V3 at 3.0 inch taken at a 46 degree grating angle.

57

Detector #V1, Angle 49°

50 GHz   75 GHz

Detector #V2, Angle 49°

50 GHz   75 GHz

Detector #V3, Angle 49°

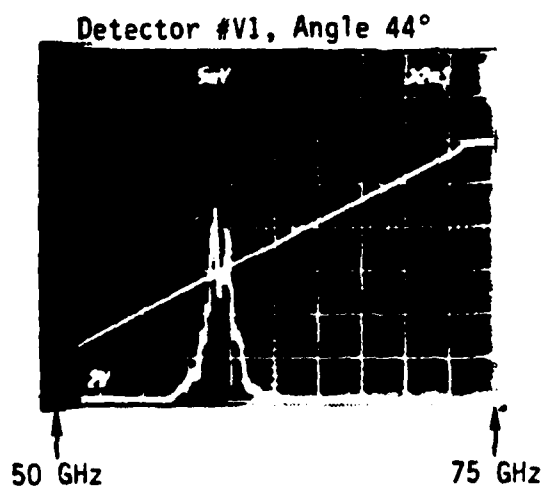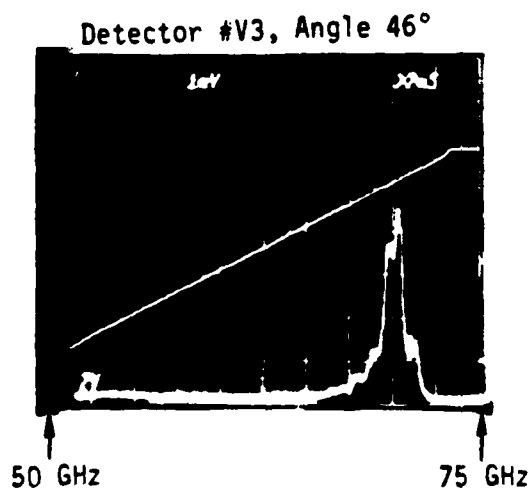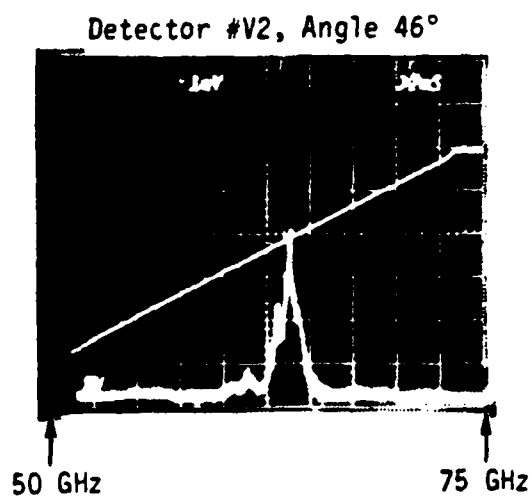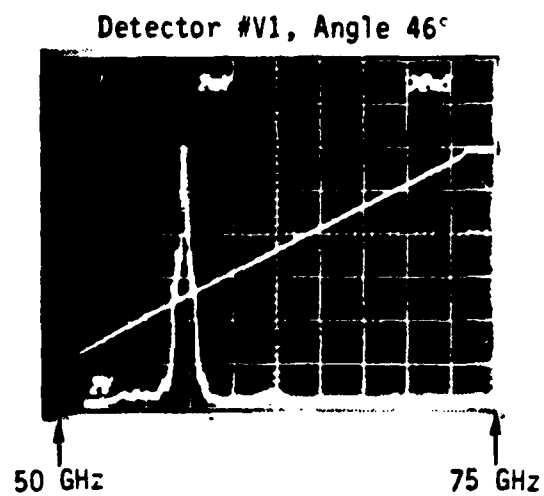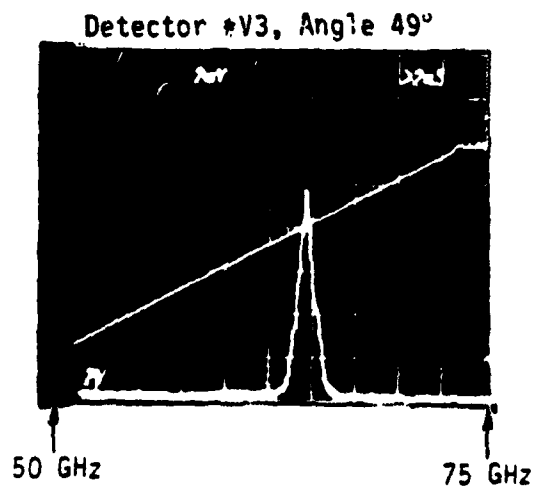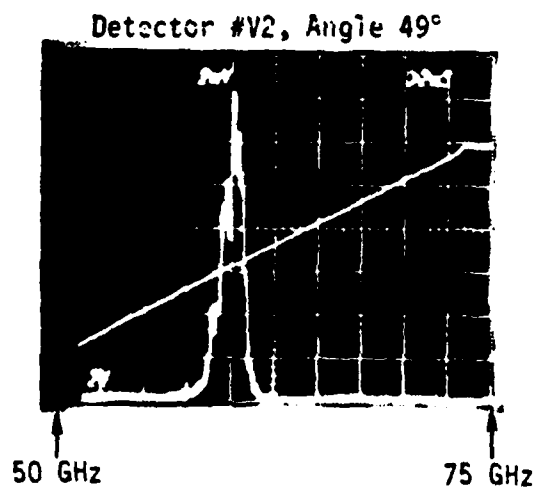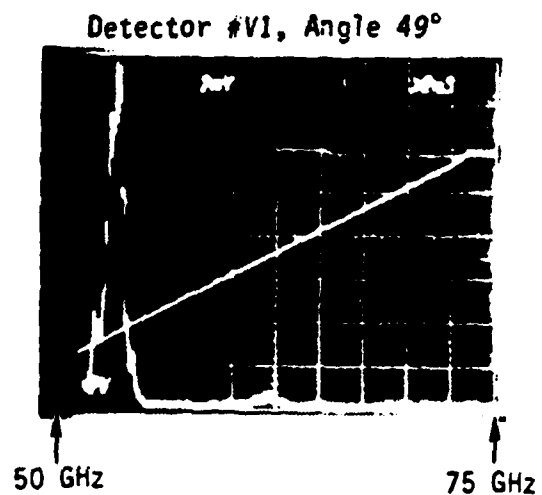50 GHz   75 GHz

Figure 30. Spectrometer calibration data for the three V-band detectors
(detector V1 at 15.5 inch, V2 at 8.0 inch, and V3 at 3.0 inch)
taken at a 49 degree grating angle.

TABLE IV. SUMMARY OF SPECTROMETER V-BAND (50-75 GHz) CALIBRATION DATA

	Detector #V1	Detector #V2	Detector #V3
Detector Position (inches)	15.5	8.0	3.0
For 44° Grating Angle: Center Frequency for Peak Sensitivity (GHz)	59.5	67.9	73.0
Output Voltage (mV)	20	3.5	1.2
Horn Gain (db)	24.8	25.1	25.2
Input Power (mW)	82	127	110
Figure of Merit (Volts/Watt)	8.97×10^{-4}	9.46×10^{-5}	3.05×10^{-5}
For 46° Grating Angle Center Frequency for Peak Sensitivity (GHz)	57.1	63.8	70.2
Output Voltage (mV)	11.5	3.8	4.3
Horn Gain (db)	24.5	24.9	25.1
Input Power (mW)	66	96	126
Figure of Merit (Volts/W)	6.87×10^{-4}	1.42×10^{-4}	1.17×10^{-4}
For 49° Grating Angle Center Frequency for Peak Sensitivity (GHz)	53.1	60.2	64.7
Output Voltage (mV)	15.8	13.8	9.6
Horn Gain (db)	24.2	24.7	25.0
Input Power (mW)	50	80	105
Figure of Merit (Volts/Watt)	1.33×10^{-3}	6.49×10^{-4}	3.21×10^{-4}

Detector #W1

Detector #W1, x10 gain

75 GHz   110 GHz

75 GHz   110 GHz

Detector #W2

Detector #W2, x5 gain

75 GHz   110 GHz

75 GHz   110 GHz

Detector #W3

Detector #W3, x4 gain

75 GHz   110 GHz

75 GHz   110 GHz
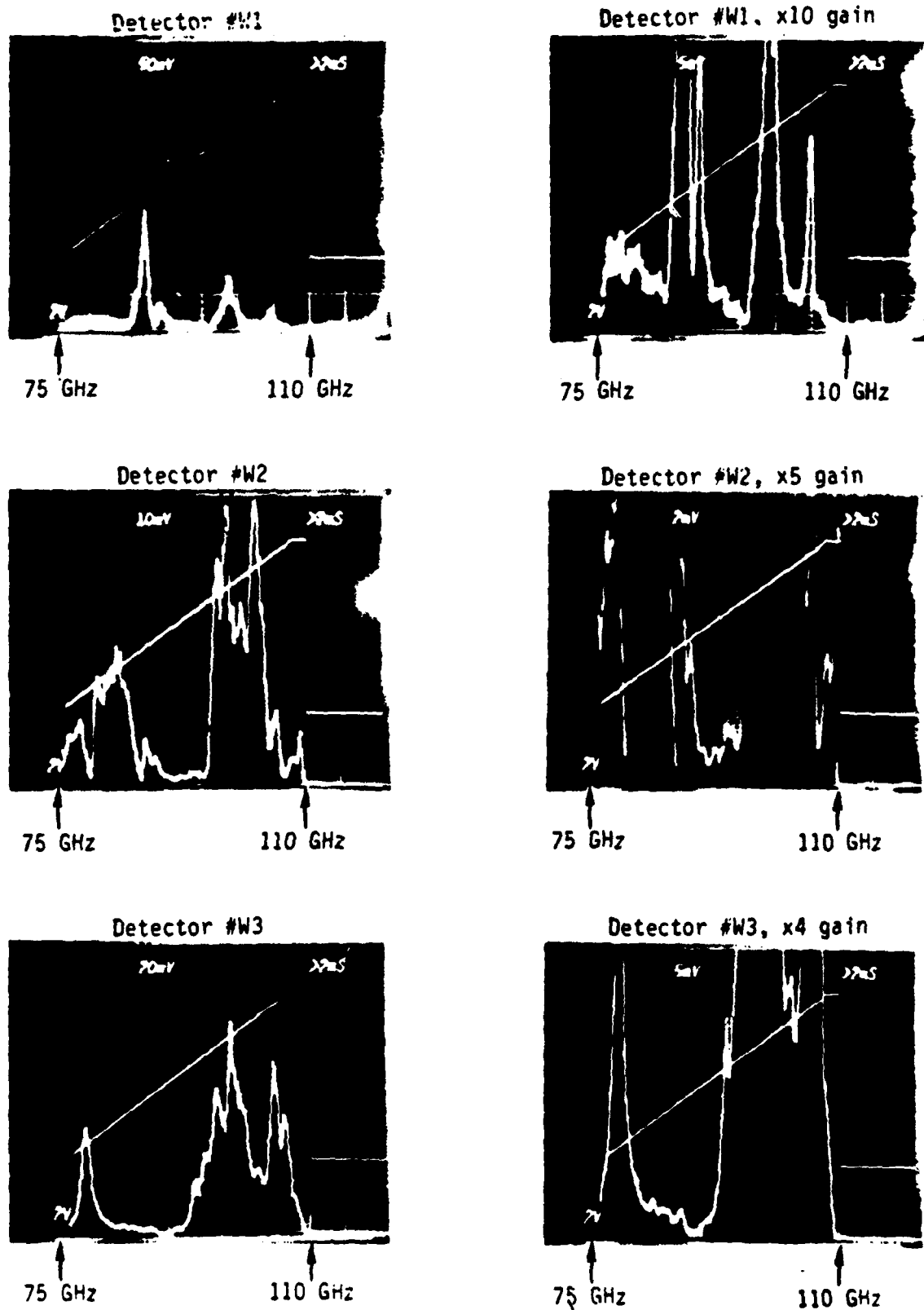
Figure 31A.   Detector calibration data for the first three W-band detectors
              W1, W2, and W3, taken using the apparatus of Figure 22. Data
              shown on the right is taken at several times the gain of the left,
              as is reflected in the labels on the scope photos.
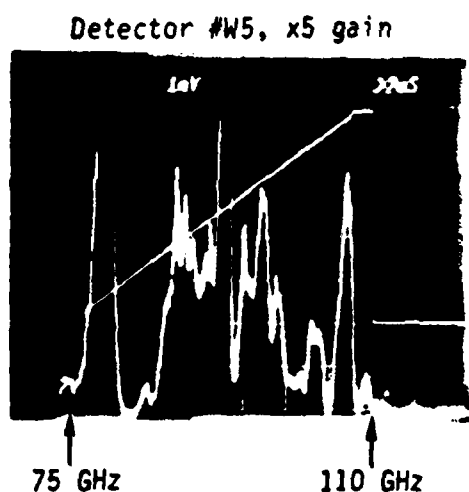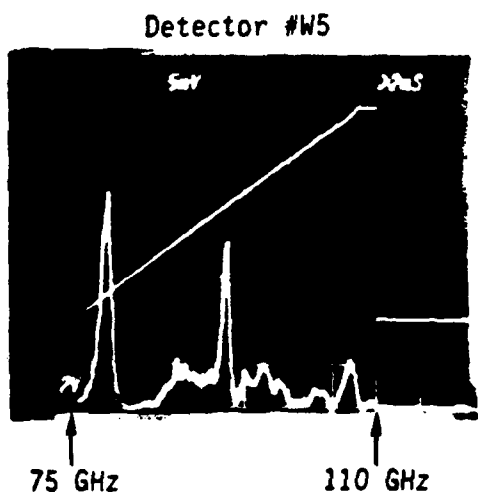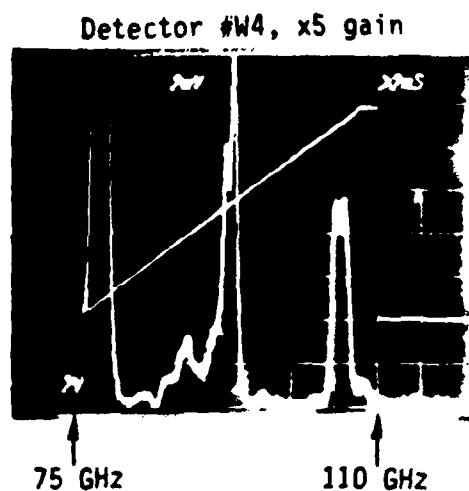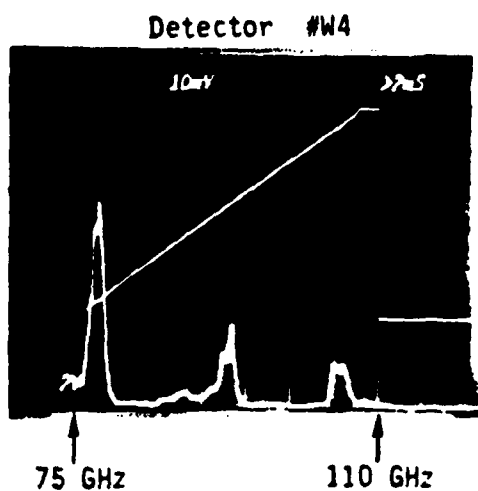
Figure 31B.   Detector calibration data for the last three W-band detectors, W4, W5, and W6, taken using the apparatus of Figure 22.   Data shown on the right is taken at several times the gain of the left, as is reflected in the labels on the scope photos.
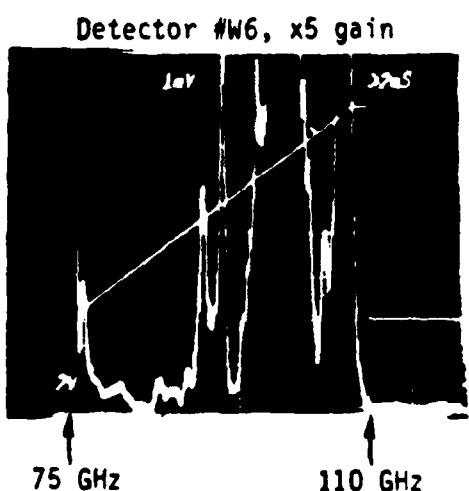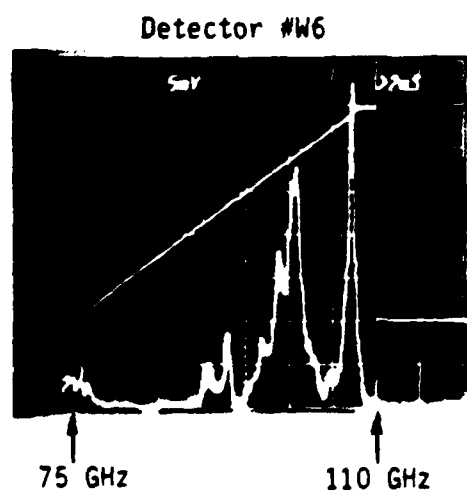
Detector #W2, Angle 44°

75 GHz   110 GHz

Detector #W3, Angle 44°

75 GHz   110 GHz

Detector #W6, Angle 44°

75 GHz   110 GHz

Detector #W6, Noise Only

75 GHz   110 GHz
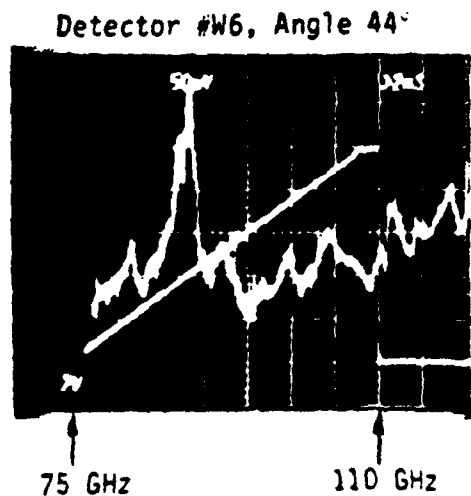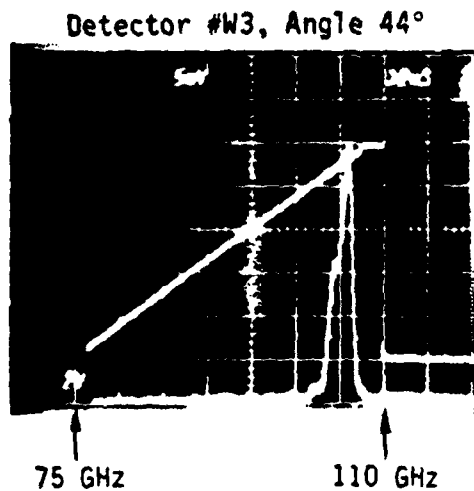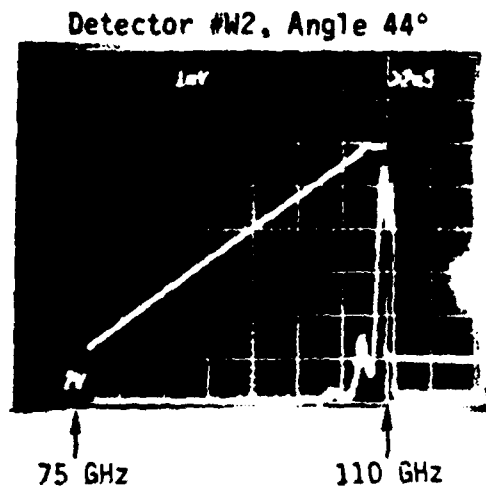
Figure 32. Spectrometer calibration data for the W-band detectors W2, W3, and
W6 (detector W2 at 5.5 inch, W3 at 8.0 inch, and W6 at 15.5 inch)
taken at a 44 degree grating angle, using the configuration of Figure 23.
Left photo is signal plus noise, right photo is noise only, taken with
microwave absorbing material covering the detector.

Detector #W1, Angle 46°

75 GHz   110 GHz

Detector #W2, Angle 46°

75 GHz   110 GHz

Detector #W3, Angle 46°

75 GHz   110 GHz

Figure 33A. Spectrometer calibration data for the W-band detectors W1-W6 (detectors W1-W6 located at 3.0, 5.5, 8.0, 10.2, 13.0, and 15.5 inch, respectively taken at a 46 degree grating angle.

Detector #W4, Angle 46°

75 GHz   110 GHz

Detector #W5, Angle 46°

75 GHz   110 GHz

Detector #W6, Angle 46°

75 GHz   110 GHz

Detector #W6, Noise Only

75 GHz   110 GHz

Figure 33B. Spectrometer calibration data for the W-band detectors W1-W6 (detectors W1-W6 located at 3.0, 5.5, 8.0, 10.2, 13.0, and 15.5 inch, respectively) taken at a 46 degree grating angle. Left photo is signal plus noise, right photo is noise only, taken with microwave absorbing material covering the detector.
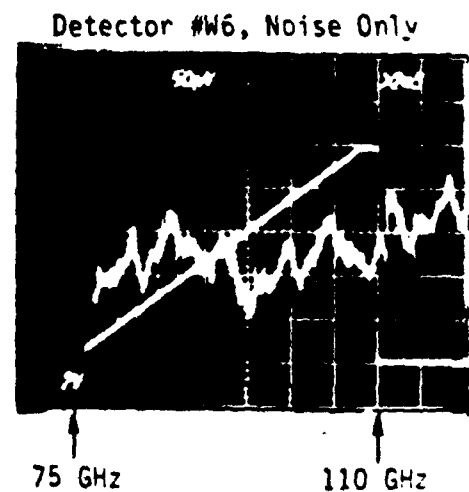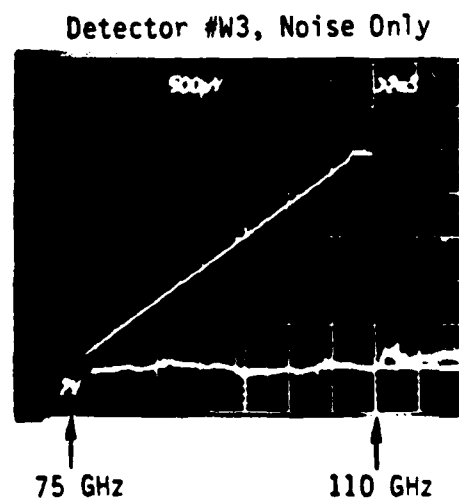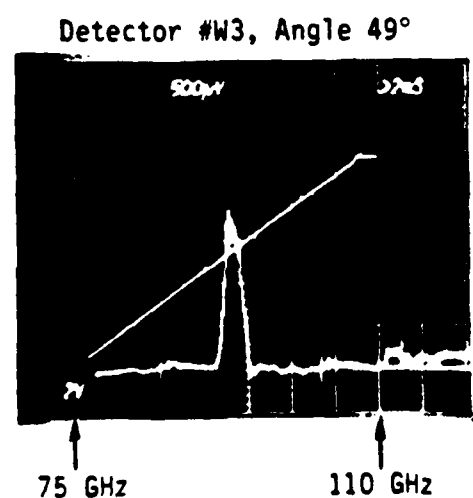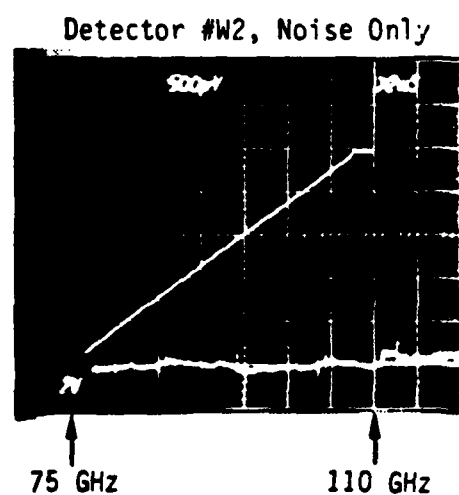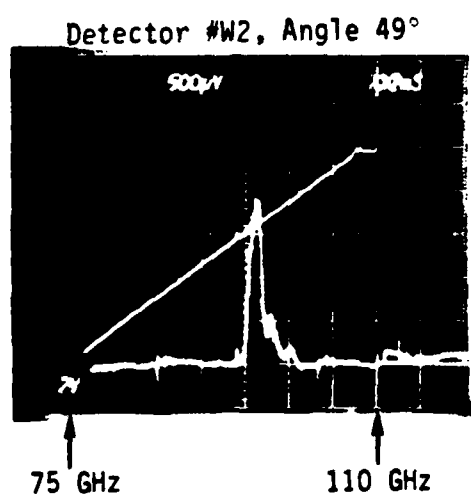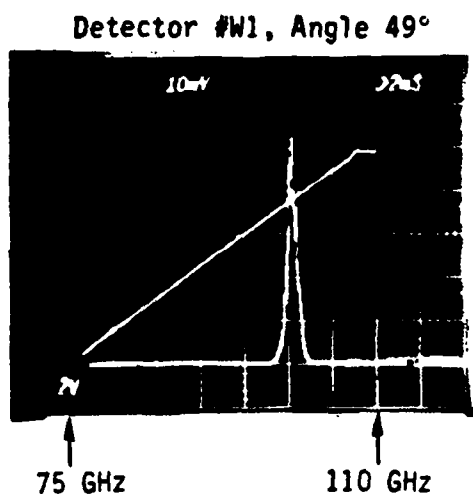
Figure 34A. Spectrometer calibration data for the W-band detectors W1-W6 (detectors W1-W6 located at 3.0, 5.5, 8.0, 10.2, 13.0, and 15.5 inch, respectively) taken at a 49 degree grating angle. Left photo is signal plus noise, right photo is noise only, taken with microwave absorbing material covering the detector.

65
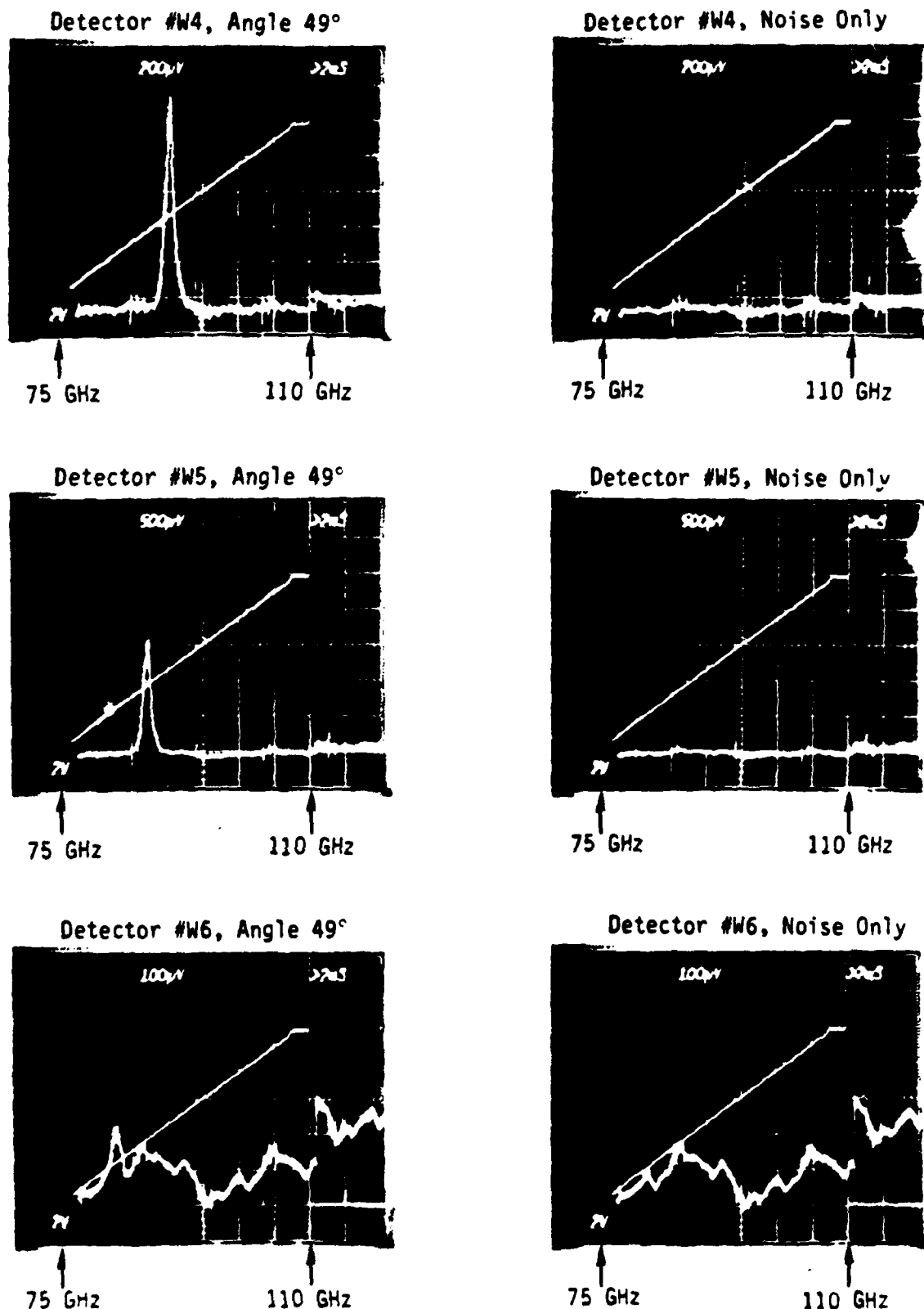
Figure 34B. Spectrometer calibration data for the W-band detectors W1-W6 (detectors W1-W6 located at 3.0, 5.5, 8.0, 10.2, 13.0, and 15.5 inch, respectively taken at a 49 degree grating angle. Left photo is signal plus noise, right photo is noise only, taken with microwave absorbing material covering the detector.

Detector #W1, Angle 51.5°

Detector #W1, Noise Only

75 GHz 110 GHz 75 GHz 110 GHz

Detector #W2, Angle 51.5°

Detector #W2, Noise Only

75 GHz 110 GHz 75 GHz 110 GHz

Detector #W3, Angle 51.5°

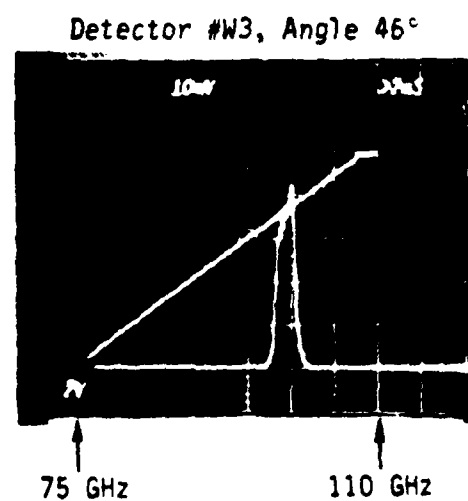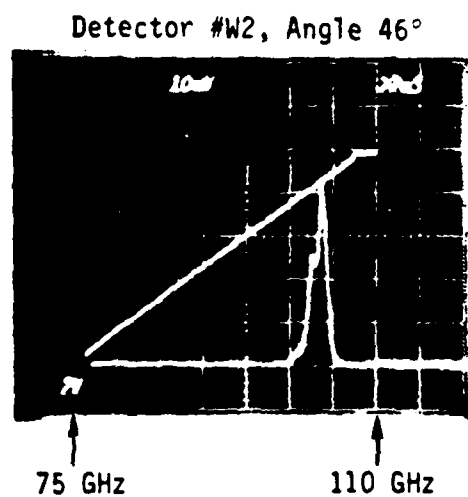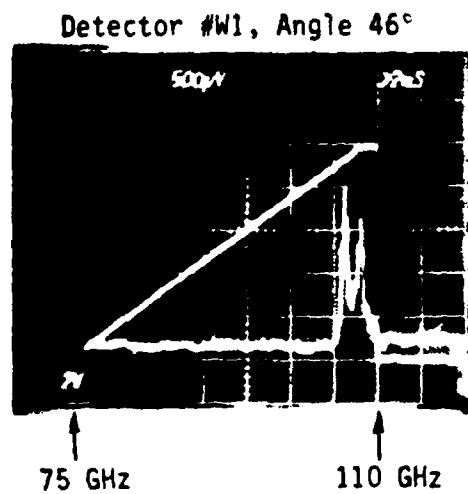**Detector #W3, Noise Only**

75 GHz 110 GHz 75 GHz 110 GHz
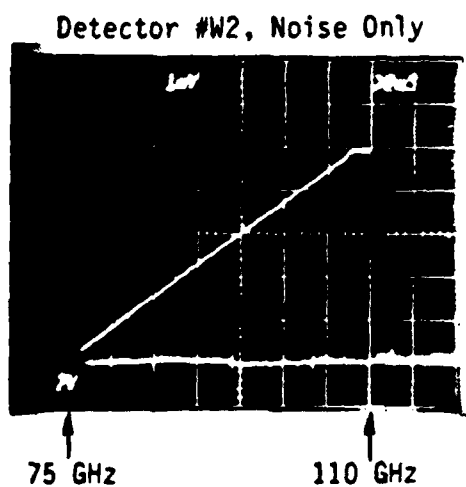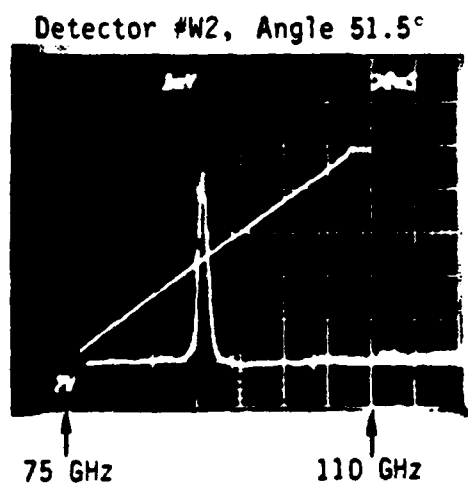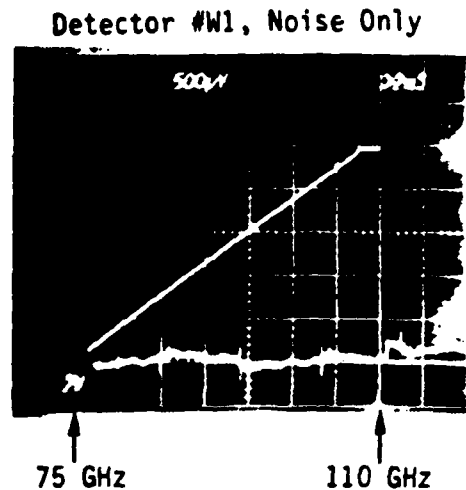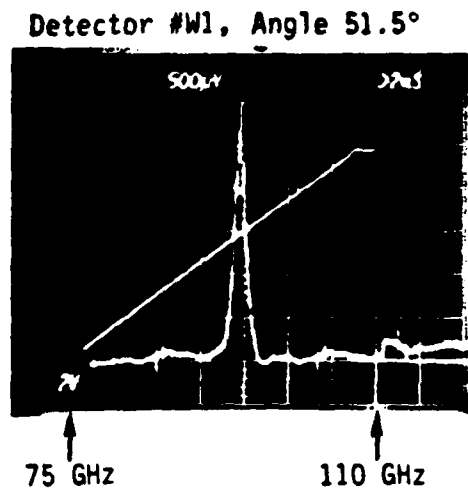
Figure 35A. Spectrometer calibration data for the W-band detectors W1-W6 (detectors W1-W6 located at 3.0, 5.5, 8.0, 10.2, 13.0, and 15.5 inch, respectively) taken at a 51.5 degree grating angle. Left photo is signal plus noise, right photo is noise only, taken with microwave absorbing material covering the detector.

67

Detector #W4, Angle 51.5° Detector #W4, Noise Only

Detector #W5, Angle 51.5° Detector #W5, Noise Only

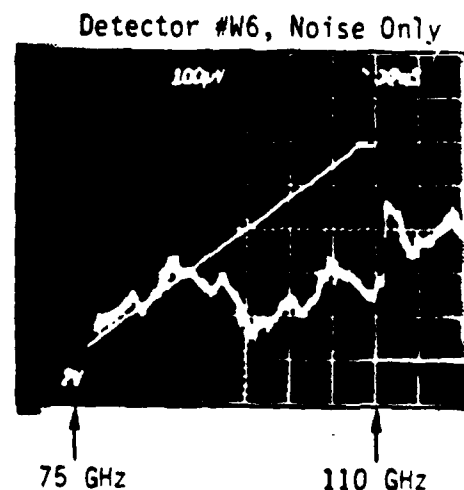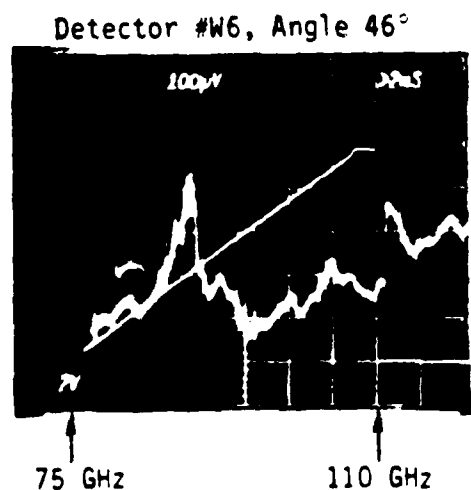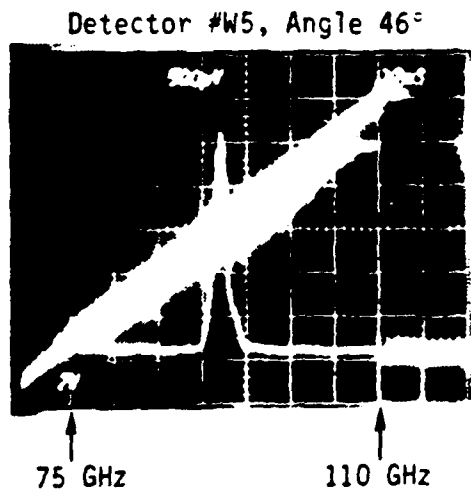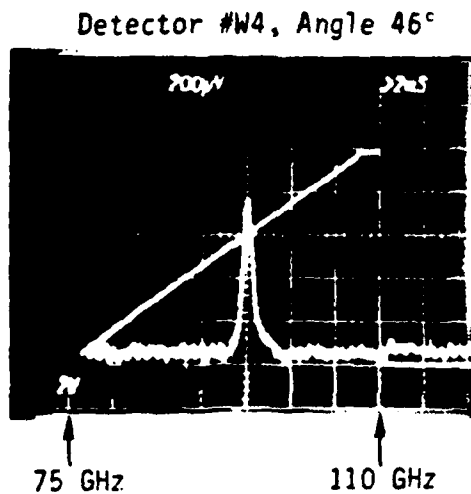Detector #W6, Angle 51.5° Detector #W6, Noise Only
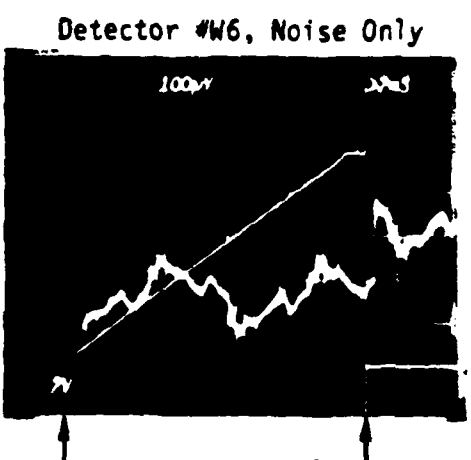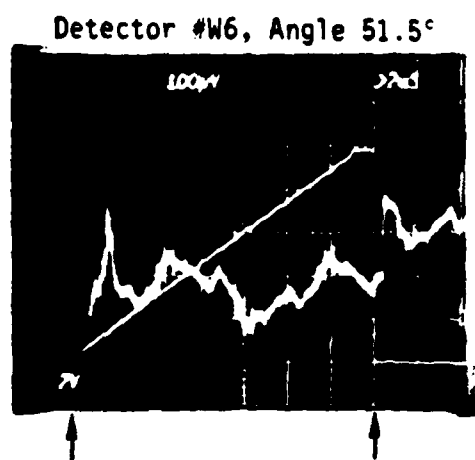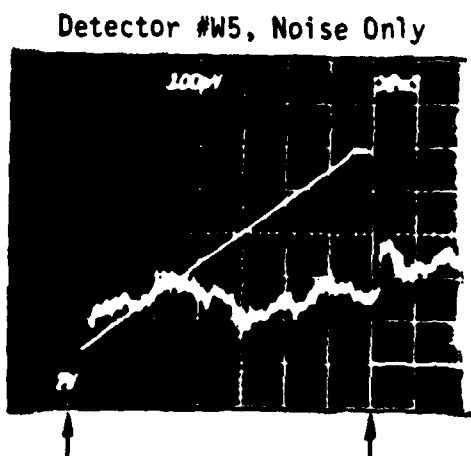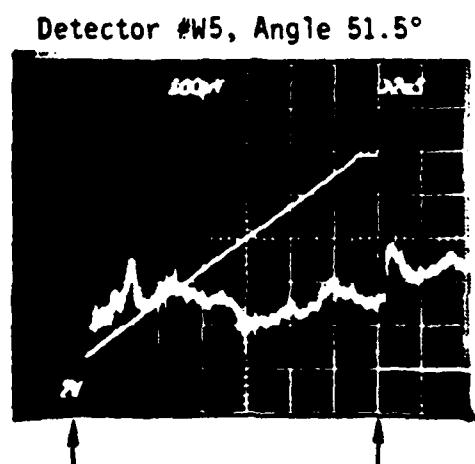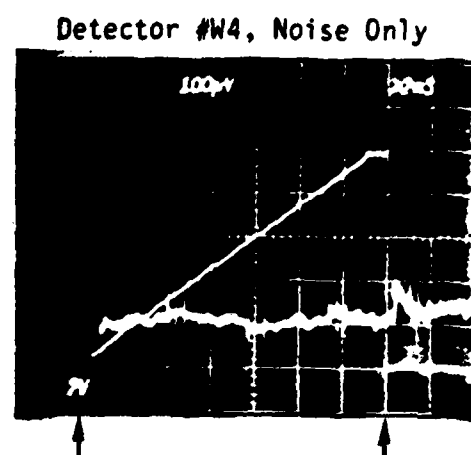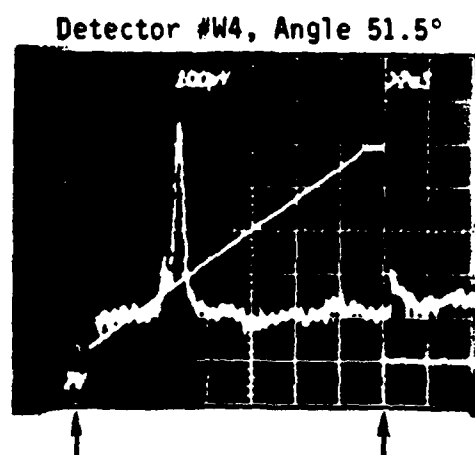
Figure 35B. Spectrometer calibration data for the W-band detectors W1-W6 (detectors W1-W6 located at 3.0, 5.5, 8.0, 10.2, 13.0, and 15.5 inch, respectively) taken at a 51.5 degree grating angle. Left photo is signal plus noise, right photo is noise only, taken with microwave absorbing material covering the detector.
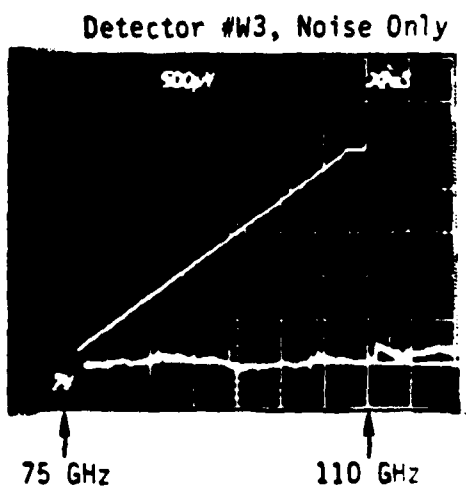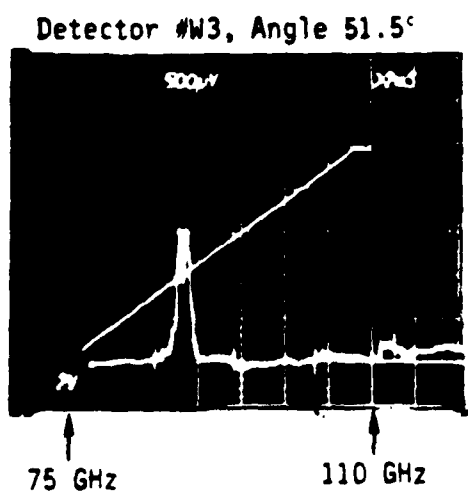
TABLE V. SUMMARY OF SPECTROMETER W-BAND (75-110 GHz) CALIBRATION DATA

PARAMETER	Detector W1	Detector W2	Detector W3	Detector W4	Detector W5	Detector W6
Detector Position (Inches)	3.0	5.5	8.0	10.2	13.0	15.5
For 44° Grating Angle:						
Center Frequency For Peak Sensitivity (GHz)	-	109.5	105.9	-	-	88
Output Voltage (mV)	-	5.35	29	-	-	0.16
Horn Gain (db)	-	25.2	25.2	-	-	24.8
Input Power (mW)	-	46	61	-	-	30
Calculated Figure of Merit (Volts/Watt)	-	3.90×10^{-4}	1.60×10^{-3}	-	-	1.96×10^{-5}
For 46° Grating Angle:						
Center Frequency For Peak Sensitivity (GHz)	107.3	103.7	99.2	95.2	92.2	88.2
Output Voltage (mV)	1.7	41	41	0.68	2.9	0.17
Horn Gain (db)	25.2	25.0	25.1	25.0	24.9	24.8
Input Power (mW)	59	36	46	46	32	26
Calculated Figure of Merit (Volts/Watt)	9.67×10^{-5}	3.82×10^{-3}	3.06×10^{-3}	5.19×10^{-5}	3.26×10^{-4}	2.41×10^{-5}
For 49° Grating Angle:						
Center Frequency For Peak Sensitivity (GHz)	100.4	96.3	92.8	90.4	87.1	82.7
Output Voltage (mV)	51.5	1.92	1.75	1.37	1.53	0.14
Horn Gain (db)	25.1	25.0	24.9	24.8	24.7	24.5
Input Power (mW)	53	46	34	30	30	22
Calculated Figure of Merit (Volts/Watt)	3.34×10^{-3}	1.47×10^{-4}	1.85×10^{-4}	1.68×10^{-4}	1.92×10^{-4}	2.51×10^{-5}
For 51.5° Grating Angle:						
Center Frequency For Peak Sensitivity (GHz)	94.6	90.7	88.2	86.7	81.8	79.4
Output Voltage (mV)	2.95	4.3	1.5	0.43	0.09	0.22
Horn Gain (db)	25.0	24.9	24.8	24.7	24.5	24.4
Input Power (mW)	37.5	28	26	29	19	17
Calculated Figure of Merit (Volts/Watt)	2.76×10^{-4}	5.52×10^{-4}	2.12×10^{-4}	5.58×10^{-5}	1.87×10^{-5}	5.22×10^{-5}

SECTION IV
ELECTRON BEAM SOURCE

The design of the pulse power system which drives the vircator e-beam diode has been previously described.[11] A schematic of the electrical system is shown in Figure 36. Briefly, the electrical equivalent of a Blumlein type pulse forming line (PFL) is built from discrete capacitors and inductors. The Blumlein is DC charged to nominally 50 kV, and the PFL is erected by a triggered spark gap switch which is driven by a time delay generator. The purpose of the time delay generator is to trigger the e-beam near peak magnetic field time, which is typically 600 μsec after the magnet circuit is fired. The artificial Blumlein, as built inside a high voltage insulated screen box, together with the charging and control components, is shown in Photo 4. A 3 cm diameter, 50 ohm high voltage cable connects the Blumlein source output to the vircator vacuum vessel shown in Photo 5.

An important consideration in the vircator diode development work has been to find a material which exhibits fast electron field emission turn on and slow gap closure. The gap closure problem is severe because the low vircator voltage requires operation at very small anode-cathode gaps, of order a few mm, in order to reach the threshold electric fields for field emission. Carbon has been tried as the cathode material because of its well-known low threshold for field emission, of order 50 kV/cm. However, the resulting slow turn on, spotty emission, and high gap closure rate (several cm/μsec) made carbon unacceptable for the cathode material.

An acceptable cathode material developed in the course of this work is the cloth fiber array. It has shown fast turn-on, as well as, very slow gap closure rates, less than 1 cm/μsec. A typical voltage and current trace for the cloth fiber array is shown in Figure 37. This data was taken

ELECTRON BEAM PULSED POWER SUPPLY
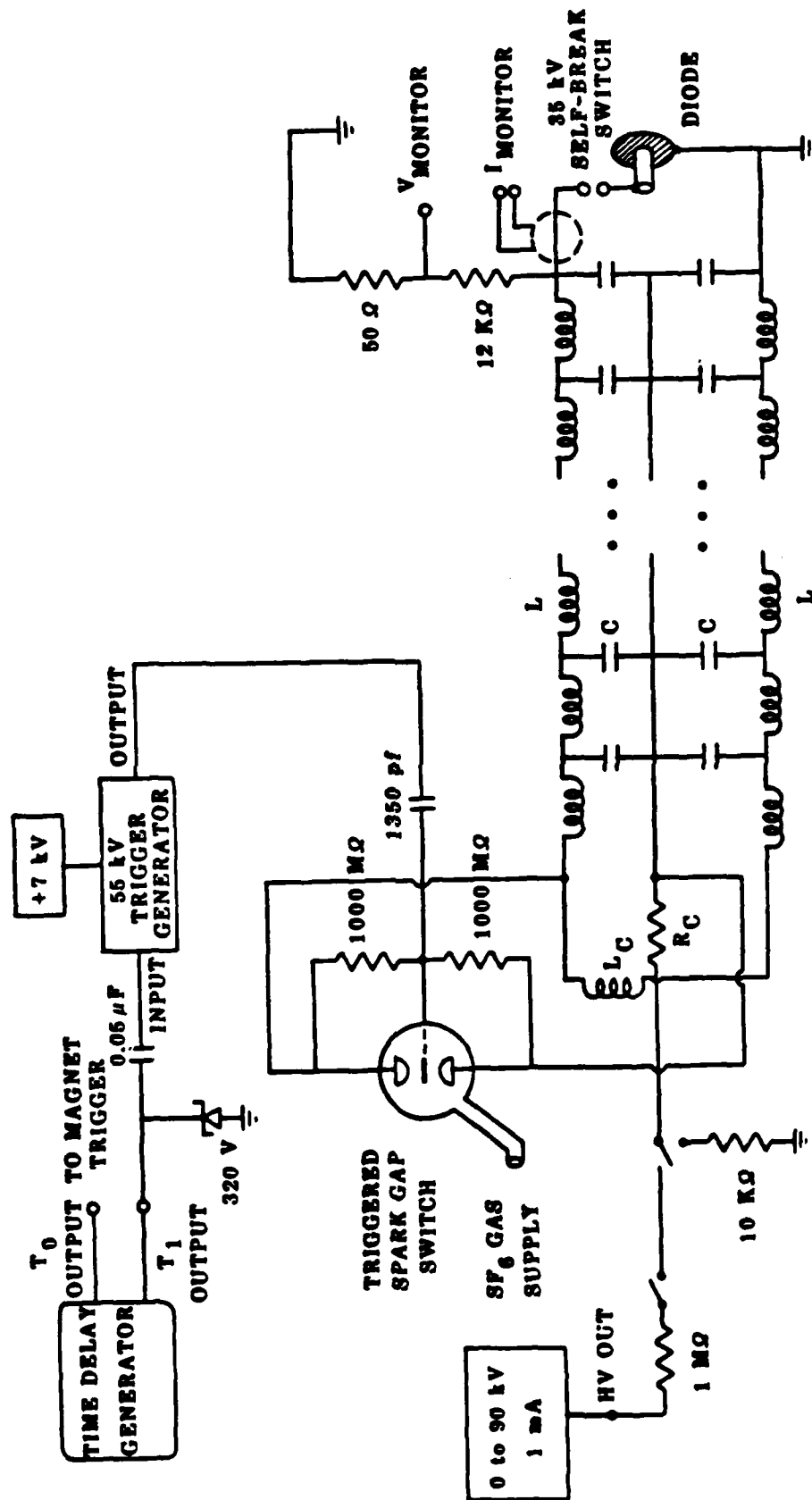
Figure 36. Schematic of the lumped element Blumlein pulse-forming line. Eight stages are used to give a pulse length of 600 nsec at a 50 ohm impedance.
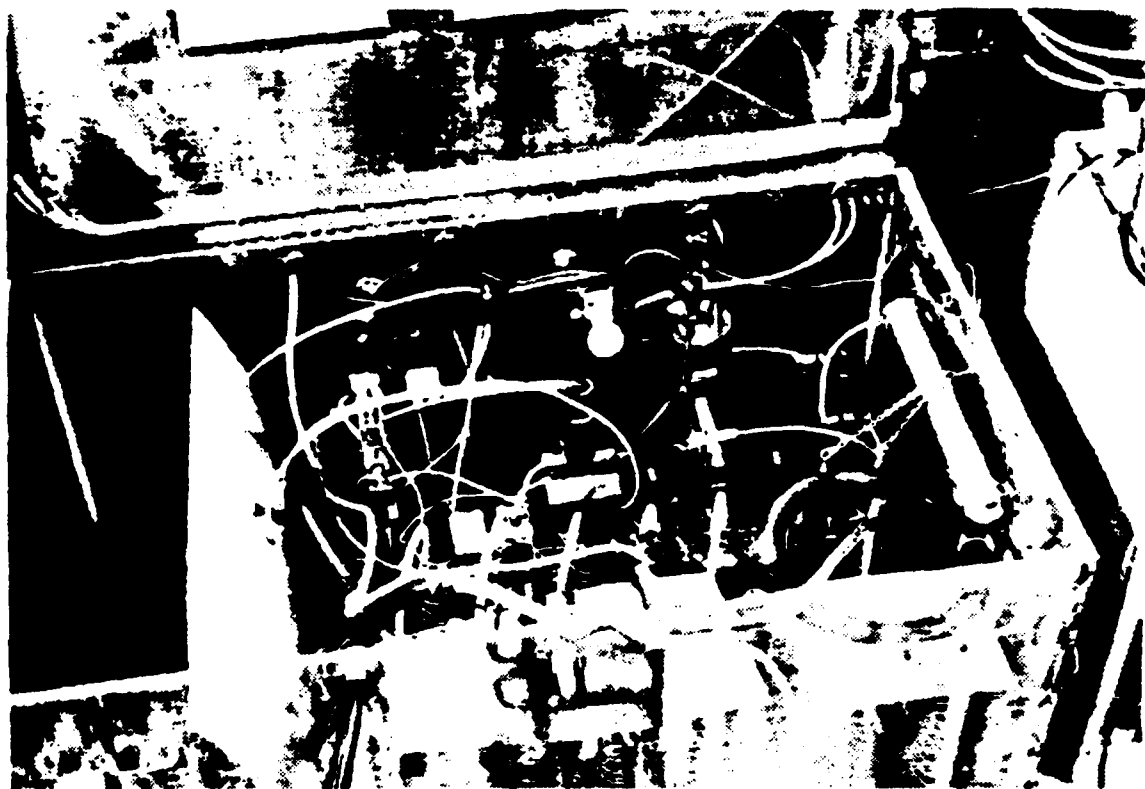
Photograph 4. The 8 stage artificial Blumlein is shown inside the high
voltage insulated screen box, together with charging and
triggering circuitry. The 16 inductors, oriented vertically,
are clearly visible. The 48 2700 pf, 40 kV rated button
capacitors, stacked in sets of 3 each located under the
white polyethylene insulation, are not visible.
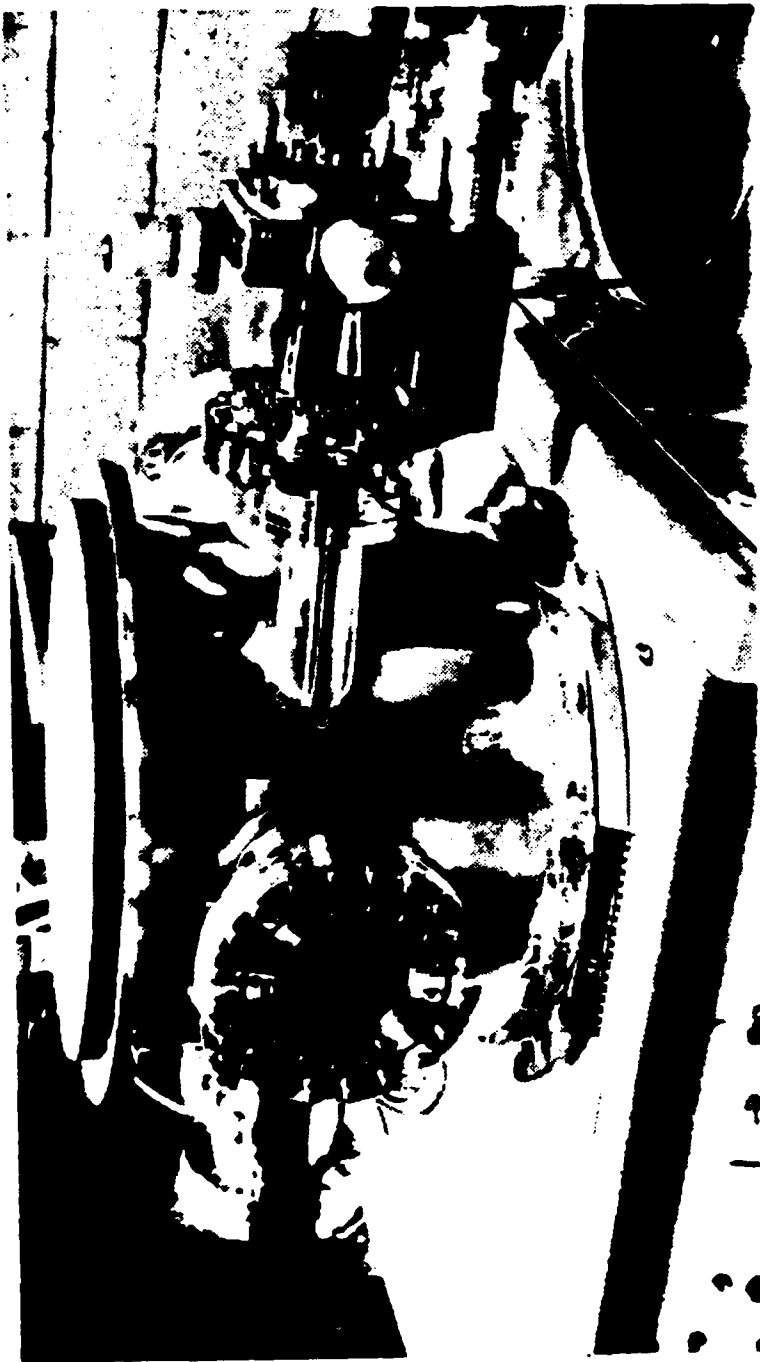
Photograph 5. Vircator vacuum vessel. The 5 degree of freedom external manipulator allowing anode-cathode gap adjustment without breaking vacuum is shown mounted on the 6 inch diameter flange at the right. Microwave emission is through the 4 inch open hole at the left. The 50Ω cable connecting the e-beam pulser to the vacuum vessel is not visible.
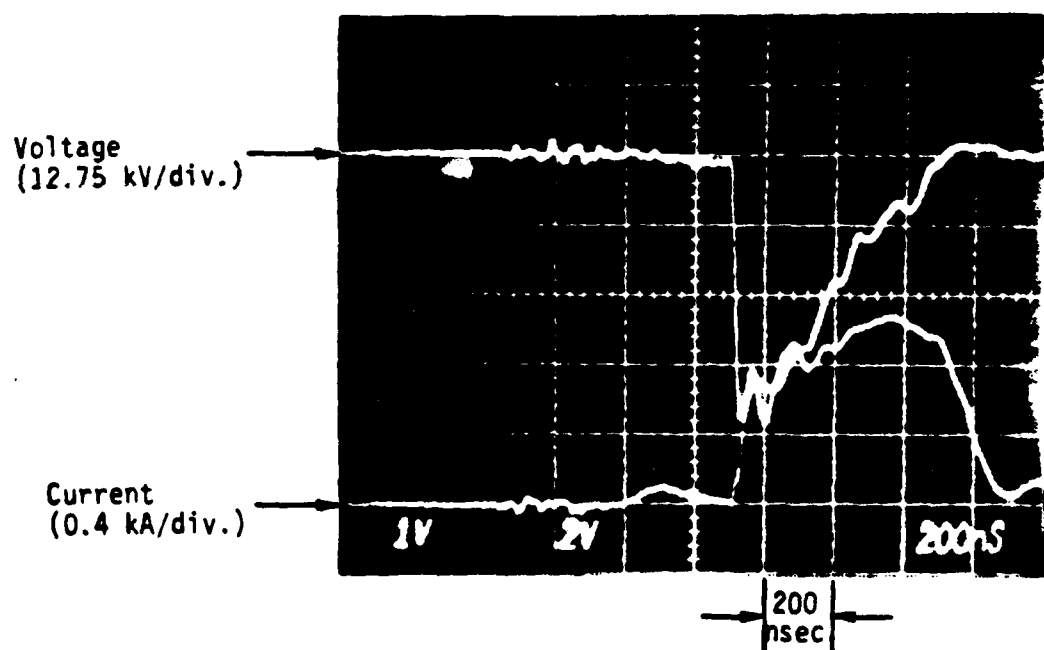
Figure 37. Voltage and current traces for a 50 kV charge voltage and a 4 mm A-K gap. Voltage risetime is 20 nsec. Peak voltage and currents are 45 kV and 1.07 kA, respectively.

with a 1.9 cm diameter-cathode, a grid type anode, and a 4 mm anode-cathode
gap operating as a standard planar diode. Emission is within a factor of
20% of the space-charge limit. Note that the current turns on as fast as
the voltage, approximately 20 nanoseconds, and that the gap stays open for
essentially the entire pulse length, 0.6 μsec. These characteristics make
the cloth fiber array the favored choice for the vircator cathode relative
to the other cold cathode emitters.

Examination of the cloth fiber array with an optical microscope shows
that it is composed of a regular array of approximately 3600 nonconducting
thin fibers per cm^2 with the fibers oriented perpendicular to a partially
transparent nonconducting cloth backing.[12] The emission region then con-
sists of an array of fibers perpendicular to a conducting cathode surface.
A surface flashover along the individual fibers contributes to the plasma
formation process, and this apparently results in the formation of more
emission sites than for the analogous carbon cold cathode. Both long life-
time and the low gap closure velocity are the result of reduced energy per
emission site. The amount of energy per site is very small, because the
breakdown mechanism is effectively a capacitive discharge of low capaci-
tance. In this sense we believe that the cloth fiber array acts like the
Corona electron source developed by Helionetics[13] for laser pre-ioniza-
tion. The axial surface flashover mechanism is more desirable than the
conventional cold cathode emission process, because production of plasma in
this manner inhibits the formation of surface cathode spots.

REFERENCES

1. W. R. Smythe, Static and Dynamic Electricity, McGraw-Hill, New York (1950).

2. J. R. Freeman, Controlling Magnetic Field Properties, Sandia National Laboratories technical report SAND-79-0678, April 1979.

3. Berni Adler, ed., Methods in Computational Physics, Volume 9, Academic Press, New York (1970).

4. D. Bruce Montgomery, Solenoid Magnet Design, Wiley, New York (1969), p. 233.

5. M. W. Garrett, J. Appl. Phys. 22, 1091 (1951).

6. M. W. Garrett, High Magnetic Fields, Chapter 2, MIT Press, Cambridge, Mass. (1962).

7. D. B. Montgomery and J. Terrel, Some Useful Information for the Design of Solenoid Magnets, National Magnet Laboratory Report 1525 (1961).

8. J. D. Jackson, Classical Electrodynamics, Wiley, New York (1962), p. 165.

9. D. Bruce Montgomery, Solenoid Magnet Design, Wiley, New York (1969), p. 190.

10. W. M. Bollen and R. H. Jackson, "A W-Band Diffraction Grating Spectrometer," Mission Research Corporation, MRC/WDC-R-046, December 1982.

11. D. J. Sullivan, D. E. Voss, W. M. Bollen, R. H. Jackson, and E. A. Coutsias, "Annual Report: Virtual Cathode Theory and Design of a Millimeter Wave Vircator," Mission Research Corporation, AMRC-R-451, January 1983.

12. R. J. Adler, G. K. Kiuttu, B. E. Simpkins, D. J. Sullivan, and D. E. Voss, "Improved Electron Emission by Use of a Cloth Fiber Cathode," Mission Research Corporation, AMRC-N-275, October 1984.

13. R. Sandstrom, J. I. Levaiter, and J. H. Morris, Proceedings of the Fourth IEEE Pulsed Power Conference, Albuquerque, NM, T. H. Martin and M. F. Rose, Eds.

APPENDIX A

LISTING OF FORTRAN SOURCE CODE FOR
MAGNETIC FIELD CALCULATION

SOLENOIDAL MAGNETIC FIELD CALCULATION

BASE CODE BY JOHN FREEMAN, MODIFIED BY DON VOSS FOR FIELD LINE
CALCULATION.

```
      COMMON /A/ RB(50),ZB(50),RF(50),ZF(50)
      COMMON /B/ RCC(100),ZCL(100),ZCR(100),XNTC(100),CCC(100)
      COMMON /VOSS1/ BRAD(41, 201), BAXIAL(41, 201)
      COMMON /VOSS2/ RADIUS, XLENG, DR, DZ, DRXDZ
      DIMENSION IHEAD(7)
      DIMENSION STO(5000)
      DIMENSION XPLOT(1001), YPLOT(1001)
      COMMON /C/ R(200),Z(200),NR,NZ,NCT
      DIMENSION IPHEAD(3)
      REAL LENGTH
      DATA IPHEAD /4HBRJ=,4HBZJ=,4HPSJ=/
      OPEN (UNIT=11, NAME='MAGIN.ECH', STATUS='NEW')
      OPEN (UNIT=12, NAME='MAGOUT.LPT', STATUS='NEW')
      PI = 3.1415926535
      RADDEG = 180. / PI
      PRINT *,'ALL DIMENSIONS ARE IN CENTIMETERS'
  100 FORMAT(7A10)
      PRINT *,'ENTER HEADING FOR THIS PROBLEM'
      READ100,IHEAD
  101 FORMAT(1X,7A10//)
      PRINT *,'FOR KEYBOARD INPUT TYPE 1; OTHERWISE TYPE 0'
      READ *,INP
      PRINT *,'FOR SHORT PRINT TYPE 1;OTHERWISE TYPE 0'
      READ *,KPT
      IF (INP.EQ.0) GO TO 30
      PRINT *,'ENTER RADIUS OF COMPUTATION'
      READ *,RADIUS
      PRINT *,'ENTER LENGTH OF COMPUTATION'
      READ *,LENGTH
      PRINT *,'ENTER NUMBER OF RADIAL MESH LINES'
      READ *,NR
      PRINT *,'ENTER NUMBER OF AXIAL MESHLINES'
      READ *,NZ
      NCT=0
    2 PRINT *,'ENTER COIL IDENT NUMBER; 0 TO TERMINATE'
      READ *,NC
```

```fortran
      PRINT *,'ENTER NUMBER OF TURNS'
      READ *, XNTC(NC)
      PRINT *,'ENTER COIL CURRENT IN AMPERES'
      READ *,CCC(NC)
      GO TO 2
 30 CONTINUE
      OPEN (UNIT=1, NAME='MAGIN.DAT', STATUS='OLD')
      READ(1,*) RADIUS
      READ(1,*) LENGTH
      READ(1,*) NR
      READ(1,*) NZ
      READ(1,*) NCT
      DO 32 I=1, NCT
      READ(1,*) RCC(I), ZCL(I), ZCR(I), XNTC(I), CCC(I)
 32 CONTINUE
  1 CONTINUE
400 FORMAT (1X, 1PE16.8)
401 FORMAT (1X, I6)
402 FORMAT (1X, 5(1PE16.8))
      WRITE (11,400) RADIUS
      WRITE (11,400) LENGTH
      WRITE (11,401) NR
      WRITE (11,401) NZ
      WRITE (11,401) NCT
      DO 31 I=1, NCT
      WRITE (11,402) (RCC(I), ZCL(I), ZCR(I), XNTC(I), CCC(I))
 31 CONTINUE
      XLENG = LENGTH
      DR = 0.
      DZ = 0.
      IF (NR .EQ. 1) GO TO 9
      NR1 = NR - 1
      DR = RADIUS / NR1
      R(1) = 0.
      DO 3 I=2, NR
  3 R(I) = R(I-1) + DR
  9 IF (NZ .EQ. 1) GO TO 8
      NZ1 = NZ - 1
      DZ = LENGTH / NZ1
      Z(1) = 0.
      DO 4 I=2, NZ
  4 Z(I) = Z(I-1) + DZ
  8 CONTINUE
      DRXDZ = DR * DZ
      PRINT 201
201 FORMAT (' COMPUTATION REGION DATA')
      PRINT 102,RADIUS,LENGTH,DR,DZ,NR,NZ
102 FORMAT (/,' RADIUS=', 1PE12.3, 5X, 'LENGTH=', 1PE12.3, 4X,
```

```fortran
202 FORMAT (' COIL DATA')
    DO 5 I=1, NCT
    PRINT 103, (RCC(I), ZCL(I), ZCR(I), XNTC(I), CCC(I))
103 FORMAT (' RCC=', 1PE9.2, ' ZCL=', 1PE9.2,
   1        ' ZCR=', 1PE9.2, ' NTC=', 1PE9.2, ' CCC=', 1PE9.2)
  5 CONTINUE
    IF (KPT .EQ. 1) GO TO 33
    PRINT 105
105 FORMAT(/, ' RADIAL MESH LINE LOCATIONS')
    PRINT 104, (R(I), I=1, NR)
    PRINT 106
106 FORMAT (/, ' AXIAL MESH LINE LOCATIONS')
    PRINT 104, (Z(I), I=1, NZ)
104 FORMAT ((10(5(1PE13.5)/)))/)
 33 CONTINUE
    WRITE (12, 201)
    WRITE (12, 102) RADIUS, LENGTH, DR, DZ, NR, NZ
    WRITE (12, 202)
    DO 250 I=1, NCT
250 WRITE (12, 103) RCC(I), ZCL(I), ZCR(I), XNTC(I), CCC(I)
    WRITE (12, 105)
    WRITE (12, 104) (R(I), I=1, NR)
    WRITE (12, 106)
    WRITE (12, 104) (Z(I), I=1, NZ)
    NT = NR * NZ
    PRINT *, ' ENTER -2 TO BYPASS, -1 FOR BR, 0 FOR BZ, 1 FOR PSI'
    READ *, IFIELD
    IF (IFIELD .LE. -2) GO TO 16
    CALL FIELD (STO, IFIELD)
 17 PRINT *, ' ENTER J-LINE FOR PRINT; 0 TO TERMINATE'
    IPT = IFIELD + 2
    READ *, J
    IF (J .EQ. 0) GO TO 16
    PRINT 108, IPHEAD(IPT), J
108 FORMAT (//1X, A7, I3)
    DO 7 L=1, NZ
    JL = (L-1) * NR + J
  7 RB(L) = STO(JL)
    PRINT 104, (RB(L), L=1, NZ)
    GO TO 17
 16 CONTINUE
    WRITE (6, 300)
300 FORMAT (/, ' TYPE A 1 IF YOU WANT TO DO FIELD LINES')
    READ (5, 301) IFLINE
301 FORMAT (I2)
    IF (IFLINE .EQ. 0) GO TO 399
    IFIELD = -1
    CALL FIELD (STO, IFIELD)
```

```
      JL = (L - 1) * NR + K
      BRAD(K,L) = STO(JL)
364 CONTINUE
365 CONTINUE
      IFIELD = 0
      CALL FIELD (STO, IFIELD)
      DO 367 K=1, NR
      DO 366 L=1, NZ
      JL = (L - 1) * NR + K
      BAXIAL(K,L) = STO(JL)
366 CONTINUE
367 CONTINUE
      WRITE (12, 305)
305 FORMAT (//, ' LISTING OF BR AND BZ OVER THE COMPUTATIONAL GRID')
      DO 369 K=1, NR
      WRITE (12, 306)
306 FORMAT (/,' K', 3X, 'L', 5X, 'R', 9X, 'Z', 6X, 'BR(K,L)', 4X,
     1      'BZ(K,L)', 4X, 'B(K,L)', 5X, 'BR/BZ', 5X, 'THETA')
      XKV = K - 1
      RADV = XKV * DR
      DO 368 L=1, NZ
      XLV = L - 1
      ZV = XLV * DZ
      RCOMP = BRAD(K,L)
      ZCOMP = BAXIAL(K,L)
      BMAG = SQRT (RCOMP * RCOMP + ZCOMP * ZCOMP)
      BRATIO = 0.
      IF (ZCOMP .NE. 0.) BRATIO = RCOMP / ZCOMP
      ANGV = RADDEG * ATAN(BRATIO)
      WRITE (12, 307) K, L, RADV, ZV, RCOMP, ZCOMP, BMAG, BRATIO, ANGV
307 FORMAT (1X, I2, I4, F9.5, F9.4, 3F11.3, 1X, 1PE10.3, OPF9.4)
368 CONTINUE
369 CONTINUE

      READ DATA FOR FIELD LINE CALCULATION

380 WRITE (6, 500)
500 FORMAT (' ENTER A 1 FOR FIELD LINE TTY INPUT, 0 FOR DISK INPUT,',
     1      ' -1 TO TERM -- ', $)
      READ (5, *) IDVOPT
      IF (IDVOPT .EQ. -1) GO TO 590
      IF (IDVOPT .EQ. 0) GO TO 555
550 WRITE (6, 501)
501 FORMAT (' HOW MANY FIELD LINES (MAX = 20) -- ', $)
      READ (5, *) IFLNUM
      IF (IFLNUM .LE. 0) GO TO 550
552 WRITE (6, 502)
502 FORMAT (' ENTER FIELD LINE STEP DISTANCE DS (CM) -- ', $)
```

```
    553 WRITE (6, 503)
    503 FORMAT (' ENTER PLOT SPACING DISTANCE DPLOT (CM) -- ', $)
        READ (5, *) DPLOT
        IF (DPLOT .LT. 0.) GO TO 553
    554 WRITE (6, 504)
    504 FORMAT (' ENTER RADIAL RANGE (2 NUMBERS) FOR FIELD LINES (CM) -- '
       1        , $)
        READ (5, *) RFLBEG, RFLEND
        IF (RFLBEG .GT. RFLEND) GO TO 554
    567 WRITE (6, 517)
    517 FORMAT (' ENTER RADIAL GRAPHICS ENHANCEMENT FACTOR -- ', $)
        READ (5, *) RFACT
        IF (RFACT .LE. 0.) GO TO 567
        WRITE (6, 505)
    505 FORMAT (' ENTER R AND Z DISTANCES FOR PLOT WINDOW',
       1         ' (2 NUMBERS) -- ', $)
        READ (5, *) RPLOTW, ZPLOTW
        GO TO 556
    555 CONTINUE
        READ (1, *) IFLNUM
        READ (1, *) DS
        READ (1, *) DPLOT
        READ (1, *) RFLBEG, RFLEND
        READ (1, *) RFACT
        READ (1, *) RPLOTW, ZPLOTW
    556 CONTINUE
        WRITE (12, 510) IFLNUM, DS, RFLBEG, RFLEND, DPLOT
    510 FORMAT (//, '    FIELD LINE PLOT SPECIFICATIONS AS FOLLOWS:', /,
       1         1X, I2, ' FIELD LINES CALCULATED WITH DS =', 1PE14.7,
       2         ' CM,',/, ' BEGINNING AT A RADIUS OF', OPF10.6, ' CM AND',
       3         /, ' ENDING AT A RADIUS OF', OPF10.6, ' CM.  FIELD LINE',
       4         /, ' (R,Z) POSITIONS RECORDED AT INTERVALS OF', OPF10.6,
       5         ' CM.')
        IF (RPLOTW .GT. 0.) GO TO 570
        RPLOTW = RADIUS
        DO 569 IDUM=1, NCT
        IF (RCC(IDUM) .GT. RPLOTW) RPLOTW = RCC(IDUM)
    569 CONTINUE
    570 IF (ZPLOTW .GT. 0.) GO TO 572
        ZPLOTW = XLENG
        DO 571 IDUM=1, NCT
        IF (ZCR(IDUM) .GT. ZPLOTW) ZPLOTW = ZCR(IDUM)
    571 CONTINUE
    572 WRITE (12, 523) RFACT, RPLOTW, ZPLOTW
    523 FORMAT (' RADIAL SCALE ON PLOTS ENHANCED BY', 1PE14.7, /,
       1         ' (R,Z) PLOT RANGE = (', OPF9.5, ',', OPF9.5, ').')
        WRITE (6, 510) IFLNUM, DS, RFLBEG, RFLEND, DPLOT
        WRITE (6, 523) RFACT, RPLOTW, ZPLOTW
```

```
      WRITE (11, 400) DPLOT
      WRITE (11, 402) RFLBEG, RFLEND
      WRITE (11, 400) RFACT
      WRITE (11, 402) RPLOTW, ZPLOTW

      START FIELD LINES AT Z=0 AND USE 'SHOOTING' TECHNIQUE FOR INTEGRATING

      DRFL = 0.
      XFLNUM = IFLNUM
      IF (IFLNUM .GT. 1) DRFL = (RFLEND - RFLBEG) / (XFLNUM - 1.)

      PLOT SET-UP --- PLOT AXES AND LABELS --- 11-30-82

      XPLOT(1) = 0.
      YPLOT(1) = 0.
      XPLOT(2) = ZPLOTW
      YPLOT(2) = RPLOTW
      RADEFF = RPLOTW * RFACT
      CALL STARTT(1)
      CALL PLOJB (XPLOT, YPLOT, 2, 1, 0, 0, 0.0, ZPLOTW,
     1            RADEFF,37H VIRCATOR VACUUM FIELD LINE STRUCTURE,
     2            -37,25H AXIAL CO-ORDINATE Z (CM),
     3            25, 2H R, 2)

      DO 560 IDUM=1, IFLNUM
      XDUM = IDUM - 1
      RSTART = RFLBEG + XDUM * DRFL
      ZSTART = 0.
      WRITE (12, 511) IDUM
  511 FORMAT (//, ' FIELD LINE NUMBER', I4, ' (R,Z) TRAJECTORY IS AS'
     1            ' FOLLOWS :')
      WRITE (12, 512)
  512 FORMAT (/,' STEP #', 5X, 'R', 9X, 'Z', 6X, 'BR(K,L)', 4X,
     1            'BZ(K,L)', 4X, 'B(K,L)', 5X, 'BR/BZ', 5X, 'THETA')
      DISTDV = DPLOT
      INC = 0
      DO 559 IDV=1, 10001
      CALL BINTRP (RSTART, ZSTART, BRINT, BZINT, IOFF)
      IF (IOFF .EQ. 1) GO TO 559
      BMAG = SQRT (BRINT * BRINT + BZINT * BZINT)
      IF (DISTDV .LT. DPLOT) GO TO 566
      BRATIO = 0.
      IF (BZINT .NE. 0.) BRATIO = BRINT / BZINT
      ANGV = RADDEG * ATAN (BRATIO)
      WRITE (12, 513) IDV, RSTART, ZSTART, BRINT, BZINT, BMAG, BRATIO,
     1            ANGV
  513 FORMAT (1X, I6, F9.5, F9.4, 3F11.3, 1X, 1PE10.3, OPF9.4)
      DISTDV = DISTDV - DPLOT
```

/1   /

```
      YPLOT(INC) = RSTART
566 IF (BMAG .GT. 0.) GO TO 557
    WRITE (12, 515)
515 FORMAT (' RUN TERMINATED DUE TO ZERO B FIELD')
    GO TO 561
557 FACDV = DS / BMAG
    RSTART = RSTART + BRINT * FACDV
    IF (RSTART .GT. 0.) GO TO 558
    WRITE (12, 514)
514 FORMAT (' RUN TERMINATED DUE TO PROJECTION THROUGH ZERO RADIUS')
    GO TO 561
558 ZSTART = ZSTART + BZINT * FACDV
    DISTDV = DISTDV + DS
559 CONTINUE
561 IF (INC .LE. 1) GO TO 560

    PLOT THE FIELD LINE JUST CALCULATED

    CALL CHOPAR (XPLOT, YPLOT, INC, ZPLOTW, RPLOTW)
    CALL PLOJB (XPLOT, YPLOT, INC, 1, 0, -1, 0.0, ZPLOTW, RADEFF,
   1            0, 0, 0, 0, 0, 0)

560 CONTINUE
399 CONTINUE

    PLOT THE POSITION OF EACH TURN OF THE COIL SET

    DO 575 IDV=1, NCT
    INC = XNTC(IDV)
    XPLOT(1) = ZCL(IDV)
    YPLOT(1) = RCC(IDV)
    IF (INC .EQ. 1) GO TO 574
    DXCOIL = (ZCR(IDV) - ZCL(IDV)) / (XNTC(IDV) - 1.)
    DO 573 IDUM=2, INC
    XDUM1 = IDUM - 1
    XPLOT(IDUM) = ZCL(IDV) + XDUM1 * DXCOIL
573 YPLOT(IDUM) = RCC(IDV)
574 ICHARP = - IDV
    CALL CHOPAR (XPLOT, YPLOT, INC, ZPLOTW, RPLOTW)
    CALL PLOJB (XPLOT, YPLOT, INC, 1, -1, ICHARP, 0.0,
   1            ZPLOTW, RADEFF, 0, 0, 0, 0, 0, 0)
575 CONTINUE

    MAKE HARDCOPY OF PLOT AND RELEASE PLOTTER

    CALL HDCOPY
    CALL STOPT
```

```
      READ *, ICORR
      IF (ICORR .EQ. 0) GO TO 20
      PRINT *,'FIELD CORRECTION FOR BZ ONLY'
      CALL ECORR(STO)
      CALL FIELD(STO,IFIELD)
   21 PRINT *,'ENTER J-LINE FOR PRINT; 0 TO TERMINATE'
      READ *,J
      IF(J.EQ.0) GO TO 22
      PRINT 108,IPHEAD(IPT),J
      DO 70 L=1,NZ
      JL=(L-1)*NR+J
   70 RB(L)=STO(JL)
      PRINT 104,(RB(L),L=1,NZ)
      GO TO 21
   22 CONTINUE
   20 CONTINUE
      STOP
      END




      SUBROUTINE TO CHOP ARRAYS

      SUBROUTINE CHOPAR (XPLOT, YPLOT, NUM, XMAX, YMAX)
      DIMENSION XPLOT(1001), YPLOT(1001)
      DO 1 I=1, NUM
      IF (XPLOT(I) .GT. XMAX) XPLOT(I) = XMAX
      IF (YPLOT(I) .GT. YMAX) YPLOT(I) = YMAX
    1 CONTINUE
      RETURN
      END




      SUBROUTINE TO DO 2-DIMENSIONAL MAGNETIC FIELD INTERPOLATION
      D. VOSS - 11/24/82.

      SUBROUTINE BINTRP (RCOORD, ZCOORD, BRINT, BZINT, IOFF)
      COMMON /VOSS1/ BRAD(41, 201), BAXIAL(41, 201)
      COMMON /VOSS2/ RADIUS, XLENG, DR, DZ, DRXDZ
      COMMON /C/ R(200), Z(200), NR, NZ, NCT
      KUPR = (RCOORD / DR) + 2.
      LUPR = (ZCOORD / DZ) + 2.
      IF (KUPR .LE. NR .AND. LUPR .LE. NZ) GO TO 3
    1 BRINT = 0.
      BZINT = 0.
      IOFF = 1

      IOFF = 1 INDICATES THAT THE (R,Z) POINT REQUESTED IS NOT ON THE GRID

    2 RETURN
    3 IF (KUPR .LE. 1 .OR. LUPR .LE. 1) GO TO 1
```

```
      CALCULATE AREAL WEIGHTS - THIS SCHEME ACCURATE TO 2ND ORDER IN DR, DZ

      RDIST = R(KUPR) - RCOORD
      ZDIST = Z(LUPR) - ZCOORD
      DRDIST = DR - RDIST
      DZDIST = DZ - ZDIST
      WLL = RDIST * ZDIST
      WLR = RDIST * DZDIST
      WUL = DRDIST * ZDIST
      WUR = DRDIST * DZDIST
      KUPR1 = KUPR - 1
      LUPR1 = LUPR - 1
      BRINT = (BRAD(KUPR1,LUPR1) * WLL + BRAD(KUPR1,LUPR) * WLR +
     1        BRAD(KUPR,LUPR1) * WUL + BRAD(KUPR,LUPR) * WUR) / DRXDZ
      BZINT = (BAXIAL(KUPR1,LUPR1) * WLL + BAXIAL(KUPR1,LUPR) * WLR +
     1        BAXIAL(KUPR,LUPR1) * WUL + BAXIAL(KUPR,LUPR) * WUR)/DRXDZ
      GO TO 2
      END




      SUBROUTINE FIELD(STO,IFIELD)
      COMMON /B/ RCC(100), ZCL(100), ZCR(100), XNTC(100), CCC(100)
      COMMON /C/ R(200), Z(200), NR, NZ, NCT
      DIMENSION STO(1)
      REAL K,K2
      TPI=6.2831853072
      EMU=2.E-1*TPI
      NT=NR*NZ
      DO 6 I=1,NT
    6 STO(I)=0.
      DO 7 J=1,NR
      DO 7 L=1,NZ
      JL=(L-1)*NR+J
      DO 8 I=1,NCT
      IF(XNTC(I) .NE. 1.) GO TO 14
      DZC=0.
      GO TO 15
   14 DZC = (ZCR(I)-ZCL(I)) / (XNTC(I)-1)
   15 NTCPAR = XNTC(I) + .0001

      PREVIOUS STATEMENT CHANGED 11-23-82 TO FLOATING - D.V.

      DO 9 IK=1, NTCPAR
      R2=R(J)/RCC(I)
      Z2=-((ZCL(I)+(IK-1)*DZC)-Z(L))/RCC(I)
      A=CCC(I)*EMU*R(J)
      A1=CCC(I)*EMU/RCC(I)
      C1=SQRT((1.+R2)**2+Z2*Z2)
      C2=(1.-R2)**2+Z2*Z2
      AK=SQRT(4.*R2)/C1
```

```
107 FORMAT (' MESH POINT COINCIDENT WITH COIL')
    K2=AK*AK
    CK2=1.-K2
    CALL CELI2(E,AK,1.,CK2,IER)
    CALL CELI2(K,AK,1.,1.,IER)
    IF(R2.NE.0.) C3=2./(TPI*AK*SQRT(R2))
    IF(IFIELD) 10,11,12
 10 BRI=-K+E*(1.+R2*R2+Z2*Z2)/C2
    IF(R2.NE.0.) BRI=A1*BRI*Z2/(TPI*R2*C1)
    IF(R2.EQ.0.) BRI=0.
    STO(JL)=STO(JL)+BRI
    GO TO 13
 11 BZI=K+E*(1.-R2*R2-Z2*Z2)/C2
    BZI=A1*BZI/(TPI*C1)
    STO(JL)=STO(JL)+BZI
    GO TO 13
 12 IF(R2.NE.0.) PSI=A*C3*((1.-.5*K2)*K-E)
    IF(R2.EQ.0.) PSI=0.
    STO(JL)=STO(JL)+PSI
 13 CONTINUE
  9 CONTINUE
  8 CONTINUE
  7 CONTINUE
    RETURN
    END



    SUBROUTINE CELI2(RES,AK,A,B,IER)
    IER=0
    CK=AK*AK
    IF(CK-1.) 7,7,5
  5 IER=1
    GO TO 100
  7 GEO=SQRT(1.-CK)
    IF(GEO) 50,10,50
 10 IF(B) 20,40,30
 20 RES=-1.E37
    GO TO 100
 30 RES=1.E37
    GO TO 100
 40 RES=A
    GO TO 100
 50 ARI=1.
    AA=A
    AN=A+B
    W=B
 60 W=W+AA*GEO
    W=W+W
    AA=AN
    AARI=ARI
```

```fortran
      IF(AARI-GEO-1.E-4*AARI) 80,80,70
   70 GEO=SQRT(GEO*AARI)
      GEO=GEO+GEO
      GO TO 60
   80 RES=.78539816*AN/ARI
  100 RETURN
      END




      SUBROUTINE ECORR(STO)
      COMMON/A/ RB(50),ZB(50),RF(50),ZF(50)
      DIMENSION STO(1),CM(100),PN(100),NRF(50),MZF(50),EHO(100)
      COMMON/B/RCC(100),ZCL(100),ZCR(100), XNTC(100),CCC(100)
      COMMON/C/R(200),Z(200),NR,NZ,NCT
      DIMENSION BE(100),EHNM(1000),IN(100),ARR(1000)
      DIMENSION BZC(100),BZA(100)
      REAL K,K2
      TPI=6.283185072
      EMU=2.E-1*TPI
      READ(2,*) ME
      DO 40 I=1,ME
      READ(2,*) NRF(I),MZF(I)
   40 CONTINUE
      DO 41 I=1,ME
      READ(2,*) EHO(I)
   41 CONTINUE
      READ(2,*) NE
      READ(2,*)CMO
      READ(2,*)PNO
      DO 42 I=1,NE
      READ(2,*) RB(I),ZB(I)
   42 CONTINUE
      DO 24 M=1,ME
      MM=MZF(M)
      NM=NRF(M)
      RF(M)=R(NM)
   24 ZF(M)=Z(MM)
      PRINT 43,CMO,PNO
   43 FORMAT(//'   CMO=',1PE13.5,'  PNO=',1PE13.5)
      DO 25 M=1,ME
   25 CM(M)=CMO
      DO 26 N=1,NE
   26 PN(N)=PNO
      PRINT 110
  110 FORMAT(//'   FIELD CORRECTION PARAMETERS')
      PRINT 111,NE,ME
  111 FORMAT(//,'   NE=',1I2,'   ME=',I2,'   EHO(M)=',1PE10.3)
      PRINT 112
  112 FORMAT(//,' RADIAL MESHS FOR FIELD CONTROL',/)
      PRINT 113,(RF(I),I=1,ME)
```

```
114 FORMAT(//,' AXIAL MESHS FOR FIELD CONTROL',/)
    PRINT 113,(ZF(I),I=1,ME)
    PRINT 115
115 FORMAT(//10X,' CURRENT LOOPS',/,10X,'RADII',/)
    PRINT 113,(RB(I),I=1,NE)
    PRINT 116
116 FORMAT(/,10X,'AXIAL POSITION',/)
    PRINT 113,(ZB(I),I=1,NE)
    DO 27 N=1,NE
    DO 27 M=1,ME
    R2=RF(M)/RB(N)
    Z2=-(ZB(N)-ZF(M))/RB(N)
    A1=EMU/RB(N)
    C1=SQRT((1.+R2)**2+Z2*Z2)
    C2=(1.-R2)**2+Z2*Z2
    AK=SQRT(4.*R2)/C1
    IF(C2.EQ.0.) PRINT 119
119 FORMAT(' GRID POINT COINCIDENT WITH CURRENT LOOP')
    IF(C2.EQ.0.) CALL EXIT
    K2=AK*AK
    CK2=1.-K2
    CALL CELI2(E,AK,1.,CK2,IER)
    CALL CELI2(K,AK,1.,1.,IER)
    NM=(M-1)*NE+N
    EHNM(NM)=K+E*(1.-R2*R2-Z2*Z2)/C2
 27 EHNM(NM)=EHNM(NM)*A1/(TPI*C1)
    DO 28 N=1,NE
    BE(N)=0.
    DO 29 M=1,ME
    I1=NRF(M)
    J1=MZF(M)
    I1J1=(J1-1)*NR+I1
    NM=(M-1)*NE+N
 29 BE(N)=BE(N)+(EHO(M)-STO(I1J1))*EHNM(NM)*CM(M)
 28 CONTINUE
    DO 30 I=1,NE
    DO 30 J=1,NE
    IJ=(J-1)*NE+I
    ARR(IJ)=0.
    DO 31 M=1,ME
    IM=(M-1)*NE+I
    JM=(M-1)*NE+J
 31 ARR(IJ)=ARR(IJ)+EHNM(IM)*EHNM(JM)*CM(M)
 30 CONTINUE
    DO 32 I=1,NE
    II=(I-1)*NE+I
 32 ARR(II)=ARR(II)+PN(I)*RB(I)
    CALL SAXB(NE,NE,1,ARR,BE,0,IN,KER)
```

```
      IF(KER.NE.0.) CALL EXIT
      PRINT 121
121 FORMAT(////,' CORRECTION CURRENTS',/)
      PRINT 113,(BE(N),N=1,NE)
      DO 33 M=1,ME
      I1=NRF(M)
      J1=MZF(M)
      I1J1=(J1-1)*NR+I1
 33 BZC(M)=EHO(M)-STO(I1J1)
      DO 34 M=1,ME
      BZA(M)=0.
      DO 34 N=1,NE
      NM=(M-1)*NE+N
 34 BZA(M)=BZA(M)+EHNM(NM)*BE(N)
      PRINT 122
122 FORMAT(//,'    CORRECTION FIELD REQUESTED',/)
      PRINT 113,(BZC(M),M=1,ME)
      PRINT 123
123 FORMAT(//,'    ACTUAL FIELD RETURNED',/)
      PRINT 113,(BZA(M),M=1,ME)
      L=NCT
      DO 35 I=1,NE
      L=L+1
      RCC(L)=RB(I)
      ZCL(L)=ZB(I)
      ZCR(L)=ZB(I)
      CCC(L)=BE(I)
 35 XNTC(L)=1
      NCT=NCT+NE
      RETURN
      END
```

APPENDIX B

REPRINTS OF JOURNAL PUBLICATIONS BASED ON WORK
CARRIED OUT UNDER AFOSR SPONSORSHIP

SPACE-CHARGE-LIMIT INSTABILITIES IN ELECTRON BEAMS

Space-charge-limit instabilities in electron beams

E. A. Coutsias and D. J. Sullivan[*]

Department of Mathematics, University of New Mexico, Albuquerque, New Mexico 87131

(Received 22 April 1982)

The method of characteristics and multiple-scaling perturbation techniques are used to study the space-charge instability of electron beams. It is found that the stable oscillating state (virtual cathode) created when the space-charge limit is exceeded is similar to a collisionless shock wave. The oscillatory solution originates at the bifurcation point of two unstable steady states. Complementary behavior (virtual anode) results when an ion beam exceeds its space-charge limit. The virtual cathode can also exist in the presence of a neutralizing heavy-ion background. The Pierce instability, where the electron and ion charge densities are equal, is a special case of this broader class. Estimates of the nonlinear growth rate of the instability at the space-charge limit are given.

I. INTRODUCTION

Since the discovery of the Child-Langmuir relation[1,2] it has been known that exceeding the limiting current of a diode leads to the development of a virtual cathode. Subsequently, numerous papers were written on experiments and theory relating to space-charge—limited flows. Reference 3 provides an excellent background and bibliography. More recently, the exact steady-state solutions for electron beams in one-dimensional relativistic diodes[4] and bounded drift spaces[5] were derived. It is easily seen that for sufficiently large currents there exist two steady states for an electron beam, only one of which is stable.[6] At the space-charge limit (SCL) these two states coalesce, and above the SCL they disappear.[7] As current is increased past the SCL, the beam develops a jump instability and relaxes into an oscillating state.

In the early 1960's, computer models were developed which quantitatively depicted the nonlinear oscillatory nature of the virtual cathode.[8-10] These were one-dimensional, nonrelativistic, electrostatic, multiple-sheet models. References 8 and 9 qualitatively pointed out many interesting dependencies of the oscillation frequency and potential minimum position on injected current, thermal spread, and circuit resistance. Reference 10 presents computer experiments with one and two species.

The phenomenon of virtual-cathode formation in intense relativistic electron beams figures prominently in a number of high-interest research areas. Devices used to produce high-current ion beams for inertial-confinement fusion—pinch reflex diodes[11,12] and reflex triodes[13,14]—depend on the virtual cathode to inhibit electron transport and use its potential well to accelerate ions. The recent concept of the spherical electron-to-ion converter[15] requires a virtual cathode.

The virtual cathode plays a dominant role in areas other than production of light-ion beams for fusion. It is attributed with the main role in collective ion acceleration in neutral gas.[16,17] Control of virtual-cathode motion is the mechanism for acceleration in the Ionization Front Accelerator.[18,19] It is also the acceleration method in two concepts for collective-effect accelerators.[20,21] A final application is the use of virtual-cathode oscillations to produce high-power short-wavelength microwaves.[22-25] Experiments using reflex triodes have already produced 1.4 GW of power with 12% beam-to-rf energy-conversion efficiency.[26]

In this paper we use multiple-scaling perturbation techniques to study the time-dependent behavior of a beam when the SCL is exceeded. We derive estimates for the nonlinear growth rate of the ensuing instability and show that even below the SCL the beam is unstable to sufficiently large perturbations. The method can be applied to a wide class of problems, but here we treat the short-circuited one-dimensional electrostatic diode depicted in Fig. 1 as the simplest model containing the appropriate physics. We show that, at least in one dimension, an arbitrary heavy-ion background does not alter the qualitative behavior of the beam and present numerical results that exhibit virtual-cathode oscillations for a neutral beam.

II. PHYSICAL DESCRIPTION

Simulations were carried out in conjunction with the theory presented in the next section using a two-dimensional, relativistic, electrostatic, particle-in-cell code. The code can solve self-consistently for the time-dependent trajectories of tens of thousands of plasma particles over thousands of plasma
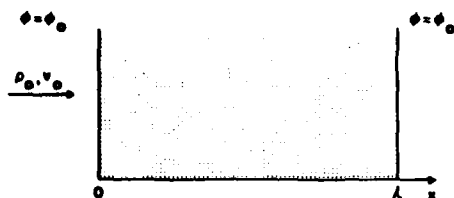
FIG. 1. Schematic of the short-circuited one-dimensional electrostatic diode modeled in this study.

FIG. 2. Electrostatic potential minimum as a function of current α. Plot depicts the various possible solutions such as normal-C flow (stable), C-overlap (unstable), the partially reflected solution (unstable), and the oscillatory virtual cathode (stable). Motion around the hysteresis loop is denoted by arrows.

periods. All variables are expressed in dimensionless terms. Therefore length is in units of c/ω_p, time is measured in units of ω_p^{-1}, and particle velocity is given by

$$v_i = \beta_i \gamma \quad (i = 1,2,3),$$

where ω_p is the initial electron plasma frequency.

In these simulations a monoenergetic 51-keV electron beam is injected into a Cartesian geometry. The left and right boundaries are grounded, representing a planar short-circuited diode. Periodic boundary conditions in the transverse direction make configuration space effectively one-dimensional. In general, the simulation had 62 cells in the longitudinal direction modeling a length of $1.0c/\omega_p$. The time step was $0.0125\omega_p^{-1}$. Twenty particles were injected per cell.

A detailed discussion of the physical dynamics of the virtual cathode based on these numerical results is appropriate here. The usual graph of potential minimum ϕ_m in the diode versus electron-beam current α is shown in Fig. 2. The parameter α will be discussed later. When α is increased above the space-charge limit, ϕ_m jumps from the stable normal-C branch to the oscillatory stable branch. The amplitude and position of ϕ_m while on the oscillatory branch describe a limit cycle, as expected for a relaxation oscillation which this represents. Typical limit cycles are depicted in Fig. 3. As α is increased further, ϕ_m, the oscillation frequency, and virtual-cathode position within the diode asymptotically approach limiting values. If α is decreased, the oscillation amplitude $\Delta\phi_m$ decreases, and the position of ϕ_m moves toward the diode center. The electron flow reverts to the equilibrium steady state when the perturbation due to the rate of change of diode current below the space-charge limit is sufficiently large. This normally occurs before the bifurcation point is reached. The entire process forms a hysteresis loop, which is depicted in Fig. 2.

The virtual cathode originates at the bifurcation point. This is the intersection of the oscillatory state with the C-overlap[7] and partially reflected solution branches.[5] The bifurcation point cannot be reached
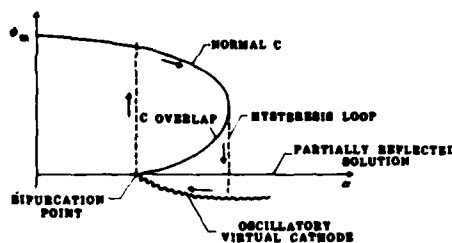
in the short-circuited diode. Of the three branches emanating from it, two (the steady ones) are physically unstable while the oscillatory branch is numerically unstable at this point. This results because the limit cycle at the bifurcation point is infinitesimally small, so that simulation codes lose resolution before it can be reached. Loss of resolution creates a small-amplitude high-frequency oscillation observed in this study and previously.[9] This result is numerical, not physical.

This problem can be overcome if we eliminate the hysteresis loop. Then the C-overlap branch disappears, and we can get to the bifurcation point along the stable normal-C branch. This can be accomplished in several ways. The most appropriate in this study is to have a retarding potential difference across the diode equal to the injected-electron kinetic energy. Then the C-overlap solution vanishes, and the bifurcation takes place at the space-charge limit α_{SCL}. The oscillation can be described as a small perturbation on the beam rather than the radical change that results in the short-circuited diode when α_{SCL} is exceeded. This analysis indicates that the onset of virtual-cathode formation occurs when the electron velocity in the steady state vanishes at some point inside the diode. For the short-circuited diode, this occurs at the diode center; for the biased diode, it occurs at $x \leq l$. Because the oscillation is a small perturbation on the steady-state fields in the biased diode, it is readily seen that the virtual-cathode oscillation period at onset is the electron transit time from the injection plane to the position where the velocity vanishes.

Finally, consider the particle dynamics during the oscillation period for counterclockwise limit cycles $(\alpha \leq \alpha_{SCL})$ as in Fig. 3(c). At the point where the virtual-cathode position is a minimum and the potential well is starting to move to the right, its amplitude is too small to stop the electrons. When its motion is to the left it opposes the electron beam
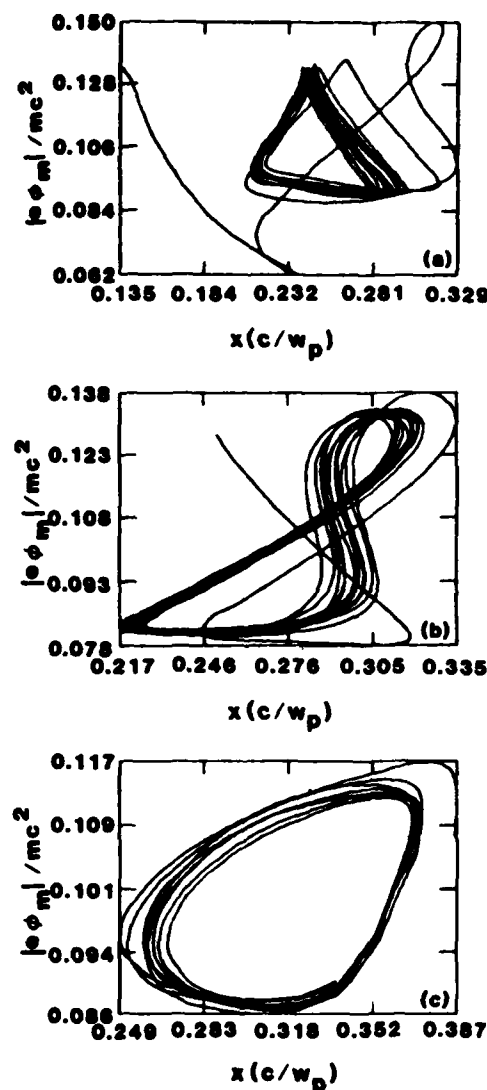
FIG. 3. Typical virtual-cathode limit cycles in the classical short-circuited one-dimensional diode with an injection energy of 51 keV. (a) $\alpha=2.5$, (b) $\alpha=2.0$, and (c) $\alpha=1.4$. Motion in (a) is clockwise and in (c) is counterclockwise. $l=1.0c/\omega_p$.

and causes particle bunching. Since the well is deeper, the stream velocity will vanish at some location and then become negative. Here, the second derivative of the velocity (d^2u/dx^2) is also negative. In this process the stream is continuously deformed to create a double-valued negative velocity protrusion. The entire system is three-valued (Fig. 4), as in a collisionless shock wave.[27] Here, the region of triple flow is not limited, as in usual collisionless shocks, by the presence of a transverse magnetic field,[28] but rather by the presence of the walls. Indeed, the reflected part detaches from the main beam and exits through the anode periodically, thus

being responsible for the onset of oscillatory behavior in beam characteristics. As the potential minimum reaches the end of its left motion the two "lips" of the back reflected stream close. At this point no more electrons are reflected, and the well moves to the right, repeating the cycle.

For larger values of α the limit cycle is distorted into a figure "8" with one lobe having a clockwise motion and the other a counterclockwise one [Fig. 3(b)]. This transition continues until the motion is completely clockwise [Fig. 3(a)]. It indicates a change in the particle bunching process and is related to the fraction of current which is reflected versus transmitted from the injected-electron beam. In Fig. 3(a) most of the beam is reflected, whereas in Fig. 3(c) most electrons are transmitted.

III. THEORY

The one-dimensional motion of electrons in the diode is given by the equations of continuity and momentum conservation for the electrons plus Poisson's equation. They are expressed here as

$$\rho_{\tilde{t}}+(\rho v)_{\tilde{x}}=0 , \tag{1a}$$

$$v_{\tilde{t}}+vv_{\tilde{x}}=-(e/m)\xi , \tag{1b}$$

$$\epsilon_0\xi_{\tilde{x}}=\rho+\rho_h , \tag{1c}$$

where $0\leq\tilde{x}\leq l$. The subscripts denote differentiation with respect to that variable. Electron and heavy-ion charge densities, and electron velocity, electric field, time, and position, are indicated by ρ, ρ_h, v, ξ, $\tilde{t}$, and $\tilde{x}$, respectively. The appropriate boundary conditions are $v(0,\tilde{t})=v_0$, $\rho(0,\tilde{t})=\rho_0$, and $\int_0^l \xi d\tilde{x}=0$. An ion component is placed in Poisson's equation in order to discuss two-species space-charge flow. Conservation equations of mass and momentum for the heavy ions are not included, because it is assumed that their velocity does not change appreciably during their passage through the diode.

In order to simplify the mathematics, we introduce dimensionless equations for our model. They are

$$n_t+(nu)_x=0 , \tag{2a}$$

$$u_t+uu_x=-\alpha E , \tag{2b}$$

$$E_x=\alpha(n+I) , \tag{2c}$$

where $n=\rho/|\rho_0|$, $u=v/v_0$,

$$E=(e\epsilon_0/m|\rho_0|)^{1/2}\xi/v_0 ,$$

$$t=v_0\tilde{t}/l , \quad \tilde{x}=x/l ,$$

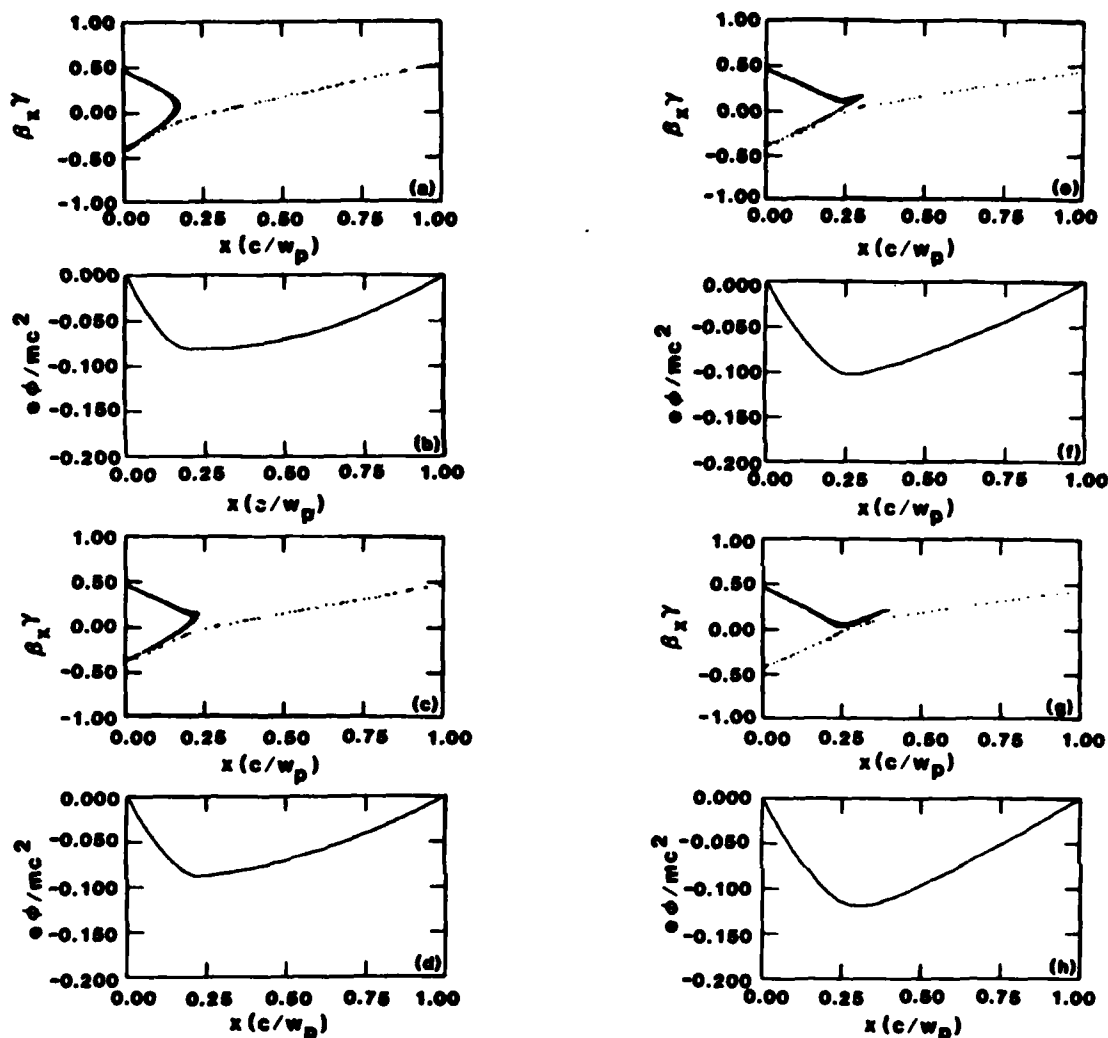$$\alpha=(e|\rho_0|/\epsilon_0 m)^{1/2}l/v_0$$

FIG. 4. Successive snapshots of electron-beam momentum space and corresponding potential shape in the diode for $\alpha = 2.0$, $l = 1.0c/\omega_p$. Time between frames is $0.5\omega_p^{-1}$. Initial beam kinetic energy is 51 kev.

(a dimensionless parameter related to current), and the ratio of heavy-ion to electron charge densities, $I = \rho_h / |\rho_0|$. Alternatively, α may be written as $l\omega_p/v_0$, where ω_p is the beam plasma frequency. The boundary conditions for electrons become $u(0,t) = 1$, $n(0,t) = -1$, and $\int_0^1 E\,dx = 0$. For an ion beam, $n(0,t) = 1$; otherwise, the following derivation is the same.

A. Unneutralized beams

For an unneutralized beam, setting $I = 0$ and solving by the method of characteristics[29,30] we find

$$n^{-1} = -\frac{1}{2}\alpha^2(t-s)^2 + \alpha E_0(s)(t-s) - 1 , \qquad (3)$$

where s is the entry time for the particle occupying

position x at time t, and $E_0(s)$ is the electric field at $x = 0$. The particle trajectories are found by utilizing Eq. (2a), from which it follows that

$$\left[\frac{\partial x}{\partial s}\right]_t = n^{-1} . \qquad (4)$$

This yields

$$x = \frac{1}{6}\alpha^2(t-s)^3 + \alpha \int_t^s E_0(s)(t-s)ds + (t-s) . \qquad (5)$$

Integration of the trajectory equation is hard for general time-dependent situations, because imposing the proper boundary conditions leads to a nonlinear integral equation for $E_0(t)$. However, several special cases can be solved exactly. The problem of injec-

tion into an empty diode can be integrated until the formation of a singularity in n, indicating the crossing of trajectories.[30] In this case, the stream velocity becomes three-valued, and one must use a Vlasov-equation description,[31] rather than system (2) that is derived assuming a single stream of monoenergetic particles. As described in Sec. II, this multistreaming is characteristic of the oscillatory state created when α exceeds its SCL value.

Using these equations we can derive a similar representation for Fig. 2 in terms of E_0 and α. For steady states, $E_0(t) = E_0$, a constant, we find

$$u = -n^{-1} = \tfrac{1}{2}\alpha^2(t-s)^2 - \alpha E_0(t-s) + 1 , \quad (6a)$$

$$x = \tfrac{1}{6}\alpha^2(t-s)^3 - \tfrac{1}{2}\alpha E_0(t-s)^2 + (t-s) . \quad (6b)$$

Imposing the conditions $x = 1$, $u = 1$ at $t-s = t_0$, the particle transit time, we note that t_0 must satisfy

$$\tfrac{1}{12}\alpha^2 t_0^3 - t_0 + 1 = 0 . \quad (7)$$

This equation has two positive solutions for $0 \leq \alpha \leq \tfrac{4}{3}$, coalescing at $\alpha = \tfrac{4}{3}$. The largest one, for $0 \leq \alpha < 2\sqrt{2}/3$ does not correspond to a real flow. In Fig. 5 we show E_0 ($= \alpha t_0/2$) vs α. This representation will be used in the discussion of nonlinear stability.

B. Neutralized beams

The Pierce instability occurs when electron and ion space-charge flow is considered in finite geometries where there is no potential difference across the boundaries.[32] The ions can be stationary or moving with respect to the electrons. Charge neutrality is maintained at the injection plane. This instability may have ramifications for charged-particle inertial confinement fusion because of its effect on neutralized-beam propagation in the reactor.[33] In this section, we show that the Pierce instability is a special case of electron and ion space-charge flow. In general, two-species flow has steady and oscillatory states analogous to one-species space-charge flow.

The steady-state behavior for the case of arbitrary I can be found in a manner similar to $I = 0$. Rewriting system (2) in characteristic coordinates, we arrive at

$$\frac{d^2}{dt^2}\left[1 + \frac{I}{n}\right] + \alpha^2 I \left[1 + \frac{I}{n}\right] = 0 . \quad (8)$$

For positive ions ($I > 0$) the solution of (8) after satisfying the boundary conditions is

$$1 + I/n = (1+I)\cos[\alpha\sqrt{I}(t-s)]$$
$$+ E_0\sqrt{I}\,\sin[\alpha\sqrt{I}(t-s)] . \quad (9)$$

Imposing conditions $x = 1$, $u = 1$ at $t-s = t_0$, we find the system

$$1 = \frac{1}{I}t_0 - \left[\frac{1-I}{\alpha I^{3/2}}\right]\sin(\alpha\sqrt{I}t_0)$$
$$+ \frac{E_0}{\alpha I}[\cos(\alpha\sqrt{I}t_0) - 1] , \quad (10a)$$

$$1 = \frac{1}{I} - \left[\frac{1-I}{I}\right]\cos(\alpha\sqrt{I}t_0)$$
$$- \frac{E_0}{I}\sin(\alpha\sqrt{I}t_0) . \quad (10b)$$

For $I = 1$, which implies charge neutralization, these equations reduce to the relations given in Ref. 34 for the Pierce instability. However, by varying I the curves shown in Fig. 6 are obtained. These are cuts at constant I through a three-dimensional contiguous surface. The space is defined by the axes $\bar{E} = E_0 I^{1/2}$, $A = \alpha I^{3/2}$, and I. The surface is 2π periodic in A with the vertical plane at $A = 2\pi$ being common for all values of I. For given A, a linearized analysis establishes that the equilibria denoted by the curves are stable (unstable) for the lowest (highest) value of $\bar{E}$. At $I = 1$, exchange of stability takes place at odd multiples of π. For $I < 1$, exchange of stability occurs at the points where $dE_0/d\alpha \to \infty$.

It is evident from Fig. 6 that, for $I < 1$, there are no stable equilibrium solutions in the neighborhood of $A = \pi$. Therefore one expects a virtual cathode to form when $I < 1$ and A adiabatically increases to π. We have found, by using numerical simulation, that in this case the beam settles to an oscillatory state, similar to the virtual cathode for unneutralized
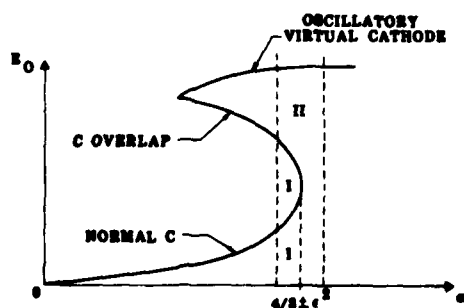

FIG. 5. Electric field at the injection plane vs current α for $I = 0$. Plot depicts the normal C-flow (stable) and C-overlap (unstable) solutions. Oscillating virtual-cathode (stable) solution is also shown. Regions I and II define the domains of attraction of the normal-C and virtual-cathode solutions near the SCL, $\alpha = \tfrac{4}{3}$.
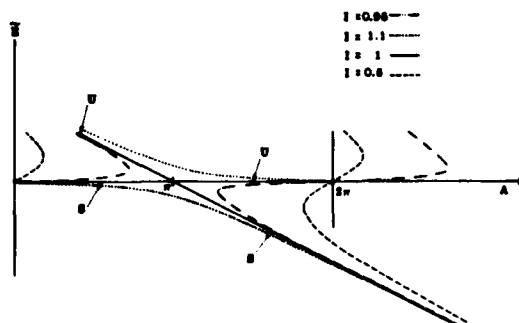
FIG. 6. Curves of scaled electric field at the injection plane $\tilde{E}$ vs scaled current A for various values of charge neutralization I. Curves represent slices through a three-dimensional surface. S and U indicate stable and unstable branches, respectively, for the $I = 1$ slice.

beams.[31] By slowly increasing I past the neutral-beam value of 1 in our simulation, we have established that this oscillation persists. Indeed, finding this oscillatory state for $I > 1$ by other means would have been difficult, because the simulation would tend to follow the stable steady-state branch that is present for all values of current.

C. Nonlinear stability analysis

For $I < 1$, it is of interest to establish the properties of the beam instability at the SCL—generalized for $I \neq 0$ to mean the point where $d\alpha/dE_0 = 0$. We shall carry out the analysis for $I = 0$, but our method can be applied to any similar jump phenomenon.

A linear stability analysis[6] about the steady state described by (7) results in the dispersion relation

$$(2 + \beta)e^{-\beta} = 2 - \beta + \beta^3/(\alpha^2 t_0^3) , \tag{11}$$

where $\beta = i\omega t_0$. We have written the expression derived in Ref. 6 in terms of our dimensionless variables. For α near the SCL value we let

$$\alpha = \tfrac{4}{3} - \epsilon^2 , \quad \epsilon \ll 1 \tag{12}$$

and find from (7) that near this value, t_0 is approximately

$$t_0 \simeq \frac{3}{2} \mp \epsilon \frac{3}{2\sqrt{2}} + O(\epsilon^2) , \tag{13}$$

where the $-$ ($+$) sign corresponds to the lower (upper) branch in Fig. 5.

By substituting in (11), and assuming β small, we find that

$$i\omega = \beta \simeq \mp 2\sqrt{2}\epsilon + O(\epsilon^2) . \tag{14}$$

Since the linearized analysis led to time factors of the form $e^{i\omega t}$ in the perturbations, it follows that the lower branch in Fig. 5 is stable and the upper un-

stable, while at the SCL ($\epsilon = 0$) we have neutral stability.

Above the value $\alpha = \tfrac{4}{3}$, linearized theory is not applicable. Utilizing multiple-scaling perturbation theory,[35] we can carry out a nonlinear stability analysis near $\alpha = \tfrac{4}{3}$. In system (2) we set $\alpha = \tfrac{4}{3} \pm \epsilon^2$. In this neighborhood, perturbations evolve on a "slow" time scale, depicted by $\tau = \epsilon t$.

Eliminating the electric field by combining (2b) and (2c) and utilizing τ, system (2) becomes

$$\epsilon n_\tau + (nu)_x = 0 , \tag{15a}$$

$$(\epsilon u_\tau + uu_x)_x = -(\tfrac{4}{3} \pm \epsilon^2)^2 n \tag{15b}$$

with conditions $u(0,\tau) = 1$, $n(0,\tau) = -1$, and $\int_0^1 E \, dx = 0$ rewritten as

$$\epsilon \int_0^1 u_\tau dx + \tfrac{1}{2}[u^2(1,\tau) - u^2(0,\tau)] = 0 . \tag{16}$$

Substituting the asymptotic expansions

$$u \sim \sum_{i=0}^{j} \epsilon^i u_i(x,\tau) + O(\epsilon^{j+1}) ,$$

$$n \sim \sum_{i=0}^{j} \epsilon^i n_i(x,\tau) + O(\epsilon^{j+1}) , \tag{17}$$

for u and n into (15) and equating coefficients of various powers of ϵ, there results a hierachy of equations for the u_i and n_i.

Solving the $O(1)$ system gives

$$(u_0 - \tfrac{1}{2})(u_0 + 1)^2 = 2(2x - 1)^2 , \tag{18a}$$

$$n_0 = -1/u_0 . \tag{18b}$$

To solve the $O(\epsilon)$ system we introduce a new variable q by

$$x = \frac{16}{9}\left[\frac{q^3}{6} - \frac{3}{8}q^2\right] + q , \tag{19}$$

so that

$$u_0 = \frac{16}{9}\left[\frac{q^2}{2} - \frac{3}{4}q\right] + 1 . \tag{20}$$

We then find

$$n_1 = \frac{1}{u_0^2}u_1 , \tag{21a}$$

$$u_1 = C\frac{q(q - \tfrac{3}{2})}{u_0} \tag{21b}$$

with C a constant of integration which is, in general, a function of the slow time τ. To find $C = C(\tau)$ which determines the slow evolution of the perturbation $u_1(x,\tau)$ we need to go to the next order, $O(\epsilon^2)$. By substituting in the expressions for u_0, u_1, n_0, n_1 and eliminating n_2, we find that $u_2(x,\tau)$ satisfies

$$(u_0 u_2)_{xx} + \frac{16}{9}\frac{1}{u_0^2}u_2 = \frac{16}{9}\frac{C_\tau}{u_0}\int_0^q \frac{q(q-\frac{3}{2})}{u_0^2}dq + C^2\frac{q^2(q-\frac{3}{2})^2}{u_0^3} - C_\tau\left[\frac{q(q-\frac{3}{2})}{u_0}\right]_x \pm \frac{8}{3}\frac{1}{u_0}, \tag{22a}$$

$$u_2(0,\tau)=0, \quad u_2(1,\tau)=+\frac{9}{16}C_\tau. \tag{22b}$$

The solution to this inhomogeneous two-point boundary-value problem exists provided a certain orthogonality condition between the right-hand side and the solution of the adjoint problem that takes account of the boundary conditions is satisfied (Fredholm alternative theorem).[36] This leads to the desired equation determining $C(\tau)$,

$$aC_\tau + bC^2 \pm c = 0, \tag{23}$$

where a, b, and c are found to be

$$a = -\int_0^{3/2}\frac{q(q-\frac{3}{2})}{u_0^2}[\frac{16}{27}q^2(q-\frac{9}{4})+\frac{3}{2}]dq = 1.6850, \tag{24a}$$

$$b = \frac{8}{3}\int_0^{3/2}\frac{q^3(q-\frac{3}{2})^3}{u_0^4}dq = -3.7968, \tag{24b}$$

$$c = \frac{8}{3}\int_0^{3/2}q(q-\frac{3}{2})dq = -1.5. \tag{24c}$$

In (23) the $(+)$ or $(-)$ signs indicate that we are above or below the SCL, respectively.
Above the SCL, we find

$$C(\tau) = -\frac{c}{b}\tan\left[\sqrt{cb}\left[\frac{\tau+\tau_0}{a}\right]\right]; \tag{25}$$

and below the SCL,

$$C(\tau) = \begin{cases} \frac{c}{b}\tanh\left[\sqrt{cb}\left[\frac{\tau+\tau_0}{a}\right]\right], & |C(0)| < (c/b)^{1/2} \tag{26} \\ \frac{c}{b}\coth\left[\sqrt{cb}\left[\frac{\tau+\tau_0}{a}\right]\right], & |C(0)| > (c/b)^{1/2} \tag{27} \end{cases}$$

where τ_0 is a constant of integration. In general, small initial perturbations will lead to the solution

$$u(x,t) \sim u_0 + \epsilon \sum_{i=1} C_i(\tau)e^{\omega_i t}u_i(x) + O(\epsilon^2), \tag{28}$$

where ω_i are the various distinct solutions of the dispersion relation (11) at $a = \frac{4}{3}$.[35,37] It is straightforward to show that all modes are such that $\text{Re}\omega_i < 0$ except one for which $\omega = 0$. Thus all other modes will decay in the fast time scale and only the neutral mode ($\omega = 0$) will persist. Our solution after a short time will look like

$$u \sim u_0 + \epsilon C(\tau)\frac{q(q-\frac{3}{2})}{u_0} + O(\epsilon^2). \tag{29}$$

From the given initial conditions it is easy to determine the initial condition for the neutral mode. Below the SCL, if the initial conditions are such that $C(0) > -(c/b)^{1/2}$, the solution will evolve to

the stable lower branch in Fig. 5 (region I), while if $C(0) < -(c/b)^{1/2}$, $C \to \infty$ in finite time (Fig. 5, region II). Blowup in finite time also occurs above the SCL for any $C(0)$. This does not mean that the actual solution blows up, just that it evolves to a final state far away from the two steady-state branches shown in Fig. 5 and thus is not accessible by perturbation theory.

As can be seen in (25), the blowup above the SCL is described by a tangent function, therefore the growth rate we find for this case must be appropriately interpreted. Note that the linearized dispersion relation seems to suggest an imaginary exponential growth rate above the space-charge limit.[3,6] In view of our results, we see that this is actually misleading. Moreover, we find that even below the SCL the stable steady-state branch can be destabilized by sufficiently large perturbations.

Our results agree with the linear theory, provided we consider the limit where the latter becomes ap-

plicable. Thus we must compare the linear theory with (26) as $\tau \to +\infty$ (near the stable branch) and (27) as $\tau \to -\infty$ (near the unstable branch). To demonstrate this we set $\tau = \epsilon t$ in (26) and consider the limit $\tau \to +\infty$. Then

$$C(t) = \frac{c}{b} \tanh \left[\frac{\sqrt{cb}}{a} (\epsilon t + \tau_0) \right]$$

$$= \frac{c}{b} \frac{1 - \exp\left[-\frac{2\sqrt{cb}}{a}(\epsilon t + \tau_0) \right]}{1 + \exp\left[-\frac{2\sqrt{cb}}{a}(\epsilon t + \tau_0) \right]}$$

$$\simeq \frac{c}{b} \left[1 - 2\exp\left[-\frac{2\sqrt{cb}}{a}(\epsilon t + \tau_0) \right] \right.$$

$$\left. + \cdots \right] . \tag{30}$$

We see that the decay rate of the perturbations as $t \to +\infty$ is equal to

$$\frac{2\sqrt{cb}}{a}\epsilon \approx 2.83\epsilon , \tag{31}$$

which is the same as that found by the linearized analysis.[6] This quantity is important as it also determines an initial "growth rate" for the jump instability above the SCL described by (25). If we substitute the original dimensional time variable into our expressions and write the deviation of α from its value at the SCL as

$$\epsilon = (\alpha - \alpha_{SCL})^{1/2} = (\alpha - \tfrac{4}{3})^{1/2} , \tag{32}$$

we find that the "growth rate" is given by

$$D = (\alpha - \tfrac{4}{3})^{1/2} \frac{\sqrt{cb}}{a} \frac{v_0}{l} \tag{33}$$

or

$$D = \left[\frac{l\omega_p}{v_0} - \frac{4}{3} \right]^{1/2} \sqrt{2} \frac{v_0}{l} . \tag{34}$$

Of course, for the expansions in (28) to be valid, we must have $C(\tau) \ll 1/\epsilon$. However, while C is not too large, (25) gives a reliable estimate for the growth rate of the instability.

ACKNOWLEDGMENTS

*Permanent address: Mission Research Corporation, 1720 Randolph Rd. S.E., Albuquerque, NM 87106.

[1]G. D. Child, Phys. Rev. (Ser. I) 32, 492 (1911).

[2]I. Langmuir, Phys. Rev. 21, 419 (1923).

[3]C. K. Birdsall and W. B. Bridges, Electron Dynamics of Diode Regions (Academic, New York, 1966), Chap. 3.

[4]H. R. Jory and A. W. Trivelpiece, J. Appl. Phys. 40, 3924 (1969).

[5]V. S. Voronin, Yu. T. Zozulya, and A. N. Lebedev, Zh. Tekh. Fiz. 42, 546 (1972) [Sov. Phys.—Tech. Phys. 17, 432 (1972)].

[6]R. J. Lomax, Proc. IEEE 108, 119 (1961).

[7]C. E. Fay, A. L. Samuel, and W. Shockley, Bell Syst. Tech. J. 17, 49 (1938).

[8]C. K. Birdsall and W. B. Bridges, J. Appl. Phys. 32, 2611 (1961).

[9]W. B. Bridges and C. K. Birdsall, J. Appl. Phys. 34, 2946 (1963).

[10]D. A. Dunn and I. T. Ho, AIAA J. 1, 2770 (1963).

[11]S. A. Goldstein and R. Lee, Bull. Am. Phys. Soc. 23, 763 (1978).

[12]R. A. Meyer, S. A. Goldstein, D. D. Hinshelwood, and G. Cooperstein, Bull. Am. Phys. Soc. 24, 977 (1979).

[13]D. S. Prono, J. M. Creedon, I. Smith, and N. Bergstrom, J. Appl. Phys. 46, 3310 (1975).

[14]D. S. Prono, J. W. Shearer, and R. J. Briggs, Phys. Rev. Lett. 37, 2 (1976).

[15]P. A. Miller, J. A. Halbleib, J. W. Poukey, and J. T. Verdeyen, J. Appl. Phys. 52, 593 (1981).

[16]J. W. Poukey and N. Rostoker, Plasma Phys. 13, 897 (1971).

[17]C. L. Olson, in Collective Ion Acceleration-Springer Tracts in Modern Physics (Springer, Berlin, 1979), Vol. 84.

[18]C. L. Olson, IEEE Trans. Nucl. Sci. NS-26, 4231 (1979)

[19]C. L. Olson, J. R. Woodworth, C. A. Frost, and R. A. Gerber, IEEE Trans. Nucl. Sci. NS-28, 3349 (1981).

[20]R. B. Miller, in Proceedings of the Second International Topical Conference on High-Power Electron and Ion Beam Research and Technology (Cornell University Press, Ithaca, N.Y., 1977), p. 613.

[21]R. B. Miller, in Collective Methods of Acceleration, edited by N. Rostoker and M. Reiser (Harwood, New York, 1979), p. 675.

[22]R. A. Mahaffey, P. Sprangle, J. Golden, and C. A. Kapetanakos, Phys. Rev. Lett. 39, 843 (1977).

[23]H. E. Brandt, A. Bromborsky, H. B. Bruns, and R. A.

Kehs, in Ref. 20, p. 649.

[24]J. M. Buzzi, H. J. Doucet, B. Etlicher, P. Haldenwang, A. Huetz, H. Lamain, C. Rouille, J. Cable, J. Delvaux, J. C. Jouys. and C. Peugnet, in Ref. 20, p. 663.

[25]D. J. Sullivan, in *Proceedings of the Third International Topical Conference on High-Power Electron and Ion Beam Research and Technology* (Institute of Nuclear Physics, Novosibirsk, USSR, 1979), p. 769.

[26]A. N. Didenko, G. P. Fomenko, I. Z. Gleizer, Ya. E. Krasik, G. V. Melnikov, S. F. Perelygin, Yu. G. Shtein, A. S. Sulakshin, V. I. Tsvetkov, and A. G. Zerlitsin, in Ref. 25, p. 683 (1979).

[27]R. Z. Sagdeev, *Reviews of Plasma Physics*, edited by M. A. Leontovich (Consultants Bureau, New York, 1966), Vol. 4, p. 23.

[28]S. S. Moiseev and R. Z. Sagdeev, Plasma Phys. $\underline{5}$, 43 (1963).

[29]G. B. Whitham, *Linear and Nonlinear Waves* (Wiley, New York, 1974).

[30]E. A. Coutsias and D. J. Sullivan (unpublished).

[31]D. J. Sullivan and E. A. Coutsias, in *High-Power Beams '81*, edited by H. J. Doucet and J. M. Buzzi (Ecole Polytechnique, Palaiseau, France, 1981), p. 371.

[32]J. R. Pierce, J. Appl. Phys. $\underline{15}$, 721 (1944).

[33]J. W. Poukey, J. P. Quintenz, and C. L. Olson, Appl. Phys. Lett. $\underline{38}$, 20 (1981).

[34]B. B. Godfrey, Mission Research Corporation Report No. AMRC-R-282, 1981 (unpublished).

[35]J. Kevorkian and J. D. Cole, *Perturbation Methods in Applied Mathematics* (Springer, Berlin, 1981).

[36]G. Birkhoff and G. Rota, *Ordinary Differential Equations* (Ginn, Boston, 1962).

[37]A. V. Paschenko and B. N. Rutkevich, Fiz. Plazmy $\underline{3}$, 774 (1977) [Sov. J. Plasma Phys. $\underline{3}$, 437 (1977)].

HIGH POWER MICROWAVE GENERATION FROM A
VIRTUAL CATHODE OSCILLATOR (VIRCATOR)

HIGH POWER MICROWAVE GENERATION FROM A VIRTUAL CATHODE OSCILLATOR (VIRCATOR)

Donald J. Sullivan
Mission Research Corporation
Albuquerque, New Mexico 87106

Abstract

High power microwaves, up to Gigawatt levels in the centimeter regime, have been observed in reflex triode, foil and foilless diode systems. Generation efficiencies range from 1% to 12%. The source of the microwaves is an oscillating virtual cathode - the nonlinear state which develops when the electron beam injection current exceeds the space-charge limiting current defined by the beam energy and wave guide geometry. This stable oscillation results in severe longitudinal charge bunching giving rise to large time dependent current variations. The experimental frequency dependence and broadband characteristics are explained by the scaling of the oscillator frequency with $\sqrt{n_b/\gamma}$, where n_b is the beam density and γ its relativistic factor, in conjunction with the Child-Langmuir relation. The optimal design for a narrow-band millimeter wave vircator is based on a foilless diode with a strong axial magnetic field. It will be tunable over an order of magnitude in frequency by varying the magnetic field strength.

Introduction

Of the several millimeter sources that are in various stages of development, the virtual cathode oscillator (Vircator) has a combination of characteristics which recommend it for high frequency use. First, the frequency of the vircator is tunable by changing the magnitude of an imposed axial magnetic field, eliminating any requirement to change the physical structure of the device. A single vircator will *be tunable over an order of magnitude in frequency* (e.g., 10 GHz - 100 GHz). Second, the bandwidth of the generator can be narrow or broad based on magnetic field shaping and the use of beam limiters described below. Third, because the vircator functions above the space-charge limiting current for the electron beam, given efficient operation, it should be capable of much higher power than other microwave sources. Finally, the lack of passive resonating structures to produce the transmitted wave reduces the problem of field emission. This also increases the maximum possible generator power.

Experimentally, the virtual cathode has already proven itself to be a copious microwave source.[1-7] Table 1 lists experiments which have been carried out to date. With the exception of the Didenko experiment at Tomsk,[4] the frequency spectra have all had a broad bandwidth and relatively low efficiency. Nevertheless, even at low efficiency the experiment at Harry Diamond Laboratories[5] using a foilless diode (1 MV, 30 kA) produced Gigawatts of power in the Ku band. It is one of the most powerful centimeter wavelength microwave sources available. It will be shown later that the foilless diode in a shaped axial magnetic field represents the best configuration for a high frequency device.

Microwave Generation

Although only scaling relations are presently available, qualitative dependencies of virtual cathode parameters on beam kinetic energy and injected current are known.[8,9] First, potential amplitude, position, and oscillation frequency all have the same functional dependence on injected beam current. These parameters

TABLE 1

HIGH POWER MICROWAVE GENERATION HAS BEEN WITNESSED IN VARIOUS ELECTRON BEAM CONFIGURATIONS WHEN VIRTUAL CATHODES ARE FORMED.

REFERENCE	SYSTEM	PEAK POWER	FREQUENCY	EFFICIENCY
1. MAHAFFEY, et al.	REFLEX TRIODE	100 MW	11 GHz* (10.0 - 12.4 GHz)	1.5%
2. BRANDT, et al.	REFLEX TRIODE	---	9.5 GHz* (7.0 - 13.0 GHz)	---
3. BUZZI, et al.	FOIL DIODE	1 GW	10 GHz* (9.0 - 14.0 GHz)	1.25%
4. DIDENKO, et al.	REFLEX TRIODE	1.4 GW	3.3 GHz* (2.1 - 5.0 GHz)	12%
5. BROMBORSKY, et al.	FOILLESS DIODE	3 GW	15 GHz* (8.2 - 18.0 GHz)	6%
6. CLARK, et al.	FOILLESS DIODE	---	WIDEBAND* (1.7 - 40.0 GHz)	---
7. EKDAHL, et al.	FOILLESS DIODE	>100 MW	>70 GHz	---

* DETECTOR BANDWIDTH IN PARANTHESES

asymptotically approach a limiting value for current above the space-charge limit. Second, the fundamental oscillation frequency is approximately the relativistic beam plasma frequency given by

$$\omega_p^{rel} = \left(\frac{4\pi n_b^0 e^2}{\gamma_0 m} \right)^{1/2} \quad (1)$$

where n_b^0 is the electron beam number density at injection γ_0 is the beam relativistic factor, e is the electron charge and m is its mass. In particular, the oscillation frequency from one-dimensional electrostatic and two-dimensional electromagnetic numerical simulations varies such that

$$\omega_p^{rel} \leq \omega_{osc} \leq \sqrt{2\pi} \, \omega_p^{rel} \quad (2)$$

The value of $\sqrt{2\pi}$ is an empirical result which has not yet been derived theoretically. The value of ω_{osc} increases with current monotonically. If the injection current exceeds the space-charge limiting current by a factor of three or greater, ω_{osc} is close to the maximum value. Equation 11 in conjunction with the Child-Langmuir law describing space-charge limited diode emission explains the experimental linear dependence of frequency on the square root of diode voltage in foil diodes and reflex triodes.

The virtual cathode oscillates stably at a set frequency in both time and space. This fluctuating potential barrier acts as a gate to reflect some electrons and transmit others. The motion of the gate bunches charge. In two dimensions the charge bunch and virtual cathode are separated spatially.

By analogy this configuration represents an LC oscillator. The virtual cathode acts as a capacitor to store the beam kinetic energy. During that portion of the limit cycle in which the potential is greater than the injected beam energy, charge is constrained to remain near the anode. This starves the virtual cathode so that its amplitude decreases below (γ_0 -1) mc^2/e. Once this occurs the charge bunch is transmitted. The electron motion represents a large time varying current through an inductor. The presence of charge away from the anode reestablishes the virtual cathode, and the cycle repeats. The effect on

beam current can be examined using simulations. A net current diagnostic is given in Fig. 1 where the probe is positioned between the anode and virtual cathode. The injected current in units of mc^3/e, v_0, is 3.4 times the limiting current, v_ℓ, and γ_0 is 3.5. Note that the virtual cathode can actually reverse the direction of current. The average current value is v_ℓ.

The oscillating current generates micro-waves.[10,11] The wave frequency is the oscillation frequency of the virtual cathode. The wave propagates down the drift tube in a TM waveguide mode, which determines the wavelength and phase velocity of the wave in the guide. The field configuration is evident in simulations where there is no axial magnetic field. If a cold beam is injected and azimuthal symmetry is assumed by the code, the only nonzero fields are E_z, E_r, and B_θ in cylindrical geometry. These three fields define a TM wave traveling in the z direction.
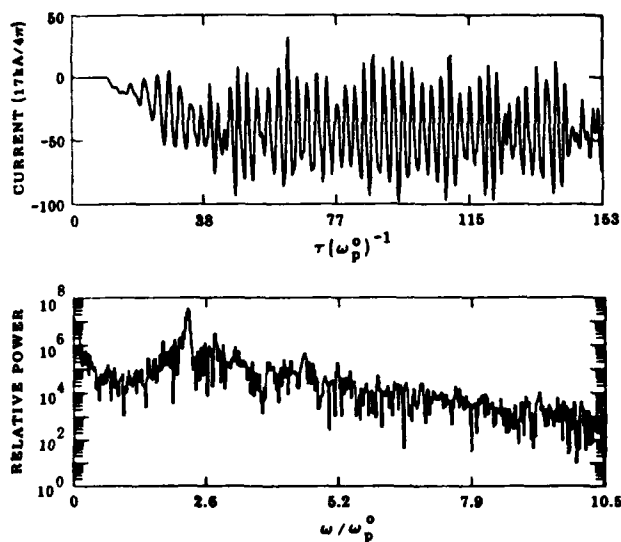

Figure 1. Net current amplitude and spectrum for a probe placed between the anode and virtual cathode. $\gamma_0=3.5$, $v_0=3.4v_\ell$.

The largest impediment to constructing an efficient vircator is the effect which heating has on the microwave generation efficiency. As noted earlier[12], beam temperature significantly damps out the amplitude of the potential oscillation. This can be understood in the following way. For a monoenergetic beam all of the charged particles bunch at the same location. Mathematically this represents a singularity where the charge density goes to infinity. In reality the charge bunch is not infinitely dense, but it does become several times greater than the initial beam injection density. The severity of the charge bunching leads to efficient microwave generation. If, on the other hand, the beam has a spread in axial momentum, the electrons will stop at different locations in the potential well. This tends to limit the charge bunching and the amplitude of the oscillating electric and magnetic fields. The effect of beam temperature in reducing the RF efficiency of the vircator has been witnessed in one-dimensional electromagnetic simulations.[13] A beam spread of less than 3% in energy reduces the microwave generation efficiency from 20% to approximately 2%. Under these conditions the vircator is nothing more than a Barkhausen oscillator.[14] Indeed, the low efficiency and broad bandwidth observed in most of the experiments to date can probably be attributed to the effects of electron reflexing in the diode region resulting in beam heating.

Vircator Design

Based on our current theoretical knowledge of the virtual cathode, numerical simulations, and experimental results, the following points must be considered in the design of a coherent, high frequency vircator. First, generation of high microwave frequencies requires large beam densities. Extremely high beam densities ($n_0 > 10^{14}$ cm^{-3}) have been obtained from a foilless diode. The beam plasma frequency scales linearly with the electron cyclotron frequency due to the magnetic field.[15] This is of significance, because it implies that a single vircator can be tuned over an order of magnitude in frequency (eg. 10-100 GHz) simply by changing the axial magnetic field strength without changing the physical structure of the device.

Second, both the oscillation frequency and net current asymptotically approach a value as injected current is increased above the space-charge limit. Thus, using a very large value of v_0/v_ℓ does not substantially increase frequency or RF efficiency where efficiency is given by

$$\eta \leq \frac{e\Delta\phi}{(\gamma_0-1)\ mc^2} \tag{3}$$

A foilless diode in a strong axial magnetic field produces a very thin annular beam. Since v_ℓ for an annular beam is larger than for a solid beam of the same area, the value of v_0/v_ℓ will be smaller for the same beam current.

In order to assure narrow bandwidth, high efficiency microwave generation at high or low frequency from the vircator, the following characteristics must be met. First, no reflexing of electrons in the region between the real and virtual cathodes must occur. Any axial magnetic field must be shaped to divert the electrons, or flux excluders must be employed to confine the magnetic field to the diode region. The latter arrangement will allow the radial space-charge electric field to perform the role of expelling electrons to the waveguide wall. In addition, if the beam is annular, a collimator may be used to help prevent reflexing of electrons back to the cathode. Second, the electron beam must be cold. Experimental[16] and theoretical[15] results indicate that foilless diodes create low emittance beams. Laminar flow, where the electron Larmor orbit is smaller than the beam thickness, is obtained when[16]

$$\omega_c > (\gamma_0 - 1)^{1/2} \frac{c}{\sqrt{a\delta/2}} \tag{4}$$

where a is the orbit radius, δ is the radial spacing between the cathode and drift tube wall (which acts as the anode) and ω_c is the electron cyclotron frequency given by eB_z/mc. Low beam scatter is also assured, because of the lack of a foil. Finally, the diode voltage and injected current must be constant. More appropriately stated, the impedance must be constant. Flat-top voltage pulses can be attained in a variety of ways in several diode configurations. However, at high voltages the foilless diode operates as a purely resistive load, therefore $\omega_{osc} = \sqrt{I/V} = 1/\sqrt{Z}$ is constant. Also, absence of diode closure in some foilless diode experiments makes a long pulse device possible.

It is evident from this discussion that the foilless diode in a strong axial magnetic field represents the optimal configuration for a high frequency vircator. It optimizes microwave power and efficiency while generating high frequency, coherent

3428

radiation. For low frequency operation a foil diode or reflex triode utilizing a high transparency mesh for the anode can be used. No axial magnetic field should be employed in order to minimize electron reflexing.

A schematic of the configuration being used in the vircator experiment[17] at Mission Research Corporation is presented in Fig. 2. The pulse power parameters are 50 kV, 66 Ω matched impedance and a pulse length of 1 μsec. The magnetic field coil is capable of attaining 60 kG. We anticipate operating at frequencies as high as 100 GHz. Even with a low efficiency of 2.5% we will produce 1 MW of RF power. A multi-channel microwave grating spectrometer in the 30-110 GHz region developed by MRC will be the chief diagnostic on this experiment.[17]

In summary, the vircator has the potential for producing very high power microwave pulses in the centimeter and millimeter wavelength regimes. In a foilless diode configuration it is tunable by adjusting the imposed axial magnetic field. In a foil diode or reflex triode tuning is accomplished by changing the A-K gap spacing. The microwave generation will be coherent and efficient, if electron reflexing into the diode region is prevented.

For an injected current $\nu_o > 3 \nu_\ell$, $f_{osc} \sim \omega_p^{rel}/\sqrt{2\pi}$. Because the oscillating beam is equivalent to a deformable dipole, the preferred waveguide mode for an axisymmetric beam in a straight-walled cylindrical guide is TM_{0n} where $n = D/\lambda_0$, D is the waveguide diameter and λ_0 is the free space wavelength. Thus, D/λ_0 should be chosen to be close to an integer value. Once n is known, the phase velocity, group velocity, wavelength and impedance of the wave in the guide are determined. Similar considerations hold for a rectangular waveguide. Note that both ν_ℓ and the cutoff wavelength, λ_c, depend on the guide dimensions and geometry. Both must be considered in choosing an experimental configuration.
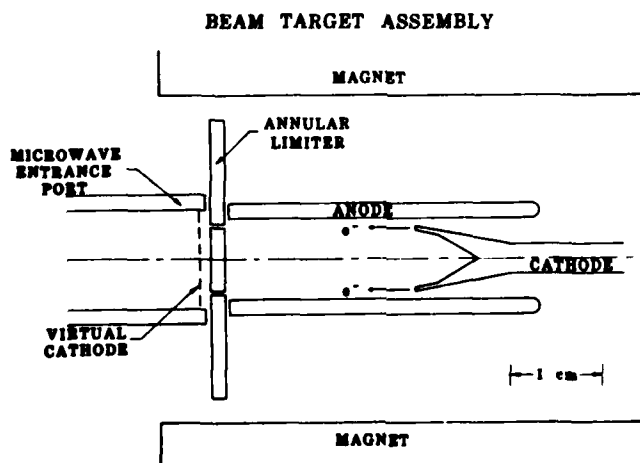
BEAM TARGET ASSEMBLY

Figure 2. Schematic of the AFOSR/MRC Vircator.

References

1. R. A. Mahaffey, P. Sprangle, J. Golden and C. A. Kapetanakos, Phys. Rev. Lett. 39, 843 (1977).

2. H. E. Brandt, A. Bromborsky, H. B. Bruns, and R. A. Kehs, in Proc. of the 2nd Intl. Top. Conf. on High Power Electron and Ion Beam Research and Technology, (Cornell University, Ithaca, New York, 1977), p. 649.

3. J. M. Buzzi, H. J. Doucet, B. Etlicher, P. Haldenwang, A. Huetz, H. Lamain, C. Rouille, J. Cable, J. Delvaux, J. C. Jouys and C. Peugnet, idem, p. 663.

4. A. N. Didenko, G. P. Fomenko, I. Z. Gleizer, Ya. E. Krasik, G. V. Melnikov, S. F. Perelygin, Yu. G. Shtein, A. S. Sulakshin, V. I. Tsvetkov, and A. G. Zerlitsin, in Proc. of the 3rd Intl. Top. Conf. on High Power Electron and Ion Beam Research and Technology, (Institute of Nuclear Physics, Novosibirsk, USSR, 1979), p. 683.

5. A. Bromborsky, H. Brandt, and R. A. Kehs, Bull. Am. Phys. Soc. 26, 165 (1981); and private communication.

6. M. C. Clark, private communication.

7. C. A. Ekdahl, private communication.

8. D. J. Sullivan and E. A. Coutsias in High Power Beams '81, Proceedings of the 4th Intl. Top. Conf. on High Power Electron and Ion Beam Research and Technology, edited by H. J. Doucet and J. M. Buzzi (Ecole Polytechnique, Palasieau, France, 1981), p. 371.

9. E. A. Coutsias and D. J. Sullivan, to be published in Phys. Rev. A., March, 1983.

10. D. J. Sullivan, Bull. Am. Phys. Soc. 25, 948 (1980).

11. D. J. Sullivan, in Proc. of the 3rd Intl. Top. Conf. on High Power Electron and Ion Beam Research and Technology, (Institute of Nuclear Physics, Novosibirsk, USSR, 1979), p. 769.

12. W. B. Bridges and C. K. Birdsall, J. Appl. Phys. 34, 2946 (1963).

13. M. A. Mostrom, T. J. T. Kwan and C. M. Snell, Bull. Am. Phys. Soc. 27, 1075 (1982).

14. H. Barkhausen and K. Kurz, Phys. Zeit. 21, 1 (1920).

15. M. E. Jones and L. E. Thode, J. Appl. Phys., 51, 5212 (1980).

16. R. B. Miller, K. R. Prestwich, J. W. Poukey, and S. L. Shope, J. Appl. Phys. 51, 3506 (1980).

17. D. J. Sullivan, D. E. Voss, W. M. Bollen, R. H. Jackson and E. A Coutsias, AMRC-R-451 (1983), unpublished.

A HIGH FREQUENCY VIRCATOR MICROWAVE GENERATOR

(Beams '83 - Fifth International Conference on
High Power Particle Beams)

A HIGH FREQUENCY VIRCATOR MICROWAVE GENERATOR

Donald J. Sullivan
Mission Research Corporation
1720 Randolph Road, S. E.
Albuquerque, New Mexico 87106

Abstract

The virtual cathode oscillator (Vircator) has the potential for producing very high power microwave pulses in the centimeter and millimeter wavelength regimes. In a foilless diode configuration it is tunable by adjusting the imposed axial magnetic field. This permits high frequency operation. In a foil diode or reflex triode tuning is accomplished by changing the A-K gap spacing. The microwave generation will be coherent and efficient, if electron reflexing into the diode region is prevented. Gigawatt power levels have already been produced in the centimeter regime.

For an injected current a factor of three greater than the limiting current, $f_{osc} \sim \omega_p^{rel)}/\sqrt{2\pi}$. Because the oscillating beam is equivalent to a deformable dipole, the preferred waveguide mode for an axisymmetric beam in a straight-walled cylindrical guide is TM_{0n} where $n = D/\lambda_0$, D is the waveguide diameter and λ_0 is the free space wavelength. Thus, D/λ_0 should be chosen to be close to an integer value. Note that both the limiting current and the cutoff wavelength depend on the guide dimensions and geometry. Both must be considered in choosing an experimental configuration.

Introduction

Of the several millimeter sources that are in various stages of development, the virtual cathode oscillator (Vircator) has a combination of characteristics which recommend it for high frequency use. First, the frequency of the vircator is tunable by changing the magnitude of an imposed axial magnetic field, eliminating any requirement to change the physical structure of the device. A single vircator will be tunable over an order of magnitude in frequency (e.g., 10 GHz - 100 GHz). Second, the bandwidth of the generator can be narrow or broad based on magnetic field shaping and the use of beam collimators described below. Third, because the vircator functions above the space-charge limiting current for the electron beam, given efficient operation, it should be capable of much higher power than other microwave sources. Finally, the lack of passive resonating structures to produce the transmitted wave reduces the problem of field emission. This also increases the maximum possible generator power.

Experimentally, the virtual cathode has already proven itself to be a copious microwave source [1-7]. With the exception of the Tomsk experiment [4] the frequency spectra have all had a broad bandwidth and relatively low efficiency. Nevertheless, even at low efficiency the experiment at Harry Diamond Laboratories [5] using a foilless diode (1 MV, 30 kA) produced gigawatts of power in the Ku band. It is one of the most powerful centimeter wavelength microwave sources available. It will be shown later that the foilless diode in a shaped axial magnetic field represents the best configuration for a high frequency device.

Microwave Generation

Although only scaling relations are presently available, qualitative dependencies of virtual cathode parameters on beam kinetic energy and injected current are known [8,9]. First, potential amplitude, position, and oscillation frequency all have the same functional dependence on injected beam current. These parameters asymptotically approach a limiting value for current above the space-charge limit. Second, the fundamental oscillation frequency is approximately the relativistic beam plasma frequency given by

$$\omega_p^{rel} = \left(\frac{4\pi n_b^0 e^2}{\gamma_0 m} \right)^{1/2} \tag{1}$$

where n_b^0 is the electron beam number density at injection γ_0 is the beam relativistic factor, e is the electron charge and m is its mass. In particular, the oscillation frequency from one-dimensional electrostatic and two-dimensional electromagnetic numerical simulations varies such that

$$\omega_p^{rel} \leq \omega_{osc} \leq \sqrt{2\pi}\, \omega_p^{rel} . \tag{2}$$

The value of $\sqrt{2\pi}$ is an empirical result which has not yet been derived theoretically. The value of ω_{osc} increases with current monotonically. If the injection current exceeds the space-charge limiting current by a factor of three or greater, ω_{osc} is close to the maximum value. Eq. (1) in conjunction with the Child-Langmuir law describing space-charge limited diode emission explains the experimental linear dependence of frequency on the square root of diode voltage in foil diodes and reflex triodes. This analysis also

shows that the freuqency is inversely proportional to the anode-cathode (A-K) gap spacing d.

The virtual cathode oscillates stably at a set frequency in both time and space. This fluctuating potential barrier acts as a gate to reflect some electrons and transmit others. The motion of the gate bunches charge. In two dimensions the charge bunch and virtual cathode are separated spatially.
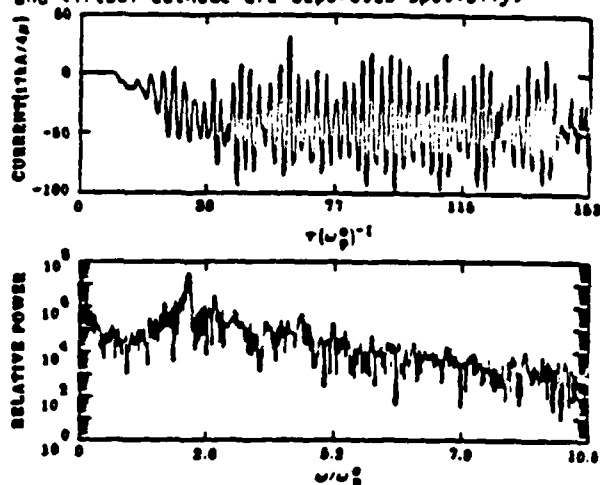

Figure 1. Net current amplitude and spectrum for a probe placed between the anode and virtual cathode. $\gamma_0 = 3.5$, $v_0 = 3.4$ v_ℓ.

By analogy this configuration represents an LC oscillator. The virtual cathode acts as a capacitor to store the beam kinetic energy. During that portion of the limit cycle in which the potential is greater than the injected beam energy, charge is constrained to remain near the anode. This starves the virtual cathode so that its amplitude decreases below $(\gamma_0 -1)$ mc^2/e. Once this occurs the charge bunch is transmitted. The electron motion represents a large time varying current through an inductor. The presence of charge away from the anode reestablishes the virtual cathode, and the cycle repeats. The effect on beam current can be examined using simulations. A net current diagnostic is given in Fig. 1 where the probe is positioned between the anode and virtual cathode. The injected current in units of mc^3/e, v_0, is 3.4 times the limiting current, v_ℓ, and γ_0 is 3.5. Note that the virtual cathode can actually reverse the direction of current. The average current value is v_ℓ.

The oscillating current generates microwaves [10,11]. The wave frequency is the oscillation frequency of the virtual cathode. The wave propagates down the drift tube in a TM waveguide mode, which determines the wavelength and phase velocity of the wave in the guide. The field configuration is evident in simulations where there is no axial magnetic field. If a cold beam is injected and azimuthal symmetry is assumed by the code, the only nonzero fields are E_z, E_r, and B_θ in cylindrical geometry. These three fields define a TM wave traveling in the z direction.

The largest impediment to constructing an efficient vircator is the effect which heating has on the microwave generation efficiency. As noted earlier [12], beam temperature significantly damps out the amplitude of the potential oscillation. This can be understood in the following way. For a monoenergetic beam all of the charged particles bunch at the same location. Mathematically this represents a singularity where the charge density goes to infinity. In reality the charge bunch is not infinitely dense, but it does become several times greater than the initial beam injection density. The severity of the charge bunching leads to efficient microwave generation. If, on the other hand, the beam has a spread in axial momentum, the electrons will stop at different locations in the potential well. This tends to limit the charge bunching and the amplitude of the oscillating electric and magnetic fields. The effect of beam temperature in reducing the RF efficiency of the vircator has been witnessed in one-dimensional electromagnetic simulations [13]. A beam spread of less than 3% in energy reduces the microwave generation efficiency from 20% to approximately 2%. Under these conditions the vircator is nothing more than a Barkhausen oscillator [14]. Indeed, the low efficiency and broad bandwidth observed in most of the experiments to date can probably be attributed to the effects of electron reflexing in the diode region resulting in beam heating.

Vircator Design

Based on our current theoretical knowledge of the virtual cathode, numerical simulations, and experimental results, the following points must be considered in the design of a coherent, high frequency vircator. First, generation of high microwave frequencies requires large beam densities. Extremely high beam densities ($n_b^0 > 10^{14}$ cm^{-3}) have been obtained from a foilless diode. The beam plasma frequency scales linearly with the electron cyclotron frequency due to the imposed axial magnetic field [15]. This is of significance, because it implies that a single vircator can be tuned over an order of magnitude in frequency (e.g., 10-100 GHz) simply by changing the axial magnetic field strength without changing the physical structure of the device.

References

1. R. A. Mahaffey, P. Sprangle, J. Golden and C. A. Kapetanakos, Phys. Rev. Lett. **39**, 843 (1977).

2. H. E. Brandt, A. Bromborsky, H. B. Bruns, and R. A. Kehs, in *Proc. of the 2nd Intl. Top. Conf. on High Power Electron and Ion Beam Research and Technology*, (Cornell University, Ithaca, New York, 1977), p. 649.

3. J. M. Buzzi, H. J. Doucet, B. Etlicher, P. Haldenwang, A. Huetz, H. Lamain, C. Rouille, J. Cable, J. De'vaux, J. C. Jouys and C. Peugnet, idem, p. 663.

4. A. N. Didenko, G. P. Fomenko, I. Z. Gleizer, Ya. E. Krasik, G. V. Melnikov, S. F. Perelygin, Yu. G. Shtein, A. S. Sulakshin, V. I. Tsvetkov, and A. G. Zerlitsin, in *Proc. of the 3rd Intl. Top. Conf. on High Power Electron and Ion Beam Research and Technology*, (Institute of Nuclear Physics, Novosibirsk, USSR, 1979), p. 683.

5. A. Bromborsky, H. Brandt, and R. A. Kehs, Bull. Am. Phys. Soc. **26**, 165 (1981); and private communication.

6. M. C. Clark, private communication.

7. C. A. Ekdahl, private communication.

8. D. J. Sullivan and E. A. Coutsias in *High Power Beams '81*, Proceedings of the 4th Intl. Top. Conf. on High Power Electron and Ion Beam Research and Technology, edited by H. J. Doucet and J. M. Buzzi (Ecole Polytechnique, Palasieau, France, 1981), p. 371.

9. E. A. Coutsias and D. J. Sullivan, Phys. Rev. A **27**, 1535 (1983).

10. D. J. Sullivan, Bull. Am. Phys. Soc. **25**, 948 (1980).

11. D. J. Sullivan, in *Proc. of the 3rd Intl. Top. Conf. on High Power Electron and Ion Beam Research and Technology*, (Institute of Nuclear Physics, Novosibirsk, USSR, 1979), p. 769.

12. W. B. Bridges and C. K. Birdsall, J. Appl. Phys. **34**, 2945 (1963).

13. M. A. Mostrom, T. J. T. Kwan and C. M. Snell, Bull. Am. Phys. Soc. **27**, 1075 (1982).

14. H. Barkhausen and K. Kurz, Phys. Zeit. **21**, 1 (1920).

15. M. E. Jones and L. E. Thode, J. Appl. Phys. **51**, 5212 (1980).

16. R. B. Miller, K. R. Prestwich, J. W. Poukey, and S. L. Shope, J. Appl. Phys. **51**, 3506 (1980).

EFFECTS OF THERMAL SPREAD ON THE SPACE CHARGE LIMIT
OF AN ELECTRON BEAM

Effects of thermal spread on the space charge limit of an electron beam

By E. A. COUTSIAS

Department of Mathematics, University of New Mexico,
Albuquerque, NM 87131

An asymptotic analysis is carried out to calculate the effects of a small thermal spread in the injection energy of an electron beam on its space charge limit. It is found that the space charge limit is lowered proportionally to the beam temperature T near $T = 0$.

1. Introduction

Recent applications of intense charged particle beams in such areas as inertial confinement fusion and microwave generation (Coutsias & Sullivan 1963, and references therein) has necessitated a deepening of our understanding of the basic physics of space charge limited flows. An excellent review of our present state of knowledge can be found in Miller (1982).

In particular, many authors have carried out calculations of the space charge limit (SCL) of electron and ion beams (Voronin, Zozulya & Lebedev 1972; Read & Nation 1975; Genoni & Proctor 1960). These are concerned mostly with mono-energetic beams in various geometries. Although the importance of thermal effects is recognized, no analytical estimates of the effect of thermal spread on the beam kinetic energy at injection have appeared.

Here we present an asymptotic method to estimate the modification of the SCL due to a small thermal spread. For simplicity we limit our discussion to one-dimensional, classical motion. However, the method can be applied to any of the other situations for which SCL estimates exist and produce appropriate corrections.

2. Effect of temperature on the space charge limit

An adequate discussion of the properties of a non-relativistic electron beam in one dimension can be found in Coutsias & Sullivan (1983). Here we shall treat the beam as a one-dimensional electron gas flowing between two conducting grid planes, at fixed potential. For the density range we consider ($\simeq 10^{13}$ cm^{-3}) the usual collisionless approximation is valid, and thus the electron distribution function satisfies the Vlasov equation

$$\partial_t f + u\, \partial_x f + (e/m_i)\, E\, \partial_u f = 0 \tag{1}$$

where t, x, u are the time, position and velocity variables, respectively, and E is the self-consistent electric field.

The electron charge density is given by

$$n = \int_u f(x,u,t)\,du, \tag{2}$$

and the electric field is found from

$$\partial_x E = (1/\epsilon_0)n, \tag{3}$$

while the potential $\phi(x,t)$ is given by

$$\partial_x \phi = -E. \tag{4}$$

The boundary conditions are given for the potential

$$\phi(0,t) = \phi_0 > 0, \quad \phi(l,t) = 0, \tag{5}$$

and the distribution function

$$\left.\begin{array}{ll} f(0,u,t) \text{ specified for } u > 0 & \text{(incoming flow at } x=0)\\ f(l,u,t) = 0 \qquad \text{for } u < 0 & \text{(no incoming flow at } x=l) \end{array}\right\} \tag{6}$$

This specification is valid also in the presence of multiple streams.

We shall model the effect of finite source temperature by specifying the incoming distribution $f(0,u,t)$, $u > 0$ as

$$f(0,u,t) = n_0 \left(\frac{m}{2\pi kT}\right)^{\frac{1}{2}} \exp\left(\frac{m(u-V)^2}{2kT}\right), \tag{7}$$

where T, assumed to be small, plays the role of an effective beam temperature.

For small enough T, we shall assume that we have a regime of steady behaviour, in analogy to the cold beam case. For steady states, particle energy is conserved and the solution to (1) is of the form (Davidson 1974)

$$f(x,u,t) = n_0 \left(\frac{m}{2\pi kT}\right)^{\frac{1}{2}} \exp\left(-\frac{m[V - (u^2 + (2e/m)(\phi(x)-\phi_0))^{\frac{1}{2}}]^2}{2kT}\right). \tag{8}$$

Then, combining (2), (3), (4) and (6) we find that the potential satisfies the equation

$$\phi_{xx} + \frac{n_0}{\epsilon_0}\left(\frac{m}{2\pi kT}\right)^{\frac{1}{2}} \int_{u_m}^{\infty} \exp\left(-\frac{m[V - (u^2 + (2e/m)(\phi(x)-\phi_0))^{\frac{1}{2}}]^2}{2kT}\right) du = 0, \tag{9}$$

where u_m, the velocity cut-off, is equal to

$$u_m(x) = \pm [(2e/m)(\phi_m - \phi(x))]^{\frac{1}{2}}. \tag{10}$$

Here ϕ_m is the potential minimum, the $(+)$ sign applies to the right and the $(-)$ to the left of the position $x = \zeta$ of the potential minimum as shown in Appendix A. We define

$$J(\phi;T) = \int_{u_m}^{\infty} \exp\left(-\frac{m[V - (u^2 + (2e/m)(\phi(x)-\phi_0))^{\frac{1}{2}}]^2}{2kT}\right) du. \tag{11}$$

So (9) can be written as

$$\phi_{xx} + \frac{n_0 e}{\epsilon_0}\left(\frac{m}{2\pi kT}\right)^{\frac{1}{2}} J(\phi;T) = 0. \tag{12}$$

By introducing the variable

$$s = (u^2 + (2e/m)(\phi(x) - \phi_0))^{\frac{1}{2}} - V \tag{13}$$

the integral $I(\phi; T)$ in (12) can be rewritten as

$$I(\phi; T) = \int_{u=|u_m|}^{\infty} \exp\left(-\frac{ms^2}{2kT}\right) du + 2H(\xi - x)\int_{u=0}^{|u_m|} \exp\left(-\frac{ms^2}{2kT}\right) du. \tag{14}$$

The first of the integrals in (14) represents the transmitted flow, while the second is due to particles without sufficient energy to cross the potential minimum and which are therefore reflected and return to the anode. Equation (12) with the integral term given by (14) is very hard to solve for a finite temperature T, but for small T we can approximate the integrals in (14) by Laplace's method. As is well known (Erdelyi 1956), in approximating integrals of this type with a strong maximum at an interior point, the dominant contribution comes from the neighbourhood of this point. Thus, in (14) we can approximate $I(\phi; T)$ by

$$I(\phi; T) \simeq \int_{-\infty}^{\infty} \exp\left(-\frac{ms^2}{2kT}\right) du + O\left(\exp\left(-\frac{ms_m^2}{2kT}\right)\right) \tag{14a}$$

where $-s_m = V - ((2e/m)(\phi_m - \phi_0))^{\frac{1}{2}}$. Then provided V is large enough so that the mean energy of the beam is never of order $O(kT)$, the correction term goes to zero faster than any power of T as $T \to 0$, and therefore is negligible to the order that we carry the calculations. Nevertheless, it gives us an estimate of the domain of validity of the subsequent discussion, for which we need

$$\exp(-ms_m^2/2kT) \ll kT. \tag{14b}$$

Therefore we write

$$I(\phi; \epsilon) \simeq \int_{-\infty}^{\infty} \exp\left(-\frac{ms^2}{2kT}\right) du = \int_{-\infty}^{\infty} \frac{(s + V)\exp(-ms^2/2kT)}{((s + V)^2 - (2\epsilon/m)(\phi(x) - \phi_0))^{\frac{1}{2}}} ds, \tag{15}$$

and we get for the potential the approximate equation

$$\phi_{xx} + \frac{n_0}{\epsilon_0}\left(\frac{m}{2\pi kT}\right)^{\frac{1}{2}} \int_{-\infty}^{\infty} -\frac{(s + V)\exp(-ms^2/2kT)}{((s + V)^2 - (2\epsilon/m)(\phi(x) - \phi_0))^{\frac{1}{2}}} ds = 0. \tag{16}$$

This can be integrated once to give

$$\tfrac{1}{2}\phi_x^2 + J(\phi; T) = J(\phi_m; T) \tag{17}$$

where

$$J(\phi; T) = -\frac{n_0 m}{\epsilon_0 e}\left(\frac{m}{2\pi kT}\right)^{\frac{1}{2}} \int_{-\infty}^{\infty} (s + V)$$

$$\times \left((s + V)^2 - \left(\frac{2\epsilon}{m}\right)(\phi(x) - \phi_0)\right)^{\frac{1}{2}} \exp(-ms^2/2kT) ds. \tag{18}$$

Integrating once more we find

$$x = \xi \pm 2^{-\frac{1}{2}} \int_{\phi_m}^{\phi} \frac{d\phi}{(J(\phi_m; T) - J(\phi; T))^{\frac{1}{2}}} \equiv \xi \pm S(\phi_m, \phi; T). \tag{19}$$

Imposing the boundary conditions at $x = 0$ and $x = l$ we are led to the two equations determining ξ and ϕ_m

$$0 = \xi - S(\phi_m, \phi_0; T), \quad l = \xi + S(\phi_m, 0, T). \tag{20}$$

Eliminating ξ we find

$$l = S(\phi_m, \phi_0; T) + S(\phi_m, 0; T) \tag{21}$$

which must be analysed in order to determine, among other things, the desired steady state for the potential ϕ (and hence the distribution function f) and the SCL for small temperature $T > 0$.

To get an approximate expression for ϕ_m as $T \to 0$ we note that $J(\phi; T)$ can be approximated by Laplace's method if we expand the non-exponential part of the integrand in a Taylor series about $s = 0$ and integrate term by term. We find, after some algebra that

$$\left(-\frac{\epsilon_0 e}{n_0 m}\right) J(\phi; T) \simeq VR(\phi) + \frac{\epsilon V}{2}\left(\frac{R^2(\phi) - (e/m)(\phi - \phi_0)}{R^3}\right) + O(\epsilon^2) \tag{22}$$

where $\epsilon = (2kT/m) \ll 1$ and $R(\phi) = (V^2 - (2e/m)(\phi(x) - \phi_0))^{\frac{1}{2}}$. Using (22) we now approximate S:

$$S(\phi_m, \phi; T) = 2^{-\frac{1}{2}}\int_{\phi_m}^{\phi}\frac{d\phi}{(J(\phi_m; T) - J(\phi, T))^{\frac{1}{2}}} \simeq \left(\frac{\epsilon_0 e}{2n_0 m V}\right)^{\frac{1}{2}}$$

$$\times \int_{\phi_m}^{\phi}\frac{d\phi}{(R - R_m)^{\frac{1}{2}}}\left(1 - \frac{\epsilon}{4}\left(\frac{(V^2 - \Phi)R_m^3 - (R_m^2 - \Phi_m)R^3}{R^3 R_m^3(R - R_m)}\right) + O(\epsilon^2)\right) \tag{23}$$

where we set $R = R(\phi)$, $R_m = R(\phi_m)$, $\Phi = (e/m)(\phi(x) - \phi_0)$, $\Phi_m = (e/m)(\phi_m - \phi_0)$ and since $d\phi = -(m/\epsilon)RdR$,

$$S(\phi_m, \phi; T) \simeq \left(\frac{2\epsilon_0 m}{9\epsilon n_0 V}\right)^{\frac{1}{2}}(R(\phi) - R(\phi_m))^{\frac{1}{2}}(R(\phi) + 2R(\phi_m)) + \epsilon\left(\frac{\epsilon_0 m}{2\epsilon n_0 V}\right)^{\frac{1}{2}}$$

$$\times \left((R - R_m)^{\frac{1}{2}}\left(\frac{3}{4R_m} - \frac{V^2}{4R_m^3} - \frac{V^2}{8RR_m^3}\right) - \frac{3V^2}{8R_m^{\frac{5}{2}}}\sec^{-1}\frac{R^{\frac{1}{2}}}{R_m^{\frac{1}{2}}}\right) + O(\epsilon^2). \tag{24}$$

This can be substituted in (21) to find ϕ_m, which in turn will allow us to determine ξ, the position of the potential minimum from (20) and, finally, we can combine all this information in (19) to get the desired relation between x and ϕ.

For simplicity we demonstrate this for the unbiased case, $\phi_0 = 0$. Letting

$$R(0) = R(\phi_0) = V, \quad s = R_m/V, \quad \hat{\epsilon} = \epsilon/V^2,$$

and introducing

$$a = 9\epsilon n_0 V^2/8\epsilon_0 m V^2,$$

(21) becomes

$$a^{\frac{1}{2}} \simeq (1 - s)^{\frac{1}{2}}\left((1 + 2s) + \frac{3}{2}\hat{\epsilon}\left(\frac{3}{4s} - \frac{1}{4s^2} - \frac{1}{8s^2} - \frac{3\sec^{-1}s^{-\frac{1}{2}}}{8s^{\frac{5}{2}}(1 - s)^{\frac{1}{2}}}\right) + O(\hat{\epsilon}^2)\right). \tag{25}$$

We note that to leading order ($\epsilon = 0$), (24) reduces to the usual expression for cold beams. By including the $O(\hat{\epsilon})$ corrections we can find the first-order correction to the SCL. This is the value of a for which (24) has a double root. We find

$$a = a_0 + \hat{\epsilon}a_1 + \dots, \quad s = s_0 + \hat{\epsilon}s_1 + \dots,$$

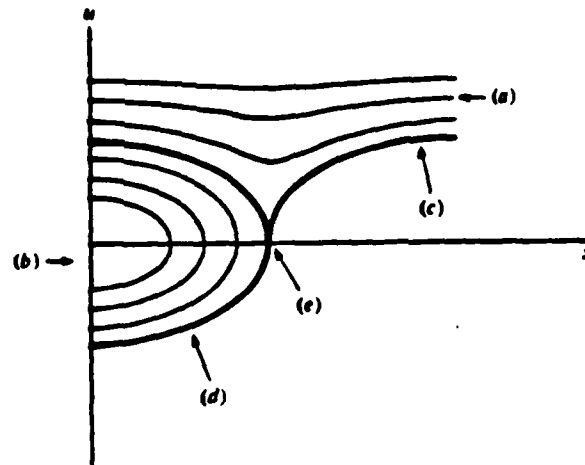and substitution yields

$$a_0 = 2, \quad s_0 = \frac{1}{3}.$$

FIGURE 1. Phase plane. (a) Transmitted particles, (b) reflected particles, (c) $u_m = ((2e/m)(\phi_m - \phi(x)))^{\frac{1}{2}}$, (d) $u_m = -((2e/m)(\phi_m - \phi(x)))^{\frac{1}{2}}$, (e) ξ, location of potential minimum, $\phi(\xi) = \phi_m$.

from which we find a_1:

$$a_1 = -3(1 + \tfrac{2}{3}\pi) = -10.07.$$

That is, the SCL is given by

$$\frac{en_0 l^2}{\epsilon_0 m l'^2} = \tfrac{1}{9} - (\tfrac{2}{3} + 2\pi)\left(\frac{2kT}{m l'^2}\right) + O(T^2)$$

so that, for $T \ll 1$, the *SCL* is decreased in proportion to the temperature.

Appendix A

From the steady-state momentum equation

$$u u_x = (e/m) E \tag{A 1}$$

we find by integration that

$$\tfrac{1}{2}u^2 + \frac{e}{m}\rho(x) = \text{constant.} \tag{A 2}$$

At $x = 0$, $u = u_0$, $\rho = \rho_0$ and

$$\tfrac{1}{2}u^2 + \frac{e}{m}\rho(x) = \tfrac{1}{2}u_0^2 + \frac{e}{m}\rho_0. \tag{A 3}$$

Since (1) is a statement of the conservation of f along particle trajectories, we find that if u and u_0 are related by (A 3) then

$$f(x, u, t) = f(0, u_0, t) \tag{A 4}$$

and expression (6) follows.

A complication arises when we are dealing with reflected particles since u in

318   *E. A. Coutsias*

(A 3) can have either sign. Assuming that the potential achieves a unique minimum $\rho = \rho_m$ at some location $x = \xi$, we find that particles that arrive at ξ with zero velocity must start at $x = 0$ with velocity $u_m(0)$ such that

$$\tfrac{1}{2}u_m^2(0) + \frac{e}{m}\rho_0 = \tfrac{1}{2}u_m^2(x) + \frac{e}{m}\rho(x) = \frac{e}{m}\rho_m.$$

At each point $x < \xi$ particles with velocities less than u_m will be reflected before reaching $x = \xi$ while faster particles will be transmitted across the potential barrier. To the left of the potential minimum therefore, we shall have particles with velocities larger than $((2e/m)(\rho_m - \rho(x)))^{\frac{1}{2}}$ composing the flow that will be transmitted, and particles with velocities in the range

$$|u| < ((2e/m)(\rho_m - \rho(x)))^{\frac{1}{2}}$$

composing the counterstreaming flow (figure 1). To the right of the potential minimum we have only particles with velocities larger than u_m, so that the potential minimum has filtered out of the flow particles whose energies were too small to traverse it.

REFERENCES

DAVIDSON, R. C. 1974 *Theory of Non-neutral Plasmas*. Benjamin.
COUTSIAS, E. A. & SULLIVAN, D. J. 1963 *Phys. Rev. A*, **27**, 1535
ERDELYI, A. 1956 *Asymptotic Expansions*. Dover.
GENONI, T. C. & PROCTOR, W. A. 1980 *J. Plasma Phys.* **23**, 129.
MILLER, R. B. 1982 *An Introduction to the Physics of Intense Charged Particle Beams*. Plenum.
READ, M. E. & NATION, J. A. 1975 *J. Plasma Phys.* **13**, 127.
VORONIN, V. S., ZOZULYA, YU. T. & LEBEDEV, A. N. 1972 *Soviet Phys. Tech. Phys.* **17**, 432

END

FILMED

11-85

DTIC